

SYNTHESIS AND TRIBOLOGICAL STUDY OF HIGH ENTROPY ALLOYS

Ph.D. Thesis

**Saurav Kumar
(2014RMT9504)**



**DEPARTMENT OF METALLURGICAL AND MATERIALS ENGINEERING
MALAVIYA NATIONAL INSTITUTE OF TECHNOLOGY JAIPUR
JANUARY, 2020**

SYNTHESIS AND TRIBOLOGICAL STUDY OF HIGH ENTROPY ALLOYS

Submitted in

fulfillment of the requirement for the degree of

Doctor of Philosophy

by

Saurav Kumar

(Student ID: 2014RMT9504)

Under the Supervision of

Dr. Ajaya Kumar Pradhan
(Supervisor)

Dr. Amar Patnaik
(Co-Supervisor)

Dr. Vinod Kumar
(External Supervisor)



DEPARTMENT OF METALLURGICAL AND MATERIALS ENGINEERING
MALAVIYA NATIONAL INSTITUTE OF TECHNOLOGY JAIPUR
JANUARY, 2020

© Malaviya National Institute of Technology Jaipur - 2020.

All rights reserved.

Dedicated to
my teachers, friends, and family
members

DECLARATION

I, **Saurav Kumar**, declare that this thesis titled, “**Synthesis and Tribological Study of High Entropy Alloys**” and the work presented in it, are my own. I confirm that:

- This work was done wholly or mainly while in candidature for a research degree at this institution.
- Where any part of this thesis has previously been submitted for a degree or any other qualification at this institution or any other university, this has been clearly stated.
- Where I have consulted the published work of others, this is always clearly attributed.
- Where I have quoted from the work of others, the source is always given. With the exception of such quotations, this thesis is entirely my own work.
- I have acknowledged all main sources of help.
- Where the thesis is based on work done by myself, jointly with others, I have made clear exactly what was done by others and what I have contributed myself.

Date:

Saurav Kumar
(2014RMT9504)

CERTIFICATE

This is to certify that the thesis entitled “**Synthesis and Tribological Study of High Entropy Alloys**” being submitted by **Mr. Saurav Kumar (ID: 2014RMT9504)** is a bonafide research work carried out under my supervision and guidance in fulfillment of the requirement for the award of the degree of **Doctor of Philosophy** in the **Department of Metallurgical and Materials Engineering**, Malaviya National Institute of Technology, Jaipur, India. The matter embodied in this thesis is original and has not been submitted to any other University or Institute for the award of any other degree.

Dr. Ajaya Kumar Pradhan
(Supervisor)

Dept. of Metallurgical &
Materials Engineering
MNIT, Jaipur, India

Dr. Amar Patnaik
(Co - supervisor)

Dept. of Mechanical
Engineering
MNIT, Jaipur, India

Dr. Vinod Kumar
(Ext. supervisor)

Discipline of
Metallurgy Engg. & Materials
science
IIT Indore, India

Date:

Place: Jaipur

ACKNOWLEDGEMENT

First, I am really indebted to my thesis supervisor(s) **Dr. Ajaya Kumar Pradhan and Dr. Amar Patnaik** who provided me precious opportunity to pursue research under their guidance. I also extend my special thankfulness to my external supervisor **Dr. Vinod Kumar** for his guidance and providing a new platform of wonderful and challenging materials world. His unique guiding quality, interest, working enthusiasm and analytical approach towards the experimental results impressed me very much. It is a great honor for me to work with him.

I would like to express my sincere thanks to **Dr. V. K. Sharma, and Dr. S. K. Gupta** for their encouragement, analytical insights and recommendations as DREC members of my PhD. I further extend my thanks to all the staff members of **Materials Research Center (MNIT Jaipur), ACMS (IIT Kanpur) and particularly Prof. Anandh Subramaniam (IIT Kanpur)** for providing arc-melting facilities. I am also thankful to all the staff members and research scholars of **Advance Research Laboratory for Tribology (MNIT Jaipur)** for helping in Air Jet Erosion and Pin-on-disk facilities and **Institute Research Grant (MNIT Jaipur)** for the financial support. I am also thankful to all **Head of Department, Metallurgical and Materials Engineering** for giving me access to all laboratories after the regular working hours. I express my deep appreciation to my friends and co-workers **Dr. Ornov Maulik, Dr. Anil Kumar, Dr. Vikas Kukshal, Dr. Devesh Kumar, Mr. Ankit Goyal** and all the post graduate students of Department of Metallurgical and Materials Engineering and Advance Research Laboratory for Tribology, MNIT Jaipur for their moral support and help. I would like to extend my sincere thanks to all the faculty and staff members of MNIT, Jaipur for their support during my Ph.D. I would like to thank **my parents, elder brother, sister and all family members** for their unconditional support without which this thesis would not have been possible.

Date:

MNIT Jaipur

(Saurav Kumar)

Abstract

In the present research work, two different high entropy alloy systems ($\text{Al}_x\text{CrFe}_{1.5}\text{MnNi}_{0.5}$ and $\text{Al}_{0.4}\text{FeCrNiCo}_x$) have been studied. The high entropy alloys are fabricated by two different techniques. The $\text{Al}_x\text{CrFe}_{1.5}\text{MnNi}_{0.5}$ ($x = 0.3$ and 0.5 mol) HEAs are developed through mechanical milling and conventional sintering route and $\text{Al}_{0.4}\text{FeCrNiCo}_x$ ($x = 0, 0.25, 0.5$ and 1.0 mol) HEAs are developed through arc melting route.

The phase analysis of $\text{Al}_x\text{CrFe}_{1.5}\text{MnNi}_{0.5}$ ($x = 0.3$ and 0.5 mol) HEAs is carried out using X-ray diffractometry, and transmission electron microscopy. The surface morphology and composition are investigated using scanning electron microscopy and energy-dispersive spectroscopy, respectively. Thermodynamic parameters are calculated and analyzed to explain the formation of a solid solution. The XRD analysis has revealed that the major and the minor phases in $\text{Al}_x\text{Fe}_{1.5}\text{CrMnNi}_{0.5}$ ($x = 0.3$ and 0.5) high-entropy alloys are of BCC and FCC structure, respectively. Analysis of selected area electron diffraction pattern of powder sample of $\text{Al}_x\text{Fe}_{1.5}\text{CrMnNi}_{0.5}$ ($x = 0.3$ and 0.5) HEAs concurred with the XRD analysis results. Microstructural features and mechanism for solid solution formation have been conferred in detail. Differential scanning calorimetric analysis have confirmed substantial change in phase at a temperature of 935.12 °C in case of the $\text{Al}_{0.3}\text{Fe}_{1.5}\text{CrMnNi}_{0.5}$ HEA. The effect of aluminum content and different sintering atmosphere on phase evolution, hardness, density, and air jet erosion property are investigated. The air jet erosion study of the sintered alloys is investigated at 90° , 75° , 60° , and 45° angle of impingement.

A sequence of $\text{Al}_{0.4}\text{FeCrNiCo}_x$ ($x=0, 0.25, 0.5$ and 1.0 mol) high entropy alloys is developed by arc melting route to investigate the effect of cobalt content on thermal, mechanical, and microstructural properties. The phase, microstructure and chemical composition are analyzed using X-ray diffraction, transmission electron microscope, and scanning electron microscope with attached energy dispersive X-ray spectrometer. The obtained results have shown that the $\text{Al}_{0.4}\text{FeCrNiCo}_x$ ($x = 0$ to 0.5 mol) high entropy alloys form a simple FCC+BCC type solid solution, and the $\text{Al}_{0.4}\text{FeCrNiCo}_{x=1}$ HEA forms a single phase FCC structure. The compressive

yield strength, microhardness and thermal conductivity are observed to decrease from 965.22 MPa to 233.37 MPa, 253.6 HV to 155.6 HV and from 4.87 W/mK to 2.674 W/mK, respectively, whereas the electrical resistivity is observed to increase from 150.30 $\mu\Omega\text{-cm}$ to 273.74 $\mu\Omega\text{-cm}$ with the addition of cobalt from $x = 0$ to 1 mol. Differential scanning calorimetry analysis has indicated that the $\text{Al}_{0.4}\text{FeCrNiCo}_x$ ($x = 0, 0.25, 0.5$ and 1.0 mol) high entropy alloys are thermally stable up to 1000°C.

The phase and microstructural characterizations of homogenized $\text{Al}_{0.4}\text{FeCrNiCo}_x$ ($x = 0, 0.25, 0.5$ and 1.0 mol) HEAs are performed by utilizing X-ray photoelectron spectroscopy and scanning electron microscope. The compressive yield strength in case of $\text{Al}_{0.4}\text{FeCrNiCo}_x$ ($x = 0, 0.25, 0.5$ and 1.0 mol) HEAs is observed to decrease from 1169.35 MPa to 257.63 MPa. Plastic deformation up to 75% is achieved in the case of $\text{Al}_{0.4}\text{FeCrNiCo}_{x=1}$ HEA. The microhardness of homogenized HEA samples is found to decrease from 377 HV to 199 HV after the addition of cobalt content from $x = 0$ to 1.0 mol. Thermal analysis is performed using a differential scanning calorimeter. It is confirmed that homogenized $\text{Al}_{0.4}\text{FeCrNiCo}_x$ ($x = 0, 0.25, 0.5$ and 1.0 mol) HEAs do not undergo any phase change up to 1000 °C.

The dry sliding wear behavior of homogenized $\text{Al}_{0.4}\text{FeCrNiCo}_x$ ($x = 0, 0.25, 0.5$ and 1.0 mol) high entropy alloys (HEAs) at room temperature are investigated by varying sliding speed, sliding distance and normal load conditions at room temperature. The wear analysis indicates that the specific wear rate is highest in the case of $\text{Al}_{0.4}\text{FeCrNiCo}_{x=1}$ HEA under all condition. The worn surface is analyzed using scanning electron microscopy with attached energy dispersive x-ray spectroscopy, 3D profiling, and X-ray photoelectron spectroscopy (XPS) in order to understand the wear mechanism and the oxides formed during the wear process. The results have indicated that the wear occurred due to adhesion along with delamination, plastic flow, and oxidative wear. XPS results have confirmed the presence of Al_2O_3 , Fe_2O_3 , Cr_2O_3 , and Co_3O_4 oxides on the worn surface.

The wear behavior of $\text{Al}_{0.4}\text{FeCrNiCo}_x$ ($x = 0, 0.25, 0.5$ and 1.0 mol) HEAs under oil lubricating conditions is also investigated under varying sliding speed, sliding distance and normal load condition at room temperature. The specific wear rate of $\text{Al}_{0.4}\text{FeCrNiCo}_{x=1}$ HEA is observed to be highest under all wear conditions. The worn surfaces are analyzed by SEM with attached energy-dispersive spectroscopy, 3D profiling, and X-ray photoelectron spectroscopy (XPS) in order to

understand the wear mechanism and oxides formed during the wear process. The mode of wear is observed to be the combined effect of adhesive, abrasive wear along with plastic flow of material. The XPS results have confirmed the presence of Al_2O_3 , Fe_2O_3 , Cr_2O_3 oxides on the worn surface of $\text{Al}_{0.4}\text{FeCrNiCo}_{x=1}\text{HEA}$ along with the presence of a high molecular weight polymer or alcoholic group.

List of Publication from PhD work

1. **Saurav Kumar**, D. Kumar, O. Maulik, A.K. Pradhan, V. Kumar, A. Patnaik, Synthesis and Air Jet Erosion Study of $Al_xFe_{1.5}CrMnNi_{0.5}$ ($x = 0.3, 0.5$) High-Entropy Alloys, *Metallurgical and Materials Transaction A*, 49, 5607-5618, 2018.
2. **Saurav Kumar**, A. Patnaik, A. K. Pradhan, V. Kumar, Effect of cobalt content on thermal, mechanical, and microstructural property of $Al_{0.4}FeCrNiCo_x$ ($x=0, 0.25, 0.5$ and 1.0 mol) high entropy alloys, *Journal of Materials Engineering and Performance*, 28, 4111-4119, 2019.
3. **Saurav Kumar**, A. Patnaik, A. K. Pradhan, V. Kumar, Dry sliding wear behavior of $Al_{0.4}FeCrNiCo_x$ ($x=0, 0.25, 0.5, 1.0$ mol) High Entropy Alloys. *Metallography, Microstructure, and Analysis*, 8, 545-557, 2019.
4. **Saurav Kumar**, A. Patnaik, A. K. Pradhan, V. Kumar, Room temperature wear study of $Al_{0.4}FeCrNiCo_x$ ($x=0, 0.25, 0.5$ and 1.0 mol) high entropy alloys under oil lubricating condition, *Journal of Material Research*, 34, 841-853, 2019.
5. **Saurav Kumar**, P. Rani, A Patnaik, A K Pradhan, V Kumar, Effect of cobalt content on wear behavior of $Al_{0.4}FeCrNiCo_x$ ($x = 0, 0.25, 0.5, 1.0$ mol) high entropy alloys tested under demineralised water with and without 3.5 % NaCl solution, *Materials Research Express*, 6, 0865b3, 2019.
6. O. Maulik, D. Kumar, **Saurav Kumar**, S. Devagan, and V. Kumar, Light weight high entropy alloys: A brief review, *Materials research express*, 5, 052001, 2018.

List of Publication other than PhD work

7. D. Kumar, O. Maulik, **Saurav Kumar**, Y.V.S.S. Prasad, V. Kumar, Phase and thermal study of equiatomic AlCuCrFeMnW high entropy alloy processed via spark plasma sintering, *Material Chemistry and physics*, 210, 71-77, 2018.
8. D. Kumar, O. Maulik, **Saurav Kumar**, Y.V.S.S. Prasad, V.K.Sharma, V. Kumar, Impact of tungsten on phase evolution in nanocrystalline AlCuCrFeMnW $_x$ ($x=0, 0.05, 0.1$ and 0.5 mol) high entropy alloys, *Material research express*, 4, 2017.
9. O. Maulik, D. Kumar, **Saurav Kumar**, D. M. Fabijanic, and V. Kumar, Structural evolution of spark plasma sintered AlFeCuCrMg $_x$ ($x=0, 0.5, 1, 1.7$) high entropy alloys, *Intermetallics*, 77, 46-56, 2016.
10. S. P. Saini, **Saurav Kumar**, R. Barman, A. Dixit, V. Kumar, Oxidation Study of Mg-Li-Al based Alloy, *Materials Today Proceeding*, 3, 3035-3044, 2016.

Table of Contents

	Page No.
DECLARATION	(i)
CERTIFICATE	(ii)
ACKNOWLEDGEMENT	(iii)
ABSTRACT	(iv)
LIST OF FIGURES	(xiv)
LIST OF TABLES	(xix)
ABBREVIATIONS	(xxi)

CHAPTER 1:

INTRODUCTION	1-5
1.1 Background and motivation	1
1.2 Development of high entropy alloys	1
1.3 Thesis framework	3

CHAPTER 2:

LITERATURE REVIEW	6-44
2.1 High Entropy Alloys (HEAs)	6
2.2 Four core effect of HEA	7
2.2.1 High-entropy effect	7
2.2.2 Severe lattice distortion effect	7
2.2.3 Sluggish Diffusion Effect	8
2.2.4 Cocktail Effect	9
2.3 High Entropy Alloys classification	9
2.3.1 Refractory HEAs	9

2.3.2	Light weight HEAs	9
2.3.3	High Entropy-Bulk Metallic Glasses (HE-BMGs)	10
2.3.4	High-Entropy Superalloys (HESAs)	10
2.4	Thermodynamics for Phase formation in high entropy alloys	10
2.5	Characteristic of different alloying elements	11
2.5.1	Enthalpy of mixing (kJ/mol) of possible atomic-pairs in Al-Fe-Cr-Ni-Co and Al-Fe-Cr-Mn-Ni high entropy alloys	12
2.6	Fabrication Technique	13
2.6.1	Melting and casting route	13
2.6.2	Laser Fabrication Method	14
2.6.3	Solid State Processing Route	15
2.6.4	Sputtering	16
2.7	Erosion and wear behavior of HEAs	17
2.7.1	Erosion behavior of HEAs	17
2.7.2	Sliding wear behavior of HEAs under different medium	19
2.7.2.1	Wear under dry condition	19
2.7.2.2	Wear under oil and other medium	26
2.8	Literature on synthesis route, phase and mechanical properties of high entropy alloys	29
2.8.1	Literature on Al-Cr-Fe-Mn-Ni HEA system	29
2.8.2	Literature on equi-atomic Al-Fe-Cr-Ni-Co HEA system	32
2.8.2.1	Effect of Al in Al-Fe-Cr-Ni-Co HEA system	34
2.8.2.2	Effect of Fe, Cr and Ni in Al-Fe-Cr-Ni-Co HEA system	38
2.8.2.3	Effect of Co in Al-Fe-Cr-Ni-Co HEA system	39
2.9	Research gap	41
2.9.1	Proposed objective of the Research work	41
2.10	Working methodology for synthesis and characterization of high entropy alloys	42
2.10.1	Working methodology for development of HEAs through mechanical milling and conventional sintering route	42
2.10.2	Working methodology for development of HEAs through arc melting route	43

CHAPTER 3:

MATERIALS AND METHODS 45-54

3.1.	Materials and synthesis technique	45
3.1.1.	Properties of alloying elements used for the development of HEAs	45
3.1.2.	Fabrication of $Al_xFe_{1.5}CrMnNi_{0.5}$ ($x = 0.3$ and 0.5 mol) HEAs through mechanical milling and conventional sintering route	46
3.1.3.	Fabrication of $Al_{0.4}FeCrNiCo_x$ ($x=0, 0.25, 0.5$ and 1.0 mol) HEAs through arc melting route	47

3.1.4	Homogenization of as-cast $Al_{0.4}FeCrNiCo_x$ ($x=0, 0.25, 0.5$ and 1.0 mol)HEAs	48
3.2.	Characterization of high entropy alloys	48
3.2.1.	Phase evolution study of HEAs using X-ray diffraction (XRD)	48
3.2.2.	Microstructural examination of HEA using scanning electron microscope (SEM)	48
3.2.3.	Phase evolution study of HEAs using Transmission electron microscopy (TEM)	49
3.3	Physical, thermal and mechanical analysis of high entropy alloys	49
3.3.1.	Density	49
3.3.2.	Thermal conductivity	50
3.3.3.	Differential scanning calorimetry	50
3.3.4.	Microhardness measurements	50
3.3.5.	Room temperature compressive testing	51
3.4	Air jet erosion and sliding wear measurement	51
3.4.1	Air jet erosion test	51
3.4.2	Sliding wear test	52

CHAPTER 4:

	Synthesis, characterization and air jet erosion study of $Al_xFe_{1.5}CrMnNi_{0.5}$ ($x= 0.3$ and 0.5) high entropy alloys	55-72
4.1	Introduction	55
4.2	Phase evolution of $Al_xFe_{1.5}CrMnNi_{0.5}$ ($x = 0.3$ and 0.5 mol) HEAs	55
4.3	Morphology and Mechanism of alloy formation	58
4.4	TEM analysis of $Al_xFe_{1.5}CrMnNi_{0.5}$ ($x=0.3$ and 0.5) HEA after milling	60
4.5	Thermal analysis of 20 hrs milled $Al_xFe_{1.5}CrMnNi_{0.5}$ ($x = 0.3$ and 0.5) HEAs Powder	63
4.6	Thermodynamic parameter of $Al_xCrFe_{1.5}MnNi_{0.5}$ ($x = 0.3$ and 0.5) HEAs	63
4.7	Microstructure and Phase Analysis of Sintered $Al_xCrFe_{1.5}MnNi_{0.5}$ ($x = 0.3$ and 0.5 mol) HEA	65
4.8	Bulk Density and Microhardness of $Al_xFe_{1.5}CrMnNi_{0.5}$ ($x = 0.3$, and 0.5 mol) HEAs	67
4.9	Air Jet Erosion Test	67
4.10	Comparison with reported results	71

CHAPTER 5:

Synthesis, and characterization of as-casted and homogenized $\text{Al}_{0.4}\text{FeCrNiCo}_x$ ($x=0, 0.25, 0.5$ and 1.0 mol) HEAs via arc melting route **73-93**

5.1	Introduction	73
5.2	Analysis of as-cast $\text{Al}_{0.4}\text{FeCrNiCo}_x$ ($x=0, 0.25, 0.5$ and 1.0 mol) HEAs	73
5.2.1	Microstructure and phase analysis of as-cast $\text{Al}_{0.4}\text{FeCrNiCo}_x$ ($x=0, 0.25, 0.5$ and 1.0 mol) HEAs	73
5.2.2	Thermal analysis of as-cast $\text{Al}_{0.4}\text{FeCrNiCo}_x$ ($x=0, 0.25, 0.5$ and 1.0 mol) HEAs	78
5.2.3	Thermal conductivity of as-cast $\text{Al}_{0.4}\text{FeCrNiCo}_x$ ($x=0, 0.25, 0.5$ and 1.0 mol) HEAs	78
5.2.4	Mechanical Property as-cast $\text{Al}_{0.4}\text{FeCrNiCo}_x$ ($x=0, 0.25, 0.5$ and 1.0 mol) HEAs	80
5.2.6	Thermodynamic Parameters of $\text{Al}_{0.4}\text{FeCrNiCo}_x$ ($x=0, 0.25, 0.5$ and 1.0 mol) HEAs	82
5.3	Analysis of homogenized $\text{Al}_{0.4}\text{FeCrNiCo}_x$ ($x=0, 0.25, 0.5$ and 1.0 mol) HEAs	85
5.3.1	Microstructural, and Phase analysis of homogenized $\text{Al}_{0.4}\text{FeCrNiCo}_x$ ($x=0, 0.25, 0.5$ and 1.0 mol) HEAs	85
5.3.2	Thermal analysis of homogenized $\text{Al}_{0.4}\text{FeCrNiCo}_x$ ($x=0, 0.25, 0.5$ and 1.0 mol) HEAs	89
5.3.3	Density of homogenized $\text{Al}_{0.4}\text{FeCrNiCo}_x$ ($x=0, 0.25, 0.5$ and 1.0 mol) HEAs	90
5.3.4	Microhardness of homogenized $\text{Al}_{0.4}\text{FeCrNiCo}_x$ ($x=0, 0.25, 0.5$ and 1.0 mol) HEAs	90
5.3.5	Compressive strength of homogenized $\text{Al}_{0.4}\text{FeCrNiCo}_x$ ($x=0, 0.25, 0.5$ and 1.0 mol) HEAs	91
5.4	Comparison with reported results	92

CHAPTER 6:

Wear behavior of $\text{Al}_{0.4}\text{FeCrNiCo}_x$ ($x=0, 0.25, 0.5$ and 1.0 mol) HEAs under dry and lubricating oil condition **94-127**

6.1	Introduction	94
6.2	Correlation between specific wear rate, hardness, and cobalt content	94
6.3	Wear behavior of $\text{Al}_{0.4}\text{FeCrNiCo}_x$ ($x=0, 0.25, 0.5$ and 1.0 mol) HEAs under dry condition	95
6.3.1	Effect of sliding Speed on wear behavior of $\text{Al}_{0.4}\text{FeCrNiCo}_x$ ($x=0,$	95

	0.25, 0.5 and 1.0 mol)HEAs	
6.3.1.1	worn surface and wear debris analysis under sliding speed condition	97
6.3.2	Effect of normal loading on wear behavior of Al _{0.4} FeCrNiCo _x (x=0, 0.25, 0.5 and 1.0 mol) HEAs	102
6.3.2.1	Worn surface and wear debris analysis under normal loading condition	104
6.3.3	Effect of sliding distance on wear behavior of Al _{0.4} FeCrNiCo _x (x=0, 0.25, 0.5 and 1.0 mol)HEAs	108
6.3.3.1	Worn Surface and wear debris Analysis under sliding distance condition	110
6.3.4	X-ray photoelectron spectroscopy of Al _{0.4} FeCrNiCo _{x=1} HEA under dry condition	112
6.4	Wear behavior of Al _{0.4} FeCrNiCo _x (x=0, 0.25, 0.5, 1.0 mol) HEAs under oil condition	115
6.4.1	Effect of Sliding Speed on wear behavior of Al _{0.4} FeCrNiCo _x (x=0, 0.25, 0.5 and 1.0 mol)HEAs under lubricating oil condition.	115
6.4.2	Effect of Sliding distance on wear behavior of Al _{0.4} FeCrNiCo _x (x=0, 0.25, 0.5 and 1.0 mol)HEAs under lubricating oil condition.	116
6.4.3	Effect of Normal Loads on wear behavior of Al _{0.4} FeCrNiCo _x (x=0, 0.25, 0.5 and 1.0 mol)HEAs under lubricating oil condition.	118
6.4.4	Worn surface and wear mechanism under lubricating oil condition	119
6.4.5	X-ray Photoelectron Spectroscopy of Al _{0.4} FeCrNiCo _{x=1} HEA under lubricating oil condition	123
6.5	Comparison with reported results	126

CHAPTER 7:

Conclusions and scope for future work **128-130**

7.1	Summary of present research work	122
7.2	Scope for future work	124

REFERENCES **131-142**

APPENDICES

LIST OF PUBLICATIONS

BRIEF BIODATA OF THE AUTHOR

List of Figures

Figure No.	Figure caption	Page No.
Figure 1.1	Summary of research and development taking place in the field of HEA	3
Figure 2.1	Classification of alloys based on configurational entropy with examples	6
Figure 2.2	Large lattice distortion in (a) BCC lattice and (b) in AlFeCuCrMg _x HEA	7
Figure 2.3	Comparison between pure metals, stainless steels, and CoCrFeMnNi HEA in terms of normalized activation energy of diffusion and melting point, for Cr, Mn, Fe, Co, and Ni in different matrices	8
Figure 2.4	Various synthesis routes of HEAs	13
Figure 2.5	Systematic diagram of arc melting method	14
Figure 2.6	Systematic diagram of Laser-engineered net shaping (LENS)	15
Figure 2.7	(a) cross-section of milling in tumbler (b) phenomena of fracture and welding during ball milling	16
Figure 2.8	Layout of SPS processing	16
Figure 2.9	Schematic diagram showing the sputtering deposition	17
Figure 2.10	XRD patterns of as-cast and aged sample of Al _x CrFe _{1.5} MnNi _{0.5} (x = 0.3 and 0.5)	29
Figure 2.11	SEM micrograph of as-cast Al _x CrFe _{1.5} MnNi _{0.5} HEA (a) x = 0.3 and (b) x = 0.5 (DR: dendrite, ID: interdendrite)	30
Figure 2.12	XRD pattern of homogenized Al _x CoCrFeNi (0 ≤ x ≤ 2) HEA	35
Figure 2.13	SEM micrograph of homogenized Al _x CoCrFeNi (0 ≤ x ≤ 2) HEA	35
Figure 2.14	TEM of Al _{0.3} CoCrFeNi HEA and the selected area diffraction patterns (SADP) of region A and B	35
Figure. 2.15	Working methodology for the development Al _x Fe _{1.5} CrMnNi _{0.5} (x = 0.3 and 0.5 mol) HEAs	42
Figure. 2.16	Working methodology for the development of Al _{0.4} FeCrNiCo _x (x = 0, 0.25, 0.5 and 1.0 mol) HEAs	43

Figure 3.1	(a) cold compacted pellet and as casted HEA samples in (b) cylindrical shape and (c) button shape	47
Figure 3.2	Specimen for compression test	51
Figure 3.3	Specimen for pin-on-disk	52
Figure 4.1	XRD patterns of milled powders after 10 min, 5 hrs, 10 hrs, 15 hrs, 20 hrs of milling in case of (a) $\text{Al}_{0.3}\text{CrFe}_{1.5}\text{MnNi}_{0.5}$ HEA and (b) $\text{Al}_{0.5}\text{CrFe}_{1.5}\text{MnNi}_{0.5}$ HEA	56
Figure 4.2	Deconvoluted XRD pattern of 20 hrs milled powder of (a) $\text{Al}_{0.3}\text{CrFe}_{1.5}\text{MnNi}_{0.5}$ HEA (b) $\text{Al}_{0.5}\text{CrFe}_{1.5}\text{MnNi}_{0.5}$ HEA	57
Figure 4.3	Crystallite size and lattice strain as a function of milling time for the BCC phase of (a) $\text{Al}_{0.3}\text{Fe}_{1.5}\text{CrMnNi}_{0.5}$ HEA and (b) $\text{Al}_{0.5}\text{Fe}_{1.5}\text{CrMnNi}_{0.5}$ HEA.	57
Figure 4.4	Morphology of $\text{Al}_{0.3}\text{Fe}_{1.5}\text{CrMnNi}_{0.5}$ (Al0.3) HEA after different milling times (a) 10 min (b) 5 hrs (c) 10 hrs (d) 20 hrs.	58
Figure 4.5	Morphology of $\text{Al}_{0.5}\text{Fe}_{1.5}\text{CrMnNi}_{0.5}$ (Al0.5) HEA after different milling time (a) 10 min (b) 5 hrs (c) 10 hrs and (d) 20 hrs.	59
Figure 4.6	TEM-EDS analysis of 20 hrs milled powder of (a) $\text{Al}_{0.3}\text{CrFe}_{1.5}\text{MnNi}_{0.5}$ and (b) $\text{Al}_{0.5}\text{CrFe}_{1.5}\text{MnNi}_{0.5}$ HEA.	60
Figure 4.7	Typical TEM micrographs of 20 h milled powder of $\text{Al}_{0.3}\text{CrFe}_{1.5}\text{MnNi}_{0.5}$ HEA, (a) bright field image, (b) SAED pattern (c) HR-TEM image, (d) TEM dark field image, and (e) crystallite size distribution which gave us an average crystallite size of 1.7396 nm	61
Figure 4.8	Typical TEM micrographs of 20 hrs milled powder of $\text{Al}_{0.5}\text{CrFe}_{1.5}\text{MnNi}_{0.5}$ HEA (a) bright field image (b) SAED pattern (c) HR-TEM image, (d) TEM dark field image, and (e) crystallite size distribution, which give an average crystallite size of 1.45793 nm.	62
Figure 4.9	DSC scan of 20h milled powder of $\text{Al}_x\text{CrFe}_{1.5}\text{MnNi}_{0.5}$ ($x = 0.3$ and 0.5) HEAs	63
Figure 4.10	XRD analysis of HEA sintered at different environment (a) $\text{Al}_{0.3}\text{CrFe}_{1.5}\text{MnNi}_{0.5}$ HEA (b) $\text{Al}_{0.5}\text{CrFe}_{1.5}\text{MnNi}_{0.5}$ HEA	66
Figure 4.11	BSE micrographs of $\text{Al}_x\text{Fe}_{1.5}\text{CrMnNi}_{0.5}$ ($x=0.3$ and 0.5) HEA (a) Al0.3, vacuum sintered (S-1) (b) Al0.3, air sintered (S-2) (c) Al0.5, vacuum sintered (S-3) (d) Al0.5, air sintered (S-4)	66
Figure 4.12	Variation of erosion value with a different angle of impingement (a) $\text{Al}_{0.3}\text{Fe}_{1.5}\text{CrMnNi}_{0.5}$ HEA and (b) $\text{Al}_{0.5}\text{Fe}_{1.5}\text{CrMnNi}_{0.5}$ HEA for sintered under different conditions.	69

Figure 4.13	Optical Macrograph of $\text{Al}_{0.3}\text{Fe}_{1.5}\text{CrMnNi}_{0.5}$ HEA showing the eroded surface at various impact angles (a) 45° (b) 75° and (c) 90°	70
Figure 4.14	Eroded surface profile of $\text{Al}_{0.3}\text{Fe}_{1.5}\text{CrMnNi}_{0.5}$ HEA at various impact angles (a) 45° (b) 75° and (c) 90°	70
Figure. 5.1	X-ray diffraction of as-cast $\text{Al}_{0.4}\text{FeCrNiCo}_x$ ($x = 0, 0.25, 0.5$ and 1.0 mol) HEAs	74
Figure. 5.2	SEM micrograph of as-cast (a) $\text{Co}=0$ HEA (b) $\text{Co}=0.25$ HEA (c) $\text{Co}=0.5$ HEA (d) $\text{Co}=1$ HEA	75
Figure. 5.3	TEM bright field, SAED pattern and dark field of as-cast HEA (a-c) $\text{Co}=0$ HEA (d-f) $\text{Co}=0.25$ HEA (g-i) $\text{Co}=0.5$ HEA	76
Figure. 5.4	STEM and TEM- EDS analysis of as-cast (a) $\text{Co}=0$ (b) $\text{Co}=0.25$ (c) $\text{Co}=0.5$ HEAs	77
Figure. 5.5	DSC analysis for as-cast $\text{Al}_{0.4}\text{FeCrNiCo}_x$ ($x = 0, 0.25, 0.5$ and 1.0 mol) HEAs	78
Figure. 5.6	Thermal conductivity of $\text{Al}_{0.4}\text{FeCrNiCo}_x$ ($x = 0, 0.25, 0.5$ and 1.0 mol) HEAs	79
Figure. 5.7	Engineering stress–strain curves of as-cast, $\text{Al}_{0.4}\text{FeCrNiCo}_x$ ($x = 0, 0.25, 0.5$ and 1.0 mol) HEAs under compression at room temperature	81
Figure. 5.8	Variation of (a) VEC, (b) enthalpy and entropy of mixing with cobalt content from $x=0$ to 1.0 mol	83
Figure. 5.9	Variation of $\delta\%$ and Ω with cobalt content from $x=0$ to 1.0 mol.	83
Figure. 5.10	(a) X-ray diffraction pattern of homogenized $\text{Al}_{0.4}\text{FeCrNiCo}_x$ ($x = 0, 0.25, 0.5, 1.0$ mol) HEAs (b) variation of phase fraction with cobalt content	86
Figure. 5.11	SEM micrographs of homogenized (a) $\text{Co}=0$ (b) $\text{Co}=0.25$ (c) $\text{Co}=0.5$ (d) $\text{Co}=1$ HEAs	86
Figure. 5.12	EDS Mapping of homogenized $\text{Al}_{0.4}\text{FeCrNiCo}_x$ ($x = 0, 0.25, 0.5$ and 1.0 mol) HEAs.	88
Figure. 5.13	DSC micrograph of homogenized $\text{Al}_{0.4}\text{FeCrNiCo}_x$ ($x=0, 0.25, 0.5, 1.0$ mol) HEAs	89
Figure. 5.14	Engineering stress-strain curve of homogenized $\text{Al}_{0.4}\text{FeCrNiCo}_x$ ($x=0, 0.25, 0.5$ and 1.0 mol) HEAs under compression at room temperature, (b) image of $\text{Co}=1$ HEA sample during the compression test.	91
Figure. 6.1	Variation of microhardness and specific wear rate of $\text{Al}_{0.4}\text{FeCrNiCo}_x$ ($x=0, 0.25, 0.5$ and 1.0 mol) HEAs as a function of cobalt content	95

Figure. 6.2	Effect of variation in sliding speed on (a) coefficient of friction and (b) specific wear rate of $Al_{0.4}FeCrNiCo_x$ ($x=0, 0.25, 0.5$ and 1.0 mol)HEAs.	96
Figure. 6.3	(a-d) Optical micrographs of worn surfaces of $Al_{0.4}FeCrNiCo_x$ ($x=0, 0.25, 0.5$ and 1.0 mol)HEAs tested under the constant wear conditions of 2 m/s sliding speed, 1000 m sliding distance, and 10 N normal load.	99
Figure. 6.4	(a, d, g and j) SEM micrographs of worn surfaces, (b, e, h and k) EDS result of worn surface and (c, f, i, and l) 3D profile of $Al_{0.4}FeCrNiCo_x$ ($x=0, 0.25, 0.5$ and 1.0 mol)HEAs tested under the constant wear conditions of 2 m/s sliding speed, 1000 m sliding distance, and 10 N normal load.	100
Figure. 6.5	(a-d) SEM micrographs of wear debris of $Al_{0.4}FeCrNiCo_x$ ($x=0, 0.25, 0.5$ and 1.0 mol)HEAs tested under the constant wear conditions of 2 m/s sliding speed, 1000 m sliding distance, and 10 N normal load.	101
Figure. 6.6	Effect of variation in normal loading on (a) coefficient of friction (b) specific wear rate of $Al_{0.4}FeCrNiCo_x$ ($x=0, 0.25, 0.5$ and 1.0 mol)HEAs.	103
Figure. 6.7	Optical micrograph of worn surface of $Al_{0.4}FeCrNiCo_x$ ($x=0, 0.25, 0.5$ and 1.0 mol)HEAs tested under 20 N normal load, 1000 m sliding distance and 1 m/s speed.	104
Figure. 6.8	(a, d, g and j) SEM micrographs of worn surfaces, (b, e, h and k) EDS result of worn surface and (c, f, i, and l) 3D profile of $Al_{0.4}FeCrNiCo_x$ ($x=0, 0.25, 0.5$ and 1.0 mol)HEAs tested under 20 N normal load, 1000 m sliding distance and 1 m/s speed.	106
Figure. 6.9	(a-d) SEM micrograph of wear debris of $Al_{0.4}FeCrNiCo_x$ ($x=0, 0.25, 0.5$ and 1.0 mol)HEAs tested under 20 N normal load, 1000 m sliding distance and 1 m/s speed.	107
Figure. 6.10	Effect of variation in sliding distance on (a) coefficient of friction and, (b) specific wear rate of $Al_{0.4}FeCrNiCo_x$ ($x=0, 0.25, 0.5$ and 1.0 mol)HEAs	109
Figure. 6.11	SEM micrograph of worn surface, wear debris, and distribution of wear debris diameter of (a-c) $Co=0$ HEA, (d-f) $Co=0.25$ HEA, (g-i) $Co=0.5$ HEA and (j-l) $Co=1$ HEA.	111
Figure. 6.12	XPS results of worn surface of $Co=1$ HEA tested at a constant wear condition of sliding speed of 1 m/s, sliding distance of 1000 m and normal load of 10 N under dry condition (a) survey spectra (b) $Al2p_{3/2}$ spectra (c) $Fe2p_{3/2}$ spectra (d) $Cr2p_{3/2}$ spectra (e) $Ni2p_{3/2}$ spectra (f) $Co2p_{3/2}$ spectra (g) $O1s$ spectra.	113
Figure. 6.13	Variation of (a) coefficient of friction and (b) specific wear rate of	115

	$\text{Al}_{0.4}\text{FeCrNiCo}_x$ ($x=0, 0.25, 0.5$ and 1.0 mol) HEAs under oil lubrication with varying sliding speed	
Figure. 6.14	Variation of (a) coefficient of friction and (b) specific wear rate of $\text{Al}_{0.4}\text{FeCrNiCo}_x$ ($x=0, 0.25, 0.5$ and 1.0 mol) HEAs under oil lubrication with varying sliding distance.	117
Figure. 6.15	Variation of (a) coefficient of friction and (b) specific wear rate of $\text{Al}_{0.4}\text{FeCrNiCo}_x$ ($x=0, 0.25, 0.5$ and 1.0 mol) HEAs under oil lubrication with varying normal load.	118
Figure. 6.16	(a-d) SEM micrographs, (e-h) 3D surface profile of worn surface of $\text{Al}_{0.4}\text{FeCrNiCo}_x$ ($x=0, 0.25, 0.5$ and 1.0 mol) HEAs at constant wear condition of (1000m, 10N, 1m/s) under oil lubrication.	122
Figure. 6.17	X-ray photoelectron spectra result of the worn surface of $\text{Al}_{0.4}\text{FeCrNiCo}_{x=1}$ HEA tested under oil lubrication condition (a) survey scan, (b) O1s spectra, (c) Al2p spectra, (d) Fe2p spectra, (e) Cr2p spectra, (f) Ni2p spectra, (g) Co2p spectra, (h) C1s spectra	124

List of Tables

Table No.	Table caption	Page No.
Table 2.1	Thermodynamic parameters predict the solid solution phase formation, and phase stability in HEA	11
Table 2.2	Atomic no., atomic weight, atomic radius, melting point, crystal structure, lattice parameter, VEC, and Pauling electronegativity of different alloying elements.	12
Table 2.3	Binary mixing enthalpy between alloying elements based on the Miedema's model	12
Table 2.4	Literature on erosion behavior of HEAs prepared through different synthesis routes, slurry, and tested under different slurry and testing parameters	18
Table 2.5	Literature on wear behavior of HEAs synthesized by different routes under dry condition and tested under different sliding condition	21
Table 2.6	Literature on wear behavior of HEAs, synthesis by different route under oil and other medium and performed at different sliding condition	27
Table 2.7	Literature on Al-Cr-Fe-Mn-Ni HEA system with synthesis route, phase, hardness, yield strength, and density	31
Table 2.8	Literature on equiatomic Al-Fe-Cr-Ni-Co HEA system with different synthesis route, phase, hardness, yield strength, and density.	33
Table 2.9	Literature on effect of Al in Al-Fe-Cr-Ni-Co HEA system	36
Table 2.10	Literature on effect of Fe, Cr and Ni in Al-Fe-Cr-Ni-Co HEA system	39
Table 2.11	Literature on effect of Co in Al-Fe-Cr-Ni-Co HEA system	40
Table 3.1	Physical and mechanical properties of various elements	46
Table 3.2	Parameters for pin-on-disk test	53
Table 4.1	EDS results (in at.%) of 20 hrs milled $Al_xFe_{1.5}CrMnNi_{0.5}$ ($x = 0.3$ and 0.5) HEAs	64
Table 4.2	Thermodynamic parameters of $Al_xFe_{1.5}CrMnNi_{0.5}$ ($x = 0.3$ and 0.5) alloys	65
Table 4.3	Variation of density and microhardness with sintering condition	68

Table 5.1	Lattice constant and volume fraction of as-cast $\text{Al}_{0.4}\text{FeCrNiCo}_x$ ($x = 0, 0.25, 0.5$ and 1.0 mol) HEAs	74
Table 5.2	EDS results (in at.%) of as-cast $\text{Al}_{0.4}\text{FeCrNiCo}_x$ ($x = 0, 0.25, 0.5$ and 1.0 mol) HEAs [AS: area scan, PS: point scan]	75
Table 5.3	Mechanical properties of $\text{Al}_{0.4}\text{FeCrNiCo}_x$ ($x = 0, 0.25, 0.5$ and 1.0) HEAs at room temperature	81
Table 5.4	EDS results of homogenized $\text{Al}_{0.4}\text{FeCrNiCo}_x$ ($x=0, 0.25, 0.5$ and 1.0 mol) HEAs	87
Table 6.1	EDS results of worn surfaces and wear debris of $\text{Al}_{0.4}\text{FeCrNiCo}_x$ ($x=0, 0.25, 0.5$ and 1.0 mol) HEAs tested under the wear conditions of 2 m/s sliding speed, 1000 m sliding distance, and 10 N normal load	101
Table 6.2	EDS results of worn surface and debris of $\text{Al}_{0.4}\text{FeCrNiCo}_x$ ($x=0, 0.25, 0.5$ and 1.0 mol) HEA tested under 20 N normal load, 1000 m sliding distance and 1 m/s speed.	108
Table 6.3	EDS results of worn surface and wear debris of $\text{Al}_{0.4}\text{FeCrNiCo}_x$ ($x=0, 0.25, 0.5$ and 1.0 mol) HEA produced under 4000 m sliding distance, 10 N normal load, and 1 m/s speed	112
Table 6.4	EDS result of worn surface of $\text{Al}_{0.4}\text{FeCrNiCo}_x$ ($x=0, 0.25, 0.5$ and 1.0 mol) HEAs at (1000 m, 10 N, 1 m/s) wear condition under oil lubrication.	120

List of Abbreviations

HEA	High Entropy Alloy
MA	Mechanical Alloying
SPS	Spark Plasma Sintering
AC	As Cast
XRD	X-Ray Diffraction
SEM	Scanning Electron Microscopy
BSE	Back Scattered Electron
EDS	Energy Dispersive X-Ray Spectroscopy
TEM	Transmission Electron Microscopy
STEM	Scanning Transmission Electron Microscopy
XPS	X-Ray Photoelectron Spectroscopy
DSC	Differential Scanning Calorimetry
BCC	Body Centered Cubic
FCC	Face Centered Cubic
SS	Solid Solution
TCP	Topologically Closed Packed
VEC	Valence Electron Concentration
ΔG_{mix}	Gibbs Free Energy of Mixing
ΔH_{mix}	Enthalpy of Mixing
ΔS_{mix}	Entropy of Mixing
ΔX	Electronegativity difference
δ	Atomic size mismatch
Ω	Thermodynamic parameter predicting solid solution formation
$T_{\text{m, th}}$	Theoretical Melting Temperature
R	Gas constant
W_s	Specific wear rate
COF	Coefficient of friction
Δm	Mass loss before and after the test
ρ	density
V_s	Sliding speed
f_n	Normal Load
BE	Binding Energy
VHP	Vacuum hot pressing

HIP	Hot isostatic pressing
PN	Plasma Nitriding
VAM	Vacuum arc melting
AM	Arc melting
IM	Induction melting
VIM	Vacuum induction melting
VLM	Vacuum-levitation melting
SEBM	Selective electron beam melting

Introduction

1.1 Background and Motivation

The development of human society is closely associated with the evolution of new materials. The saga of human civilization is categorized into stone, bronze, iron, and steel age etc. based on the wide spread use of definite materials. In the 18th century, during the period of the first industrial revolution and in the subsequent years the development of new materials started to satisfy the need of the newer application fields. It resulted in the development of countless metallic materials along with advanced alloys. These metallic materials were synthesized with various compositions and were fabricated using different processing routes. In recent years, with increasing innovation and growing industrial demand, the working environment of different materials is increasingly becoming difficult, e.g., agriculture, power generation, automobile, chemical industry, aviation industry and in heavy equipment, etc. Traditionally, in order to match the needs of specific applications, the materials (metallic) are designed based on the one or two elements as the base metal or solvent and various alloying elements or solute atom are then added to achieve the enhanced property. In general, all the existing materials can be thought to be present at the corners region and the edges of a phase diagram. This opens up countless opportunities to investigate the hidden materials in the central part of the phase diagram which have never been innovated.

1.2 Development of High entropy alloys

Cantor et al. and Yeh et al. working separately in different times put forward a new alloy design concept called the equiatomic and non-equiatomic multi-component alloying or the high entropy alloying [1, 2]. Cantor et al. have developed a five component $\text{Fe}_{20}\text{Cr}_{20}\text{Mn}_{20}\text{Ni}_{20}\text{Co}_{20}$ system on melt spinning, forming a FCC type solid solution, and they called it multi-component alloys. On the other hand, Yeh et al. have developed forty equiatomic alloys with 5 to 9 components by arc melting route, and they called them as High Entropy Alloys (HEAs). The configurational entropy

of these alloys is supposed to be very high in their random solution state which drives the system to form simple solid solutions, rather than complex microstructures with many compounds.

Traditionally, in conventional alloy system, only a small corner portion of a phase diagram is focused. However, after the development of new HEA concept, researchers have also concentrated on the central area of the phase diagram. Cantor et al. have also suggested that the overall feasible number of alloys (N) that can be developed with (C) no. of component when each alloy varies in composition by X % can be estimated as $N = (100/x)^{C-1}$ [1]. If the total number of elements in a periodic table that can make the alloys will be considered and if it will be assumed that each alloy varies by 1%, then the overall alloys that can be formed is 10^{78} , which is huge number.

The overall research and development that is taking place in the field of HEA can be summarized by the HEA hypertetrahedron (Fig. 1.1), whose corners denote a particular factor relating to the HEA like synthesis, composition, structure, properties, and modeling. The synthesis of HEAs can be made possible by ball milling and followed by various sintering methods like spark plasma sintering, conventional sintering, or microwave sintering. The fabrication of HEAs can also be carried out through melting route which includes arc melting and induction melting. It may be noted that each element present in the HEAs may be either of equiatomic or of non-equiatomic compositions and the percentage of individual elements lies in between 5 at.% to 35 at. %. The phase formed in HEAs is generally simple FCC, BCC or mixed phase of FCC and BCC. The reason behind the formation of these simple phases in multicomponent alloy is high mixing entropy. Phase diagram of HEAs can be predicted by the ThermoCal software, and CALPHAD is used to calculate their elastic properties. It is reported that these HEAs have better oxidation, corrosion resistance, and good wear resistance than the traditional alloys.

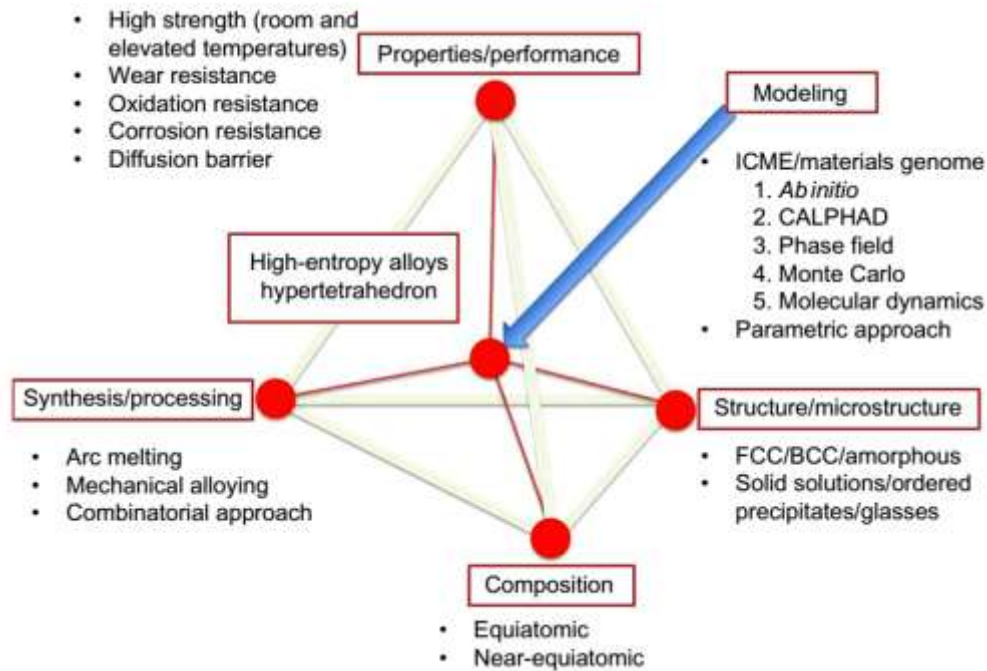


Fig.1.1 Summary of research and development taking place in the field of HEA [1]

1.3 Thesis Framework

The framework of the present research work is described as follows:

Chapter 1: Introduction

This chapter gives a brief background of high entropy alloys and indicating this research work includes seven chapters.

Chapter 2: Literature review

This chapter describes the HEAs, their core effects, and a literature review on the development of HEAs from the initials years to the present day. The main issues in the reported literature are highlighted and explained, which are related to the present study. The discussion related to the erosion, wear, phase formation and microstructures, thermal, mechanical, and physical properties of HEAs are also included in this chapter.

Chapter 3: Materials and methods

This chapter includes a elucidation of the fabrication techniques used for the development of the HEAs. A brief description of various equipment & theories related to synthesis, characterization and property evaluation of HEAs is also included.

Chapter 4: Synthesis and characterization of $Al_xCrFe_{1.5}MnNi_{0.5}$ ($x= 0.3$ and 0.5 mol) HEA through mechanical milling and conventional sintering route

This chapter includes discussion relating to the characterization of mechanically milled powder as well as the sintered $Al_xCrFe_{1.5}MnNi_{0.5}$ ($x= 0.3$ and 0.5 mol) HEAs from the view point of phase and microstructural evolution. Physical, thermal, and mechanical properties of the HEAs and air jet erosion behavior of sintered $Al_xCrFe_{1.5}MnNi_{0.5}$ ($x= 0.3$ and 0.5 mol) HEAs are also presented and discussed in this chapter.

Chapter 5: Synthesis and characterization of $Al_{0.4}FeCrNiCo_x$ ($x=0, 0.25, 0.5$ and 1.0 mol) HEA through arc melting route

This chapter includes characterization of $Al_{0.4}FeCrNiCo_x$ ($x=0, 0.25, 0.5$ and 1.0 mol) HEAs in as-cast and homogenized condition. Physical, thermal and mechanical properties of concerned HEAs in as-cast, as well as in homogenized condition are also presented and discussed.

Chapter 6: Wear study of $Al_{0.4}FeCrNiCo_x$ ($x=0, 0.25, 0.5$ and 1.0 mol) HEA under dry and oil lubricating condition

This chapter includes wear analysis of HEAs under varying sliding speed, sliding distance, and normal loading conditions, tested under different operating medium like, dry, and oil lubrication. Besides, scanning electron microscopy (SEM), energy dispersive spectroscopy (EDS), 3D profiling, X-ray photoelectron spectroscopy (XPS) of the worn surface and that of wear debris are also presented and discussed.

Chapter 7: Conclusions and future scope

This chapter summarizes, the research based on the outcome of various experiments and also highlights the future possible work related to the present study.

In the next chapter literature review has been done related to high entropy alloys.

Literature Review

2.1 High Entropy Alloys (HEAs)

High entropy alloys is the brand new alloy design concept and it can be defined in two different ways. High-entropy alloys have at least five principal elements, each of them has a concentration between 5 and 35 at.%. It is noted that no elements in high entropy alloys exceed 35 at.%. According to this definition, the high entropy alloys have three kinds of composition, equi-molar composition, non-equimolar compositions, and composition with minor additions of other elements [1, 3].

Figure 2.1 shows the division of alloys based on the configurational entropy. If the configurational entropy is greater than $1.5 R$ (R : gas constant) at the random-solution state it is called high entropy alloys and no. of elements in such system is 4 or more. If the configurational entropy is between $1R$ and $1.5 R$ it is called medium entropy alloys and number of elements in such system in between 3 to 4. If the configurational entropy is less than $1R$, it is called low entropy alloys and the number of elements in such system is less than 3 [1, 3].

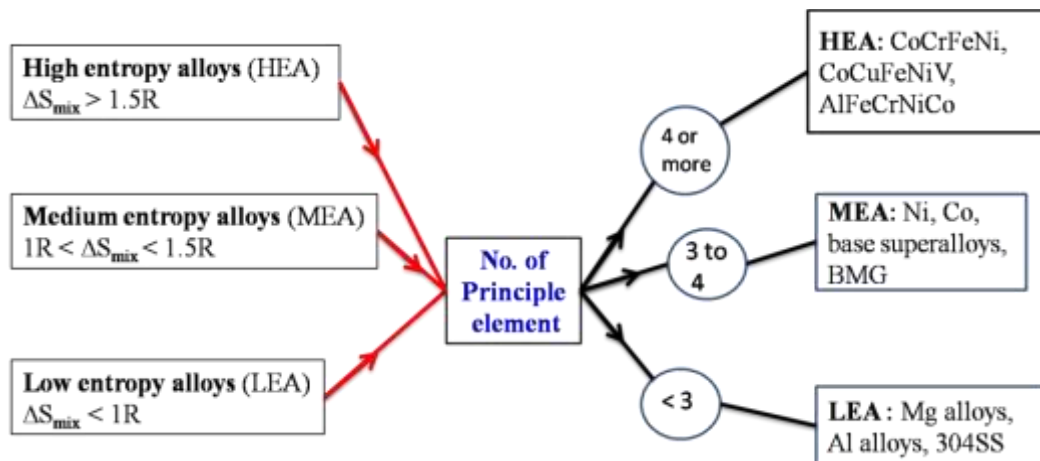


Fig. 2.1 Classification of alloys based on configurational entropy with examples [1]

2.2 Four core effect of HEA

The properties and microstructure of high entropy alloys depend upon many factors they are called four core effect.

2.2.1 High-entropy effect

Due to high number of element involved in the synthesis of HEA configurational entropy (ΔS_{mix}) becomes large which tends to reduce ΔG_{mix} and makes formation of simple solid solution structure more stable [4].

The governing equation known as Gibbs equation given by eq (1.1). It represents, if a system has lowest free energy of mixing (ΔG_{mix}) than that system is in thermodynamic equilibrium.

$$\Delta G_{mix} = \Delta H_{mix} - T\Delta S_{mix} \quad (1.1)$$

Where ΔS_{mix} and ΔH_{mix} are the mixing enthalpies and mixing entropy, it is observed that as the number of participating element increase, the free energy of mixing ΔG_{mix} decreases by increasing the entropy of mixing ΔS_{mix} [1, 2].

2.2.2. Severe lattice distortion effect

The matrix of multi-element in the solid solution for the HEAs leads to high lattice stress and strain mainly due to the different atomic radius associated with the individual elements. Figure 2.2 shows the lattice distortion effect neighboring where neighboring atom are not similar when compared to the traditional alloys.

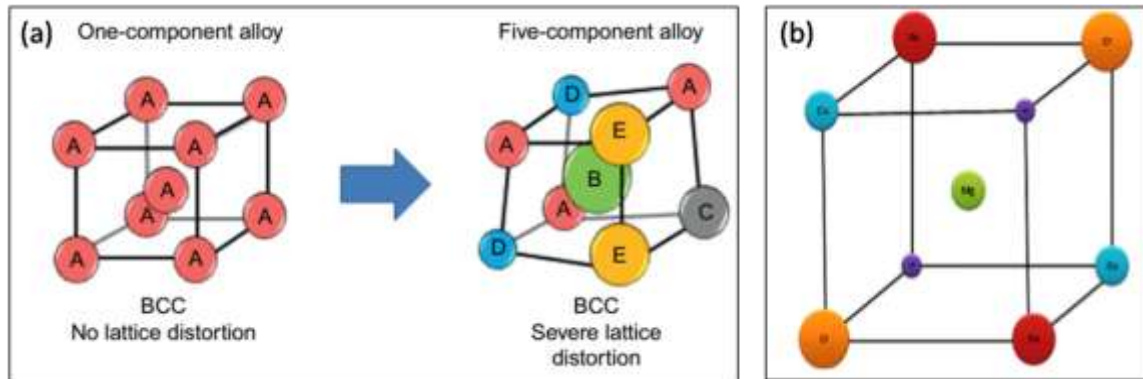


Fig. 2.2 Large lattice distortion in (a) BCC lattice and (b) in AlFeCuCrMg_x HEA [1, 5]

It affects various properties like increasing the hardness and strength by large solution strengthening, and significantly reduces the electrical and thermal conductivity. For example, In refractory HEA such as MoNbTaW and MoNbTaVW HEA, the large lattice distortion effect increases their strength many times like 4455 MPa and 5250 MPa and increases their microhardness three times as calculated from the rule of mixture [6].

2.2.3. Sluggish Diffusion Effect

It had been proposed that the sluggish diffusion in HEAs lowers the rate of diffusion in atoms which intern slows the phase conversion rate in the matrix of multi-element phase. The new phase formation from the old phase demands cooperative diffusion of many different kinds of atoms to fulfill the partitioning of the composition. In crystalline HEA, the equilibrium vacancy with least free energy of mixing at a fixed temperature is generated by the contest among the mixing enthalpy and the entropy.

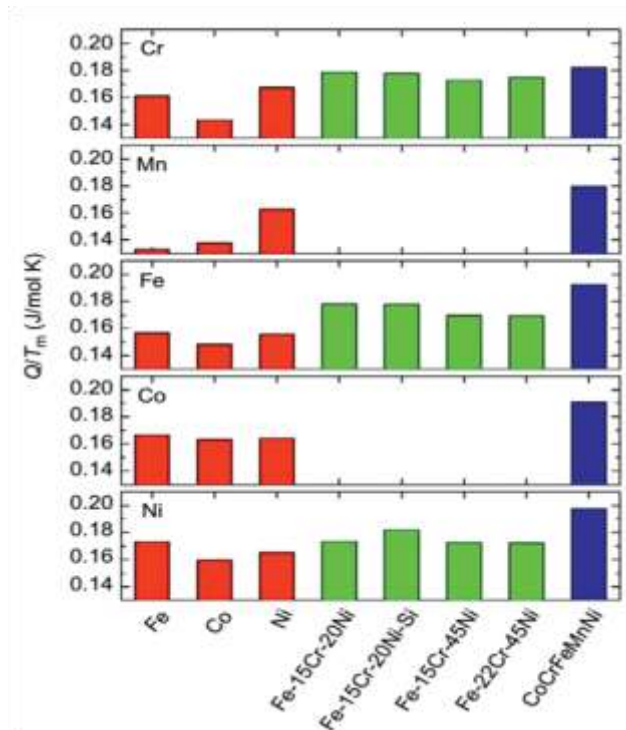


Fig. 2.3 Comparison between pure metals, stainless steels, and CoCrFeMnNi HEA in terms of normalized activation energy of diffusion and melting point, for Cr, Mn, Fe, Co, and Ni in different matrices [1, 7]

Therefore, the slow diffusion in HEA brings several advantages like, easy to achieve the supersaturated state, higher temperature of recrystallization, increased creep resistance, reduced particle coarsening rate, and slower grain growth. Figure 2.3 indicates that CoCrFeMnNi HEA has the highest melting point and normalized activation energy.

2.2.4. Cocktail Effect

The effect cocktail usually proposes that here can be unexpected properties obtained after mixing numerous elements in an alloy system, which could not be obtained from any single element. It is predicted that the total property of HEAs comes from the each phases. It results due to grain and phase boundaries, grain-size distribution grain morphology and properties of each phase. Following example are considered for better understanding. Refractory HEA like MoNbTaW and MoNbTaVW have a melting point nearly 2600°C which is higher than those of superalloys having Ni and Co. It is because the selected elements for alloying are refractory elements and, these alloys have higher resistance to softening than superalloys and having a mechanical strength of 400 MPa at 1600°C [8].

2.3. High Entropy Alloys classification

The development of materials is generally based on the requirements of particular application and the selection of proper control elements plays an essential role in the end properties of the material. Therefore, HEAs can be divided based on the suitable selection of the control elements. On the basis of the control elements, the HEAs are divided as light weight HEAs, bulk metallic glass HEAs, super alloys HEAs and refractory HEAs. These HEAs are discussed below.

2.3.1. Refractory HEAs

The refractory HEAs are the group of metallic material which has a melting point above 2123 K. and It consists of the refractory elements like Cr, Ta, Mo, Ti, Nb, Zr, etc. Some examples of the refractory HEAs are $\text{AlMo}_{0.5}\text{NbTa}_{0.5}\text{TiZr}$, TaNbHfZrTi , TiZrNbMoV_x , and HfMoTaTiZr [9-11].

2.3.2. Lightweight HEAs

In lightweight HEAs elements having lower density like, Al, Mg, Sc, Li, Ti, etc are normally selected. Some examples of the light weight HEAs are AlFeCuCrMg_x ($x = 0, 0.5, 1, 1.7$) HEAs

with density in the range of 6.0- 4.9 g/cm³ [12], Mg_x(MnAlZnCu)_{100-x} having density in the range of 4.29 - 2.20 g/cm³ [13], and Al₂₀Li₂₀Mg₁₀Sc₂₀Ti₃₀ with density 2.67 g/cm³ [14].

2.3.3. High entropy bulk metallic glasses

The HE-BMGs consist of a mixture of different elements like transition metals, p-block elements, s-block and lanthanides. Some of the HE-BMGs are Ca₂₀(Li_{0.55}Mg_{0.45})₂₀Sr₂₀Yb₂₀Zn₂₀, Be_{16.7}Cu_{16.7}Ni_{16.7}Hf_{16.7}Ti_{16.7}Zr_{16.7}, and Cu₂₀Hf₂₀Ni₂Ti₂₀Zr₂₀, [15, 16].

2.3.4. High-Entropy Super alloys (HESAs)

Traditionally, the Ni-based superalloys have excellent high-temperature properties which further improve upon the addition of refractory elements. The new HESAs follow the four core effect of the HEAs which give an advantage for high-temperature application. It is observed that Co_{1.5}CrFeNi_{1.5}Ti_{0.5} HEAs have a higher hardness than IN718 at higher temperatures and hence performs well in high-temperature application [17].

2.4. Thermodynamics for Phase formation in HEAs

In classical alloy design, the Hume-Rothery rule is the primary criteria to predict the solubility of the binary alloy systems. According to this criterion, for solubility of one element into the other, few conditions needs to be satisfied like, the elements should have same crystal structure, electronegativity between the elements should be minimum, the valency of the elements should be same and difference in atomic size between the elements should be less than 15%. However, in case of HEAs, these conditions are not significant to predict the solid solution formation.

In HEA Hume – Rothery rule are not applicable because it does not give any explanation why the addition of Al (FCC) changes the FCC type CoCrCuFeNi HEA to a BCC structure [18, 19] and the equi-atomic alloys like, Cu(FCC)-Cr(BCC)- Fe(BCC)-Ni(FCC)-Co(HCP) alloys form an FCC type solid solution. Zhang and Guo [19, 20] give the certain thermodynamic parameter which can guess the solid solution phase formation, and phase stability in HEA. The parameters are given in the Table 2.1.

Table 2.1 Thermodynamic parameters predict the solid solution phase formation, and phase stability in HEA

Enthalpy of mixing (ΔH_{mix})	$\Delta H_{\text{mix}} = \sum_{i=1, i \neq j}^n \Omega_{ij} C_i C_j$ $\Omega_{ij} = 4 \Delta H_{\text{mix}} (\text{AB})$
Entropy of mixing	$\Delta S_{\text{mix}} = -R \sum_{i=1}^n C_i \ln C_i$
Atomic size mismatch	$\delta = 100 \sqrt{\sum_{i=1}^n C_i \left(1 - \frac{r_i}{\bar{r}}\right)^2}$ $\bar{r} = \sum_{i=1}^n C_i r_i$
Valence electron concentration (VEC)	$\text{VEC} = \sum_{i=1}^n C_i (\text{VEC})_i$
Parameter Ω	$\Omega = \frac{T_m \Delta S_{\text{mix}}}{ \Delta H_{\text{mix}} }$
Pauling electronegativity	$\Delta X = \sqrt{\sum_{i=1}^N C_i (X_i - X_{\text{avg}})^2}$ $X_{\text{avg}} = \sum_{i=1}^N C_i X_i$
Theoretical melting point	$T_{\text{m,th}} = \sum_{i=1}^n C_i (T_{\text{m}})_i$

Where, $\Delta H_{\text{mix}} (\text{AB})$ is the binary mixing enthalpy between AB and $\Delta H_{\text{mix}} (\text{AB})$ (KJ/mol) is estimated using Miedema's model in case of binary atomic pairs. C_i and C_j are the atomic percentage of the i^{th} and the j^{th} component. R is the gas constant whose value is taken as $8.314 \text{ JK}^{-1} \text{ mol}^{-1}$. No. of elements in the alloy system (n) and \bar{r} is the average value of atomic radius, and r_i is the atomic radius of each of the constituting elements. X_i is the electronegativity of the i^{th} element and X_{avg} is the average value of electronegativity. $(T_{\text{m}})_i$ is the melting point of the individual elements present in the system and $T_{\text{m, th}}$ is the theoretical melting point of the HEA.

2.5. Characteristics of different alloying elements

Table 2.2 shows some the relevant properties of different alloying elements like their atomic no., atomic weight, atomic radius. melting point, crystal structure, lattice parameter, VEC, and Pauling electronegativity.

Table 2.2 Atomic no., atomic weight, atomic radius, melting point, crystal structure, lattice parameter, VEC, and Pauling electronegativity of different alloying elements [19]

Element	Atomic No.	Atomic Weight (amu)	Atomic Radius (Å)	Melting point (°C)	Crystal structure	Lattice Parameter (Å)	VEC	Pauling Electro negativity
Al	13	26.98	1.432	660.4	FCC	4.049	3	1.61
Fe	26	55.85	1.241	1538	BCC	2.866	8	1.83
Cr	24	51.99	1.249	1875	BCC	2.884	6	1.66
Mn	25	54.94	1.27	1246	BCC	8.912	7	1.55
Ni	28	58.69	1.246	1455	FCC	3.524	10	1.91
Co	27	58.93	1.251	1495	HCP	3.545	9	1.88

2.5.1. Enthalpy of mixing (kJ/mol) of possible atomic-pairs in Al-Fe-Cr-Ni-Co and Al-Fe-Cr-Mn-Ni high entropy alloys

Table 2.3 shows the binary enthalpy of mixing of different atomic pairs used for calculating various thermodynamic parameters of $Al_xFe_{1.5}CrMnNi_{0.5}$ ($x = 0.3$ and 0.5 mol) HEAs and $Al_{0.4}FeCrNiCo_x$ ($x=0, 0.25, 0.5$ and 1.0 mol) HEAs which can predict the phase formation.

Table 2.3 Binary mixing enthalpy between alloying elements based on the Miedema's model [21, 22]

Elements	Al	Cr	Fe	Mn	Ni	Co
Al	0	-10	-11	-19	-22	-19
Cr		0	-1	2	-7	-4
Fe			0	0	-2	-1
Mn				0	-8	-5
Ni					0	0
Co						0

2.6. Fabrication Techniques

Different techniques are available for the synthesis of HEAs as that of the conventional alloys. The HEAs can be processed into different forms by processes like bulk casting, mechanical alloying followed by sintering and coatings as represented in Fig. 2.4. The synthesis routes for HEAs can be broadly divided into three parts powder metallurgy route, melting and casting route, and deposition.

2.6.1. Melting and casting route

Melting and casting route has been popularly used for the synthesis of traditional alloys and as well as HEAs [4]. The maximum numbers of HEAs reported are synthesized by melting and casting route and different variations of this process are melting due to arcing, melting due to induction heat, melting due to electric resistance, laser melting, laser cladding, and laser enhanced net shape (LENS) forming. Melting and casting route has advantages such as energy saving, cost-efficient, and reduced synthesis time which gives it an edge over other alloy synthesis techniques. Basic limitations involved in the synthesis of HEAs through this route is that at low cooling rates typically dendritic and interdendritic microstructures are formed in HEAs due to elemental segregation [4].

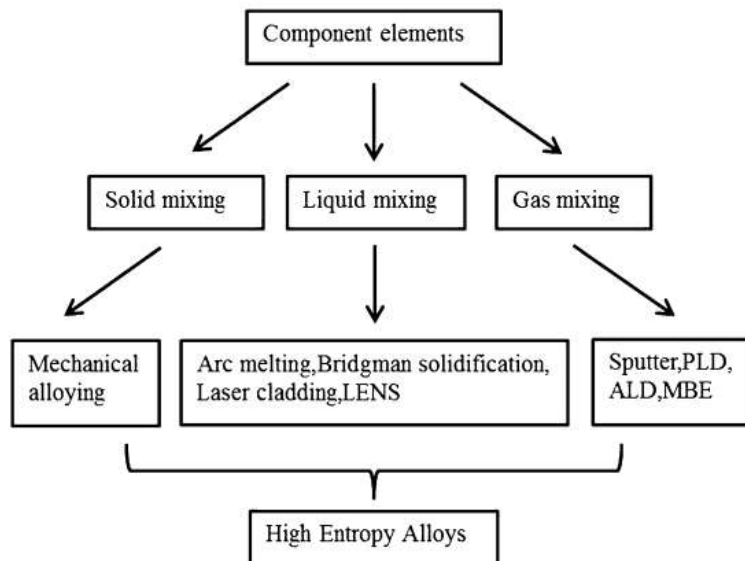


Fig. 2.4 Various synthesis routes of HEAs [2]

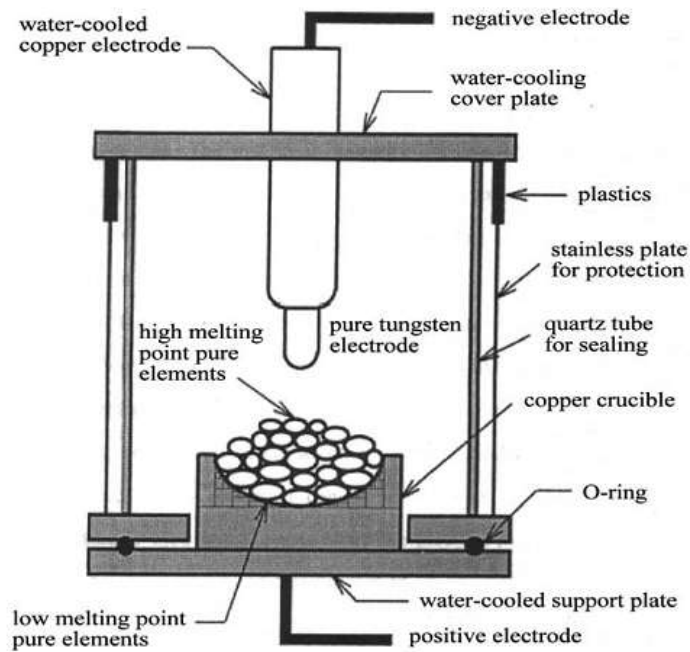


Fig. 2.5 Schematic diagram of arc melting method [23]

Zhou et al. [24] have processed the AlCoCrFeNiTi_x HEAs through arc melting route as represented in Fig. 2.5 and have revealed that the HEAs have BCC solid solution structure with better compressive strength, fracture strength, and work hardening capabilities.

2.6.2. Laser Fabrication

Direct laser fabrication process is used for the synthesis of HEAs as represented in Fig. 2.6. The synthesis includes use of two hopper systems to avoid powder segregation. By controlling the flow-rate of the elemental powder to the melt, alloys with different compositions can be synthesized. To prevent oxide formation, high purity argon gas is regularly purged through the sealed melt deposition region [4].

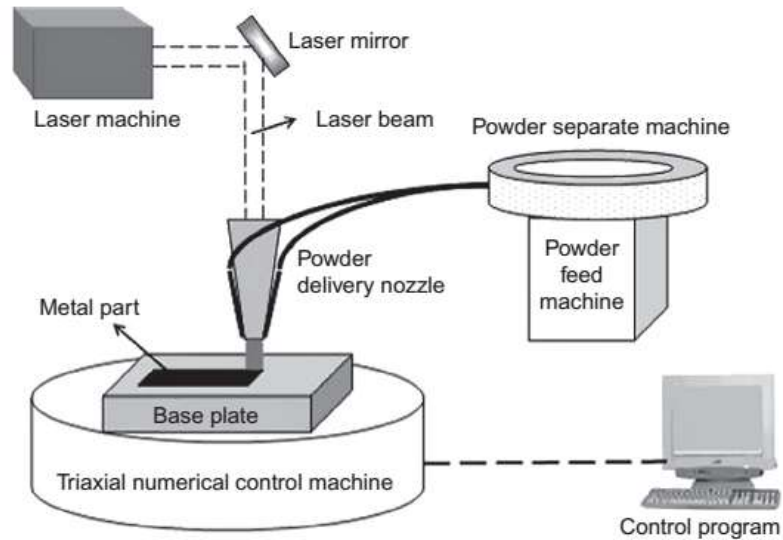


Fig. 2.6 Schematic diagram of laser-engineered net shaping (LENS) [1]

2.6.3. Solid State Processing Route

Mechanical alloying involves solid state processing that allows the synthesis of a product from both immiscible and miscible alloy materials. The process of mechanical milling is shown in Fig. 2.7 (a). Synthesis of HEAs through mechanical alloying technique was first reported by Varalakshmi et al. [25], and the final microstructure was consisted of a BCC structure. In high energy ball milling the mechanically alloyed powders are produced by continuous cold welding and fracturing process as represented in Fig. 2.7 (b).

Compaction and then sintering of the milled powder is carried out to fabricate bulk alloys in solid state processing and is mostly been done by a traditional method which leads to coarse grains microstructure due to long duration heating. For the processing of nanocrystalline microstructure, HEAs are prepared by spark plasma sintering (SPS) technique, as represented in Fig. 2.8. They have many advantages over other traditional sintering process, such as, more control over sintered materials like, density, porosity, and microstructure, energy efficient, and fast sintering process.

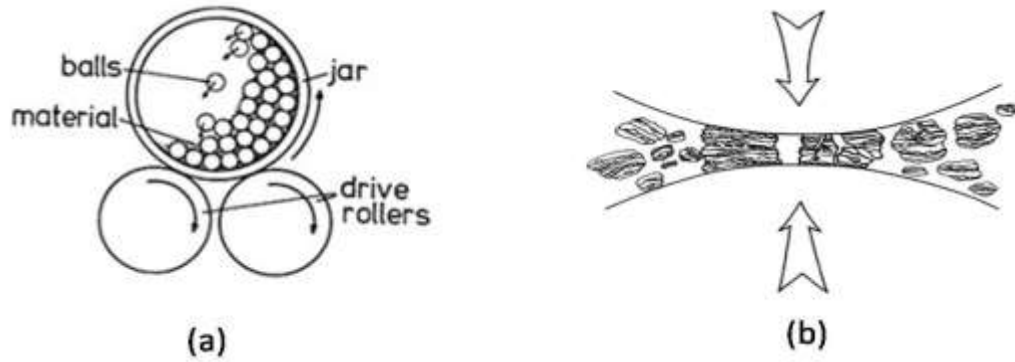


Fig. 2.7 (a) cross-section of milling in tumbler (b) phenomena of fracture and welding during ball milling [1, 2]

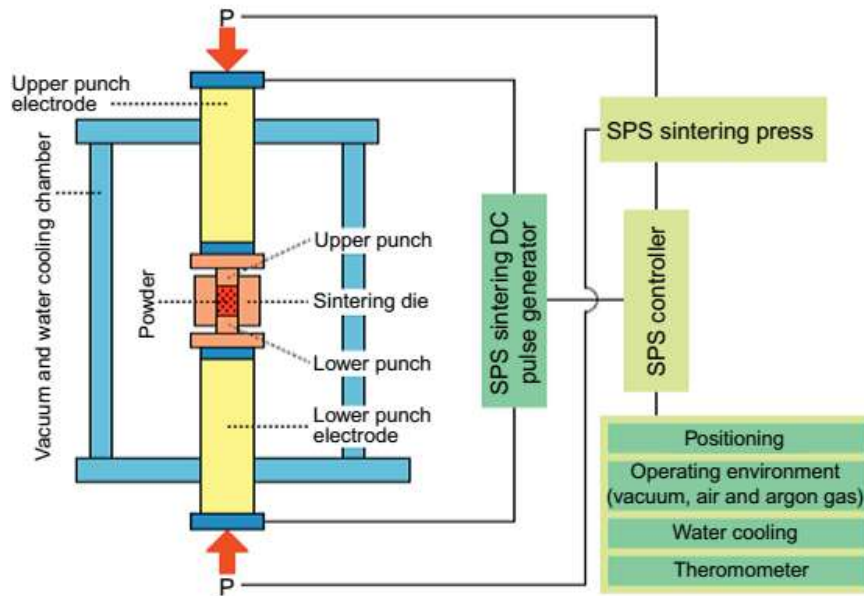


Fig. 2.8 Layout of SPS processing [2]

2.6.4. Sputtering

Sputtering is a process in which thin films are deposited over a substrate by the process atoms by atom deposition from a selected material due to the bombardment of charged gas ions over the target as represented in Fig. 2.9. The sputtering can be divided as direct current (DC) sputtering, radio frequency (RF) sputtering and magnetron sputtering. Among these, magnetron sputtering deposition is the most suitable method to fabricate the HEA films [1, 2, 4].

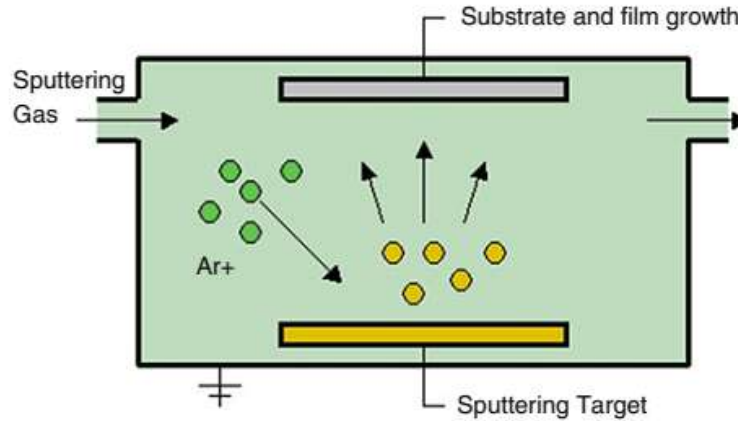


Fig. 2.9 Schematic diagram showing the sputtering deposition process [2]

2.7. Erosion and wear behavior of HEAs

2.7.1. Erosion behavior of HEAs

Table 2.4 lists the previous work on erosion behavior of HEAs. From Table 2.4, it may be observed that limited study has been done on the erosion behavior of HEAs. The summary gives a brief idea about different synthesis routes of HEAs, type of erodent particle, medium and the values of various parameters during the experiment on the erosion behavior of the HEAs. For more illustration, some of the reported works are explained in detail as follows.

Wang et al. [26] have reported the air jet erosion wear behavior of Fe–2.5C–27Cr–0.8Si-x (x= V, Nb, W, and B) HEAs. It is observed that with the addition of Nb, V, W, and B elements, various types of carbides are getting formed and this helps in improving the hardness from 475 HV to 903 HV. The solid particle erosion test is performed using sand of particle size 50-70 AFS, at a velocity of 50–80 m/s, at two different impingement angles of 45° and 90°. The result indicated that at 45°, there is not much variation in the wear rate of all samples. However, in the case of 90° impingement angle, the HEA with Tungsten is observed to exhibit maximum wear rate. It is also observed that the erosion at 90° impingement angle is higher than that at 45°.

Zhao et al. [27] have reported the erosion- corrosion resistance of AlCrFeCoNiCu HEA after annealing it at 600°C and 1000°C. They have varied the rotational speed of shaft in the range of

300 rpm to 700 rpm and have used an angle of 90° between the slurry and the sample. The slurry was consisting of 5 wt.% of sand particle with size range between 80-120 µm and 3.5wt.% NaCl in 10 L of water in a pot erosion tester. It is observed that the sample annealed at 600°C has maximum hardness and hence exhibits lowest mass loss. The reason behind the lowest erosion is stated as the formation of less and shallow craters during the test, and the enhancement of the hardness.

Nair et al. [28] reported the slurry erosion behavior of Al_{0.1}CoCrFeNi HEAs at constant velocity of 20 m/s and at different impingement angles of 30°, 60° and 90°. The test slurry was consisting of sand particles with size range in between 75–150 mm and concentration 5 kg/m³ mixed with tap water. The distance between the nozzle and the sample was 20 mm. It is observed that as the impingement angle decreases, the erosion rate against the slurry increases. The mentioned possible reason is that at normal impingement angle the governing mechanism is plastic deformation and at an oblique angle, hardness is the dominant factor that modulates the erosion.

Table 2.4 Literature on erosion behavior of HEAs prepared through different synthesis routes, slurry, and tested under different slurry and testing parameters.

S. No.	Year	HEAs	Synthesis Route	Particle	Slurry	parameter	Major finding	Ref.
1.	2018	Al _x Fe _{1.5} Cr MnNi _{0.5} (x = 0.3,0.5)	MM and CS	Al ₂ O ₃ 50µm	Al ₂ O ₃ + dry air	Mass flow rate 2 g/min, velocity 70 m/s, angle 45, 60, 75, 90 deg.	Max erosion occur at 45 deg., ductile mode of erosion.	[29] Present work
2.	2013	Fe–2.5C–27Cr–0.8Si–1B–2V–0.67Nb–3.3W	AM	sand (AFS 50–70)	Sand + dry air	Angle 45, 90 deg. velocity 50 to 80 m/s, mass flow rate 177 g/min,	Erosion at 90 deg. Higher than 45 deg.	[26]
3.	2016	AlCrFeCo NiCu	AM	Sand (80–120 µm)	Sand +3.5% NaCl sol	300, 500 and 700 rpm, angle of 90°	Annealing at 600°C HEA show better erosion –corrosion	[27]
4.	2017	Al _{0.1} CrCo FeNi	IM and (HIP)	Sand (75–150 mm)	Sand + tap water	velocity of 20 m/s, angle 30°, 60° and 90°	Max. erosion occur at 30 deg. HEA show ductile mode of wear	[28]
5.	2018	Al _{0.1} CoCr FeNi	IM and HIP.	Sand (75–150 µm)	Sand+ 3.5 wt% NaCl sol.	Velocity 20 m/s, angle 30 and 90 deg.	Max. erosion occur at 30 deg.	[30]

6.	2018	Al _{0.1} CoCrFeNi	VAM and (HIP)	-	DI-water with and with out 3.5 wt. % NaCl	Cavitation erosion tests- frequency of 20 ±0.5 kHz, amplitude 50 µm, time 20hrs,	Erosion rates for HEA - 0.0166 mm ³ /hr and SS316L -0.1464 mm ³ /hr	[31]
7.	2018	AlCrFeCoNiCu	AM	SiO ₂ 350–600 µm	Water + 1%wt SiO ₂	Velocity 10.08m/s angle 90 deg., time 30 min	linear related to erosive wear resistance and H/E ratio (R ² =0.89)	[32]

2.7.2. Sliding wear behavior of HEAs under different medium

2.7.2.1. Wear under dry condition

Table 2.5 lists the previous literature reports on wear behavior of HEAs tested under dry condition. The summary gives a brief idea about different synthesis routes of HEAs, machine configuration for testing, different parameters of the experiments, hardness and major findings of the experiments. For more illustration, some of the reported works are explained in detail as follows.

Hsu et al. [33] have reported the abrasive wear resistance of CuCoNiCrAl_{0.5}FeB_x HEA. They have observed that as boron content added hardness increases, and a maximum hardness is reached at boron content x=1.0, which is 736 HV. The formation of more amounts of Cr and Fe borides is mentioned as its reason. The abrasive wear test is conducted on a pin-on-belt tribometer using 8mm diameter pin under a load of 3 kg and at a belt speed of 0.5 m/s. An Al₂O₃ belt of 100-mesh is used for the current test. The result indicates that the wear resistance increases with the increase of boron and this may be due to the increases in volume fraction of boride precipitates.

Tong et al. [34] have studied the wear behavior of Al_xCoCrCuFeNi (x = 0 to 3.0) HEAs synthesized by arc melting in vacuum at 0.01 atm. The wear test is conducted on a pin-on-belt tribometer under a different load of 9.8N and 29.4N without any lubrication. A test pin of 8 mm diameter is used with a Al₂O₃ counter belt of 149µm mesh and belt sliding speed of 0.5 m/s is

maintained. It has been observed that with increase in aluminium content the hardness and wear resistance and hardness increases due to transformation of FCC phase to BCC phase.

Chen et al. [35] have studied the vanadium content effect on wear resistance of $\text{Al}_{0.5}\text{CoCrCuFeNiV}_x$ ($x = 0$ to 2.0) HEAs prepared by arc melting. The wear test is performed on a pin-on-belt tribo-meter without any lubrication and under a load of 29.4N . In this test a test pin of 8 mm diameter is made to slide over $149\text{-}\mu\text{m}$ Al_2O_3 particles sand belt at velocity of 0.5 m/sec . It is reported when the vanadium content is in between 0.6 to 1.2 , highest wear resistance is achieved.

Chen et al. [36] have studied the titanium content effect on wear resistance of $\text{Al}_{0.5}\text{CoCrCuFeNiTi}_x$ ($x = 0$ to 2.0) HEAs synthesized by arc melting. It is observed that when titanium content varies from $x = 0$ to 0.4 , there is gradual increase in hardness. However, a sharp increase occur when the titanium content varies from $x = 0.4$ to 1.0 and the hardness decreases when titanium content is greater than $x = 1.0$. The decrease in hardness is reported to be due to weak hardening in the FCC and BCC phases. The wear test is performed on a pin-on-belt wear tester using a 8 mm diameter pin and under a load of 29.4N without any lubrication. The sliding velocity is maintained at 0.5 m/s and the tests are conducted for a total sliding distance of 20 m against a $149\text{-}\mu\text{m}$ Al_2O_3 particle belt. The results of the test indicated that when titanium content is in the range of 0 and 0.6 , the samples exhibit wear resistance similar to that of $\text{Al}_{0.5}\text{CoCrCuFeNi}$ HEA and the wear resistance increases from 0.93 m/mm^3 to 1.24 m/mm^3 as the titanium content increases from $x = 0.6$ to 1.0 .

Liu et al. [37] have studied the wear behavior of $\text{Al}_{0.5}\text{CoCrCuFeNiSi}_x$ ($x = 0, 0.4, 0.8$) HEAs under dry condition and the alloy is prepared by arc melting in argon atmosphere. It is observed that as silicon content increases BCC phase increases and FCC phase completely disappears at $x = 0.8$. The wear test is performed on a pin-on-disk wear testing machine using a pin of 6 mm diameter and height of 12 mm and a 70 mm diameter Cr_{12}MoV steel disk 760 HV as the counter material. They have observed that on increasing the Silicon content from $X=0.4$ to $X=0.8$, the hardness increases from 263 HV to 653 HV and the wear resistance increases from 0.10 km/mm^3 to 0.86 km/mm^3 .

Table 2.5 Literature on wear behavior of HEA synthesized by different routes under dry condition and tested under different sliding condition. [SR: synthesis route, CB: counter body, config : configuration]

S. No.	Year	HEA	SR	Config.	Parameter	Hardness	Major finding	Ref.
1.	2019	Al _{0.4} FeCrNi Co _x (x = 0, 0.25, 0.5, 1.0 mol)	AM and homogenization	Pin on disk	CB: EN 31, Load: (5,10, 15, 20)N, speed:(0.5, 1, 1.5, 2.0) m/s, distance:(1000, 2000, 3000, 4000)m	377.7 HV to 199.5 HV	X=1 has max. wear rate.	[38] Present work
2.	2004	CuCoNiCr Al _{0.5} FeB _x (x=0,0.2,0.6, 1.0)	IM	Pin-on-belt	CB:100-mesh Al ₂ O ₃ . Belt speed: 0.5 m/s, distance : 20 m, load: 3Kg	232HV to 736 HV	wear resistance of B=1 (1.76 m/mm ³ , and higher wear resistance than B=0 due to higher boride precipitates.	[33]
3.	2005	Al _x CoCrCu FeNi (x=0.5, 1.0, 2.0)	AM	Pin-on-belt	CB:149 μm Al ₂ O ₃ belt, Belt speed: 0.5m/s load: 9.8 and 29.4 N	133 HV to 655 HV	Al=0.5 better wear resistance than Al=1 due to better surface hardening capability	[34]
4.	2006	Al _{0.5} CoCrCu FeNiV _x (x= 0 to 2.0)	AM	Pin-on-belt	CB:149 μm Al ₂ O ₃ belt, Belt speed: 0.5m/s, load:29.4 N, distance :20 m	295 HV to 749 HV and at x=1, 998 HV	Wear resistance increase x=0.6 to1.2, and in bet. x = 1.2 to 2.0 no significant change in wear resistance	[35]
5.	2006	Al _{0.5} CoCrCu FeNiTi _x (x= 0 to2.0)	AM	Pin-on-belt	CB:149 μm Al ₂ O ₃ belt, Belt speed: 0.5m/s, load:29.4 N, distance :20 m	225 HV to 660 HV	maximum wear resistance occur at x=1, wear resistance 0.93 m/mm ³ to1.24 m/mm ³	[36]
6.	2006	Al _x CoCrCu FeNi (x=0.5,1.0,2.0)	AM	pin-on-disk	speed : 0.5 m/s and load: 29.4 N, distance :6000m	Al=2.0 has 560 HV	With increasing Al content BCC phase, hardness, wear resistance increases	[39]
7.	2009	Al _{0.3} CrFe _{1.5} MnNi _{0.5}	VM,	pin-on-disk	CB:SKH-51 steel, speed: 0.5 m/s, distance : 64800 m, load :29.4 N	273 to 462 HV	Wear rate are minimum for AC-D-H-F 2.93 x 10 ⁻⁵	[40]
8.	2010	AlCoCrFe _x Mo _{0.5} Ni (x=0.6, 1.0, 1.5, 2.0)	arc smelting	pin-on-disk	CB: SKH51 steel Speed: 0.5 m/s, time : 24 hrs, load :29.4 N.	356 HV to 730 HV	With addition of Fe content hardness and the wear	[41]

							resistance decreases	
9.	2010	$Al_xCrFe_{1.5}MnNi_{0.5}$ ($x = 0.3$ and 0.5)	AM	pin-on-belt	CB: Belt- Al_2O_3 100 grit, speed :50 cm/s, distance : 20 m, load:5 kg	297 HV to 480 HV	Age-hardened Al(0.5) has good wear resistance	[42]
10.	2010	$AlFeTiCrZnCu$	MA and (VHP) and (HIP)	pin-on-disc	CB: Ni-hard faced disc (650 HV), load: 3 kg, track distance : (450, 800, 1200, and 1600 m).	9.50 GPa	wear resistance of $AlFeTiCrZnCu$ is higher than the commercially materials	[43]
11.	2010	$Al_{0.5}CrFe_{1.5}MnNi_{0.5}$	VM	pin-on-disc	CB: SKH-51 steel	1250 HV.	the nitrided Al0.5 HEA is 46–77 times better wear resistance than unnitrided	[44]
12.	2011	(Fe–20Cr–5C)-Ti(x)-V(y)-Mo(z)	AM	pin-on-disc	Speed : 0.5 cm/s, load :10 N, rotations: 10,000 , CB: ball (silicon nitride).	565 HV to 670 HV	With increase in Ti,V,Mo content, the volume loss rate decreases.	[45]
13.	2011	$Al_xCo_{1.5}CrFeNi_{1.5}Ti_y$	AM	pin-on-disk	speed : 0.5 m/s, load: 29.4 N, distance: 5400 m	487 HV To717 HV	Al00Ti05 and Al02Ti05 undergo severe	[46]
14.	2012	$Al_{0.3}CrFe_{1.5}MnNi_{0.5}$	VC.	pin-on-disc	CB:-SKH-51 steel (890 HV), speed : 0.5 m/s, distance: 43,200 m, load:3 kg	445 HV to 633 HV	nitrided Al0.3 is 49 to 80 times better than un-nitrided	[47]
15.	2013	$Al_{0.3}CrFe_{1.5}MnNi_{0.5}$	VIM	pin-on-belt	CB: Belt-400 mesh- Al_2O_3 belt, load: 1 kg, speed: 0.5 m/s	317 to 840 HV	HEA1.4 time better wear resistance than SUJ2 and SKD61 steels	[48]
16.	2015	$Al_{0.5}CoCrCuFeNiSi_x$ ($x = 0, 0.4, 0.8$)	AM	pin-on-disk	CB: Cr12MoV steel, speed: 0.8 mm/s, load: 100 N,	263 HV to 653 HV	$x = 0.8$ is 8.6 times than $x = 0$	[37]
17.	2015	$Al_xFeCuCoNiCrTi$ ($x = 0, 0.5, 1.0, 1.5, 2.0$)	VAM	-	Speed: 1 mm/s, time: 1 hrs, Load: 100 N	600 to 1100HV _{0.1}	$x = 1.5$ better wear resistance than others,	[49]
18.	2017	$CoCu_{0.5}FeNiVTi_x$ ($x = 0, 0.5, 1, 1.5$ and 2)	AM	pin-on-disc	CB: SUJ2 bearing steel, load: 21 N, speed: 0.4 m/s distance: 1500 m	214 HV to 660 HV	Max wear resistance occur at $x=1$ and it is due to large volume fraction of BCC. wear mechanism includes	[50]

							adhesive wear and abrasive wear.	
19.	2018	CoCrCuFeNi Mo _x (x = 0, 0.2, 0.4 and 0.8)	MA and SPS	Pin-on-Disc	-	329 HV	With increase of Mo content from 0 to 0.8, coefficient of friction decreased to 0.65.	[51]
20.	2017	CoCrFeNi-(Ag-BaF ₂ /CaF ₂)	MA and SPS	ball-on-disk	CB: Ball-Inconel-718 superalloy (6 mm), temp.: (RT, 200, 400, 600, and 800 C), load: 5 N, speed: 0.28 m/s, time:30 min, distance: 504 m	151 HV	Addition of Ag and BaF ₂ /CaF ₂ maintain the COF (0.20-0.26) from RT to 800 C,	[52]
21.	2017	Al _{0.25} Ti _{0.75} CoCrFeNi	AM	ball-on-disc	CB: Ball-WC (3mm) Load: 10N, 15N and 20N, stroke length: 1mm, frequency: 5Hz, time : 20min, distance :15m	1090 HV	COF : (~0.3) and wear rate (~1.2 x 10 ⁻⁵ mm ³ /Nm).	[53]
22.	2017	Fe ₂₅ Cr ₂₀ Ni ₂₀ Mn ₁₅ Co ₁₀ Al ₁₀	-	-	CB: 65G steel (HRC = 55–57), load: (0.5 and 1) MPa, sliding speed: (6.8 and 12 m/sec)	H _{IT} - 4.7 GPa	The wear intensity varies from 6.1 x 10 ⁻¹⁰ to 1.6x 10 ⁻⁹ g/km	[54]
23.	2017	AlCoCrFeNi Ti _{0.5}	AM	ball-on-flat	CB:- AISI 52100 steel ball (9.6mm) relative humidity: 40% , , loads : 20 to 60 N, time :20 min, frequency : 15 Hz, stroke: 1 mm	655 HV _{0.49}	wear mechanism includes abrasive, adhesive and oxidative wear	[55]
24.	2018	(AlCrFeMnV) 100 _x Bi _x) and (CuCrFeTiZn) 100 _x Pb _x)	MA and SPS	ball-on-disk	CB: Ball Steel, Load: 2, 5, 7, 10N, cycles: 40,000, speed :0.41 m/sec, humidity: 50%,	Pbx = 643 HV to 396 HV Bix= 321 to 392 HV	COF does not change with Pb content, and Bi decrease COF	[56]
25.	2018	FeCoCrNiMo	MA and SPS	ball-on-disc	sintered temp. : (1000, 1050 or 1100°C) and pressures: (30, 35 or 40 MPa) for 480 s, and load: 50 N, frequency: 15 Hz, time: 5 min,	350–520 HV	Variation of the temperature and pressure has no obvious influence on the wear.	[57]
26.	2018	AlCoCrFeNi Si _x (x = 0, 0.3, 0.6	MA and SPS	pin-on-disk	CB:- WC (1550 HV), speed: 500 rpm, load:	890 HV to 1009 HV	better wear resistance were achieved as the	[58]

		and 0.9)			50N,		Si content increased from 0 to 0.9	
27.	2018	Co _{1.5} CrFeNi _{1.5} Ti _{0.5}	AM	ball-on-disk	Load: 5 N, Speed:0.1 m/s, CB: Al ₂ O ₃ ball, 100Cr6 steel ball (6mm), Distance: 1000m,	368 ± 13 HV _{0.5}	Wear rate not varies	[59]
28.	2018	CoCrFeNiS _{0.5}	MM and SPS	ball-on-disk	CB: Si ₃ N ₄ ceramic ball, Load: 5 N, Speed: 0.28 m/s, Time: 30 min	259 HV	Good wear performance at high temperature due to formation of metal oxide and CrxSy	[60]
29.	2018	CrCoNiMo _x (x = 0, 0.25, 0.5, 0.75 and 1.0)	MM and SPS	ball-on-disk	CB:Si ₃ N ₄ ball Load: 5 N Speed: 0.28 m/s., Time: 30min	244 HV to 656 HV	Mo=1.0 shows best wear performance and mechanism changes from abrasive wear to adhesive wear	[61]
30.	2018	Al _x CrCo _{2-x} FeNi (x=1.0,1.2,1.4,1.6)	MM and SPS	-	-	486 to 541 HV	With decrease of Co and increase of Al wear performance increases	[62]
31.	2018	AlCrFeNiTi and AlCrFeNiTiMn _{0.5}	VAM	pin-on-disk	CB: GCr15 steel, Load:20N, Speed:0.8m/s, Distance:1000m	616.0 and 539.5 HV	Mn0.5 shows higher mass loss, and wear mechanism: adhesive, delamination	[63]
32.	2019	CoCrFeNiCu _x (x = 0, 0.2, 0.4, 0.6, 0.8, 1.0)	AM	pin-on-disk	Load: 100 N, Speed: 95 rpm time: 1000 s	136 HV to 169 HV	Cu=1.0 have better wear resistance, wear mechanism: abrasive to adhesive with addition of Cu at elevated temperature.	[64]
33.	2019	Al _{0.25} CoCrFeNi	AM	ball-on-disk	CB: Si ₃ N ₄ ball, Load: 10 N time: 30 min	2.53 GPa	With increasing temperature wear rate increases from 20°C to 600°C	[65]
34.	2019	Al _{0.6} CoCrFeNi	AM	ball-on-disk	CB: Si ₃ N ₄ ball, Speed: 300 r/min, Time:30min, Load:10N	278 to 480 HV	wear rate increases with increasing temp. from 20°C to 600°C	[66]

35.	2019	NiCoCrAl- (Ag, MoS ₂ , LaF ₃ and CeF ₃)	MM and SPS	ball-on- disk	CB: Si ₃ N ₄ balls (1700 HV, 6.35 mm), Speed: 18.8 cm/s, Time :60min, load: 10 N, Radius:5 mm, Temp.: RT, 200, 400, 600 and 800 °C.	430.6 HV _{0.3}	Max. wear occur at 400°C and min wear occur at 800°C due to formation of silver molybdates and metallic oxide which act like a film.	[67]
36.	2019	Al _x CoCrCu FeNi (x = 0, 0.5, 1, 1.5, 2)	VAM	ball-on- disk	CB: Zr ₂ O ₃ ball (5mm) Load: 10 N, time:30 min Distance: 10mm	45 HRA to 75 HRA	With Al addition wear resistance increases	[68]
37.	2019	CoCrFeNi Nb _x (x =0.5, 0.65 and 0.8)	AM	pin-on- disk	CB: Si ₃ N ₄ ball (6.35mm) Temp: (RT, 25 C, 200 C, 400 C, 600 C and 800 C) Load: 5 N, Speed: 0.188 m/s Time: 30 min	542 HV, to 344 HV (1000°C)	From RT to 400°C the wear mechanism changes from abrasion to adhesion and near 600°C it was oxidation and mechanical wear	[69]

2.7.2.2. Wear under oil and other medium

Table 2.6 summarize the reported work on wear behavior of high entropy alloys under different sliding medium like oil, demineralized water and other medium, synthesis route, machine configuration, working parameter, hardness and major finding. From Table 2.6 it has been observed that the limited work is done. For more illustration, some of the reported work can be explained in detail as follows.

Duan et al. [70] has conducted the wear study of AlCoCrFeNiCu HEA under lubrication with 90% hydrogen peroxide solution and 10W-40 grade of lubricating oil. The wear test is performed on pin-on-disk machine with test pin of 8 mm diameter x 15mm height and on counter part of Si₃N₄ ceramics disk of 50 mm diameter and 8 mm thickness. The ceramic disk is rotated with a speed of 0.471 m/s under a load of 30N. Under lubricating condition the friction coefficient achieved a constant value from 0.05 to 0.045 with little variation. The wear weight loss is higher under 90% hydrogen peroxide solution than lubricating oil, this is due to repetitive action of oxidation and polishing effect during sliding. Many ploughed grooves occur under lubricating oil condition indicates abrasion and micro-cutting wear.

Yu et al. [71] studied the wear behavior of AlCoCrFeNiTi_{0.5} HEA under 90% concentrated hydrogen peroxide solution. The test was performed on pin-on-disc with a normal load of 30N, rotating speed of 0.471m/s against the counter body of SiC and ZrO₂. It is observed that the COF in case of ZrO₂/ AlCoCrFeNiTi_{0.5} HEA is 0.39 and in case of SiC/ AlCoCrFeNiTi_{0.5} HEA is in the range of 0.06 to 0.09. The wear losses in case of SiC are lower than that when it is sliding against ZrO₂.

Gorban et al. [72] studied the wear characteristics of Fe₂₅Cr₂₀Ni₂₀Mn₁₅Co₁₀Al₁₀ high entropy alloys under greased and ungreased condition with varying loads and sliding speed. 65G steel is used as a counterpart with hardness of 55-57 HRC at a pressure of 0.5 MPa and 1.0 MPa and sliding speed of 6–12 m/s. It is observed that under greased condition the COF varies in the range of 0.26 to 0.21 and in case of without greased condition the COF varies in between 0.32 to 0.34. The wear loss in case of greased condition is one order lesser than without greased condition.

Liu et al.[73] studied the tribological performance of AlCrCuFeNi₂ HEA under different sliding condition like in dry, artificial rain water, and DI water. The wear test is performed on ball-on-block wear tester against Si₃N₄ ceramic ball under varying loads of 5N to 15N. In case of dry sliding condition at 5N the coefficient of friction varies in between 0.25 to 0.48, at load of 10N the coefficient of friction (COF) fluctuate in between 0.3 to 0.5 and at load of 15N the coefficient of friction varies in between 0.2 to 0.35. The coefficient of friction also decreases with increasing loads in case of deionized water, and rain water. The wear mode in dry sliding condition is mainly adhesive wear, and oxidation. In case of deionized water the wear is mainly due to abrasive, adhesive, and plastic deformation.

Table 2.6 Literature on wear behavior of HEAs, synthesis by different route under oil and other medium and performed at different sliding condition

[SR: Synthesis route, Config.: configuration]

S. No.	Year	HEA	SR	Config.	Medium	Parameter	Hardness (HV)	Major finding	Ref.
1.	2018	Al _{0.4} FeCrNiCo _x (x=0, 0.25, 0.5, 1.0 mol)	AM	Pin on disc	SAE Grade: 20W-40 Engine oil	Load: (5,10, 15, 20)N, speed:(0.5, 1, 1.5, 2.0) m/s, distance:(1000, 2000, 3000, 4000)m	377.7 HV to 199.5 HV	Max specific wear occur at x=1, normal load is the most influencing parameter.	[74] Present work
2.	2013	AlCoCrFeNiCu	AM	pin-on-disk	90% hydrogen peroxide, and SAE 10W-40 lubricant oil	normal load - 30 N, velocity-0.471 m/s, time- 30 min, counter disk-Si ₃ N ₄ ceramics	475.3 HV	High wear resistance was observed in oil. Wear under hydrogen peroxide sol due to oxidation , peel of oxide, abrasive wear	[70]
3.	2014	AlCoCrFeNiTi _{0.5}	VIM	pin-on-disc	90% hydrogen peroxide	Counter disk SiC and ZrO ₂ , normal load-30N, speed-0.471 m/s, sliding time-30min,	655 to 750 HV	SiC ceramic: COFs and wear loss are lower than wear against ZrO ₂ ceramic.	[71]
4.	2015	Fe ₂₅ Cr ₂₀ Ni ₂₀ Mn ₁₅ Co ₁₀ Al ₁₀	casting	Reciprocating unit	Grease and dry	Counter disk-65G steel, Load: 0.5 and 1.0 MPa, sliding speed : 6–12 m/s,	HIT / Er-0.032	COF with grease: 0.26 COF without grease :0.34	[72]
5.	2016	AlCrCuFeNi ₂	AM	ball-on-block	dry, simulated	Counter body-Si ₃ N ₄ ceramic ball,	400 HV	wear resistance better in simulated	[73]

					rain water (PH=2), and DI water	loads : 5, 10, and 15 N, sliding speed: 0.2 m/s,		rainwater at 15 N, and wear under dry condition worst	
6.	2015	AlCoCr CuFeNi and AlCoCr FeNiTi _{0.5}	AM	pin-on-disc	90% H ₂ O ₂ Con.	CB:1Cr18Ni9Ti steel, ZrO ₂ and SiC ceramic disk, load - 35 N, sliding speed (0.690 m/s), time - 30 min.	4.757 GPa and Ti(0.5) 6.707 GPa	Ti0.5/SiC ceramic have better wear properties than the ZrO ₂	[75]
7.	2016	AlCoCr FeNiTi _{0.5}	AM	ball-on-flat	gear oil, and multiply alkylated cyclopentanes (MACs)	humidity - 40%, steel ball- AISI 52100, load- 100 and 200 N, frequencies of 20–30 Hz (linear speed of 0.04–0.06 m/s), time- 1 mm and 20 min	780 HV _{0.49}	Under gear oil, abrasive grooves occur with some delamination, and Under MACs, both grooves and delamination behaviors occur	[76]
8.	2017	Al _{1.3} Co CuFeNi ₂	AM and PN	ball-on-block	dry , DI water and acid rain (PH=2) condition	Ball- Si ₃ N ₄ (5mm), load -3N, sliding speed- 0.2m/s, Amplitude-5mm, time- 1200s.	As cast (340 HV) to nitrided (587 HV)	Both in as-cast and nitrided condition COF under acid rain is lower than dry and deionized condition	[77]
9.	2018	CoCrFe MnNi and Al _{0.1} Co CrFeNi	VAM	ball-on-flat	dry and marine environments	Ball-Si ₃ N ₄ (3mm), Normal load – 1N, frequency : 20 Hz, stroke length :1 mm, Time: 30 min	1.32 to 1.52 GPa	Wear property in marine environment is better than dry condition	[78]
10.	2018	AlCoCr FeNi	AM and PN	ball-on-block	dry , DI water and acid rain (PH=2) condition	Ball- Si ₃ N ₄ (5mm), load -3N, sliding speed- 0.2m/s, Amplitude-5mm, time- 1200s.	As-cast (522 HV) to nitrided (720 HV)	The lowest wear rate for the as-cast and nitrided HEAs were obtained in the acid rain condition	[79]
11.	2018	Al _{0.6} Co CrFeNi	AM	ball-on-flat	Dry, DI water, simulated acid rain (PH 5 2), and simulated seawater	GCr15 steel ball, amplitude- 5 mm, sliding time- 1800 s, humidity of 55± 5%, normal load - 5 N, frequencies at 2, 3, 4, and 5 Hz	120 to 740 HV	COF is highest in dry than simulated seawater	[80]
12.	2019	AlCoCr	AM	Pin-	90 wt.%	CB: Si ₃ N ₄	Ti(0.5)	Ti(0.5) better	[81]

		FeNiTi _{0.5} and AlCoCr FeNiCu		on- disk	H2O2 sol.	(15GPa), track radius: 22 mm, Load: 50 N, Speed: 0.69 m/s H2O2 con.: 0 wt.% 30 wt. %, 60 wt. % and 90 wt. %; Time: 1800 s.	:6.70 GPa and 4.75 GPa	corrosion resistance after 14 days, HEA/Si ₃ N ₄ reaction give better wear resistance.	
--	--	--	--	-------------	--------------	--	------------------------------------	--	--

2.8. Literature on synthesis route, phase and mechanical properties of high entropy alloys

2.8.1. Literature on Al-Cr-Fe-Mn-Ni HEA system

Table 2.7 summarizes the previous literature on Al-Cr-Fe-Mn-Ni HEA system. It gives brief idea about synthesis route, phase formed, density, hardness and yield strength achieved. It has been also observed that limited work is done on this system and for more illustration, some of the reported work can be explained in detail as follows.

Chen et al.[42] synthesized the Al_xCrFe_{1.5}MnNi_{0.5} (x = 0.3 and 0.5) HEA through arc melting route and formed FCC+ BCC and BCC phase in as-cast. It observed that when it is aged at 700°C for 20hrs it forms FCC, BCC, Cr₅Fe₆Mn₈ phase and BCC, Cr₅Fe₆Mn₈ phase for Al_xCrFe_{1.5}MnNi_{0.5} (x = 0.3 and 0.5) HEA respectively and shown in Fig. 2.10.

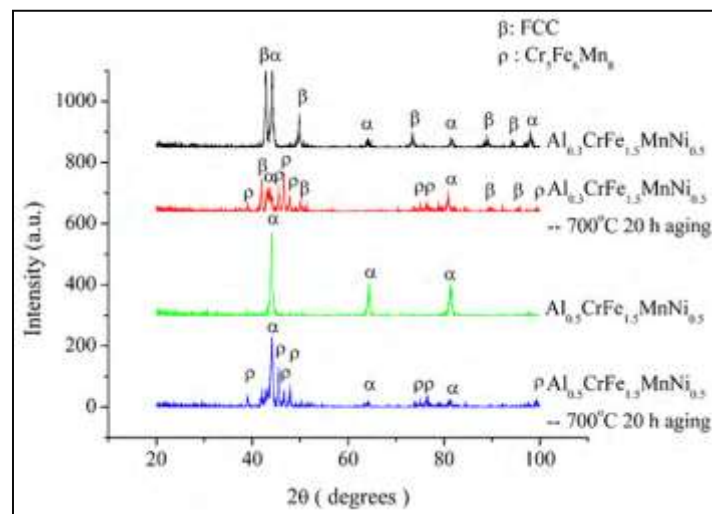


Fig 2.10 XRD patterns of as-cast and aged sample of Al_xCrFe_{1.5}MnNi_{0.5} (x = 0.3 and 0.5) [42]

The SEM micrograph of as-cast $\text{Al}_x\text{CrFe}_{1.5}\text{MnNi}_{0.5}$ ($x = 0.3$ and 0.5) HEA is shown in Fig. 2.11 and representing dendrite and interdendrite region. It is observed from the EDS results that the dendrite region rich in Al and Cr content than interdendrite zone. Hardness result indicating that $\text{Al}_x\text{CrFe}_{1.5}\text{MnNi}_{0.5}$ ($x = 0.3$ and 0.5) HEA in as-cast condition achieved hardness of 297HV and 396 HV respectively.

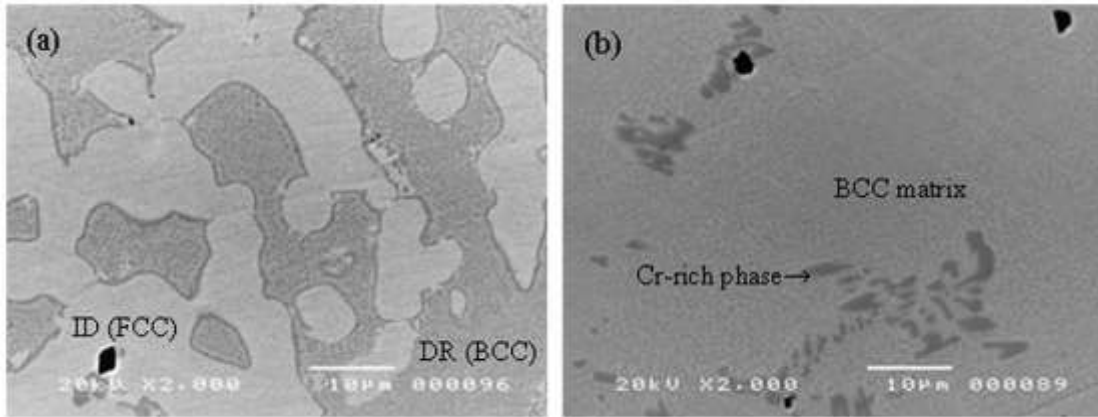


Fig. 2.11 SEM micrograph of as-cast $\text{Al}_x\text{CrFe}_{1.5}\text{MnNi}_{0.5}$ HEA (a) $x = 0.3$ and (b) $x = 0.5$ (DR: dendrite, ID: interdendrite) [42]

Meng et al.[82] synthesis FeNiMnAlCr HEA by utilizing arc melting and annealed at 800°C . The results indicated the formation of FCC and B2 phase. The FCC phases have rich content of Fe, and Mn and B2 phase have rich content of Al and Ni. It is observed that the hardness varies from 261 HV to 303 HV for as cast HEA.

Wang et al. [83] processed $\text{Fe}_{40.4}\text{Ni}_{11.3}\text{Mn}_{34.8}\text{Al}_{7.5}\text{Cr}_6$ HEA system through arc melting and XRD result indicating the formation of FCC phase in as-cast condition and FCC, BCC phase formed after cold rolling and annealing. It is observed that on varying the annealing condition the yield strength varies from 416MPa to 219 MPa. The possible reason reported for the decrease in the yield strength is because of the increase in grain size from $5\mu\text{m}$ to $19\mu\text{m}$.

Table 2.7 Literature on Al-Cr-Fe-Mn-Ni HEA system with synthesis route, phase, hardness, yield strength, and density

S.No.	Year	HEA	Synthesis Route	Phase	Hardness	Yield Strength	density	Ref.
1.	2018	$Al_xCrFe_{1.5}MnNi_{0.5}$ ($x = 0.3$ and 0.5 mol.)	MM and conventional sintering	BCC+FCC	210.0 HV to 386.7 HV	630 MPa to 1160.1 MPa	5.797 to 5.852 g/cm ³	[29] Present work
2.	2008	$Al_xCrFe_{1.5}MnNi_{0.5}$ ($0, 0.3$ or 0.5 mol)	AM	-	300 to 450 HV	-	-	[84]
3.	2008	$Al_xCrFe_{1.5}MnNi_{0.5}$ ($x=0, 0.3, 0.5$)	AM	-	-	-	-	[85]
4.	2010	$Al_xCrFe_{1.5}MnNi_{0.5}$ ($x = 0.3$ and 0.5)	AM	FCC+BCC	X=0.3 (297 HV), x=0.5 (396 HV)	-	-	[42]
5.	2012	$Al_{0.3}CrFe_{1.5}MnNi_{0.5}$	AM	FCC+BCC+AlNi and Cr ₅ Fe ₆ Mn ₈	298.8 HV	-	-	[86]
6.	2013	$Al_{0.3}CrFe_{1.5}MnNi_{0.5}$	VIM	FCC+BCC+AlCr+MnNi	317HV	-	-	[48]
7.	2015	FeNiMnAlCr	AM	FCC+B2	261HV	-	-	[82]
8.	2016	FeNiMnCr	AM	FCC	-	450MPa	-	[87]
9.	2016	$Fe_{40.4}Ni_{11.3}Mn_{34.8}Al_{7.5}Cr_6$	AM	FCC	-	159 ± 11 MP	-	[88]
10.	2017	$Fe_{40.4}Ni_{11.3}Mn_{34.8}Al_{7.5}Cr_6$	AM	FCC	-	219MPa to 416 MPa	-	[83]
11.	2017	$Fe_{36}Mn_{21}Cr_{18}Ni_{15}Al_{10}$	AM	BCC1+BCC2	420	990	7.18	[89]
12.	2018	$(Fe_{40}Mn_{25}Cr_{20}Ni_{15})_{100-x}Al_x$ ($x=0,2,6,10,14$)	VAM	FCC, BCC, B2	-	200MPa to 1000 MPa	-	[90]
13.	2018	AlCrFeMn- <i>M</i> (<i>M</i> =Mg, Ti, Ni)	MM	BCC, FCC	-	-	-	[91]

14.	2019	AlCrFeNiMn	VAM	BCC	378 HV	-	-	[92]
15.	2019	Al _x CrFeMnNi (x = 0.5 – 0.8)	AM	BCC, B2	353 HV- 386 HV	1091- 1200 MPa		[93]

2.8.2. Literature on equiatomic Al-Fe-Cr-Ni-Co HEA system

Table 2.8 summarizes the reported work on equiatomic AlFeCrNiCo HEA with different fabrication technique, phase formed, hardness, tensile or compressive strength and density of the equimolar AlFeCrNiCo high entropy alloys. For more illustration, some of the reported work can be explained in detail as follows.

Munitz et al. [94] synthesis the AlFeCrNiCo HEA through arc melting. XRD results indicated that the as-cast HEA formed BCC and B2 phase. It is observed that the SEM micrograph represents dendrite and interdendrite region and EDS results indicating that dendrite core contain Ni and Al rich and interdendrite region contain Cr and Fe rich. The hardness result of as cast HEA indicated that the dendrite region have 4.5 GPa and interdendrite region have 5.1 GPa. The compressive yield strength of as-cast sample have 1380 MPa with strain of 10%.

Shiratori et al. [95] fabricated the AlFeCrNiCo HEA by using selective electron beam melting (SEBM) and conventional casting method. It is found that FCC, BCC, B2 phase appear in (SEBM) and BCC, B2 phase appear in casting method and the BCC and B2 region region have rich content of Fe-Cr and Al-Ni respectively. The hardness value in case of SEBM is 400 HV and in case of casting is 500 HV. The compressive yield strength and strain % in case of SEBM is 1015 MPa, and 26%. In case of cast HEA sample yield strength is 1308MPa and strain % is 5.6%.

Tang et al.[96] synthesis the AlFeCrNiCo HEA through arc melting and further by hot isostatic pressed and homogenized (HP). The XRD result indicate that the as-cast HEA have (A2+B2) phase phase and HP sample have (A2+B2+A1+σ) phase. It is observed that the SEM micrograph of as-cast sample shows the dendrite and interdendtrite region. EDS result indicated that the dendrite region rich in Al-Ni and and interdendtrite region have rich content of Fe-Cr and Co is uniformly distributed. HP sample indicate that the B2 phase rich in AlNi and A2 and σ rich in

Fe, Cr, and nano precipitate rich in Fe, Cr, Co. The yield strength of as-cast 395 MPa and HP sample has value of 295 MPa. Strain % in case of as-cast sample is 1% and in case of HP sample is 11%.

Table 2.8 Literature on equiatomic Al-Fe-Cr-Ni-Co HEA system with different synthesis route, phase, hardness, yield strength, and density.

S.No	Year	HEA	Synthesis route	Phase	Hardness (HV)	Yield strength (MPa)	Stain %	density (g/cm ³)	Ref.
1.	2013	AlCoCrFeNi	VLM	Cr-Fe and Al-Ni rich precipitate	-	-	-	-	[97]
2.	2015	AlCoCrFeNi	AM	B2	543 HV0.5	-	-	-	[98]
3.	2015	AlCoCrFeNi	IM	B2	-	1308.3 ± 77.3	-	-	[99]
4.	2015	AlCoCrFeNi	AM and HIP	BCC+B2	4.3 to 8.9 GPa	395 and 295	1% and 11%	7.0	[96]
5.	2016	AlCoCrFeNi	AM	BCC+B2	4.6 to 5.1 GPa	1380	10%	-	[94]
6.	2016	AlCoCrFeNi	SEBM	BCC+B2+ FCC	400	1015	26%	-	[95]
7.	2016	AlCoCrFeNi	AM	BCC	-	1320	-	-	[100]
8.	2017	AlCoCrFeNi	MA+ SPS	BCC+ FCC+σ	-	-	-	-	[101]
9.	2018	AlCoCrFeNi/ Al composite	VIM and MM, SPS	BCC and BCC, FCC	0.47GPa to 8.884 GPa	96MPa to 137 MPa	36% to 50%	-	[102]
10.	2019	AlCoCrFeNi	AM	BCC, B2	-	-	-	-	[103]
11.	2019	AlCoCrFeNi	Con. sintering	BCC, B2, FCC, sigma phase	4.9 GPa to 5.2 GPa	1203 MPa to 1461 MPa	26% to 32 %	-	[104]
12.	2019	AlCoCrFeNi	SLM, IM	BCC and FeCr, AlNi	-	-	-	-	[105]
13.	2019	(AlCoCrFeNi) _{100-x} C _x (x=0 to 8)	AM	BCC, FCC	7.2-7.8 GPa	1426 MPa to 1376 MPa	29% to 35%	-	[106]
14.	2019	AlCoCrFeNi	SLM	BCC, A2, B2 phase	632.8 HV	-	-	6.25 g/cm ³	[107]

15.	2019	AlCoCrFeNi	LM and AM	BCC, B2	519HV and 493 HV	1631 MPa and 1209 MPa	17% and 25%	-	[108]
16.	2019	AlCoCrFeNi	AM	FCC, BCC, B2	-	-	-	-	[109]

2.8.2.1. Effect of Al in Al-Fe-Cr-Ni-Co HEA system

Table 2.9 summarizes the previous work on effect of Al in AlFeCrNiCo HEA system with different fabrication technique, phase formed, hardness, tensile or compressive strength and density of the $Al_xFeCrNiCo$ high entropy alloys. For more illustration, some of the reported work can be explained in detail as follows.

Shun et al. [110] have synthesized the $Al_{0.3}CoCrFeNi$ HEA through induction melting and aged further at 700°C and 900°C for 72 hrs. The results indicated that FCC structure formed in case of as-cast and aged sample. The second phase appears in case of sample aged at 900°C and form B2 structure. Yield strength under tension for as-cast and aged sample varies from 170 MPa to 330 MPa and strain varies from 60% to 45% in case of as-cast to aged sample respectively.

Kao et al. [111] synthesized the $Al_xCoCrFeNi$ ($0 \leq x \leq 2$) HEA through vacuum arc melting and compared with homogenized and deformed condition. The XRD pattern of as-cast result indicates that as the Al content increases the transformation from FCC phase to BCC phase occur. On increasing the Al content hardness increases from 116 HV to 509 HV and in case of Al=0.375 HEA is 130 HV. After homogenization at 1100°C for 24hrs. XRD results indicate that transformation of FCC to BCC occur along with formation of B2 phase which are rich in AlNi as shown in Fig. 2.12. The SEM micrograph of homogenized $Al_xCoCrFeNi$ ($0 \leq x \leq 2$) HEA as shown in Fig. 2.13 indicate the formation of needle shaped morphology which are rich content of Al-Ni inside the FCC matrix. The hardness of homogenized $Al_xCoCrFeNi$ ($0 \leq x \leq 2$) HEA varies from 113 HV to 512 HV and in case of Al= 0.375 HEA is 196 HV.

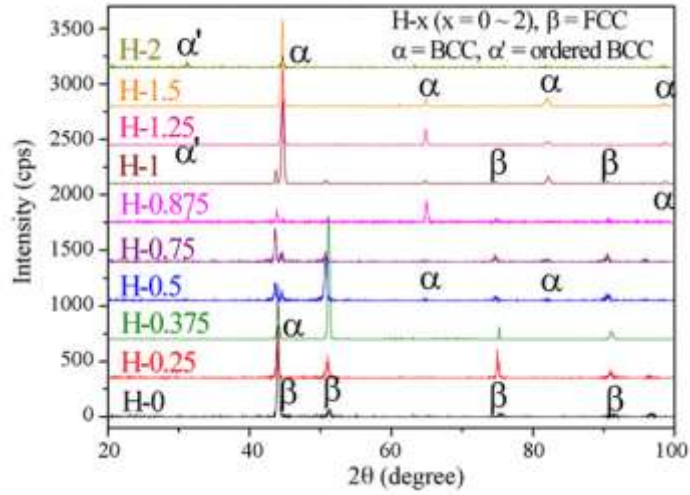


Fig. 2.12 XRD pattern of homogenized $\text{Al}_x\text{CoCrFeNi}$ ($0 \leq x \leq 2$) HEA [111]

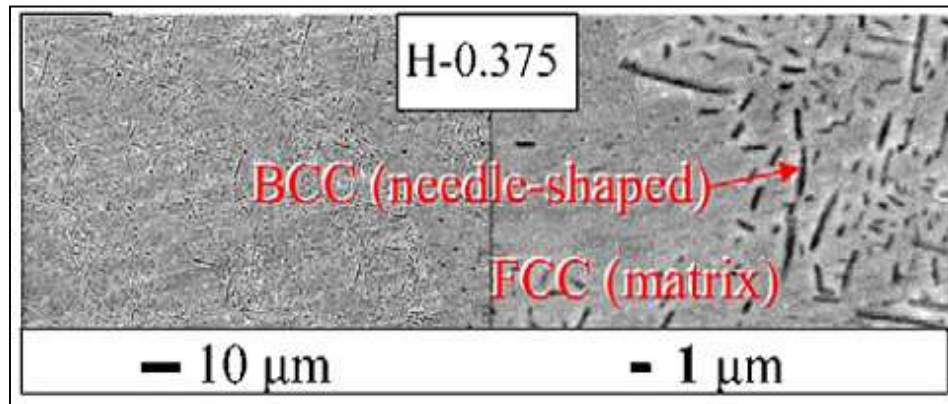


Fig. 2.13 SEM micrograph of homogenized $\text{Al}_x\text{CoCrFeNi}$ ($0 \leq x \leq 2$) HEA [111]

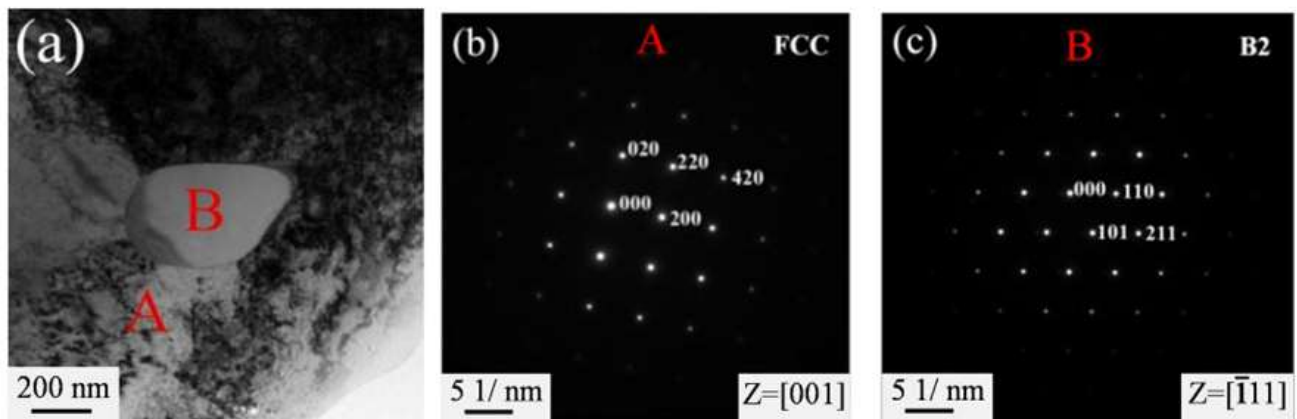


Fig. 2.14 TEM of $\text{Al}_{0.3}\text{CoCrFeNi}$ HEA and the selected area diffraction patterns (SADP) of region A and B [112]

Li et al. [112] have developed the $Al_{0.3}CoCrFeNi$ HEA through vacuum levitation melting. Further the HEA ingot is hot drawn into smooth fibers. The XRD result indicated that the as-cast formed FCC structure and TEM result of hot drawn $Al_{0.3}CoCrFeNi$ HEA fibers confirms the formation of FCC and B2 phase as shown in Fig. 2.14.

Table 2.9 Literature on effect of Al in Al-Fe-Cr-Ni-Co HEA system

S.No	Year	HEA	Synthesis route	Phase	Hardness (HV)	Yield strength (MPa)	Strain %	density (g/cm ³)	Ref.
1.	2009	$Al_{0.3}CoCrFeNi$	IM	FCC+ BCC	-	170 to 330MPa	As-cast : 60% and aged: 45%	-	[110]
2.	2009	$Al_xCoCrFeNi$ ($0 \leq x \leq 2$)	AM	FCC, FCC+ BCC, and BCC	116 to 509 HV	-	-	-	[111]
3.	2011	$Al_{0.5}CoCrFeNi$	AM	FCC+ BCC	247	-	-	-	[113]
4.	2015	$Al_xCoCrFeNi$ (x= 0.3,0.6, and 0.85)	AM	FCC, BCC, B2	-	200 to 1400	78% - 25%	-	[114]
5.	2016	$Al_{0.1}CoCrFeNi$	AM	FCC	135 to 482	100 Mpa	-	-	[115]
6.	2017	$Al_{0.3}CoCrFeNi$	VLM	FCC	-	1147	-	-	[112]
7.	2017	$Al_{0.1}CoCrFeNi$	VIM	FCC	181.3 ± 10	300	10 % - 45%	-	[116]
8.	2017	$Al_{0.6}CoCrFeNi$	AM	FCC+ BCC	-	1100	-	-	[117]
9.	2018	$Al_xCoCrFeNi$ (x = 0.3, 0.6, 0.9) HEAs	AM	FCC to FCC+ BCC	-	50MPa to 180 MPa (in Temp.)	More than 90%	-	[118]
10.	2018	$Al_{0.5}FeCoCrNi$	SLM	BCC, FCC	262 HV	579 MPa	22%	-	[119]
11.	2018	$Al_xCoCrFeNi$	AM	FCC to	-	160 MPa to	64% to	-	[120]

		(x=0.3, 0.7)		BCC and L12		1076 MPa	20%		
12.	2018	Al _{0.3} CoCrFeNi	AM	FCC, BCC, B2		160MPa to 1850 MPa	65% to 5%	-	[121]
13.	2019	Al _{0.3} CoCrFeNi	AM	FCC, and BCC	150H V to 366 HV	243MPa to 463MPa	60% to 40%		[122]
14.	2019	Al _{0.3} CoCrFeNi	VAM	FCC, B2, sigma phase	-	900 MPa	25%	-	[123]
15.	2019	Al _{0.5} CoCrFeNi	AM	BCC, FCC	-	325 MPa to 390 MPa	40%	-	[124]
16.	2019	Al _{0.25} CoCr FeNi	PAF	FCC to FCC,B CC, B2, CrB	188 HV _{0.5} to 1136 HV _{0.5}	-	-	-	[125]

AM-Arc melting, MA-mechanical alloying, SPS, spark plasma sintering, IM-Induction melting,
VIM- Vacuum induction melting, VLM- vacuum-levitation melting

2.8.2.2. Effect of Fe, Cr and Ni in Al-Fe-Cr-Ni-Co HEA system

Table 2.10 summarizes the previous work on effect of Fe, Cr, and Ni in AlFeCrNiCo HEA system with different fabrication technique, phase formed, hardness, tensile or compressive strength and density of the AlFeCrNiCo high entropy alloys. For more illustration, some of the reported work can be explained in detail as follows.

Lu et al. [126] have processed AlCoCrFeNi_{2.1} HEA through vacuum induction melting. The XRD results shows that the major phase formed is FCC and the minor phase formed is B2. The major phase rich in CoCrFe and the B2 phase rich in AlNi. The tensile strength at room temperature in case of AlCoCrFeNi_{2.1} HEA is 150 MPa and strain of 25%.

Chen et al. [127] synthesized the AlCoCrFe_xNi (0.2 to 2.0) HEAs through arc melting. The XRD results indicate that with addition of Fe content BCC and B2 are the main phase. It is found that with the increase in Fe content, the hardness value decreases from 637.2 HV to 460.2 HV. The compressive yield strength decreases from 2335 MPa to 2100 MPa and strain increases from 10% to 40%.

Chen et al. [128] studied the Al_{20-x}Cr_{20+0.5x}Fe₂₀Co₂₀Ni_{20+0.5x} (x= 2, 4.5, 7, 9.5) HEA and reported that as Cr and Ni content increases, the Al content decreases. The XRD patterns indicated that with increase of Cr and Ni content BCC phase increases and microstructure shows dendrite and interdendrite structure. At higher content of Cr and Ni the microhardness decreases from 508 HV to 245 HV and impact toughness increases from 12 KJ/m² to 477 KJ/m². At highest Cr and Ni content maximum strain of 25% observed at 750 MPa of yield strength.

Table 2.10 Literature on effect of Fe, Cr and Ni in Al-Fe-Cr-Ni-Co HEA system

S.No.	Year	HEA	Synthesis route	Phase	Hardness (HV)	Yield strength (MPa)	Strain (%)	density (g/cm ³)	Ref.
1.	2014	AlCoCrFeNi _{2,1}	VIM	FCC+ B2	-	150	25%	7.38	[126]
2.	2015	Al _{0.25} CoCrFe _{1.25} Ni _{1.25}	AM	FCC	167	92		-	[129]
3.	2015	AlCoCrFe _x Ni (0.2 to 2.0)	AM	B2, BCC, Cr ₃ Ni ₂	637.2 to 460.2	2335 to 2100	10% to 40%	-	[127]
4.	2016	Al _{20-x} Cr _{20+0.5x} Fe ₂₀ Co ₂₀ Ni _{20+0.5x} (x= 2, 4.5, 7, 9.5)	AM	FCC + BCC	508-245HV		6% to 25%	-	[128]
5.	2017	AlCoCrFeNi _{2,1}	VIM	FCC+ BCC	-	1100	-	-	[130]
6.	2017	AlCoCrFeNi _{2,1}	AM	FCC+ BCC	-	-	-	-	[131]
7.	2017	AlCoCrFeNi _{2,1}	IM	FCC+ BCC	-	-	-	-	[132]
8.	2018	Al _{0.7} NiCoFe _{1.5} Cr _{1.5}	AM	BCC, FCC, B2, sigma	562 HV to 334 HV	1523 MPa to 941 MPa	8% to 38%		[133]
9.	2018	AlCoCrFeNi _{2,1}	AM	FCC, BCC B2, L12	-	1150 MPa to 250 MPa	18% to 48%	-	[134]
10.	2019	AlCoCr ₂ FeNi ₂	AM	FCC, BCC B2,	-	840 MPa	7.4%	-	[135]

VIM- Vacuum induction melting

2.8.2.3. Effect of Co in Al-Fe-Cr-Ni-Co HEA system

Table 2.11 summarizes the previous work on effect of Co in AlFeCrNiCo HEA system with different fabrication technique, phase formed, hardness, tensile or compressive strength and density of the AlFeCrNiCo HEA. For more illustration, some of the reported work can be explained in detail as follows.

Qin et al. [136] developed the (AlCoCrFeNi)_{100-x}Co_x (x=0, 4, 8, 12, 16,) HEA system through arc melting technique. The XRD result indicated that as cobalt content added from 0% to 16% the

FCC phase fraction increases from 0% to 77%. The microstructure has two regions indicating FCC and BCC structure. The FCC region poor in Al and BCC region rich in Al. With the increase of Co content the compressive yield strength decreases from 1300 MPa to 750 MPa and plastic strain increases from 27% to 40%.

Kang et al. [137] synthesized the $\text{AlCo}_x\text{CrFeNi}$ ($x = 0, 0.25, 0.5, 0.75, \text{ and } 1$) HEAs through suction casting technique. XRD results indicated that as the Co content increases, the HEA sample have similar A2 (BCC) and B2 (ordered BCC) structure. After heat treatment at 1300°C for 6 hrs, the XRD pattern shows FCC, BCC, B2 and sigma phase. The compressive yield strength of as HEA indicate that as cobalt content increases the yield strength varies in between 1271.2 MPa to 1363.3 MPa and strain varies in between 14% to 20%.

Table 2.11 Literature on effect of Co in Al-Fe-Cr-Ni-Co HEA system

S.No.	Year	HEA	Synthesis route	Phase	Hardness (HV)	Yield strength (MPa)	Strain (%)	density (g/cm^3)	Ref.
1.	2019	$\text{Al}_{0.4}\text{FeCrNiCo}_x$ ($x=0, 0.25, 0.5,$ and 1.0 mol)	AM	FCC+ BCC+ B2	253.6 to 155.6	965.22 to 233.37	70%	7.224 to 7.787	Present work
2.	2015	$\text{Al}_{0.75}\text{FeNiCr}_x$ ($x=\text{Co, Ti}$)	MA+ SPS	FCC+ BCC	577	2221		-	[138]
3.	2018	$\text{Al}_x\text{CrCo}_{2-x}\text{FeNi}$ ($x=1.0, 1.2, 1.4,$ 1.6)	MA+ SPS	FCC+ BCC+ B2+ σ	486 to 576 HV0.05	860 to 105		-	[62]
4.	2018	(AlCoCrFeNi) _{100-x} Co_x ($x=0, 4, 8, 12,$ 16,)	AM	FCC+ BCC	-	1300 to 750	27% to 40%	-	[136]
5.	2018	$\text{AlCo}_x\text{CrFeNi}$ ($x = 0, 0.25, 0.5,$ 0.75, and 1)	AM	A2, B2	B2: 7.25 to 6.13 GPa A2: 4.19 to 4.95 GPa	1271.2 to 1313.7	14% to 20%		[137]

2.9. Research Gap

The literature review is carried out based on the various criteria like synthesis route, property-based, alloying element based, most cited HEA system, etc. Following research gap are concluded.

- ❑ Limited works on erosion behavior of high entropy alloys under different operating condition are available.
- ❑ Limited studies are available on sliding wear of high entropy alloys under different operating condition.
- ❑ Large numbers of literature are available on equimolar high entropy alloys which have higher strength and lower ductility. However, wear study of HEAs having higher strength and higher ductility is rare.

2.9.1. Proposed objective of the present research work

Based on the research gap from the available literature, the objectives of the research work are outlines as follows:

- ❖ To study the thermodynamic aspect of the HEA formation.
- ❖ Development of $\text{Al}_x\text{Fe}_{1.5}\text{CrMnNi}_{0.5}$ ($x = 0.3$ and 0.5 mol) HEAs through mechanical milling and conventional sintering technique.
- ❖ To investigate the thermal, mechanical and erosion behavior of $\text{Al}_x\text{Fe}_{1.5}\text{CrMnNi}_{0.5}$ ($x = 0.3$ and 0.5 mol) HEAs.
- ❖ Development of $\text{Al}_{0.4}\text{FeCrNiCo}_x$ ($x = 0, 0.25, 0.5$ and 1.0 mol) HEAs through arc melting route.
- ❖ To investigate the effect of cobalt content on thermal, mechanical and physical property of $\text{Al}_{0.4}\text{FeCrNiCo}_x$ ($x = 0, 0.25, 0.5$ and 1.0 mol) HEAs.
- ❖ To study the effect of cobalt content on wear behavior of $\text{Al}_{0.4}\text{FeCrNiCo}_x$ ($x = 0, 0.25, 0.5$ and 1.0 mol) HEAs under dry and under oil lubricating conditions at room temperature.

2.10. Working methodology for synthesis and characterization of HEAs

2.10.1. Working methodology for the development of HEAs through mechanical milling and conventional sintering route

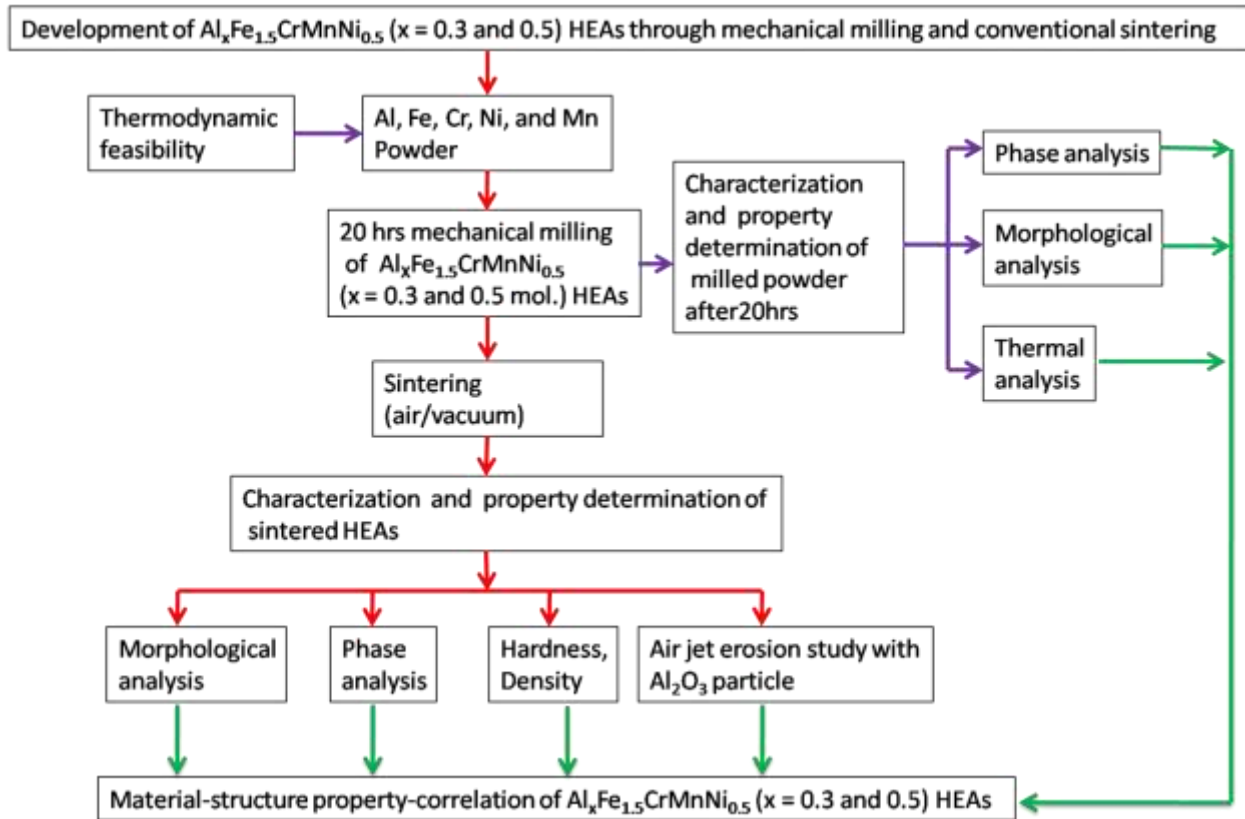


Fig. 2.15 Working methodology for the development $Al_xFe_{1.5}CrMnNi_{0.5}$ ($x = 0.3$ and 0.5 mol) HEAs

2.10.2. Working methodology for the development of HEAs through arc melting route

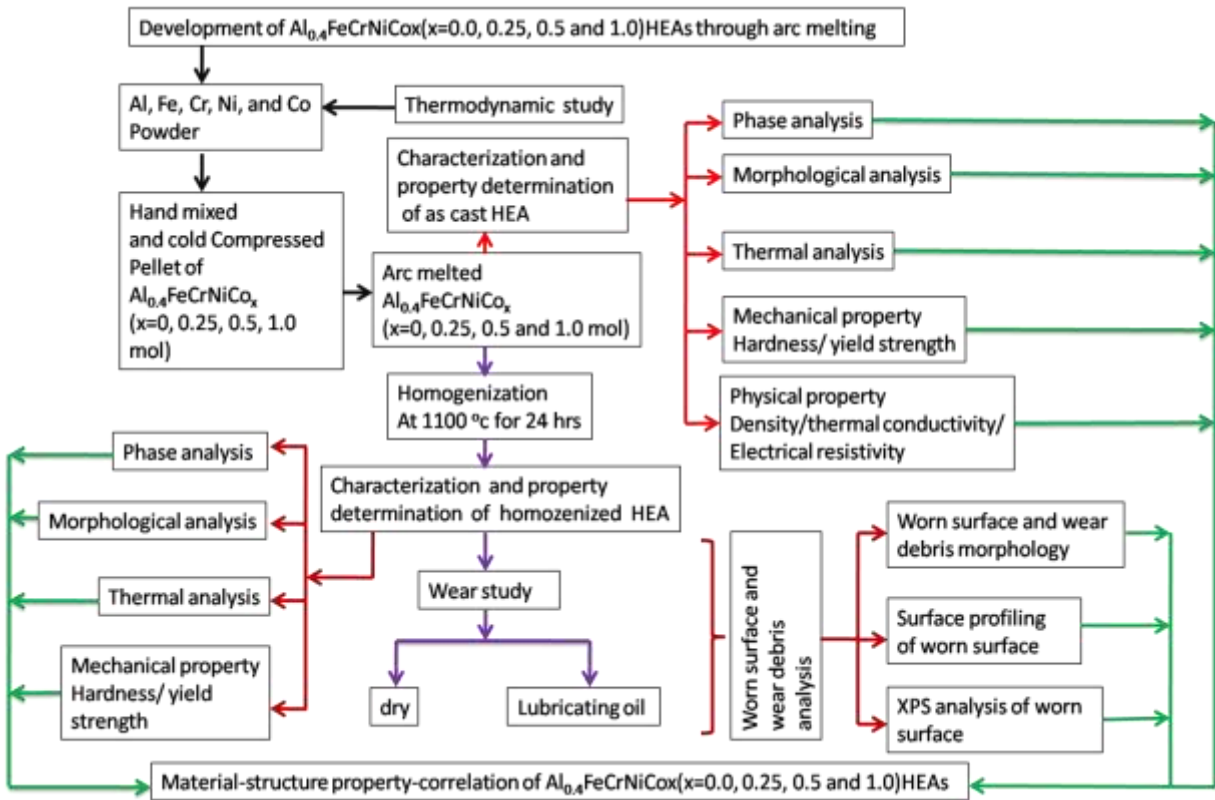


Fig. 2.16 Working methodology for the development of $Al_{0.4}FeCrNiCo_x(x = 0, 0.25, 0.5 \text{ and } 1.0 \text{ mol})$ HEAs

Chapter Summary

This chapter includes

- Previous literature on various aspects of HEAs.
- The research gap based on the reported studies on HEAs.
- The objectives of the research work based on the research gap.

In the next chapter fabrication of high entropy alloys and various characterization techniques were briefly discussed.

Materials and Methods

This chapter discusses about the different materials used and the methods adopted for the development as well as testing of the HEAs.

In the present work, two different HEA systems have been developed using two different synthesis techniques as highlighted below.

1. Synthesis of $\text{Al}_x\text{Fe}_{1.5}\text{CrMnNi}_{0.5}$ ($x = 0.3$ and 0.5 mol) HEAs through mechanical alloying and conventional sintering route.
2. Synthesis of $\text{Al}_{0.4}\text{FeCrNiCo}_x$ ($x=0, 0.25, 0.5$ and 1.0 mol) HEAs through arc melting route.

3.1. Materials and synthesis technique

3.1.1. Properties of alloying elements used for the development of HEAs

The research on HEAs indicates that elements from the entire part of the periodic table can be used as the alloying elements, whether it is s, p, d, or f-block elements. Each element has its unique characteristic features which can play an important role to develop the desired property in the HEA for a specific application. Generally, the most common alloying elements used for the development of HEAs are the d-block (transition) elements.

In the present study, two different HEA systems are designed with two different synthesis techniques. The first HEA system is consisting of Al, Fe, Cr, Mn, and Ni elements, whereas the other HEA system has Al, Fe, Cr, Ni, and Co elements. The physical and the mechanical properties of individual elements are listed in Table 3.1.

Table 3.1 Physical and mechanical properties of various elements [139, 140]

S.No.	Physical property	Al	Fe	Cr	Ni	Co	Mn
1.	Structure	FCC	BCC	BCC	FCC	HCP	BCC
2.	Melting Point (°C)	660.4	1538	1875	1455	1495	1244
3.	Boiling Point (°C)	2480	2750	2672	2732	2927	2095
4.	Density at 20 °C (g/cm ³)	2.71	7.87	7.19	8.90	8.9	7.44
5.	Thermal conductivity (W/mK)	237	80.2	93.7	83	100	29.7
6.	Vicker Hardness	167	608	1060	640	1043	9.81
7.	Tensile strength (MPa)	90-100	193-206	-	317	255	-
8.	Elastic modulus (GPa)	70.2	211	145	220	204	196

3.1.2. Fabrication of Al_xFe_{1.5}CrMnNi_{0.5} (x = 0.3 and 0.5 mol) HEAs through mechanical milling and conventional sintering route

Fritsch Pulverisette (P6) high-energy planetary ball mill with tungsten carbide balls was used to mechanically alloyed the metallic elemental powders of Al (98 %), Fe (99.5 %), Cr (99 %), Ni (99.9 %), and Mn (99 %) purity. The elemental powders used for the development of HEA is purchased from Loba chemical, India. The weight ratio of ball-to-powder was kept as 10:1 and to avoid excessive cold welding and protecting the medium to avoid oxidation, toluene is used as a process controlling agent (PCA) [141, 142]. The rotational speed of the disk over which the vial was attached is maintained at 300 rpm, which resulted in a vial speed of 546 rpm. During milling the alloy formation is confirmed by taken out the powder first after 10 minutes of milling and then after every 5 hrs of interval (5 hrs, 10 hrs, 15 hrs, and 20 hrs of milling). After 20 hrs of milling, the powder is taken out for further consolidation and characterization.

Hot compaction of Al_{0.3}Fe_{1.5}CrMnNi_{0.5} and Al_{0.5}Fe_{1.5}CrMnNi_{0.5} HEA is carried out in a 12 mm inner-diameter high-speed steel die under a load of 10 tons by utilizing a manual hydraulic press (Kimaya Engineers-15 tons) at a temperature of 230 °C. Sintering of the compacted HEAs is performed in an electric resistance furnace and in a vacuum induction furnace at a temperature of

800 °C and for a time period of 2 hrs. The sintering atmosphere in case of the electric resistance furnace was normal furnace atmosphere, and in case of the vacuum induction furnace, it was protective vacuum environment having vacuum level of 10^{-1} atm.

3.1.3. Fabrication of $\text{Al}_{0.4}\text{FeCrNiCo}_x$ ($x=0, 0.25, 0.5$ and 1.0 mol) HEAs through arc melting route

The bulk ingots of $\text{Al}_{0.4}\text{FeCrNiCo}_x$ ($x=0, 0.25, 0.5$ and 1.0 mol) HEAs are synthesized by arc melting method under a protecting atmosphere of argon in a water-cooled copper mold. The bulk material is prepared using the cold compacted pellet (Fig. 3.1) as the raw material in arc melting furnace. The cold compaction is carried out in manual hydraulic press (Kimaya Engineers - 15 Tones) at load of 10 tone in a high-speed steel die of 12 mm inner diameter at room temperature. The elemental powders of Al, Fe, Cr, Ni, Co (Loba Chemie, India) with purity more than 99.5% are used for this purpose, and are hand mixed in appropriate proportion before compaction. The bulk ingot samples are flipped and remelted several times to achieve the better chemical homogeneity. The final ingots are either near cylindrical in shape with dimension of ($\text{Ø} 14$ mm x 45 mm) or circular button shape with dimension of ($\text{Ø} 16$ mm x 12 mm) as shown in Fig.3.1.



Fig. 3.1 (a) cold compacted pellet and as casted HEA samples in (b) cylindrical shape and (c) button shape

3.1.4. Homogenization of as-cast $\text{Al}_{0.4}\text{FeCrNiCo}_x$ ($x = 0, 0.25, 0.5$ and 1.0 mol) HEAs

Homogenization of as cast HEA samples were performed in chemical vapour deposition (CVD) furnace. In which argon is utilized to give protective environment to the samples. The sample is induction heated from room temperature ($25\text{ }^\circ\text{C}$) to $1100\text{ }^\circ\text{C}$ and than the samples is kept at $1100\text{ }^\circ\text{C}$ for 24 hrs. The HEA samples is than cool inside the furnace to room temperature and than removed for further processing.

3.2. Characterization of high entropy alloys

3.2.1. Phase evolution study of HEAs using X-ray diffraction (XRD)

The phase examination of samples after milling for different periods of time, after conventional sintering of the as-milled powders, as-cast ingots and of homogenized samples is carried out using a X-ray diffractometer (Panalytical, X'pert Pro USA) fitted with Cu target (Cu $K\alpha$, $\lambda = 0.1540598\text{ nm}$), operated at 40 A , 40 V , and at a scan rate of 2 deg/min . X-ray diffraction results are also used to calculate the crystallite size, lattice strain, phase fraction and lattice parameter of as-milled powder. Gaussian function is used to deconvolute the overlapped peaks and Scherrer formula is used to calculate the crystallite size which is given by equation (1).

$$D = \frac{k\lambda}{\beta \cos\theta} \quad (1)$$

Where, k is the shape factor whose value is generally taken as 0.9 [143], λ is the X-ray wavelength, β is the FWHM i.e full width at half maxima, θ is the Bragg angle and D is the crystallite size.

3.2.2. Microstructural examination of HEA using scanning electron microscope (SEM)

The morphology of as-milled powder and the microstructure of sintered, as cast, and homogenized HEAs are analyzed by FE-SEM (Nova Nano 450SEM, FEI, North America) which is operated at 30 kV . The sample is analyzed in both the imaging modes, i.e., secondary electron (SE) mode, and back scattered electron (BSE) mode. The as-milled powder samples are examined by spreading the as-milled powder over the double side carbon tape.

In case of sintered, as-cast and homogenized samples, it is first mounted and grounded over a series of SiC emery paper from 120 to 2000 grit size. Then fine polishing is done using 3 micron alumina powder and then 1 micron, polycrystalline diamond suspension over a cloth polisher. The chemical composition of the phases are obtained with the help of energy dispersive x-ray spectroscopy (EDS) detector (Bruker, Germany).

3.2.3. Phase evolution study of HEAs using Transmission electron microscopy (TEM)

The nanocrystalline nature of the as-milled powder is confirmed from the TEM study. In order to examine the crystallite size, morphology, d-spacing, and phases of as-milled powder. TEM dark field, bright field, HRTEM images, and selected area electron diffraction (SAED) pattern are obtained. The transmission electron microscope (Tecnai G2 20 FEI) is operated at 200 KV. For TEM studies, powder samples are ultrasonicated for about 50 minutes in ethanol, and then are allowed to settle down for 10 minutes. Powder sample is then collected from the top part of the ethanol and is then spread over the top surface of a carbon-coated Cu grid (200 mesh). TEM-EDS of as-milled powder and as-cast HEA samples were also obtained to know the chemical composition homogeneity.

In case of the as-casted HEA sample, grinding and polishing operation is performed in a MetaServ® 250 (Buehler) high-speed twin grinder-polishers, so as to achieve a thickness of less than 100 microns. After that, the pre-thinned sample is cut into a circular shape with the help of a disc cutter. Then it is followed by precision ion milling system (PIPS II, GATAN) to thin down the material by ions in order to allow the electron to pass through the sample.

3.3. Physical, thermal and mechanical analysis of high entropy alloys

3.3.1. Density

The densities of the sintered and as-cast HEA samples were measured according to Archimedes principle using water as a medium in a density measuring instrument (Mettler Toledo). The working formula to calculate the density is given by equation (2).

$$\rho_{exp} = \left[\frac{W_a}{(W_a - W_m)} \right] X \rho_m \quad (2)$$

Where ρ_{exp} is the experimental density, w_a is the weight in air, w_m is the weight in a medium and ρ_m is the density of the medium.

3.3.2. Thermal conductivity

The thermal conductivity of the as-cast HEA samples is measured by the hot disk thermal constant analyzer (Model: TPS 500, Gothenburg, SWEDEN). The thermal conductivity experiment is based on the principle of transient plane source (TPS) in which heat source coated with Kapton film on a spiral shaped hot disk, and temperature response sensor was placed in between the HEA samples of dimension ($\text{Ø } 16 \text{ mm} \times 5 \text{ mm}$). The electrical power flows through the sample, and the thermal conductivity is measured as a function of time. The data recorded with the help of hot disk software, and each experiment is performed five times to ensure the repeatability of the result.

3.3.3. Differential scanning calorimetry (DSC)

The thermal stability of as-milled powder, as-cast and homogenized sample are analyzed by differential scanning calorimetry (Netzsch, DSC 404 F3) in the temperature range of ambient ($23 \text{ }^\circ\text{C}$) to $1000 \text{ }^\circ\text{C}$ with a heating rate of 10 K/min . In this analysis the sample is placed in an alumina crucible, and a baseline correction is performed before acquisition of the heat flow curve in each experiment. It is tried to maintain zero temperature difference between the sample holder and the referenced. For any phase change, heat may be absorbed or evolved, and the system is required to maintain the zero temperature difference by flowing an appropriate amount of heat to either the sample or the holder.

3.3.4. Microhardness measurements

For microhardness measurement, the sintered, as-cast and homogenized HEA samples are prepared according to ASTM E3-11 standards and then tested in a microhardness tester (VMHT, Walter-Uhl) by applying a load of 200 gf for a dwell time of 15 s . For each sample average of ten measurements are recorded on the mirror polished surface. The hardness is evaluated by the equation (3).

$$HV = 0.1891 \frac{N}{D^2} \quad (3)$$

Where N is the applied normal load in (Kgf) and D is the diagonal length of the indentation.

A empirical relation is used to calculate the yield strength of the sintered HEA from corresponding hardness.

$$\sigma_Y \text{ (MPa)} = 3 \times \text{Hv (HVN)} \quad (4)$$

3.3.5. Room temperature Compression testing

The compression testing of the as-cast and the homogenized sample of $\text{Al}_{0.4}\text{FeCrNiCo}_x$ ($x = 0, 0.25, 0.5$ and 1.0 mol) HEAs is performed on BISS UT 21 testing machine according to ASTM E 9 standards. Cylindrical samples of dimension ($\text{Ø}4 \text{ mm} \times 4 \text{ mm}$) are prepared with the help of electric discharge machining (EDM). The tests are performed at room temperature with a rate of 0.5 mm/min .



Fig. 3.2 Specimen for compression test

3.4 Air jet erosion and sliding wear measurement

3.4.1 Air jet erosion test

Air jet erosion study of sintered $\text{Al}_x\text{Fe}_{1.5}\text{CrMnNi}_{0.5}$ ($x = 0.3, 0.5$ mol) HEAs is performed according to ASTM G76 standards by utilizing air jet erosion tester (DUCOM, TR-471-800) at four different angles, i.e., 90° , 75° , 60° , and 45° . The tester consists of a nozzle made up of alumina with a diameter of 1.5 mm and a length of 50 mm , an erodent feeding device and the

target mount. Alumina (Al_2O_3) particles with an average particle size of $50\ \mu\text{m}$ are used as the erodent material. The mass flow of the erodent is fixed at $2\ \text{g}/\text{min}$, and the erodent velocity on the target was maintained at $70\ \text{m}/\text{s}$. The distance between the nozzle exit and the target is maintained at $10\ \text{mm}$. The erosion value is calculated using the following equation.

$$\text{Erosion Value} = \frac{\text{Volume loss of the specimen}(\text{mm}^3)}{\text{Erodent Consumed (g)}} \quad (4)$$

3.4.2 Sliding wear test

The wear tests of homogenized $\text{Al}_{0.4}\text{FeCrNiCo}_x$ ($x = 0, 0.25, 0.5$ and $1.0\ \text{mol}$) HEAs is performed according to ASTM G99 standards at room temperature using a pin on disk tribometer (DUCOM, CM9112). Cylindrical specimens of dimensions ($\text{Ø} 8\text{mm} \times 23\ \text{mm}$) as shown in Fig. 3.3 are tested under dry condition as well as under commercially available engine oil (SAE Grade: 20W-40) with viscosity of (13.5 -15.5 at $100\ ^\circ\text{C}$, cSt), viscosity index of (114), flash point of ($240\ ^\circ\text{C}$), pour point of ($-21\ ^\circ\text{C}$). The HEA pin samples are slid against a standard EN-31 steel disc of dimensions ($\text{Ø}100\ \text{mm} \times 8\ \text{mm}$) and with a hardness of 60-65 HRC. The HEA samples are grounded before each experiment with a series of emery papers (220, 400, 600, 800, 1000 grit) followed by ultrasonic cleaning in an acetone bath. The wear tests are carried out under different sliding parameters as listed in Table 3.2. The coefficient of friction (COF) is recorded automatically through computer-controlled LabVIEW software.

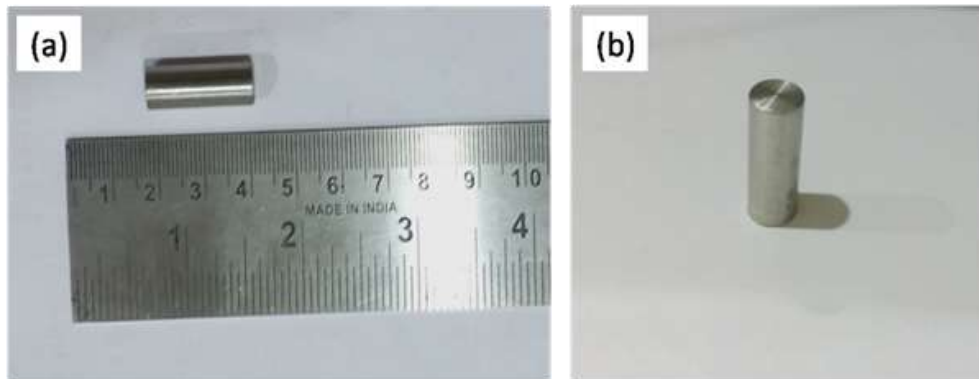


Fig. 3.3 Specimen for pin-on-disk

Table 3.2 Parameters for pin-on-disk test

Parameters	Value
HEA Pin Composition (mol)	0, 0.25, 0.5, 1
Sliding speed (m/s)	0.5, 1, 1.5, 2
Sliding distance (m)	1000, 2000, 3000, 4000
Normal load (N)	5, 10, 15, 20
Track radius (mm)	25 mm
Medium	Dry and 20W-40 oil
Temperature	Room temperature (25 °C)
Counter Part	EN-31 disk

Each experiment is repeated three times, on separate samples, to ensure the repeatability of the result. The specific wear rate of the HEA specimens is calculated according to the following equation.

$$W_s = \frac{\Delta m}{\rho \times V_s \times t \times f_n} \quad (5)$$

Where, W_s is the specific wear rate in mm^3/Nm , Δm is the mass loss after the wear test in grams, ρ is the density of HEAs in g/cm^3 , V_s is the sliding speed in m/s, t is the wear test duration time in second, f_n is the normal load in Newton. After the wear test the worn surface morphology and the composition of the HEA pin samples are analyzed using a SEM and EDS, respectively to predict the wear mechanism. White light interferometer attached with a 10X objective lens was used to generate the 3D profile of the worn surfaces. The oxide and the other unknown compounds formed on the worn surface during the wear process are analyzed using X-ray photoelectron spectroscopy (XPS).

Chapter summary

This chapter includes.

- Various properties of alloying elements.
- Brief discussion about the fabrication technique.
- Thermal, mechanical and physical characterization.
- Erosion and sliding wear characterization.

In the next chapter results and discussion of synthesis, characterization and air jet erosion study of $Al_xFe_{1.5}CrMnNi_{0.5}$ ($x = 0.3$ and 0.5 mol) HEAs is briefly discussed.

Synthesis, characterization and air jet erosion study of $\text{Al}_x\text{Fe}_{1.5}\text{CrMnNi}_{0.5}$ ($x = 0.3$ and 0.5 mol) HEAs

4.1 Introduction

The $\text{Al}_x\text{Fe}_{1.5}\text{CrMnNi}_{0.5}$ ($x = 0.3$ and 0.5 mol) HEAs are synthesized by mechanical alloying (MA) and conventional sintering technique. The effect of aluminium content on the phase evolution of HEAs is investigated using XRD, SEM, EDS, HRTEM, SAED. Thermal, mechanical, and physical properties are measured. Air jet erosion test is performed to investigate erosion behavior of sintered HEA. For convenience in writing, $\text{Al}_{0.3}\text{Fe}_{1.5}\text{CrMnNi}_{0.5}$ HEA is denoted as (Al0.3), $\text{Al}_{0.3}\text{Fe}_{1.5}\text{CrMnNi}_{0.5}$ HEA sintered in a vacuum is designated as S-1, and $\text{Al}_{0.3}\text{Fe}_{1.5}\text{CrMnNi}_{0.5}$ HEA sintered in the air is designated as S-2 in subsequent text. Similarly, $\text{Al}_{0.5}\text{Fe}_{1.5}\text{CrMnNi}_{0.5}$ HEA is being denoted as (Al0.5), $\text{Al}_{0.5}\text{Fe}_{1.5}\text{CrMnNi}_{0.5}$ HEA sintered in vacuum designated as S-3, and $\text{Al}_{0.5}\text{Fe}_{1.5}\text{CrMnNi}_{0.5}$ HEA sintered in the air is designated as S-4 in subsequent text.

4.2 Phase evolution of $\text{Al}_x\text{Fe}_{1.5}\text{CrMnNi}_{0.5}$ ($x = 0.3$ and 0.5 mol) HEAs

Figure 4.1(a) represent the XRD pattern of milled powder of $\text{Al}_{0.3}\text{Fe}_{1.5}\text{CrMnNi}_{0.5}$ HEA for different milling times. It can be observed that the individual peaks of all elements can be identified after only 10 mins of milling and then after every 5hrs. As the time progresses, Al is the first element to dissolve, and it completely disappears after 5 hrs of milling. In a similar manner, the intensity of peaks of other elements also decreases as the milling progresses from 10 min to 20 hrs. The width of peaks corresponding to (110) plane is observed to increase throughout the milling process. All other peaks vanish with the progress of milling which indicates the formation of the solid solution [144, 145].

The d-spacing and the lattice parameter value of the 20 hrs of milled powder in the reflecting plane (110) are observed to be $d = 2.043 \text{ \AA}$ and $a = 2.889 \text{ \AA}$, respectively. In case of pure Cr, the d-spacing and the lattice parameter value for the (110) plane is observed to be $d = 2.039 \text{ \AA}$ and a

= 2.884 Å, respectively. This gives an indication that other elements prefer to diffuse into the (110) plane lattice site of Cr. Due to higher melting point and lower diffusion coefficient, the diffusion of Cr into another lattice site become difficult. [48, 146]

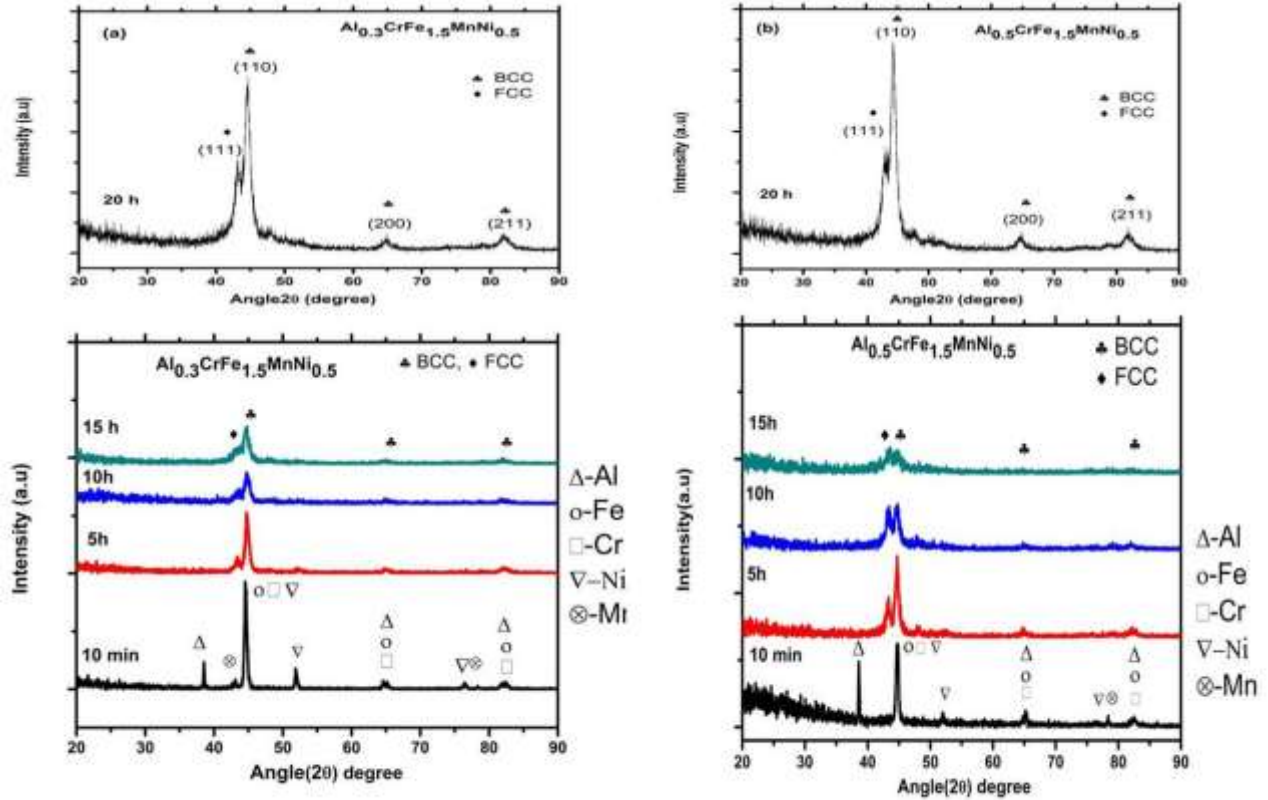


Fig. 4.1 XRD patterns of milled powders after 10 min, 5 hrs, 10 hrs, 15 hrs, 20 hrs of milling in case of (a) $\text{Al}_{0.3}\text{CrFe}_{1.5}\text{MnNi}_{0.5}$ HEA and (b) $\text{Al}_{0.5}\text{CrFe}_{1.5}\text{MnNi}_{0.5}$ HEA.

In case of the $\text{Al}_{0.5}\text{Fe}_{1.5}\text{CrMnNi}_{0.5}$ HEA, as shown in Fig. 4.1(b), the d-spacing and the lattice parameter values of the 20 hrs of milled powder in the reflecting plane (110) are found to be $d = 2.04315 \text{ \AA}$, and $a = 2.889 \text{ \AA}$, respectively, and that of pure Cr corresponding to the (110) plane is found to be 2.039 \AA and 2.899 \AA , respectively. This observation also suggests that all other elements diffuse into Cr [48, 146]. In case of both the HEAs, i.e., $\text{Al}_x\text{Fe}_{1.5}\text{CrMnNi}_{0.5}$ ($x = 0.3$, and 0.5), primarily BCC phase is observed to be getting formed after 20 hrs of ball milling along with a small fraction of FCC phase. The phase fraction of FCC in BCC matrix is calculated after deconvoluting the peaks as seen in Fig. 4.2(a) and Fig. 4.2(b) using eq. (1) [147]. The minor

FCC peak and the major BCC peak have shown a lattice parameter of 3.645 Å and 2.889 Å, respectively. The phase fraction of FCC in BCC phase after 20 hours of milling in $Al_xFe_{1.5}CrMnNi_{0.5}$ ($x = 0.3, 0.5$ mol) HEAs is found out to be 29.35 % and 24.76 %, respectively.

$$\text{Fraction of FCC phase} = \frac{I_{FCC}}{I_{FCC} + I_{BCC}} \quad (1)$$

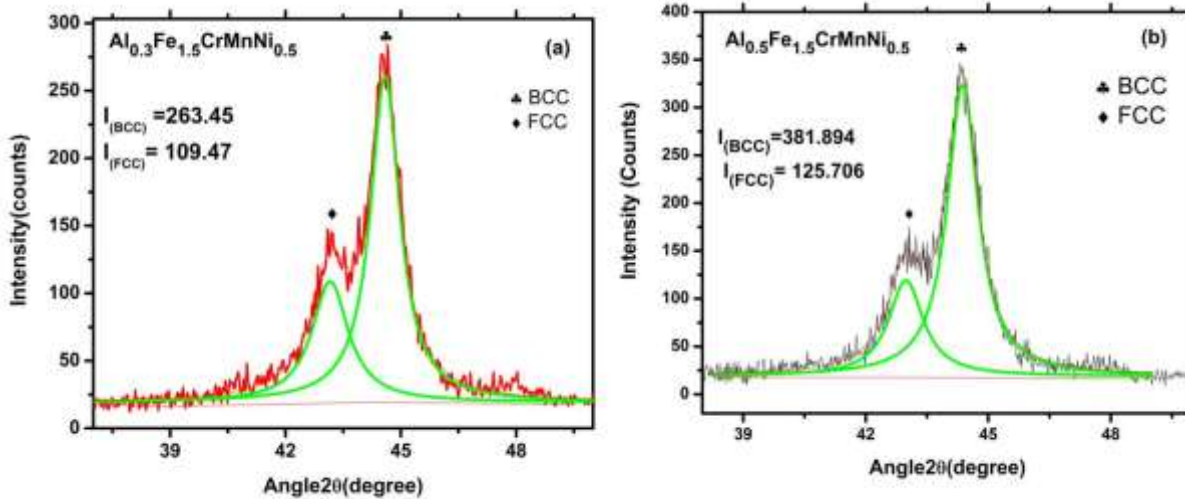


Fig. 4.2 Deconvoluted XRD pattern of 20 hrs milled powder of (a) $Al_{0.3}CrFe_{1.5}MnNi_{0.5}$ HEA (b) $Al_{0.5}CrFe_{1.5}MnNi_{0.5}$ HEA

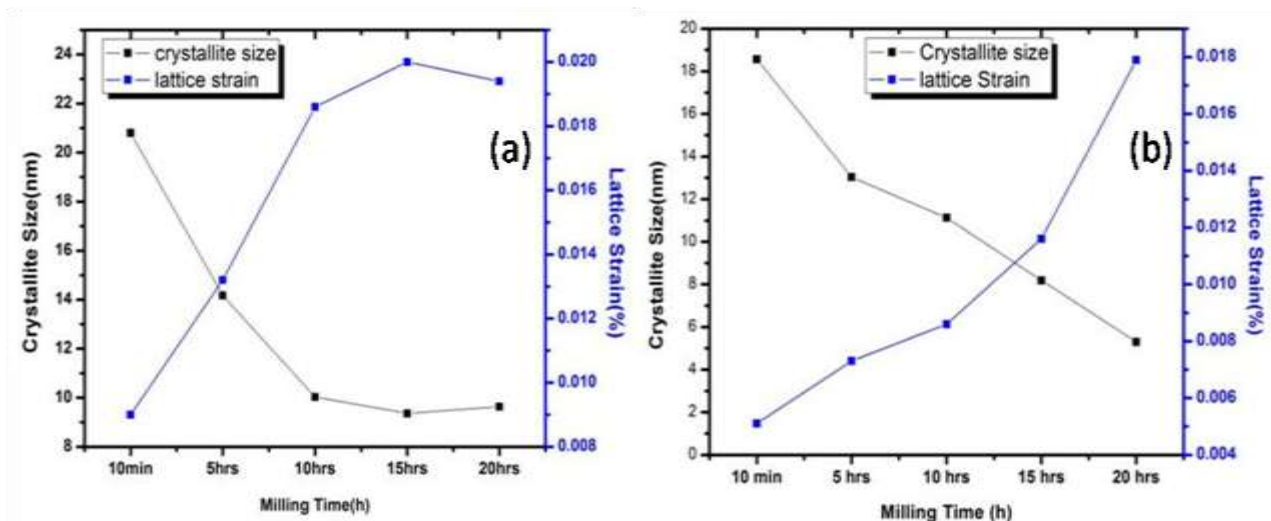


Fig. 4.3 Crystallite size and lattice strain as a function of milling time for the BCC phase of (a) $Al_{0.3}CrFe_{1.5}MnNi_{0.5}$ HEA and (b) $Al_{0.5}CrFe_{1.5}MnNi_{0.5}$ HEA.

Figure 4.3(a) and Fig. 4.3(b) shows the variation in crystallite size and lattice strain of the BCC phase formed in $Al_xFe_{1.5}CrMnNi_{0.5}$ ($x = 0.3$ and 0.5) HEA. Crystallite size and lattice strain are calculated using Scherrer's formula [143]. It can be observed from Fig. 4.3(a) that as the milling time increases from 0 hrs to 20 hrs, the crystallite size decreases from 20.8 nm to 9.64 nm in case of the $Al_{0.3}CrFe_{1.5}MnNi_{0.5}$ HEA, and in case of the $Al_{0.5}CrFe_{1.5}MnNi_{0.5}$ HEA, it decreases from 18.56 nm to 5.3 nm as shown in Fig. 4.3(b). The calculation has been carried out only considering the BCC phase. At the same time, the lattice strain is observed to increase with the increase in milling time, and it reaches up to 1.94 % and 1.79 % for the BCC phase in case of $Al_{0.3}CrFe_{1.5}MnNi_{0.5}$ HEA and $Al_{0.5}CrFe_{1.5}MnNi_{0.5}$ HEA as shown in Fig. 4.3(a) and Fig. 4.3(b) respectively.

4.3 Morphology and mechanism of alloy formation

At the start of the milling, all the elemental powders get combined and decrease the inter lamellar spacing of the resultant crystal due to cold welding. As the milling progresses, work hardening of the powder particles increases, and this increases the brittleness, which in turn starts the fracturing of the particles.

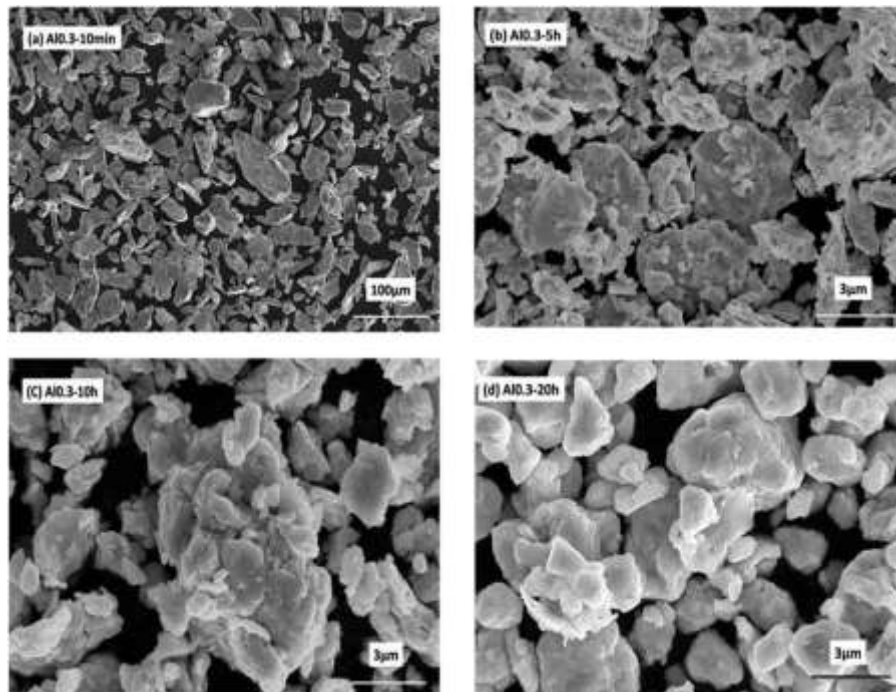


Fig. 4.4 Morphology of $Al_{0.3}Fe_{1.5}CrMnNi_{0.5}$ (Al0.3) HEA after different milling times (a) 10 min (b) 5 hrs (c) 10 hrs (d) 20 hrs.

With the increase in milling time, the crystallite size decreases as shown in Fig. 4.3 and the diffusion of the individual atoms start. However, the diffusion is only possible when the inter lamellar spacing between the elements decreases to a certain level. Microstrain increases as a result of diffusion of one atom into the lattice defect of other elements which in turn have originated from severe plastic deformation during milling.

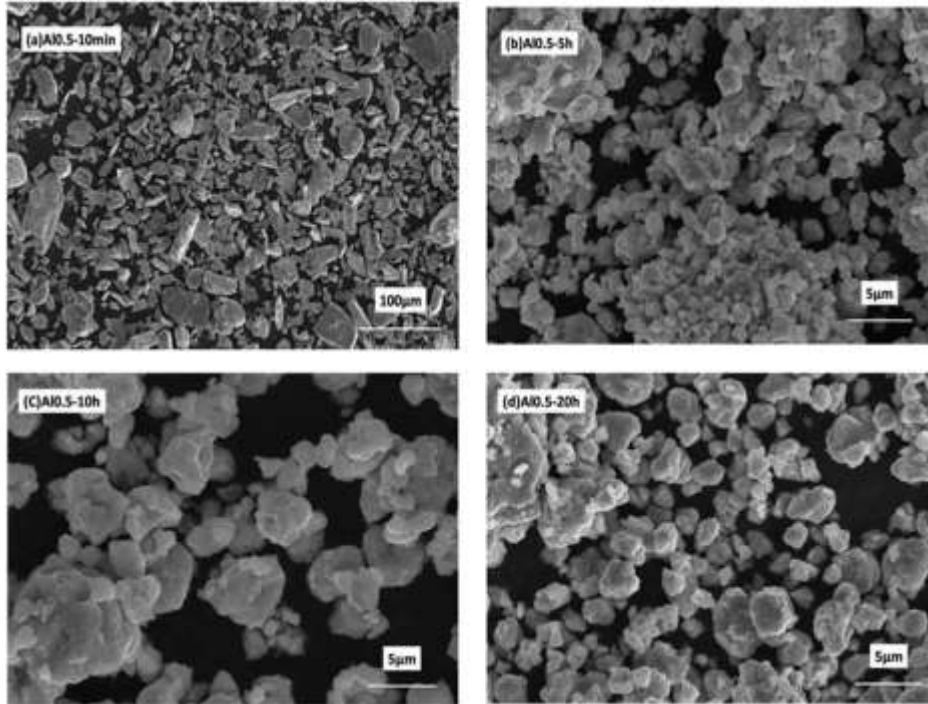


Fig. 4.5 Morphology of $Al_{0.5}Fe_{1.5}CrMnNi_{0.5}$ (Al0.5) HEA after different milling time (a) 10 min (b) 5 hrs (c) 10 hrs and (d) 20 hrs.

SEM images of as-milled powders after a milling period of 10 mins, 5 hrs, 10 hrs, and 20 hrs, in the case of $Al_{0.3}Fe_{1.5}CrMnNi_{0.5}$ and $Al_{0.5}Fe_{1.5}CrMnNi_{0.5}$ HEAs are shown in Fig. 4.4 and Fig. 4.5, respectively. From Fig. 4.4 and Fig. 4.5, it is observed that most of the particles are irregular and the average particle size is in between 2 μm and 5 μm. It has also been found that as the aluminum content increases from $x=0.3$ to 0.5 mol, the amount of cold welding also increases in comparison to the fracturing process and this causes the formation of layered structure [148].

4.4 TEM analysis of $\text{Al}_x\text{Fe}_{1.5}\text{CrMnNi}_{0.5}$ ($x = 0.3$ and 0.5) HEA after milling

Figure 4.6 shows the variation between the expected and the observed chemical compositions of 20 hrs milled powder measured from TEM-EDS, and this indicates little variation between expected and observed value as shown in Fig. 4.6(a) and Fig. 4.6(b). Figures 4.7 and Fig. 4.8 show the TEM bright-field, dark-field, SAED, and HRTEM images of the 20 hrs of milled $\text{Al}_{0.3}\text{Fe}_{1.5}\text{CrMnNi}_{0.5}$ HEA and $\text{Al}_{0.5}\text{Fe}_{1.5}\text{CrMnNi}_{0.5}$ HEA, respectively which confirm the nano crystalline nature of the milled powder. SAED analysis verifies the formation of the BCC phase. The average crystallite sizes of $\text{Al}_{0.3}\text{Fe}_{1.5}\text{CrMnNi}_{0.5}$ HEA and $\text{Al}_{0.5}\text{Fe}_{1.5}\text{CrMnNi}_{0.5}$ HEA as observed in TEM dark field image are observed to be 1.739 nm and 1.457 nm, respectively.

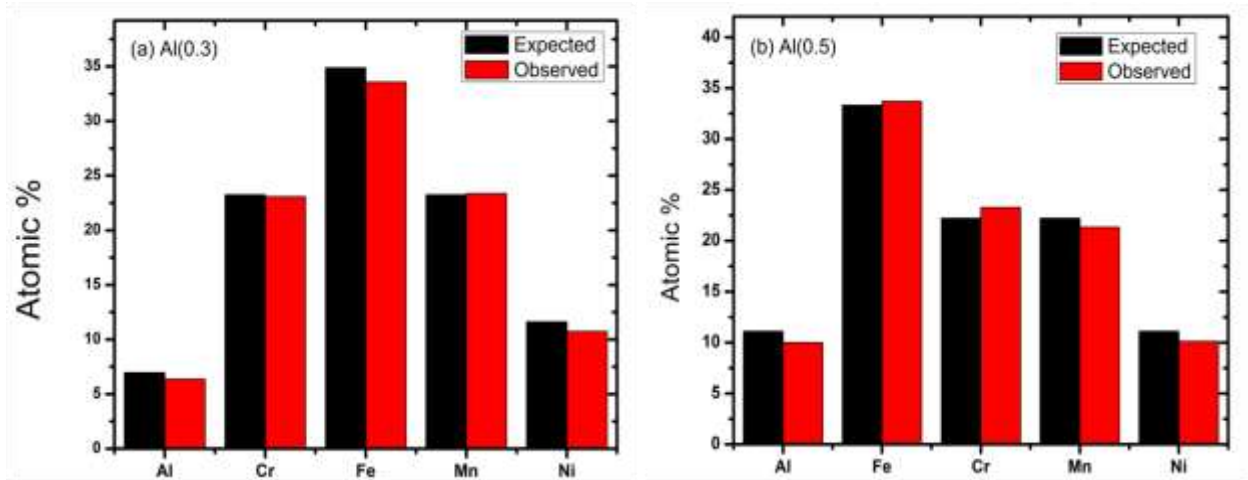


Fig. 4.6 TEM-EDS analysis of 20 hrs milled powder of (a) $\text{Al}_{0.3}\text{CrFe}_{1.5}\text{MnNi}_{0.5}$ and (b) $\text{Al}_{0.5}\text{CrFe}_{1.5}\text{MnNi}_{0.5}$ HEA.

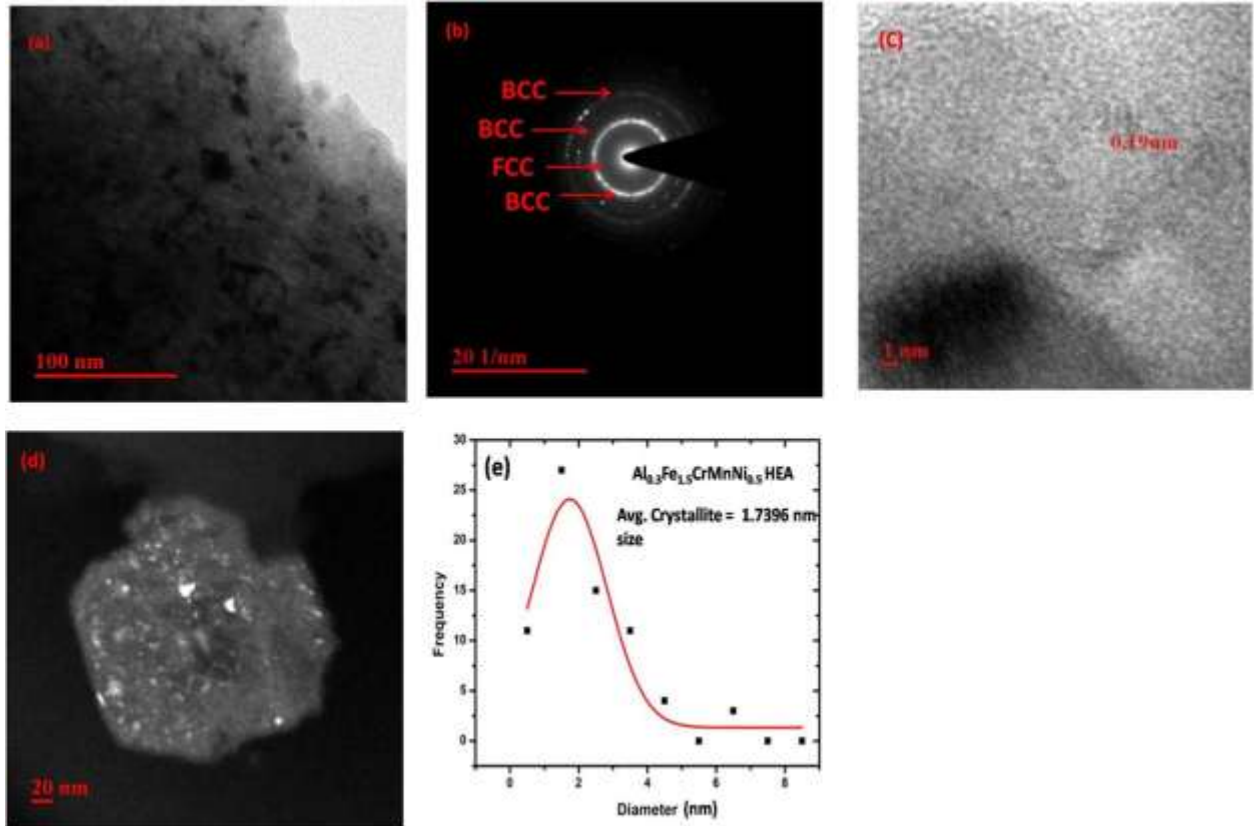


Fig. 4.7 Typical TEM micrographs of 20 h milled powder of $\text{Al}_{0.3}\text{CrFe}_{1.5}\text{MnNi}_{0.5}$ HEA, (a) bright field image, (b) SAED pattern (c) HR-TEM image, (d) TEM dark field image, and (e) crystallite size distribution which gave us an average crystallite size of 1.739 nm

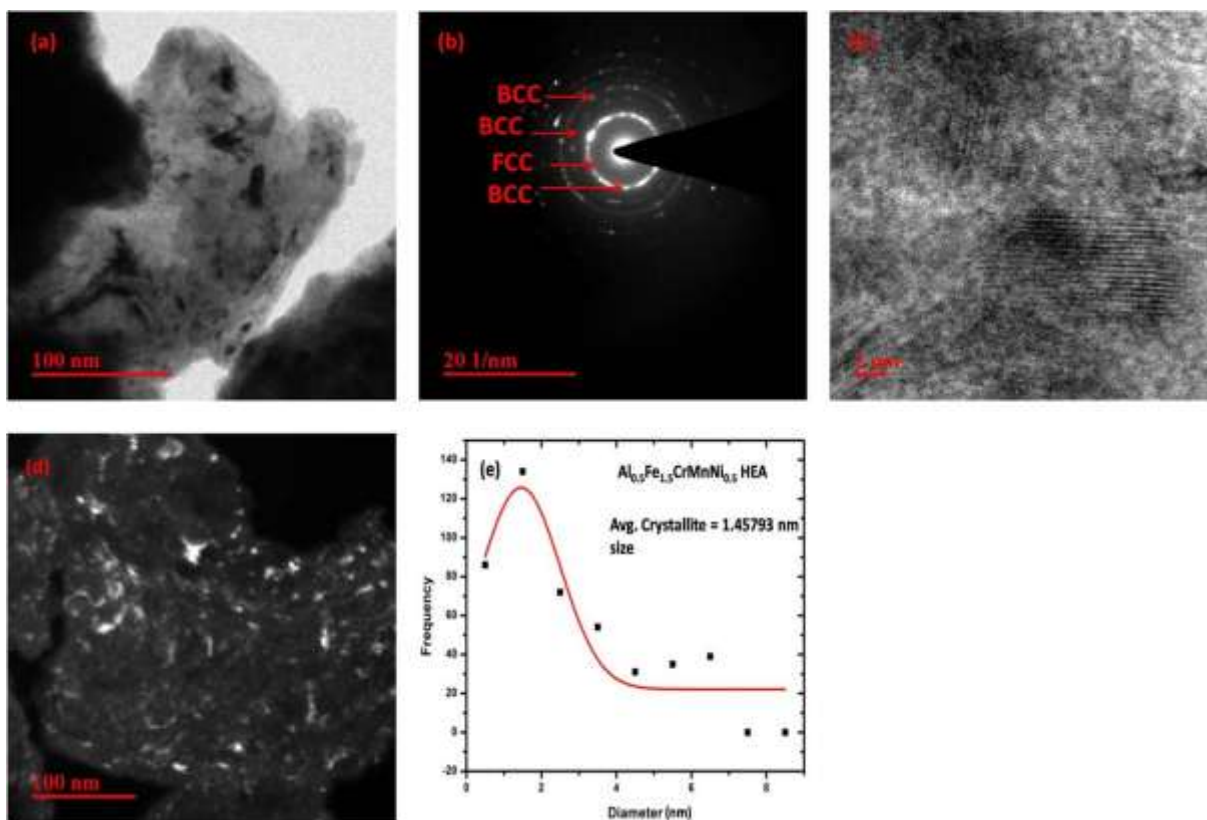


Fig. 4.8 Typical TEM micrographs of 20 hrs milled powder of $\text{Al}_{0.5}\text{CrFe}_{1.5}\text{MnNi}_{0.5}$ HEA (a) bright field image (b) SAED pattern (c) HR-TEM image, (d) TEM dark field image, and (e) crystallite size distribution, which give an average crystallite size of 1.457 nm.

The inter planar spacing as determined from the X-ray diffraction analysis is 0.2023 nm for the $\text{Al}_{0.3}\text{CrFe}_{1.5}\text{MnNi}_{0.5}$ HEA, and 0.2094 nm for the $\text{Al}_{0.5}\text{CrFe}_{1.5}\text{MnNi}_{0.5}$ HEA is in close agreement with the inter planar spacing measured from the HR-TEM image and from the SAED patterns. In case of $\text{Al}_{0.3}\text{CrFe}_{1.5}\text{MnNi}_{0.5}$ HEA, the d-spacing as determined from SAED pattern is 0.201 nm and from HR-TEM is 0.198 nm. In case of the $\text{Al}_{0.5}\text{CrFe}_{1.5}\text{MnNi}_{0.5}$ HEA, the d-spacing value as measured from the XRD analysis, SAED pattern, and HRTEM image are 0.2094 nm, 0.1986 nm, and 0.195 nm, respectively.

4.5 Thermal analysis of 20 hrs milled $\text{Al}_x\text{Fe}_{1.5}\text{CrMnNi}_{0.5}$ ($x = 0.3$ and 0.5) HEAs

Figure 4.9 shows the DSC curve of 20 hrs milled powder of $\text{Al}_x\text{Fe}_{1.5}\text{CrMnNi}_{0.5}$ ($x=0.3$ and 0.5) HEAs over the temperature range from ambient ($23\text{ }^\circ\text{C}$) to $1000\text{ }^\circ\text{C}$ and for a heating rate of $10\text{ }^\circ\text{C}/\text{min}$.

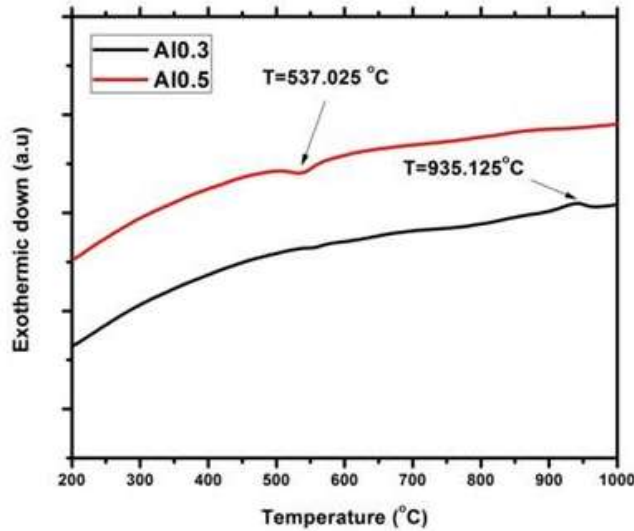


Fig. 4.9 DSC scan of 20h milled powder of $\text{Al}_x\text{CrFe}_{1.5}\text{MnNi}_{0.5}$ ($x = 0.3$ and 0.5) HEAs

At the temperature of around $537\text{ }^\circ\text{C}$, the mechanically alloyed $\text{Al}_{0.5}\text{Fe}_{1.5}\text{CrMnNi}_{0.5}$ HEA shows an exothermic peak at $537.025\text{ }^\circ\text{C}$ which is associated with release of internal stresses and the peak around $935.12\text{ }^\circ\text{C}$ for $\text{Al}_{0.3}\text{Fe}_{1.5}\text{CrMnNi}_{0.5}$ HEA shows an endothermic peak which is related with phase change.

4.6 Thermodynamic Parameter of $\text{Al}_x\text{CrFe}_{1.5}\text{MnNi}_{0.5}$ ($x = 0.3$ and 0.5) HEAs

Thermodynamic parameters such as: the atomic size difference (δ), the enthalpy of mixing (ΔH_{mix}) and the entropy of mixing (ΔS_{mix}) were commonly used to characterize the collective behavior of the constituent elements in the multi-component alloys [149].

The atomic size difference (δ) is defined by eq. (2)

$$\delta = 100 \sqrt{\sum_{i=1}^n C_i \left(1 - \frac{r_i}{r}\right)^2} \quad (2)$$

Where, $r = \sum_{i=1}^n C_i r_i$, c_i and r_i are the atomic percentage and atomic radius of the i^{th} element. The numerical factor 100 is used to amplify the data for clarity. The theoretical value of c_i is taken from Table 4.1.

The enthalpy of mixing (ΔH_{mix}) can be represented by eq. (3)

$$\Delta H_{\text{mix}} = \sum_{i=1, i \neq j}^n \Omega_{ij} C_i C_j \quad (3)$$

Where $\Omega_{ij} = 4 \Delta_{\text{mix}}(\text{AB})$; $\Delta_{\text{mix}}(\text{AB})$ is the enthalpy of mixing of binary liquid AB alloys, and entropy of mixing (ΔS_{mix}) can be represented by eq. (4)

$$\Delta S_{\text{mix}} = -R \sum_{i=1}^n C_i \ln C_i \quad (4)$$

Where, R is the gas constant. In addition to the above thermodynamic parameters, VEC is another parameter which helps in determining the phase stability of alloys [149]. VEC is defined by eq. (5)

$$\text{VEC} = \sum_{i=1}^n C_i (\text{VEC})_i \quad (5)$$

Where, $(\text{VEC})_i$ is the VEC for the i^{th} element. Thermodynamic parameters are calculated by using the required data listed in Table 2.2 and Table 4.1 [19]. The enthalpy of mixing (kJ/mol) of different atomic pairs in the $\text{Al}_x\text{Fe}_{1.5}\text{CrMnNi}_{0.5}$ HEA system is shown in Table 2.3 [150] and they have been used to calculate the enthalpy of mixing of the HEA.

Table 4.1 EDS results (in at.%) of 20 hrs milled $\text{Al}_x\text{Fe}_{1.5}\text{CrMnNi}_{0.5}$ ($x = 0.3$ and 0.5) HEAs

Composition	elements	Al%	Fe%	Cr%	Mn%	Ni%
Al(0.3)	theoretical	6.97	34.88	23.25	23.25	11.62
	average	6.37	33.56	23.07	23.36	10.73
Al(0.5)	theoretical	11.11	33.33	22.22	22.22	11.11
	average	10.01	33.71	23.28	21.34	10.12

Table 4.2 Thermodynamic parameters of $\text{Al}_x\text{Fe}_{1.5}\text{CrMnNi}_{0.5}$ ($x = 0.3$ and 0.5) HEAs.

Composition	ΔS_{config} (J/mol·K)	Delta (δ)	ΔH_{mix} (kJ/mol)	VEC	ΔX	T_m (°C)	Ω	Ref.
Al(0.3)	10.2389	0.03709	-5.5041	7.1857	0.1559	1484.96	2.762	[149]
Al(0.5)	12.661	0.04502	-7.2576	6.9993	0.1287	1448.22	2.526	[149, 151]

Calculated values of ΔS_{mix} , ΔH_{mix} , VEC and δ for the present $\text{Al}_x\text{Fe}_{1.5}\text{CrMnNi}_{0.5}$ ($x = 0.3$ and 0.5) HEA is listed in Table 4.2, which is consistent with the criteria of solid solution formation and the phase stability of HEA given in previous studies of Zhang and Guo [19, 20], i.e., if $15 \text{ kJ/mol} \leq \Delta H_{\text{mix}} \leq 5 \text{ kJ/mol}$, and $\text{VEC} \geq 8.0$ forms FCC, $\text{VEC} < 6.87$ forms BCC and $6.87 < \text{VEC} < 8.0$ mixed FCC and BCC phases provided, $\Omega \geq 1$ and $1 \leq \delta \leq 6$. The high value of entropy of mixing (ΔS_{mix}) is mainly responsible for the formation of solid solution, and the value of VEC confirms the mixture of BCC and FCC phases [3, 151].

4.7 Microstructure and phase analysis of sintered $\text{Al}_x\text{CrFe}_{1.5}\text{MnNi}_{0.5}$ ($x = 0.3$ and 0.5) HEAs

HEAs

Figures 4.10(a) and Fig. 4.10(b) show the detailed XRD analysis of $\text{Al}_x\text{CrFe}_{1.5}\text{MnNi}_{0.5}$ ($x = 0.3$ and 0.5) HEAs sintered at 800°C in the air and vacuum atmosphere. In both the air and vacuum sintering conditions, similar XRD pattern are observed for $\text{Al}_x\text{CrFe}_{1.5}\text{MnNi}_{0.5}$ ($x = 0.3$ and 0.5) HEAs. The crystal structure of the sintered alloys consists of FCC and BCC solid solutions in both air- and vacuum-sintered conditions. The regions rich in (Fe, Ni, Cr) mainly have BCC phase with a lattice parameter of 2.87 \AA . This is because the binary enthalpy of mixing of FeCr is (1 kJ/mol) and that of FeNi is (2 kJ/mol) [150] and Al and Cr elements are BCC stabilizers. On the other hand, the regions rich in (Mn, Ni, Cr) have FCC phase because Mn and Ni elements are FCC stabilizers and binary enthalpy of mixing of MnNi is (-8 kJ/mol), and that of CrNi is (7 kJ/mol) [150]. It is also expected that in the BCC matrix, AlNi precipitate of ordered BCC (B2) structure may form due to the highest negative binary enthalpy of mixing of AlNi (22 kJ/mol) [3, 44, 48]. In addition to this, many X-ray diffraction peaks are observed to appear in between 40° and 50° , which denote ρ phase (JCPDS No.-00-036-1373) and is composed of $\text{Cr}_5\text{Fe}_6\text{Mn}_8$ having a tetragonal structure with lattice constants $a = 9.09 \text{ \AA}$ and $c = 9.99 \text{ \AA}$ as reported in previous literature [42, 44].

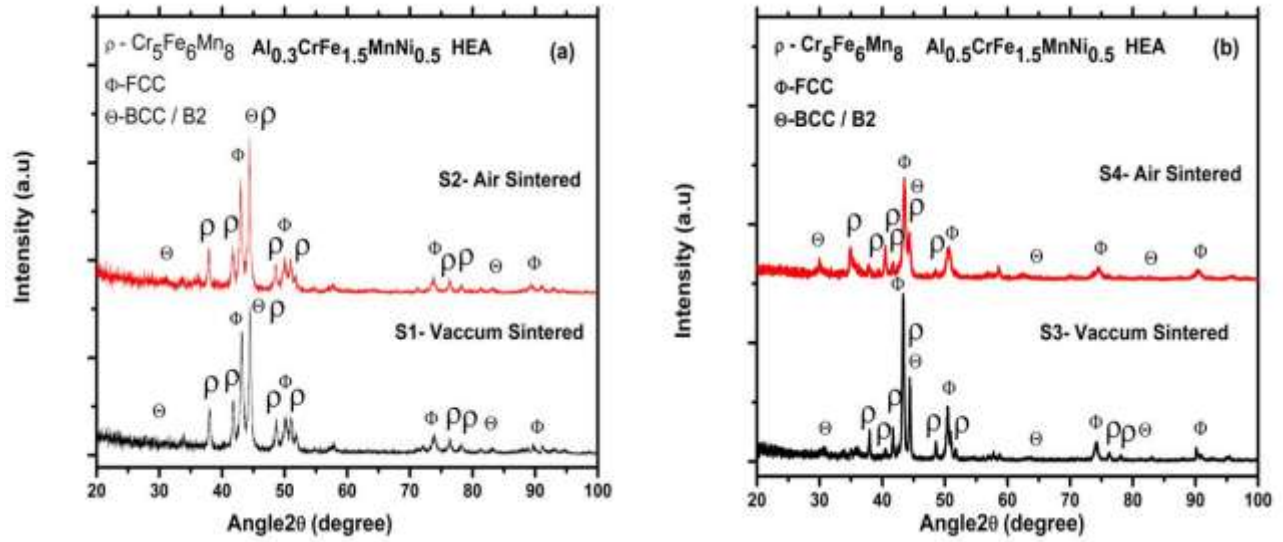


Fig. 4.10 XRD analysis of HEA sintered at different environment (a) $Al_{0.3}CrFe_{1.5}MnNi_{0.5}$ HEA (b) $Al_{0.5}CrFe_{1.5}MnNi_{0.5}$ HEA

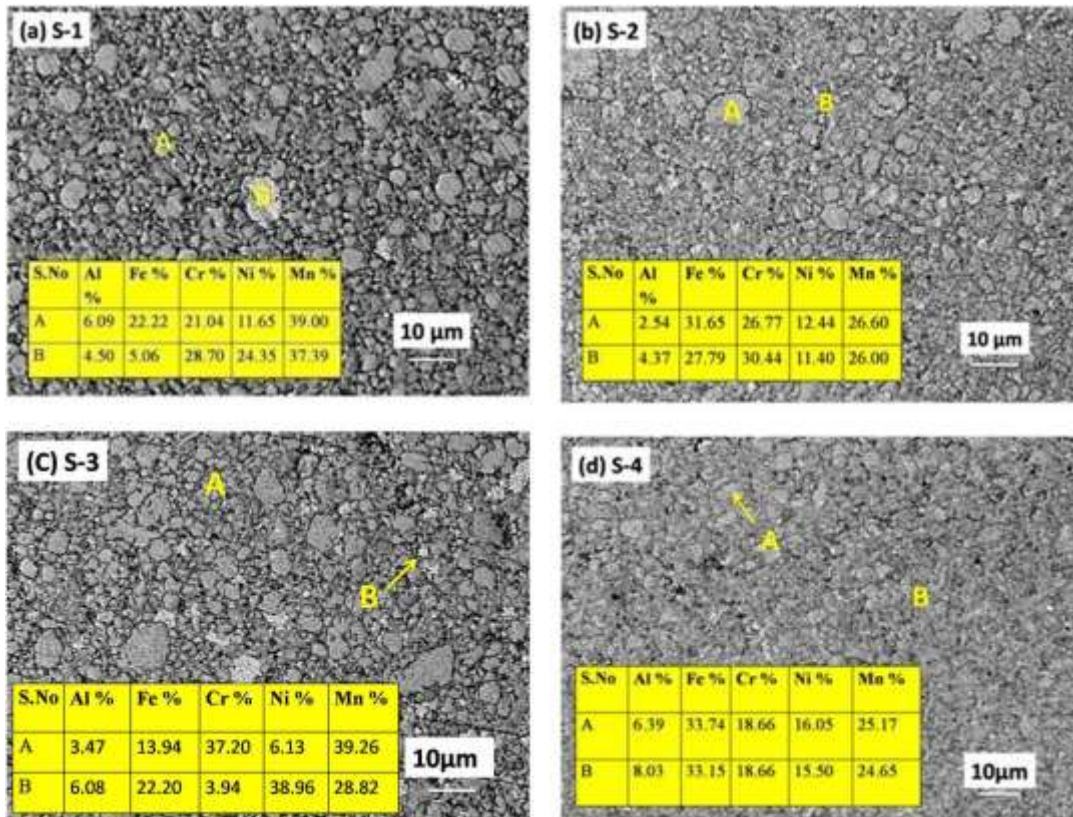


Fig. 4.11 BSE micrographs of $Al_xFe_{1.5}CrMnNi_{0.5}$ HEA (a) $Al_{0.3}$, vacuum sintered (S-1) (b) $Al_{0.3}$, air sintered (S-2) (c) $Al_{0.5}$, vacuum sintered (S-3) (d) $Al_{0.5}$, air sintered (S-4)

The formation ρ phase occurs due to the transformation of BCC phase, as with an increase in ρ phase, the BCC phase is observed to decrease. Figure 4.11 shows the BSE micrograph, and the chemical compositions of $\text{Al}_{0.3}\text{CrFe}_{1.5}\text{MnNi}_{0.5}$ HEA and $\text{Al}_{0.5}\text{CrFe}_{1.5}\text{MnNi}_{0.5}$ HEA, in the air- and vacuum-sintered conditions. The black spot in the BSE micrograph corresponds to the porosity. The morphology is observed to be like a circular plate. The approximation of grain size is made by assuming the grain to be circular in 2D view of the SEM image for both air- and vacuum-sintered conditions in case of $\text{Al}_x\text{Fe}_{1.5}\text{CrMnNi}_{0.5}$ ($x = 0.3$ and 0.5) HEAs. It has been found that the average grain size diameter in S1 is $1.79 \mu\text{m}$, in S2 is $1.37 \mu\text{m}$, in S3 is $1.27 \mu\text{m}$, and in S4 is $1.12 \mu\text{m}$. Hence, the sizes of the grains in the samples sintered in the air are slightly smaller than that of the samples sintered in a vacuum. This may be due to faster cooling during air sintering.

4.8 Bulk density and microhardness of $\text{Al}_x\text{Fe}_{1.5}\text{CrMnNi}_{0.5}$ ($x = 0.3$ and 0.5 mol) HEAs

Table 4.3 shows the variation of density and microhardness with the sintering condition. The experimental density is calculated by Archimedes principle, and the theoretical density calculated using the rule of mixture as shown below [152].

$$\rho_{mix} = \frac{\sum C_i A_i}{\sum \frac{C_i A_i}{\rho_i}} \quad (6)$$

Here, A_i and ρ_i are the atomic weight, and the density of i^{th} element, respectively. The calculated value of ρ_{mix} for $\text{Al}_{0.3}\text{Fe}_{1.5}\text{CrMnNi}_{0.5}$ and $\text{Al}_{0.5}\text{Fe}_{1.5}\text{CrMnNi}_{0.5}$ HEAs are 7.228 g/cm^3 and 6.959 g/cm^3 , respectively. The microhardness of $\text{Al}_x\text{Fe}_{1.5}\text{CrMnNi}_{0.5}$ ($x = 0.3$ and 0.5) HEAs are listed in Table 4.3, and based on the following empirical relation and is used to calculate the yield strength of the corresponding HEAs.

$$\sigma_Y \text{ (MPa)} = 3 \times \text{Hv (HVN)} \quad (7)$$

The yield strength as determined from eq. (7) is listed in Table 4.3. It is observed that the $\text{Al}_{0.5}\text{Fe}_{1.5}\text{CrMnNi}_{0.5}$ HEA sintered in air exhibits a maximum value of hardness and yield strength of 386.7 HV and 1160.1 MPa , respectively.

Table 4.3 Variation of density and microhardness with sintering condition

Sample	Sintering condition	Sintering Temp. (°C)	Micro hardness (HV)	Yield strength (MPa)	Density (Exp.) g/cm ³	Theoretical Density g/cm ³	Theoretical MP (°C)
Al _{0.3} Fe _{1.5} CrMnNi _{0.5}	Vacuum	800	210	630	5.797	7.228	1484.96
Al _{0.3} Fe _{1.5} CrMnNi _{0.5}	Air	800	253.1	759.3	5.752		
Al _{0.5} Fe _{1.5} CrMnNi _{0.5}	Vacuum	800	319.9	959.7	5.852	6.959	1448.22
Al _{0.5} Fe _{1.5} CrMnNi _{0.5}	Air	800	386.7	1160.1	5.823		

The higher value of hardness and in turn yield strength in case of air sintered sample is due to the presence of finer grains as a result of faster cooling rate in case of air-sintering as compared to sintering of HEA in vacuum environment. It is suggested that the density and mechanical strength may further be improved by selecting suitable sintering process such as spark plasma sintering (SPS) and hot iso-static pressing (HIP).

4.9 Air jet erosion test

The air jet erosion behavior of the Al_xFe_{1.5}CrMnNi_{0.5} (x = 0.3 and 0.5) HEAs is evaluated using an air-jet erosion tester. The tester consists of a nozzle made up of alumina with a diameter of 1.5 mm and a length of 50 mm, an erodent feeding device and the target mount. Alumina (Al₂O₃) particles with an average particle size of 50 μm are used as the erodent material. The mass flow of the erodent is fixed at 2 g/min, and erodent velocity on the target is maintained at 70 m/s. The target is mounted at different jet impact angles of 90°, 75°, 60°, and 45°. The distance between the nozzle exit and target is maintained at 10 mm. The erosion value is calculated using the following eq. (8) for duration of 10 minutes.

$$Erosion\ Value = \frac{Volume\ loss\ of\ the\ specimen\ (mm^3)}{Erodent\ Consumed} \quad (8)$$

From Fig. 4.12(a) and Fig. 4.12(b), it may be observed that there is an increase in erosion value of the alloys with decreasing angle of impingement irrespective of the sintering conditions and presence of the alloying elements. The maximum erosion occurs at a 45° impingement angle in case of both the alloys. On comparing the erosion value of Al_{0.3}Fe_{1.5}CrMnNi_{0.5} HEA and

$\text{Al}_{0.5}\text{Fe}_{1.5}\text{CrMnNi}_{0.5}$ HEAs in both air- and vacuum-sintered conditions, it is observed that the $\text{Al}_{0.5}\text{Fe}_{1.5}\text{CrMnNi}_{0.5}$ HEA exhibits lesser erosion value under all sintering conditions. However, a comparison of the erosion value between the air- and the vacuum-sintered HEAs shows that the erosion value is less for the air-sintered HEAs. This is because of the higher value of hardness of the HEA sintered under air [153].

Figure 4.13 shows the optical macrographs of eroded surfaces of the $\text{Al}_{0.3}\text{Fe}_{1.5}\text{CrMnNi}_{0.5}$ HEA tested at impingement angles of 45° , 75° , and 90° . It is seen that at 45° impact angle, elliptical eroded shape gets formed on the surface, and this is attributed to the higher divergence of the eroded particle stream [154]. On the other hand, at 90° and 75° impact angles, circular and oval shape depression is observed. The eroded surface reveals three regions; first region ‘A’ where severe erosion has taken place, second region ‘B’ of faint color, where medium erosion has occurred, and an outside region ‘C’, where lowest amount of erosion has taken place.

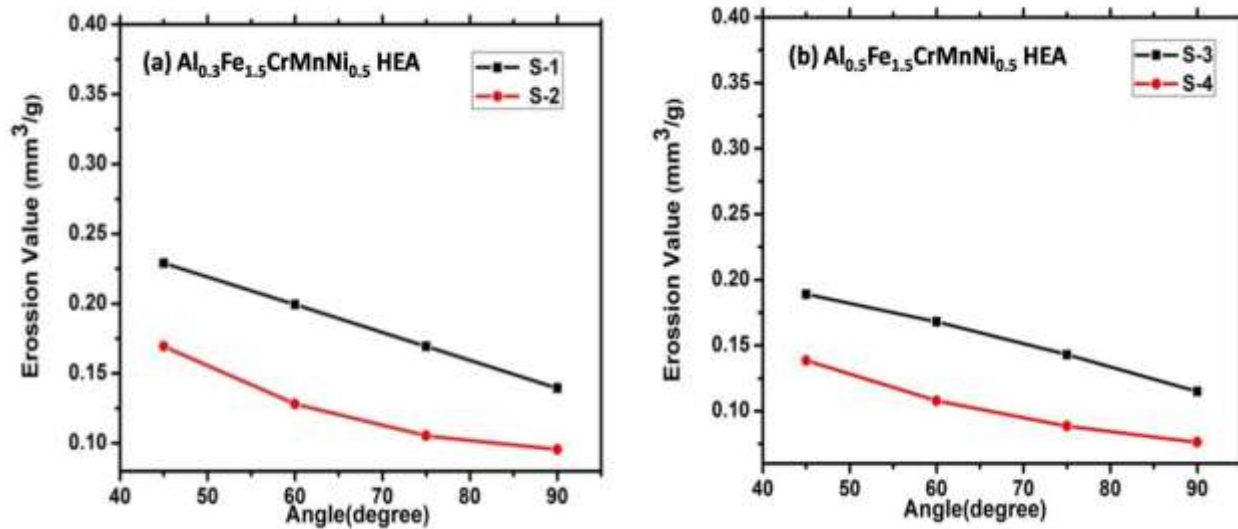


Fig. 4.12 Variation of erosion value with a different angle of impingement (a) $\text{Al}_{0.3}\text{Fe}_{1.5}\text{CrMnNi}_{0.5}$ HEA and (b) $\text{Al}_{0.5}\text{Fe}_{1.5}\text{CrMnNi}_{0.5}$ HEA for sintered under different conditions.

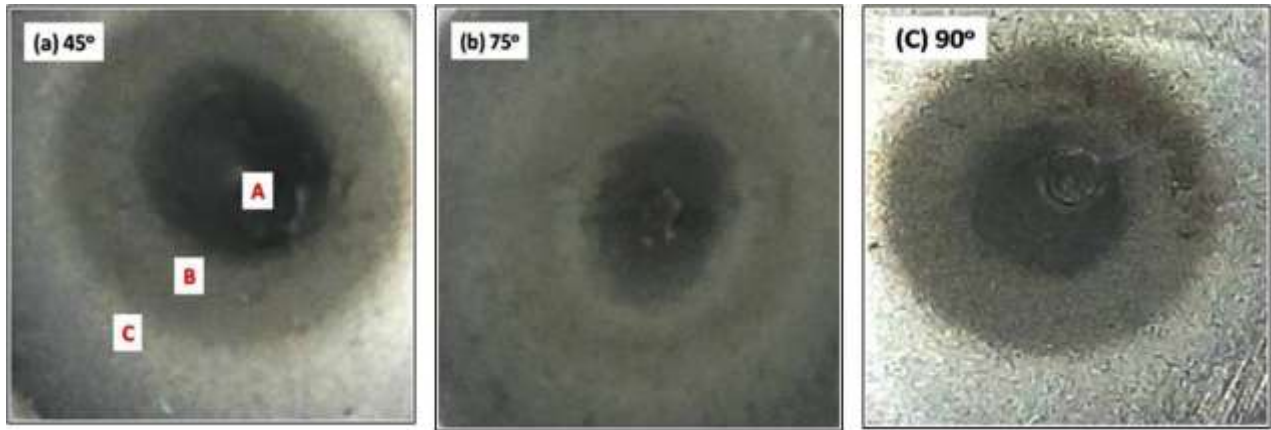


Fig. 4.13 Optical macrograph of $Al_{0.3}Fe_{1.5}CrMnNi_{0.5}$ HEA showing the eroded surface at various impact angles (a) 45° (b) 75° and (c) 90° .

From Fig. 4.12, it is seen that the erosion rate at 45° impact angle is higher as compared to 90° impact angle. This is due to more systematic formation and cutting of platelets by the erodent. At lower angles of erosion, shear-type plastic deformation occurs as a result of sliding action of the erodent particles and at higher angles, indentation and crater are formed due to the impact of the erodent, and these features generally occur in the ductile mode of erosion [155].

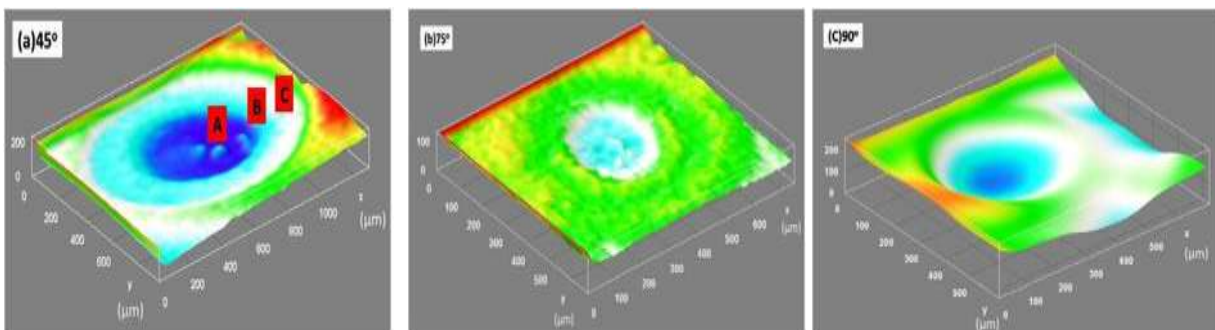


Fig. 4.14 Eroded surface profile of $Al_{0.3}Fe_{1.5}CrMnNi_{0.5}$ HEA at various impact angles (a) 45° (b) 75° and (c) 90°

Figure 4.14 shows the eroded surface profiles of $Al_{0.3}Fe_{1.5}CrMnNi_{0.5}$ HEA at different impact angles of 45° , 75° , and 90° . The change in eroded surface profile depends upon the angle of impact and velocity [156]. It can be seen that at 45° impingement angle, elliptical erosion shape

gets formed and at 90° oval shape with the deepest point of profile gets formed. The different region represented by various colors in an eroded profile shows the intensity of erosion. In Figure 4.14(a), region A (dark blue color) has highest erosion rate while region B (cyan color) has moderate erosion and region C (white color) has the lowest erosion.

4.10 Comparison with reported results

Chen et al. [42] have synthesized $Al_xCrFe_{1.5}MnNi_{0.5}$ ($x = 0.3$ and 0.5) HEAs through arc melting route and have reported that the as-cast samples of $x=0.3$ and $x=0.5$ form FCC + BCC and BCC type structure, respectively. The hardness of the as-cast samples is observed to vary in between 297 HV and 396 HV. Lee et al. [84] have developed $Al_xCrFe_{1.5}MnNi_{0.5}$ ($x = 0, 0.3$ and 0.5) HEA system through arc melting route. They have reported that the HEA forms primarily BCC structure along with some amount of FCC and α -FeCr phases. The hardness is observed to increase from 300 HV to 450 HV with increase in aluminium content from $x= 0$ to 0.5 . Chuang et al. [48] have developed $Al_{0.3}CrFe_{1.5}MnNi_{0.5}$ HEA system through arc melting route and reported that the system forms FCC + BCC type structure along with $Cr_5Fe_6Mn_8$ tetragonal structure.

In the present study the $Al_xCrFe_{1.5}MnNi_{0.5}$ ($x = 0.3$ and 0.5) HEA system were developed through ball milling and conventional sintering route. After ball milling the major and the minor phase are observed to be BCC and FCC, respectively. After conventional sintering the BCC and FCC phases appeared along with $Cr_5Fe_6Mn_8$, which is of tetragonal structure. The microhardness is observed to vary from 210 HV to 386 HV which are similar to the reported result.

Chapter Summary

This chapter includes

- Characterization of milled and sintered $\text{Al}_x\text{Fe}_{1.5}\text{CrMnNi}_{0.5}$ ($x = 0.3$ and 0.5 mol) HEAs.
- Physical, thermal and mechanical analysis of $\text{Al}_x\text{Fe}_{1.5}\text{CrMnNi}_{0.5}$ ($x = 0.3$ and 0.5 mol) HEAs.
- Air jet erosion of $\text{Al}_x\text{Fe}_{1.5}\text{CrMnNi}_{0.5}$ ($x = 0.3$ and 0.5 mol) HEAs.

In the next chapter result and discussion of synthesis and characterization of as-cast and homogenized $\text{Al}_{0.4}\text{FeCrNiCo}_x$ ($x = 0, 0.25, 0.5$ and 1.0 mol) HEAs is briefly discussed.

Synthesis and characterization of as-cast and homogenized $\text{Al}_{0.4}\text{FeCrNiCo}_x$ ($x = 0, 0.25, 0.5$ and 1.0 mol) HEAs through arc melting route

5.1 Introduction

The $\text{Al}_{0.4}\text{FeCrNiCo}_x$ ($x = 0, 0.25, 0.5$ and 1.0 mol) HEAs is fabricated through arc melting route. The phase and microstructure of as-casted ingot and homogenized samples were carried out by using X-Ray diffractometry (XRD), scanning electron microscopy (SEM), and energy dispersive spectroscope (EDS). Physical, thermal and mechanical properties were also measured. For ease of representation, $\text{Al}_{0.4}\text{FeCrNiCo}_{x=0}$, $\text{Al}_{0.4}\text{FeCrNiCo}_{x=0.25}$, $\text{Al}_{0.4}\text{FeCrNiCo}_{x=0.5}$, and $\text{Al}_{0.4}\text{FeCrNiCo}_{x=1}$ HEAs were denoted as Co=0, Co=0.25, Co=0.5 and Co=1 HEAs in the text, respectively.

5.2 Analysis of as-cast $\text{Al}_{0.4}\text{FeCrNiCo}_x$ ($x=0, 0.25, 0.5$ and 1.0 mol) HEAs

5.2.1 Microstructure and phase analysis of as-cast $\text{Al}_{0.4}\text{FeCrNiCo}_x$ ($x = 0, 0.25, 0.5$ and 1.0 mol) HEAs

Figure 5.1 shows the XRD pattern of as-cast $\text{Al}_{0.4}\text{FeCrNiCo}_x$ ($x = 0, 0.25, 0.5$ and 1.0 mol) HEAs. The peak reflection for $\text{Al}_{0.4}\text{FeCrNiCo}_x$ ($x = 0$ to 0.5 mol) HEAs has mixed phase of FCC plus BCC solid solution. Whereas in case of Co=1 HEA has FCC structure. The lattice constants and volume fraction of BCC and FCC are calculated from the x-ray diffraction and SEM micrograph as listed in Table 5.1. The calculated value of lattice constant for both the phases is in close agreement with the available literature [111, 157, 158]. As the concentration of cobalt increases from $x = 0$ to 0.5 mol, BCC peaks start vanishes and completely disappear at $x = 1.0$ mol. The volume fractions of FCC phase increases from 83% to 98% and BCC phase decreases from 16% to 1.4%. It is also observed from XRD graph as seen in Fig. 5.1, that the peak intensity of (111) plane is gradually increasing with increase in the amount of cobalt. From the above

discussion, one can conclude that cobalt is an FCC former in $\text{Al}_{0.4}\text{FeCrNiCo}_x$ ($x = 0, 0.25, 0.5$ and 1.0 mol) HEAs.

Figure 5.2 shows the SEM micrograph of as-cast HEAs with varying cobalt content and it is observed that the $\text{Co}=0, \text{Co}=0.25, \text{Co}=0.5$ HEA form mixed phase of face-centered cubic (FCC) plus body-centered cubic (BCC) structure and the two regions is designated as region A and region B. The microstructure for $\text{Co}=1$ HEA shows only single region of FCC phase. The compositional analysis of different region obtained from EDS and listed in Table 5.2.

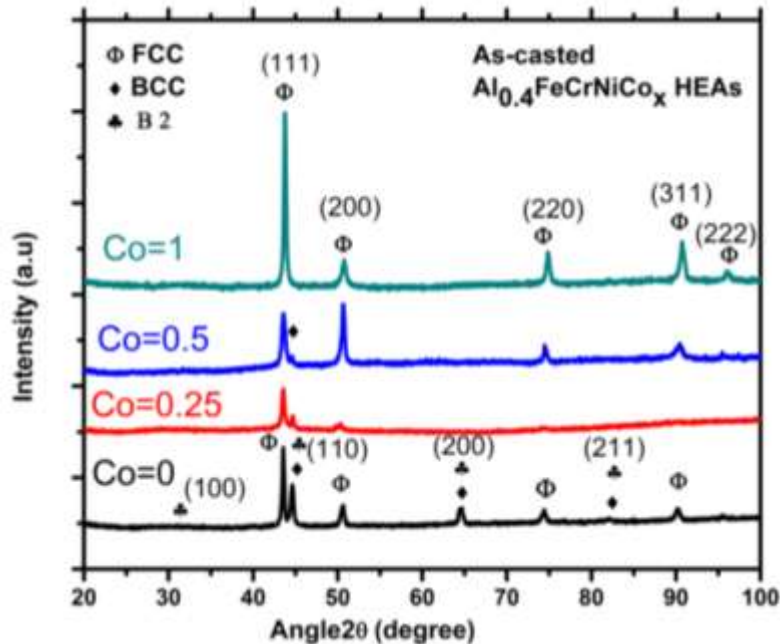


Fig. 5.1 X-ray diffraction of as-cast $\text{Al}_{0.4}\text{FeCrNiCo}_x$ ($x = 0, 0.25, 0.5$ and 1.0 mol) HEAs

Table 5.1 Lattice constant and volume fraction of as-cast $\text{Al}_{0.4}\text{FeCrNiCo}_x$ ($x = 0, 0.25, 0.5$ and 1.0 mol) HEAs

HEAs	Lattice Constant (Å)		Volume fraction (%)	
	FCC phase	BCC phase	FCC phase	BCC phase
Co=0	3.594	2.868	83.5	16.5
Co=0.25	3.595	2.867	93.0	7.0
Co=0.5	3.593	2.870	98.5	1.5
Co=1	3.578	0.0	100	0.0

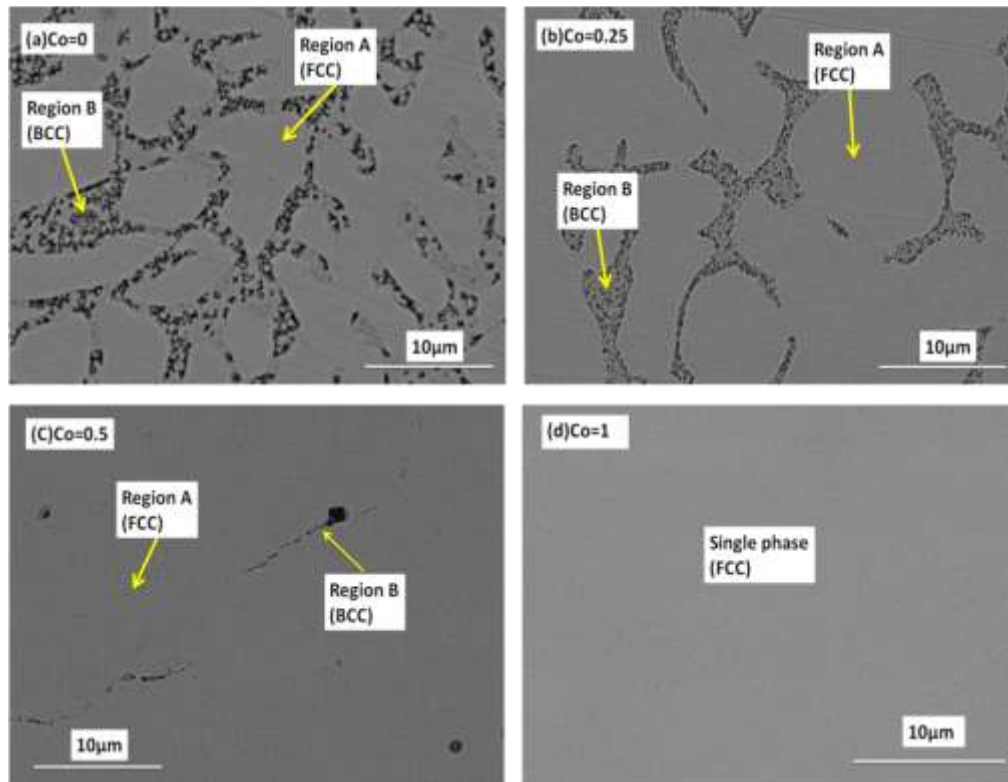


Fig. 5.2 SEM micrograph of as-cast (a) Co=0 HEA (b) Co=0.25 HEA(c) Co=0.5 HEA (d) Co=1 HEA

Table 5.2 EDS results (in at.%) of as-cast $Al_{0.4}FeCrNiCo_x$ ($x = 0, 0.25, 0.5$ and 1.0 mol) HEAs[AS: area scan, PS: point scan]

HEAs	Region	Al(at%)	Fe(at%)	Cr(at%)	Ni(at%)	Co(at%)
Co=0	Theoretical	11.76	29.41	29.41	29.41	-
	Overall, (AS)	13.78	27.67	28.14	30.41	-
	A (FCC), (PS)	10.60	30.24	27.82	31.34	-
	B (BCC), (PS)	21.56	22.01	26.81	29.62	-
Co=0.25	Theoretical	10.95	27.39	27.39	27.39	6.84
	Overall, (AS)	10.23	27.96	28.37	26.50	6.94
	A (FCC), (PS)	9.96	28.18	28.09	26.18	7.59
	B (BCC), (PS)	19.0	20.87	26.23	27.88	6.02
Co=0.5	Theoretical	10.25	25.64	25.64	25.64	12.82
	Overall, (AS)	7.96	27.02	25.80	25.79	13.49
	A (FCC), (PS)	8.06	25.59	26.21	26.79	13.35
	B (BCC), (PS)	17.50	16.06	42.16	15.82	8.46
Co=1	Theoretical	9.09	22.72	22.72	22.72	22.72
	Overall, (AS)	6.57	23.68	22.01	23.71	24.03

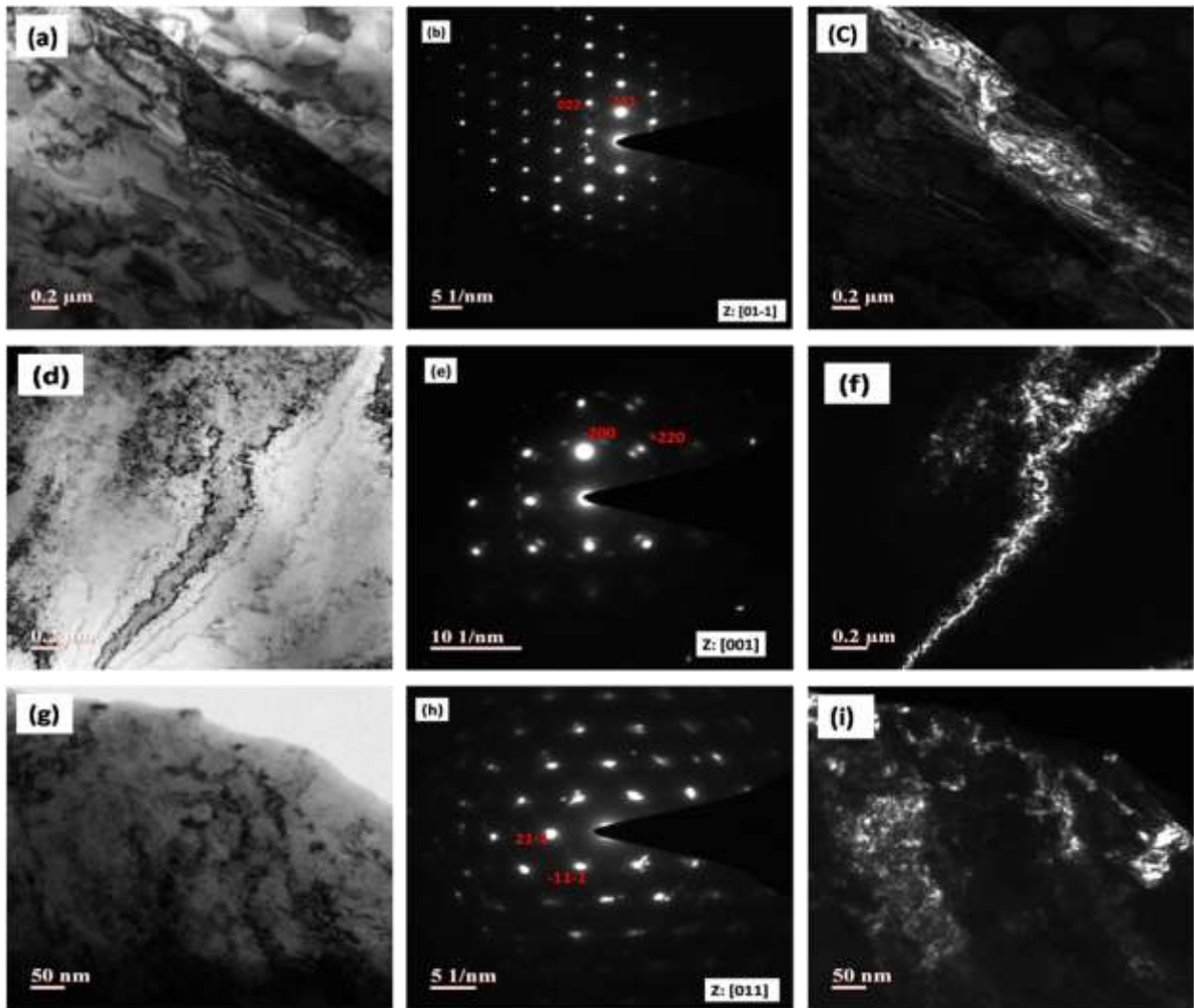


Fig. 5.3 TEM bright field, SAED pattern and dark field of as-cast HEA (a-c) Co=0 HEA (d-f) Co=0.25 HEA (g-i) Co=0.5 HEA

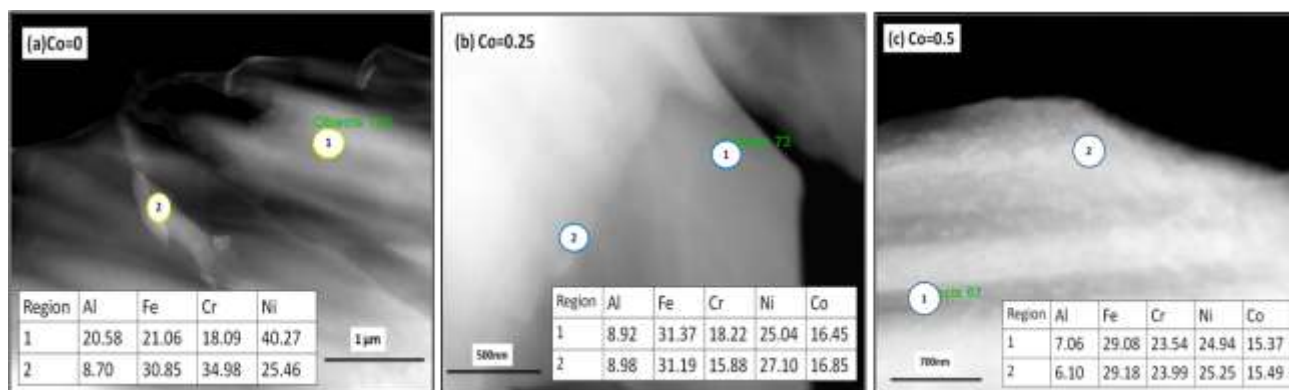


Fig. 5.4 STEM and TEM- EDS analysis of as-cast (a) Co=0 (b) Co=0.25 (c) Co=0.5 HEAs

The EDS results show that the region poor in Al formed FCC structure as reported in the previous literatures [136, 159]. Region rich in Al and (Fe, Cr) formed BCC structure and the rich Al combined with Ni to form Al-Ni rich phases or B2 phase. The reason behind the formation of Al-Ni is due to the larger negative enthalpy of mixing between Al-Ni (-22KJ/mol) than the other atomic pairs present in the alloy system and this inference is consistent with the previous studies [110, 111].

Figure 5.3 shows the TEM bright field, dark field, and SAED pattern of as-cast $Al_{0.4}FeCrNiCo_x$ ($x = 0, 0.25$ and 0.5 mol) HEAs. In the bright field image Fig. 5.3(a, d and g) all the phases can be easily distinguished by image contrast. Chemical composition (in at.%) of phase present in as cast HEAs are identified by the TEM-EDS as seen in Fig. 5.4. The result indicates that both darker and lighter portion has uniform composition of (Co, Cr, Fe and Ni). Fig. 5.3(b, e, h) shows the SAED pattern of brighter region indicating FCC phase of $Al_{0.4}FeCrNiCo_x$ ($x = 0, 0.25$ and 0.5 mol) HEAs.

As the cobalt concentration increases, uniform homogeneous mixture (Fe, Cr, Ni, Co) forms. It is in accordance with the TEM-EDS results of HEAs, and this confirms the formation uniform solid solution of (Fe, Cr, Ni, Co) as seen in Fig. 5.4. The solid solution of (Co, Cr, Fe, Ni) having FCC crystal structure as reported in previous studies also [160].

5.2.2 Thermal analysis of $\text{Al}_{0.4}\text{FeCrNiCo}_x$ ($x=0, 0.25, 0.5$ and 1.0 mol) HEAs

Thermal behavior of $\text{Al}_{0.4}\text{FeCrNiCo}_x$ ($x=0, 0.25, 0.5$ and 1.0 mol) HEAs was carried out by using differential scanning calorimetry (DSC) in the temperature range from room temperature to 1000°C with a heating rate of 10 K/min . The DSC curve as seen in Fig. 5.5 indicates that there is no evidence of significant peak up to 1000°C . This confirms that the $\text{Al}_{0.4}\text{FeCrNiCo}_x$ ($x = 0, 0.25, 0.5$ and 1.0 mol) HEA is does not show any phase transition up to 1000°C .

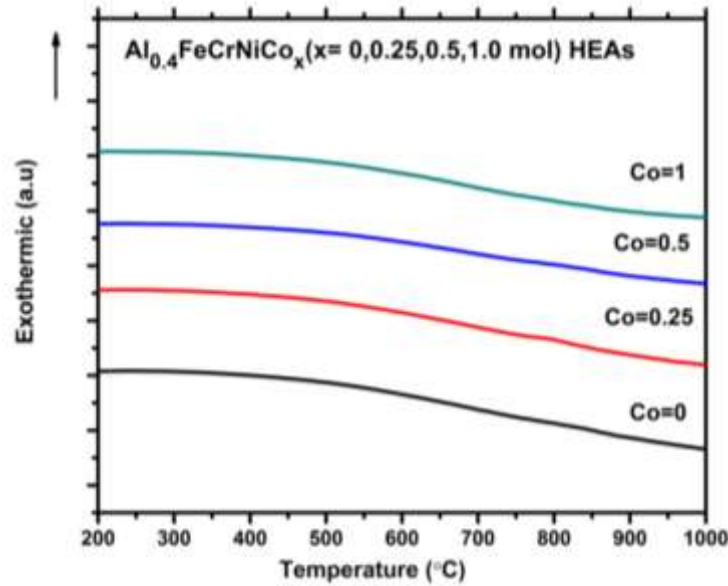


Fig. 5.5 DSC analysis for as-cast $\text{Al}_{0.4}\text{FeCrNiCo}_x$ ($x = 0, 0.25, 0.5$ and 1.0 mol) HEAs

5.2.3 Thermal conductivity of as-cast $\text{Al}_{0.4}\text{FeCrNiCo}_x$ ($x = 0, 0.25, 0.5$ and 1.0 mol) HEAs

Figure 5.6 shows the variation in thermal conductivity of $\text{Al}_{0.4}\text{FeCrNiCo}_x$ ($x = 0, 0.25, 0.5$ and 1.0 mol) HEAs with cobalt content. The thermal conductivity was recorded by average of five readings. From the figure it is observed that with increase in cobalt content from $x = 0$ to 1.0 mol the thermal conductivity decreases from 4.87 W/mK to 2.674 W/mK . It is because as the aluminium content decreases as listed in Table 5.2, on addition of cobalt content from $x = 0$ to 1.0 mol, the BCC phase decreases from 16.5% to 0% as listed in Table 5.1.

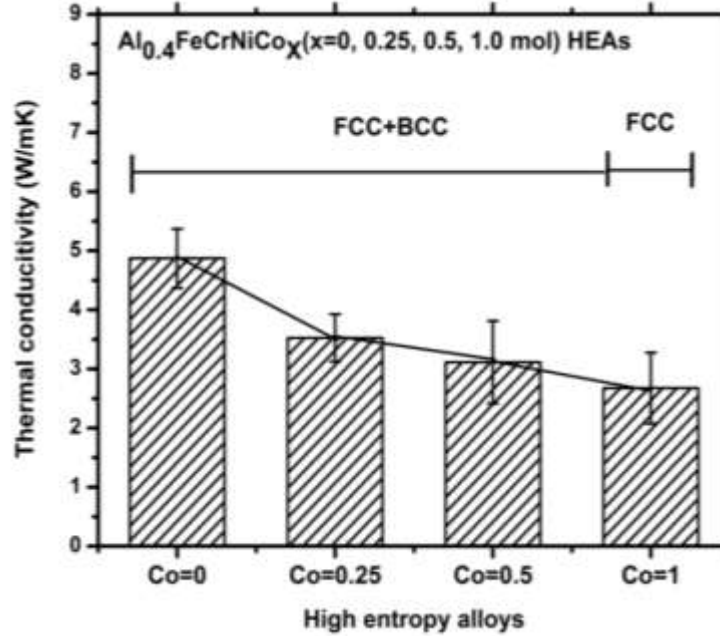


Fig. 5.6 Thermal conductivity of Al_{0.4}FeCrNiCo_x (x = 0, 0.25, 0.5 and 1.0 mol) HEAs

It is noted that the thermal conductivity of Al is highest among all other elements and as Al content decreases thermal conductivity decreases. Similar results were reported in the previous study [161, 162] indicated that BCC structure have more open structure than FCC structure and which has higher phonon velocity than FCC structure. Therefore, as the cobalt content increases the BCC phase decreases which results in decreases of thermal conductivity.

The phonon velocity is calculated from equation (1) [161].

$$\text{phonon velocity} = \left(\frac{E}{\rho}\right)^{1/2} \quad (1)$$

Where, E is the Young's modulus (in GPa), and ρ is the density (in g/cm³). It is observed that the phonon velocity decreases from 919.66 m/s to 775.24 m/s with an increase in cobalt content from x = 0 to 1.0 mol and therefore thermal conductivity decreases from 4.87 W/mK to 2.674 W/mK. According to Wiedemann–Franz law [161], the ratio of thermal conductivity (k) to electrical conductivity (σ) of a metal is directly proportional to temperature, and it is represented by equation (2).

$$\frac{k}{\sigma} = LT \quad (2)$$

Where L is the proportionality constant known as the Lorenz number. The value of L is $2.44 \times 10^{-8} \text{ W}\Omega\text{K}^{-2}$ and T is the temperature in Kelvin. From the equation (2), the electrical conductivity of $\text{Al}_{0.4}\text{FeCrNiCo}_x$ ($x=0, 0.25, 0.5, 1.0$ mol) HEAs is observed to decrease from $6.65 \times 10^5 \text{ m}^{-1}\Omega^{-1}$ to $3.65 \times 10^5 \text{ m}^{-1}\Omega^{-1}$. The electrical resistivity (ρ) is defined as the reciprocal of the electrical conductivity and is given by equation (3).

$$\rho = \frac{1}{\sigma} \quad (3)$$

Based upon the above equation, the electrical resistivity of the $\text{Al}_{0.4}\text{FeCrNiCo}_x$ ($x=0, 0.25, 0.5$ and 1.0 mol) HEAs are observed to vary from $150.30 \mu\Omega\text{-cm}$ to $273.74 \mu\Omega\text{-cm}$ which is consistent to the values as reported in previous literature [161, 162]. It can be concluded that the amount of phases present and the chemical composition of these phases are the key parameters to decide the thermal and electrical conductivity of HEAs.

5.2.4 Mechanical Property of as-cast $\text{Al}_{0.4}\text{FeCrNiCo}_x$ ($x = 0, 0.25, 0.5$ and 1.0 mol) HEAs

The microhardness of as-casted $\text{Al}_{0.4}\text{FeCrNiCo}_x$ ($x = 0, 0.25, 0.5$ and 1.0 mol) HEAs were measured under a load of 200 gf and dwell time of 15 seconds and average of ten value are recorded from each specimen and listed in Table 5.3. It is found that as cobalt content increases hardness decreases from to 253.6 HV to 155.6 HV.

The engineering stress-strain curve of as-cast $\text{Al}_{0.4}\text{FeCrNiCo}_x$ ($x = 0, 0.25, 0.5$ and 1.0 mol) HEAs, under compression at room temperature is shown in Fig. 5.7. The compressive yield strength (σ_y), Plastic strain (ϵ_p), of $\text{Al}_{0.4}\text{FeCrNiCo}_x$ ($x = 0, 0.25, 0.5$ and 1.0 mol) HEAs are listed in Table 5.3.

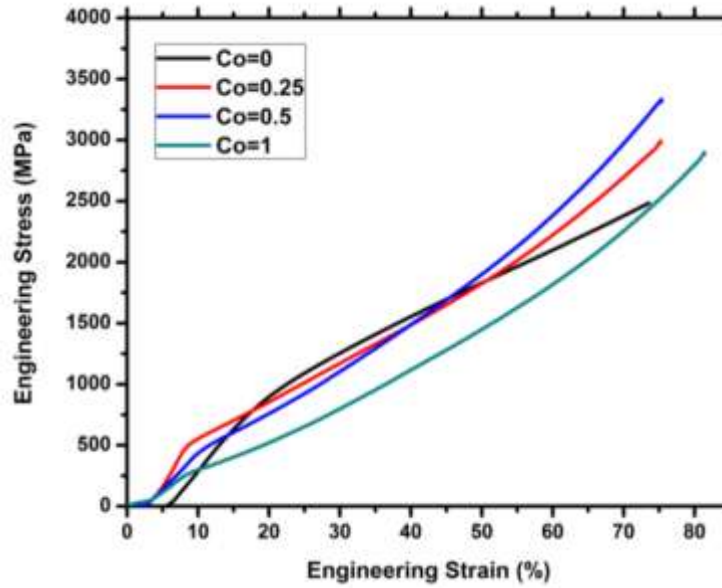


Fig. 5.7 Engineering stress–strain curves of as-cast, $\text{Al}_{0.4}\text{FeCrNiCo}_x$ ($x = 0, 0.25, 0.5$ and 1.0 mol) HEAs under compression at room temperature.

Table 5.3 Mechanical properties of $\text{Al}_{0.4}\text{FeCrNiCo}_x$ ($x = 0, 0.25, 0.5$ and 1.0) HEAs at room temperature

HEAs	Yield strength (σ_y) in Mpa	Plastic strain (ϵ_p %)	Microhardness (HV)	Volume fraction of BCC (%)
Co=0	965.22	73.31	253.6	16.5
Co=0.25	521.91	75.08	205.4	7.0
Co=0.5	464.37	75.58	189.3	1.5
Co=1	233.37	81.32	155.6	0

It is noted that the compressive yield strength decreases from 965.22 MPa to 233.37 MPa for the rise in cobalt content from $x=0$ to 1.0 mol. A maximum plastic strain of 81% was observed in case of $\text{Al}_{0.4}\text{FeCrNiCo}_{x=1}$ HEA and the sample remains unfractured at the end of the experiment. There are two potential reasons for the decrease in compressive yield strength and microhardness values in case of $\text{Al}_{0.4}\text{FeCrNiCo}_x$ ($x=0, 0.25, 0.5$ and 1.0 mol) HEAs: (i) the vol.% of BCC phase varies from 16.5% to 0% as a result of addition of cobalt which plays a key role, and (ii) the amount of stacking faulty present in FCC phase and its corresponding energy change their mechanical characteristics, responsible to lowering of its mechanical strength.

5.2.5 Thermodynamic Parameters of Al_{0.4}FeCrNiCo_x (x=0, 0.25, 0.5 and 1.0 mol) HEAs

In conventional alloys the solid solution only forms when it satisfies the condition of the Hume-Rothery rule such as atomic size difference (less than 15%), and having similar crystal structure, valency, and electronegativity [1]. In case of high entropy alloys simple solid solution like face-centered cubic (FCC), body-centered cubic (BCC) or mixed phase of (FCC+BCC) can be predicted, when it follows certain thermodynamic equations as discussed below [163].

$$\Delta H_{\text{mix}} = \sum_{i=1, i \neq j}^n \Omega_{ij} C_i C_j \quad (4)$$

$$\Delta S_{\text{mix}} = -R \sum_{i=1}^n C_i \ln C_i \quad (5)$$

$$\delta = 100 \sqrt{\sum_{i=1}^n C_i \left(1 - \frac{r_i}{r}\right)^2} \quad (6)$$

$$\Omega = \frac{T_m \Delta S_{\text{mix}}}{|\Delta H_{\text{mix}}|} \quad (7)$$

$$\text{VEC} = \sum_{i=1}^n C_i (\text{VEC})_i \quad (8)$$

$$\Delta X = \sqrt{\sum_{i=1}^N C_i (X_i - X_{\text{avg}})^2} \quad (9)$$

$$T_m = \sum_{i=1}^n C_i (T_m)_i \quad (10)$$

Where ΔH_{mix} is the enthalpy of mixing of a multi-component alloy, ΔS_{mix} is the entropy of mixing of regular solid solution, δ is the atomic size mismatch, Ω is the thermodynamic parameter used to predict the solid solution formation, VEC is the valence electron concentration which helps in predicting the formation of FCC, BCC and dual phase of FCC+BCC, ΔX is the electronegativity difference which help in understanding the phase stability, and T_m is the theoretical melting point of multi component alloys. The value of individual elements were taken from the previous literature [19, 140, 164-165] and listed in Table 2.2 and Table 2.3.

Figure 5.8(a, b) and Fig. 5.9 show the variation of thermodynamic parameter with cobalt content. From the Fig. 5.8(a) it can be seen that valence electron concentration (VEC) increases from 7.4

to 7.8 with addition of cobalt content from $x=0$ mol to $x=1.0$ mol which indicate the transformation of FCC+BCC to FCC. Fig. 5.8(b) represents variation of enthalpy of mixing (ΔH) and entropy of mixing (ΔS) with cobalt content. From the figure it is observed that ΔS increases from $11.0 \text{ J/K}^{-1}\text{mol}^{-1}$ to $13.0 \text{ J/K}^{-1}\text{mol}^{-1}$ and ΔH varies from -9.4 KJ/mol to -8.2 KJ/mol with addition of cobalt from $x=0$ mol to $x=1.0$ mol. Figure. 5.9 shows the variation of thermodynamic parameter Ω and $\delta\%$ and from the figure it is observed that Ω increases from 1.177 to 2.38 and atomic radius mismatch ($\delta\%$) decreases from 0.047 to 0.041

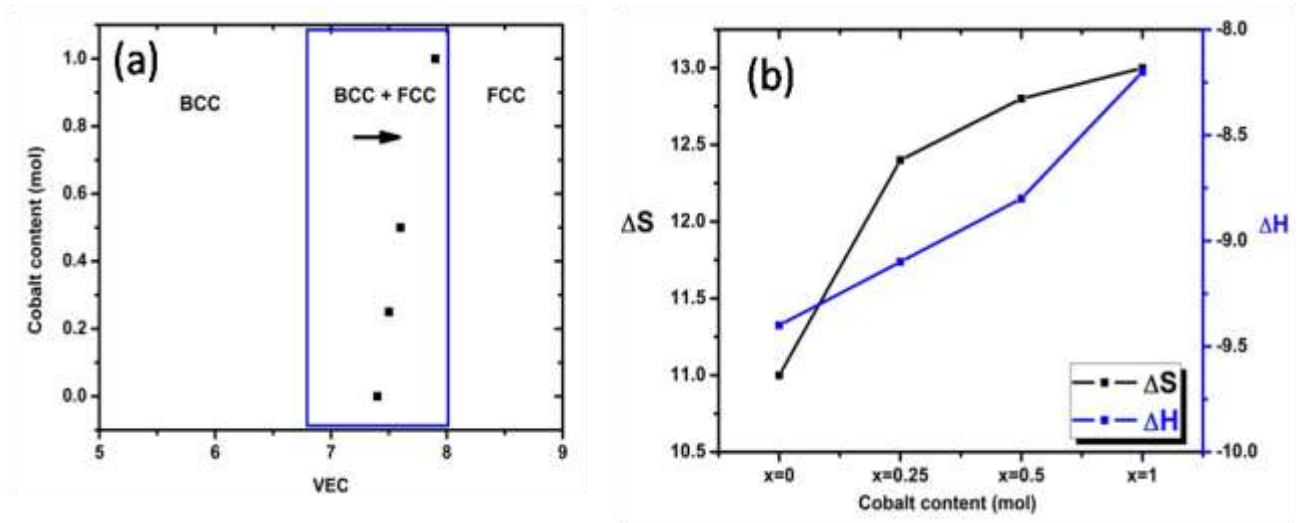


Fig. 5.8 Variation of (a) VEC, (b) enthalpy and entropy of mixing with cobalt content from $x = 0$ to 1.0 mol.

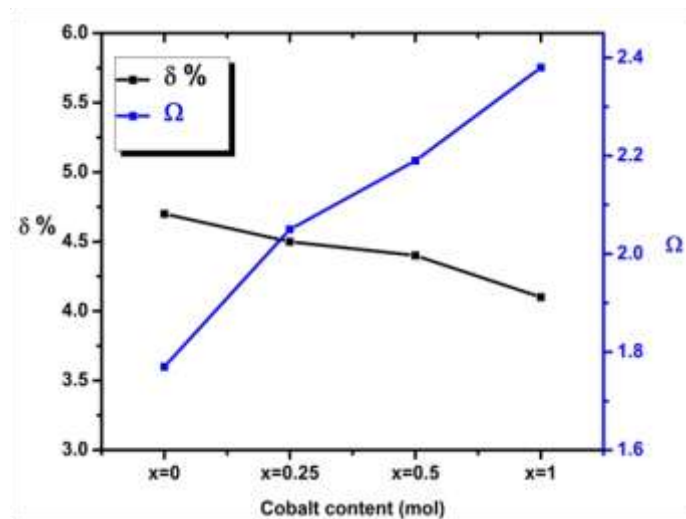


Fig. 5.9 variation of $\delta\%$ and Ω with cobalt content from $x= 0$ to 1.0 mol.

It indicates that if $\Omega > 1$ then $T\Delta S$ is more than that of ΔH_{mix} and HEA form a solid solution. ΔX varies from 0.115 to 0.110 which satisfy the condition of no topologically close-packed (TCP) phase formation i.e. $\Delta X < 0.117$ [166]. Theoretical melting temperature of HEAs estimated from the equation (7) and which varies from 1509.06 °C to 1506.16 °C with addition of cobalt content from $x=0$ mol to $x=1.0$ mol respectively.

It is noted that the calculated values of thermodynamic parameter satisfies the Zhang et al. [164] and Guo et al. [19, 165] criterion for solid solution formation i.e. $11 < \Delta S_{\text{mix}} < 19.5$ J/(K mol), $-22 < \Delta H_{\text{mix}} < 7$ KJ/mol, $0 < \delta < 8.5$ and $\text{VEC} < 6.87$ only body-centered cubic (BCC) would form, when $6.87 < \text{VEC} < 8$ both BCC + FCC will form and when $\text{VEC} > 8$ only FCC phase will form.

5.3 Analysis of homogenized $\text{Al}_{0.4}\text{FeCrNiCo}_x$ ($x=0, 0.25, 0.5$ and 1.0 mol) HEAs

5.3.1 Microstructural, and Phase analysis of homogenized $\text{Al}_{0.4}\text{FeCrNiCo}_x$ ($x=0, 0.25, 0.5$ and 1.0 mol) HEAs

Figure 5.10(a) shows the X-ray diffraction pattern of homogenized $\text{Al}_{0.4}\text{FeCrNiCo}_x$ ($x=0, 0.25, 0.5$ and 1.0 mol) HEAs samples. The graph reveals that with the addition of cobalt content from $x = 0$ to 0.5 mol, a mixed phase of FCC+BCC gets formed and a single phase FCC gets formed for $x=1.0$ mol [167]. It is observed that as cobalt content increases the intensity of the BCC phase decreases and it completely disappears for $x=1.0$ mol. The lattice parameter of the BCC phase increases from $(2.869 \text{ \AA}$ to $2.891 \text{ \AA})$ and that of the FCC phase increases from $(3.592 \text{ \AA}$ to $3.594 \text{ \AA})$ which are in accordance with the previous literature [62, 111, 136]. Figure 5.10(b) shows the variation of phase fraction with cobalt content (as calculated from the XRD graph). The graph indicates that with the addition of cobalt content from $x = 0$ to 0.5 mol, the BCC phase decreases from 91 % to 35 % and it completely vanishes at $x=1.0$ mol.

Figure 5.11 shows the SEM micrographs of homogenized $\text{Al}_{0.4}\text{FeCrNiCo}_x$ ($x=0, 0.25, 0.5$ and 1.0 mol) HEAs, representing the microstructural evolution with the addition of cobalt. The SEM micrographs indicate that for $\text{Co}=0$, the HEA shows dendritic and interdendritic regions along with various precipitates as shown in Fig. 5.11(a). The different regions in the microstructure are denoted as A, B, C, D, and E and their chemical compositions were listed in Table 5.4. The region A denotes the dendritic region, and region B denotes the interdendritic region, and the various precipitates are denoted as C, D, and E as reported in previous literatures [111, 168].

The EDS results as listed in Table 5.4 indicated that the dendritic region (A) is rich in Fe, Cr, and Ni and is poor in Al and the interdendritic region (B) is rich in Fe, Cr, and Ni and is rich in Al. The precipitates are observed to be rich in Al and Ni and poor in Fe and Cr. In order to examine the distribution of elements and phases, the EDS mapping of $\text{Al}_{0.4}\text{FeCrNiCo}_x$ ($x = 0, 0.25, 0.5$ and 1.0 mol) HEAs were analysed as shown in Fig. 5.12. The result of $\text{Al}_{0.4}\text{FeCrNiCo}_{x=0}$ confirms that the dendrite region (A) rich in Fe, and Cr and poor in Al, and Ni. Interdendritic region (B) along with various precipitates are rich in Al and Ni and poor in Fe and Cr. Similar findings have also been reported by Zhao et al. [62]. It is observed that as Co content increases,

the interdendritic region (B) decreases and completely disappears at $x=1.0$ mol with the formation of a homogenized region rich in Fe, Cr, Ni, and Co as listed in Table 5.6 and shown in Fig. 5.11(d).

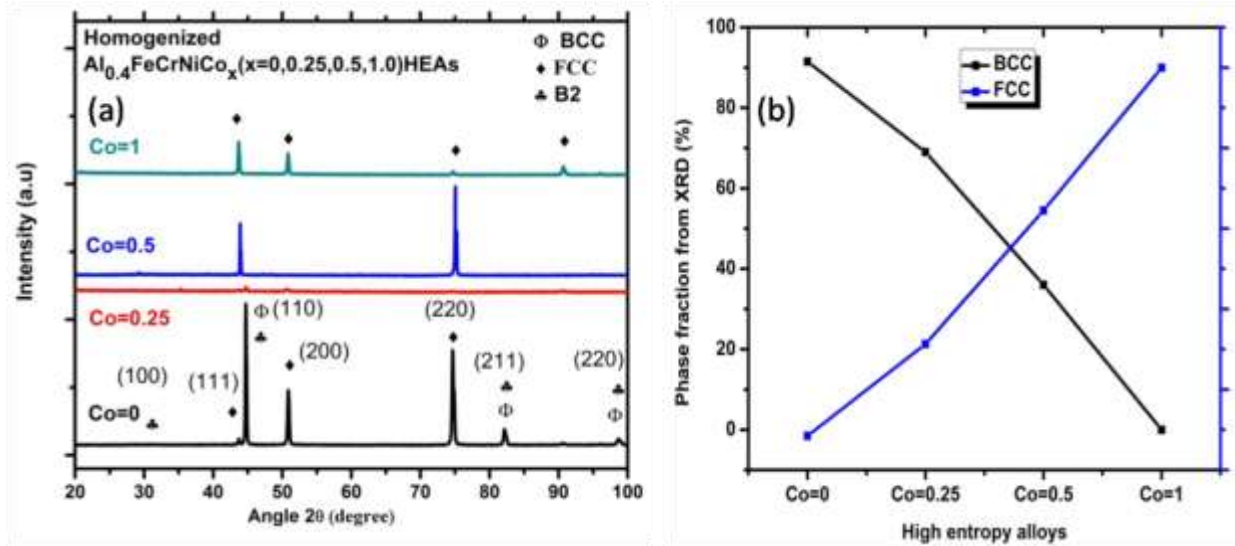


Fig. 5.10 (a) X-ray diffraction pattern of homogenized Al_{0.4}FeCrNiCo_x ($x=0, 0.25, 0.5$ and 1.0 mol) HEAs (b) variation of phase fraction with cobalt content

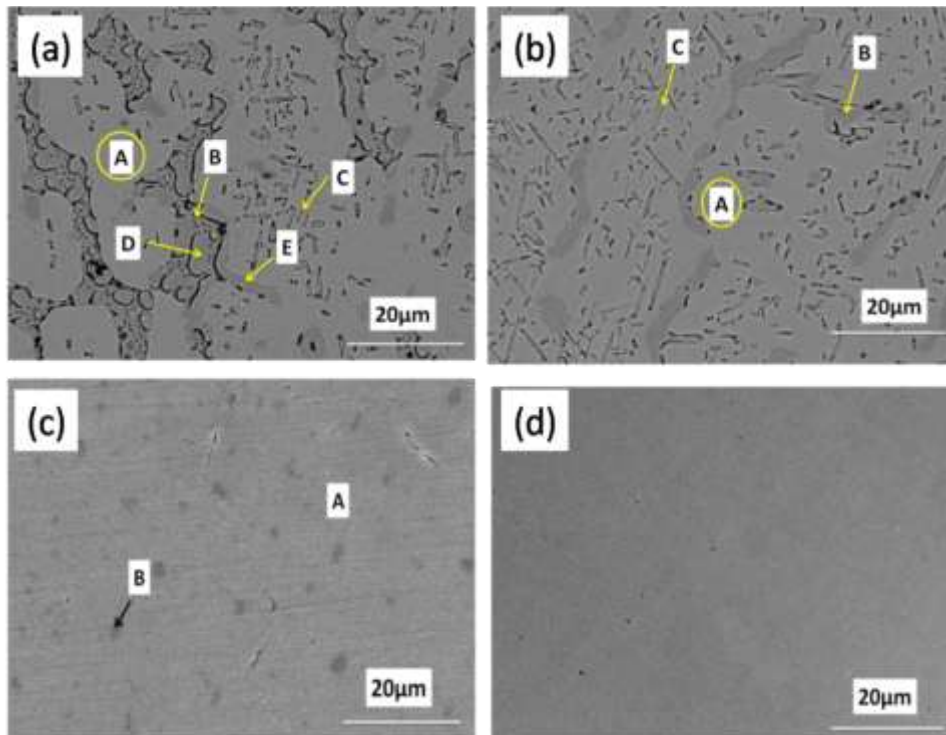


Fig. 5.11 SEM micrographs of homogenized (a) Co=0 (b) Co=0.25 (c) Co=0.5 (d) Co=1 HEAs.

Table 5.4 EDS results of homogenized Al_{0.4}FeCrNiCo_x(x=0, 0.25, 0.5, 1.0 mol) HEAs

HEA	region	Al (at.%)	Fe (at.%)	Cr (at.%)	Ni (at.%)	Co (at.%)
Co=0	Overall	12.01	29.98	27.81	30.20	-
	A	7.25	33.48	27.61	31.66	-
	B	11.85	27.13	38.39	22.63	-
	C	30.98	17.09	13.80	38.13	-
	D	38.56	11.19	6.51	43.75	-
	E	39.64	11.51	6.88	41.97	-
Co=0.25	Overall	11.64	25.87	27.12	27.82	7.55
	A	8.18	29.29	28.88	25.02	8.63
	B	7.29	29.84	30.38	24.73	7.76
	C	34.19	13.68	9.72	37.65	4.76
Co=0.5	Overall	8.09	14.12	25.19	26.26	14.12
	A	7.04	26.57	25.58	26.15	14.67
	B	30.11	12.23	14.32	35.56	7.78
Co=1	Overall	7.48	22.67	21.79	23.60	24.46

It is also observed that the interdendritic region (B) is rich in Al and Ni as indicated by the EDS results and listed in Table 5.4. The region rich in Al and Ni has B2 phase and it is formed because of relatively large negative enthalpy of mixing between the Al and the Ni than the other atomic pair in the alloy system. The enthalpy of mixing of various atomic pairs according to Miedema's approach is Al-Ni (-22 KJ/mol), Fe-Cr (-1 KJ/mol), Cr-Co (-4 KJ/mol) Cr-Ni (-7 KJ/mol), Fe-Co (-1 KJ/mol), and Fe-Ni (-2 KJ/mol). According to EDS results as listed in Table 5.6, with the addition of cobalt, the Al content decreases and Fe, Cr, Ni, and Co content increases. Therefore, the chance of formation of region rich in (Al, Ni) is reduces, in the interdendritic region (B) with the increasing content of cobalt and completely disappear at x=1.0 mol.

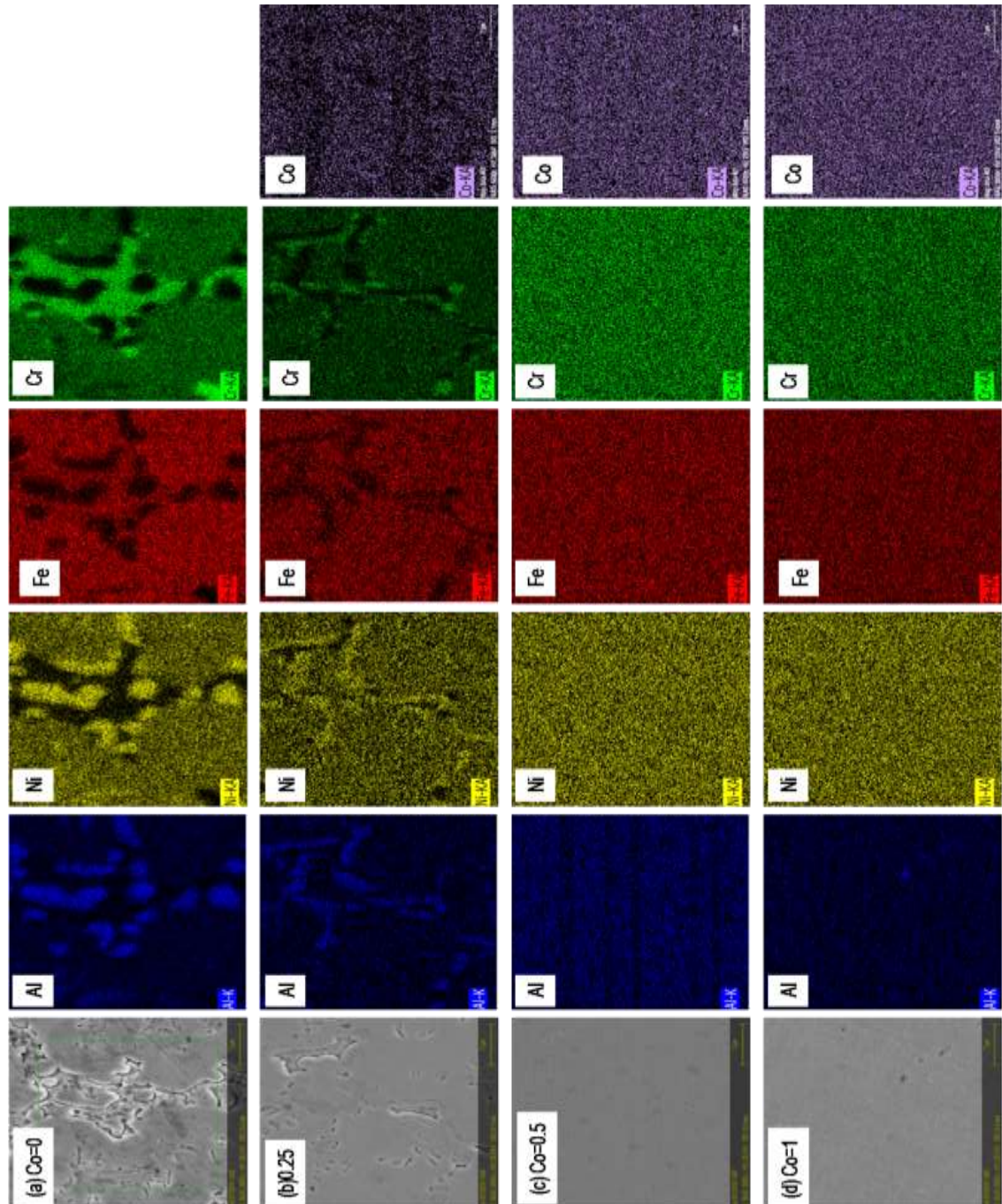


Fig. 5.12 EDS Mapping of homogenized $\text{Al}_{0.4}\text{FeCrNiCo}_x$ ($x = 0, 0.25, 0.5$ and 1.0 mol) HEAs.

It is clear that the dendrite formation takes place when a solid grows into a super cooled liquid and the heat transfer takes place through the liquid rather than the solid. The dendrite arm growth direction depends upon the direction of preferential heat transfer and the direction of low-energy atomic planes. Based on the present study, it can be concluded that the addition of cobalt not

only changes the thermal conductivity of the system, but also leads to a change in low energy atomic planes. Both of these factors is believed to change the direction, shape, and size of the dendrites and its arms, which in turn results in a change in interdendritic region.

5.3.2 Thermal analysis of homogenized $\text{Al}_{0.4}\text{FeCrNiCo}_x$ ($x=0, 0.25, 0.5$ and 1.0 mol) HEA

Figure 5.13 shows the DSC micrograph of homogenized $\text{Al}_{0.4}\text{FeCrNiCo}_x$ ($x=0, 0.25, 0.5$ and 1.0 mol) HEA in the temperature range from ambient to $1000\text{ }^\circ\text{C}$ with a heating rate of 10 K/min . The graph indicates that the homogenized $\text{Al}_{0.4}\text{FeCrNiCo}_x$ ($x=0, 0.25, 0.5$ and 1.0 mol) HEA does not show any significant endothermic or exothermic peak. For $\text{Co}=0$ HEA there is a small exothermic peak appears at $470.77\text{ }^\circ\text{C}$.

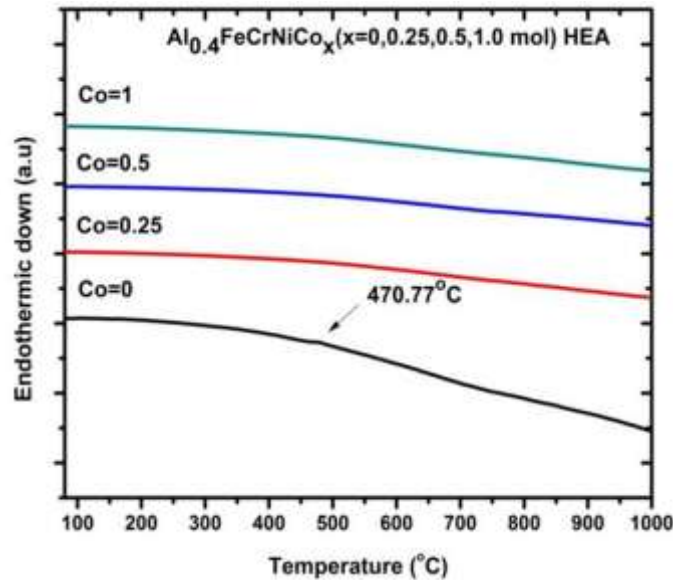


Fig. 5.13 DSC micrograph of homogenized $\text{Al}_{0.4}\text{FeCrNiCo}_x$ ($x=0, 0.25, 0.5$ and 1.0 mol) HEAs

The small exothermic peak appears at $470.77\text{ }^\circ\text{C}$ may be due to the formation of a very small amount of FeCr based sigma phase [169]. This type of transformation behavior has been observed in case of only one sample i.e. $\text{Co}=0$ HEA. It can be concluded that the increase in the Co content in the proposed series of the HEAs may lead to the suppression of unwanted transformation i.e. crystallization of sigma phase.

5.3.3 Density of homogenized $\text{Al}_{0.4}\text{FeCrNiCo}_x$ ($x=0, 0.25, 0.5$ and 1.0 mol) HEAs

The density of homogenized $\text{Al}_{0.4}\text{FeCrNiCo}_x$ ($x=0, 0.25, 0.5$ and 1.0 mol) HEAs is observed to increase with the addition of cobalt from $x=0$ to 1.0 mol. The experiments were performed in water as a medium. The recorded density values for $\text{Al}_{0.4}\text{FeCrNiCo}_x$ ($x=0, 0.25, 0.5$ and 1.0 mol) HEAs is found to be 7.224 g/cm^3 , 7.294 g/cm^3 , 7.430 g/cm^3 and 7.787 g/cm^3 respectively.

5.3.4 Microhardness of homogenized $\text{Al}_{0.4}\text{FeCrNiCo}_x$ ($x=0, 0.25, 0.5$ and 1.0 mol) HEAs

The microhardness measurements of homogenized $\text{Al}_{0.4}\text{FeCrNiCo}_x$ ($x = 0, 0.25, 0.5$ and 1.0 mol) HEAs were performed at a load of 200 gf and dwell time of 15 s . The average value of ten different sites across the polished sample was recorded. It is found that with the addition of cobalt from $x=0$ to 1.0 mol, the microhardness of the HEAs decreases. The microhardness values are observed to be $377.7 \pm 16.57 \text{ HV}$, $264.3 \pm 21.47 \text{ HV}$, $211.9 \pm 11.93 \text{ HV}$ and $199.5 \pm 8.23 \text{ HV}$, respectively for the HEAs with cobalt content from $x=0$ to 1.0 mol. The high values of standard deviation are due to the presence of grains with precipitate in the microstructure which has different responses against the applied load [170].

The following might be the reasons for the decrease in microhardness as cobalt content increases from $x=0$ to 1.0 mol. First, as the cobalt content increases in the HEAs, the amount of FCC phases increases and the amount of BCC phase decreases and hence the hardness decreases. This has been reported by many researchers previously [62, 136, 171].

Second, the chemical enthalpy of mixing of Co-Cr, Co-Fe, Co-Ni, Co-Al are 8 kJ mol^{-1} , 13 kJ mol^{-1} , 17 kJ mol^{-1} , -24 kJ mol^{-1} , respectively. On the other hand, the chemical enthalpy of mixing of Cr-Fe, Cr-Ni, Cr-Al, Fe-Ni, Fe-Al, and Ni-Al are 13 kJ mol^{-1} , 3 kJ mol^{-1} , -6 kJ mol^{-1} , -10 kJ mol^{-1} , and -30 kJ mol^{-1} respectively. Similarly, if the chemical mixing enthalpy of all other elements will be considered, then it will be observed that the combinative force of cobalt with other elements in the alloy is weakest. Therefore, with the addition of cobalt, the combinative force decreases and this in turns decreases the strength and hardness of the system [172].

Third, the atomic size of cobalt is (1.251 \AA) is lower than that of the aluminium (1.432 \AA). Hence, when the aluminium atom occupies the lattice sites, the lattice distortion energy increases

to a greater extent than when the cobalt atoms occupy the lattice sites. For this reason, the addition of cobalt causes solid solution strengthening to a lesser extent than the addition of aluminium and thus the strength and hardness decreases with the addition of cobalt [172].

Fourth, the formation of Al-Ni type precipitate or B2 phase as shown in Fig. 5.11(a-d) and confirmed from EDS results as listed in Table 5.6. It is reported that these precipitates help in increasing the hardness of the high entropy alloy [110, 111]. Since the amount of aluminium in the high entropy alloy decreases with the addition of cobalt from $x=0$ to 1.0 mol, and it reduces the probability of formation of the Al-Ni precipitates and hence the hardness decreases.

5.3.5 Compressive strength of homogenized $\text{Al}_{0.4}\text{FeCrNiCo}_x$ ($x=0, 0.25, 0.5$ and 1.0 mol) HEAs

Figure 5.14(a) shows the engineering stress strain curve under compression at room temperature and Fig. 5.14(b) represents the image of the sample before and after the experiment. From the Figure 5.14(a) it is observed that the compressive yield strength of homogenized $\text{Al}_{0.4}\text{FeCrNiCo}_x$ ($x=0, 0.25, 0.5$ and 1.0 mol) HEAs decreases from 1169.35 MPa to 257.63 MPa with addition of cobalt content from $x=0$ to 1.0 mol.

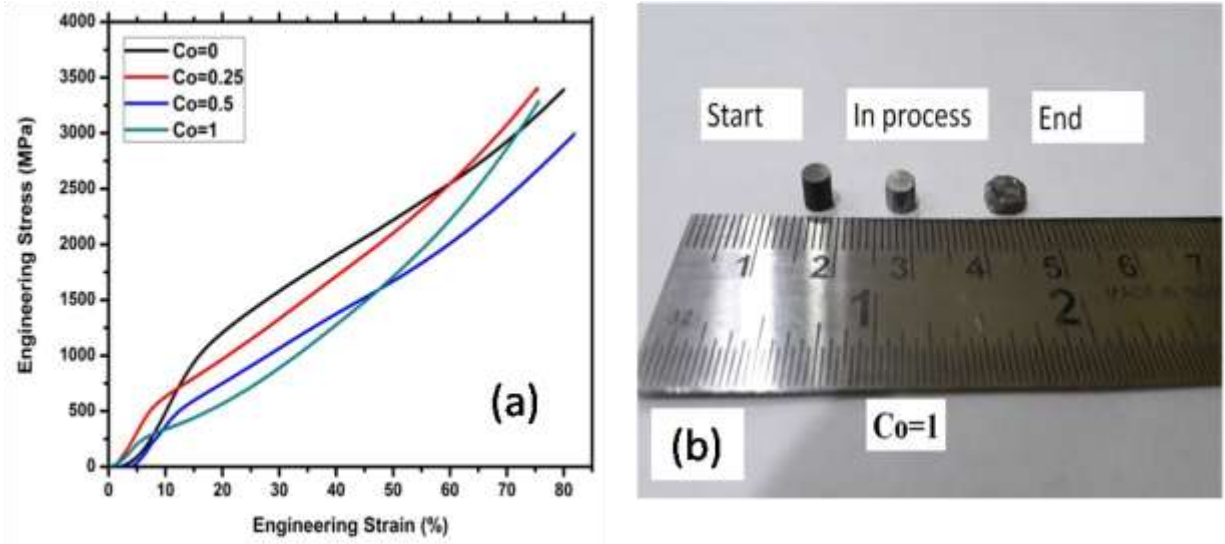


Fig. 5.14 (a) Engineering stress-strain curve of homogenized $\text{Al}_{0.4}\text{FeCrNiCo}_x$ ($x=0, 0.25, 0.5$ and 1.0 mol) HEAs under compression at room temperature, (b) image of $\text{Co}=1$ HEA sample during the compression test.

The decrease in compressive yield strength is due to the increase in FCC phase with the addition of cobalt as shown in Fig. 5.10(b). It may be noted that the BCC phase is stronger than the FCC phase because the slip along the closest packed plane in BCC structure {110} is more difficult than slip along closest packed plane in FCC structure {111} [35]. Plastic strain more than 75% is achieved in all the HEAs without failure of the sample as shown in Fig. 5.14(a). The compressive yield strength of Co=1 HEA is observed to be 257.63 MPa, and similar results were also reported by Joseph et al.[114].

5.4 Comparison with reported results

Shun et al. [110] have developed $Al_{0.3}CoCrFeNi$ HEA system through induction melting and casting route and have reported FCC and B2 phase formation in their system. The yield strength and the strain of the as-cast sample are observed to be approximately 175 MPa and 60 %. Kao et al. [111] have synthesized the $Al_xCoCrFeNi$ ($0 \leq x \leq 2$) HEAs through vacuum arc melting and have compared them with homogenized one. The XRD patterns of the as-cast samples indicates that as the Al content increases the transformation from FCC phase to BCC phase occur. On increasing the Al content hardness increases from 116 HV to 509 HV and in case of Al=0.375 HEA it is observed to be 130 HV. After homogenization (at 1100°C for 24hrs) transformation of FCC phase to BCC phase is observed to occur along with the formation of B2 phase which are rich in AlNi. The hardness of the homogenized $Al_xCoCrFeNi$ ($0 \leq x \leq 2$) HEAs are observed to vary from 113 HV to 512 HV and in case of Al= 0.375 HEA, it is observed to be 196 HV. Qin et al. [136] have developed the $(AlCoCrFeNi)_{100-x}Co_x$ ($x=0, 4, 8, 12, 16,$) HEAs systems through arc melting technique. The XRD results of their samples have indicated that as the cobalt content increases from 0% to 16%, the FCC phase fraction increases from 0% to 77%. The microstructure of the HEAs is observed to have two regions indicating FCC and BCC structure. The FCC region is poor in Al and BCC region is rich in Al. With the increase of Co content, the compressive yield strength decreases from 1300 MPa to 750 MPa and the plastic strain increases from 27% to 40%.

In the present study, $Al_{0.4}FeCrNiCo_x$ ($x = 0, 0.25, 0.5$ and 1.0 mol) HEAs developed through arc melting technique and the XRD patterns of as-cast ingots shows FCC and BCC structure along with B2 structure for X=0. It is observed that the volume fraction of BCC phase decreases from

16% to 0% with the increase in cobalt content from $x=0$ to $x=1.0$. The microhardness of the as-cast ingot decreases from 253.6 HV to 155.6 HV, and the compressive yield strength decreases from 965.22 MPa to 233.37 MPa with the addition of cobalt from $x = 0$ to $x = 1.0$ mol. Plastic strain increase from 73.31 % to 81.32 % at the same time. On homogenization at 1100°C for 24 hrs, FCC, BCC and B2 phases get formed in the structure and the volume fraction of the BCC phase decreases from 91 % to 35 %. The microhardness of homogenized samples decreases from 377.7 HV to 199.5 HV and the compressive yield strength decreases from 1169.35 MPa to 257.63 MPa with a maximum plastic strain of 75 % after the homogenization.

Chapter Summary

This chapter includes

- phase analysis of as-cast and homogenized $Al_{0.4}FeCrNiCo_x$ ($x=0, 0.25, 0.5$ and 1.0 mol) HEAs.
- Include microstructural and thermal characterization of as-cast and homogenized $Al_{0.4}FeCrNiCo_x$ ($x=0, 0.25, 0.5$ and 1.0 mol) HEAs.
- Mechanical analysis of as-cast and homogenized $Al_{0.4}FeCrNiCo_x$ ($x=0, 0.25, 0.5$ and 1.0 mol) HEAs.

In the next chapter wear behavior of $Al_{0.4}FeCrNiCo_x$ ($x=0, 0.25, 0.5$ and 1.0 mol) HEAs were discussed under dry and oil lubrication condition

Wear behavior of $\text{Al}_{0.4}\text{FeCrNiCo}_x$ ($x=0, 0.25, 0.5$ and 1.0 mol) HEAs under different environment

6.1 Introduction

In this chapter the wear behavior of $\text{Al}_{0.4}\text{FeCrNiCo}_x$ ($x=0, 0.25, 0.5$ and 1.0 mol) HEAs is investigated at different sliding condition like, varying sliding speed of (0.5, 1, 1.5, 2) m/s, varying sliding distance of (1000, 2000, 3000, 4000) m, and normal loads of (5, 10, 15, 20) N under dry and lubricating oil medium. The worn surface and wear debris were also analyzed by using scanning electron microscopy (SEM), energy dispersive X-ray spectroscopy (EDS) and 3D profiling to understand the wear mechanism. The unknown oxides formed during the sliding were examined by X-ray photoelectron spectroscopy.

6.2 Correlation between specific wear rate, hardness, and cobalt content

Figure 6.1 shows the relationship between specific wear rate and hardness along with the cobalt content. For correlation, the wear is carried out under the constant wear conditions of 1000 m sliding distance, 1 m/s sliding speed, and 10 N normal load for all HEA samples.

From the Fig. 6.1 it is observed that as the cobalt content increases from $x=0$ to 1.0 mol, the hardness decreases from 377.7 HV to 199.5 HV and the specific wear rate increases, therefore follows Archard's wear law which indicate hardness is inversely proportional to material loss. The specific wear rate of $\text{Al}_{0.4}\text{FeCrNiCo}_x$ ($x=0, 0.25, 0.5$ and 1.0 mol) HEAs is inversely related to their hardness which in turn depends upon the phase transition from FCC+BCC to FCC as seen in Fig. 5.10. This observation is also closely related to the findings of Khrushov et al.[173].

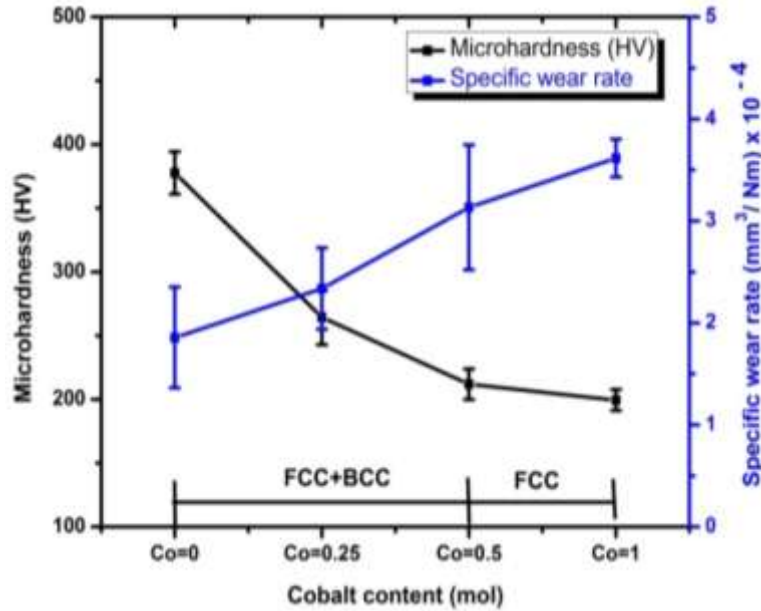


Fig. 6.1 Variation of microhardness and specific wear rate of $\text{Al}_{0.4}\text{FeCrNiCo}_x$ ($x=0, 0.25, 0.5$ and 1.0 mol) HEAs as a function of cobalt content

6.3 Wear behavior of $\text{Al}_{0.4}\text{FeCrNiCo}_x$ ($x=0, 0.25, 0.5$ and 1.0 mol) HEAs under dry condition

6.3.1 Effect of sliding Speed on wear behavior of $\text{Al}_{0.4}\text{FeCrNiCo}_x$ ($x=0, 0.25, 0.5$ and 1.0 mol) HEAs

Figure 6.2 (a) shows the variation of the average coefficient of friction with varying sliding speed under constant wear conditions of 10 N normal load and 1000 m sliding distance. From the graph it is observed that at sliding speed of 0.5 m/s the COF values for $\text{Al}_{0.4}\text{FeCrNiCo}_x$ ($x=0, 0.25, 0.5$ and 1.0 mol) HEAs is 0.307, 0.366, 0.356, and 0.419 respectively and in case of 2 m/s for $\text{Al}_{0.4}\text{FeCrNiCo}_x$ ($x=0, 0.25, 0.5$ and 1.0 mol) HEAs are 0.198, 0.213, 0.215, and 0.228 respectively. Therefore the percentage decrease in COF value with increase in speed from 0.5 m/s to 2 m/s for $\text{Al}_{0.4}\text{FeCrNiCo}_x$ ($x=0, 0.25, 0.5$ and 1.0 mol) HEAs are 35.50%, 33.60%, 39.60%, and 45.58% respectively. The results indicate that as the sliding speed increases, the coefficient of friction decreases. It is because at higher sliding speed the interface temperature between the sliding disk and HEA sample is high which helps in forming a protective oxide

layer, and in turns smoothens the surface [174, 175] and it is confirmed by SEM and EDS analyses listed in Fig. 6.4 and Table 6.1.

The coefficient of friction of $\text{Al}_{0.4}\text{FeCrNiCo}_x$ ($x=0, 0.25, 0.5$ and 1.0 mol) HEAs is observed to vary in two different regimes as seen in Fig. 6.2 (a). In the first regime (sliding speed up to 1 m/s), the coefficient of friction decreases rapidly and in the second regime, (sliding speed between 1 m/s and 2 m/s), the coefficient of friction changes gradually. It is because at lower sliding speed the oxide formation is insufficient and formation of the smooth protective surface is restricted. Therefore more metal to metal contact occurs, and coefficient of friction has a higher value [176]. At higher sliding velocity the contact temperature is higher which help in the formation of the oxide layer and smooth surface, therefore coefficient of friction decreases.

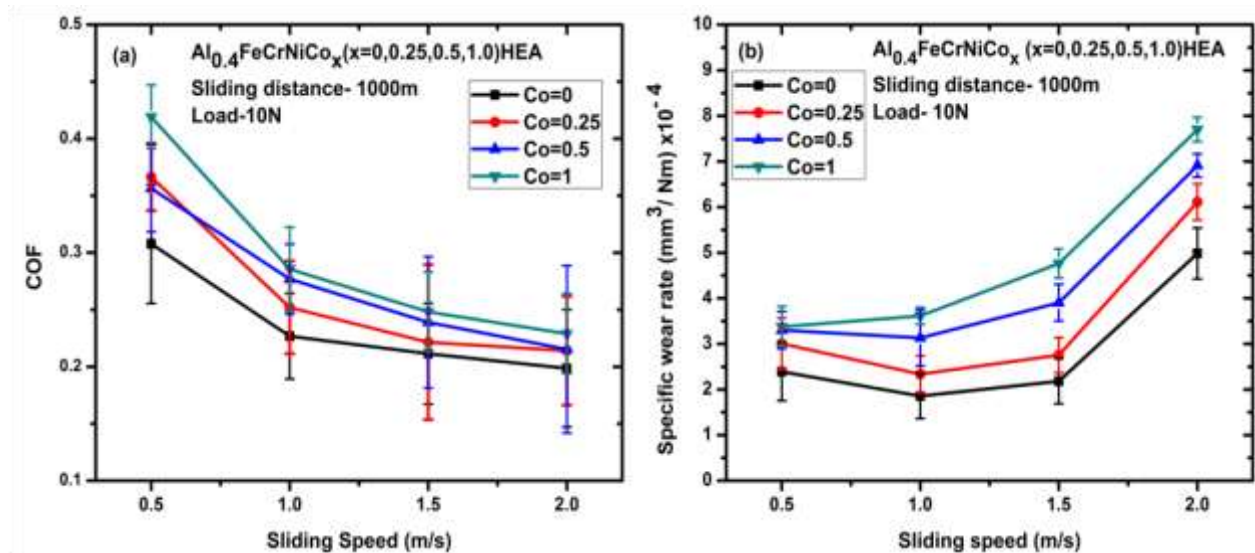


Fig. 6.2 Effect of variation in sliding speed on (a) coefficient of friction and (b) specific wear rate of $\text{Al}_{0.4}\text{FeCrNiCo}_x$ ($x=0, 0.25, 0.5$ and 1.0 mol) HEAs

Figure 6.2 (b) shows the variation in specific wear rate with sliding speed. It is observed that in case of 0.5 m/s sliding speed the specific wear rate of $\text{Al}_{0.4}\text{FeCrNiCo}_x$ ($x=0, 0.25, 0.5$ and 1.0 mol) HEAs are $2.391 \times 10^{-4} \text{ mm}^3/\text{Nm}$, $3.006 \times 10^{-4} \text{ mm}^3/\text{Nm}$, $3.303 \times 10^{-4} \text{ mm}^3/\text{Nm}$ and $3.375 \times 10^{-4} \text{ mm}^3/\text{Nm}$ respectively. The specific wear rate in case of 2 m/s sliding speed for $\text{Al}_{0.4}\text{FeCrNiCo}_x$ ($x=0, 0.25, 0.5$ and 1.0 mol) HEAs are $4.983 \times 10^{-4} \text{ mm}^3/\text{Nm}$, $6.112 \times 10^{-4} \text{ mm}^3/\text{Nm}$, $6.912 \times 10^{-4} \text{ mm}^3/\text{Nm}$, and $7.702 \times 10^{-4} \text{ mm}^3/\text{Nm}$. Therefore the percentage increase in specific wear rate on

increasing the sliding speed from 0.5 m/s to 2 m/s for $\text{Al}_{0.4}\text{FeCrNiCo}_x$ ($x=0, 0.25, 0.5$ and 1.0 mol) HEAs are 108.40%, 103.32%, 109.32% and 128.20% respectively.

The results indicate that as the cobalt content increases from $x=0$ to $x=1.0$ mol, the specific wear rate increases for all high entropy alloy samples and maximum specific wear rate occurs in the case of $\text{Co}=1$ HEA. It is due to increase in FCC phase with the addition of cobalt content which in turn decreases the hardness. Furthermore, with the increase in sliding speed, the temperature at the contact point of the sample and the counter material increases and this leads to damage to the sample surface. The damage, in turn, leads to enhanced adhesive wear and delamination. Okonkwo et al. have reported the effect of sliding speed for steel-tool steel pair and found that the increase in sliding speed leads to the rise in interface temperature [177].

6.3.1.1 worn surface and wear debris analysis under sliding speed condition

Figure 6.3 (a-d), Fig. 6.4 (a-1), and Fig. 6.5 (a-d) shows the optical micrograph of worn surface, SEM micrograph of worn surface, EDS results, 3D profile and wear debris of $\text{Al}_{0.4}\text{FeCrNiCo}_x$ ($x=0, 0.25, 0.5$ and 1.0 mol) HEAs after the wear test operating at the constant dry sliding condition (i.e. 2 m/s sliding speed, 10 N normal load and 1000 m sliding distance). It is observed from the Fig. 6.4 (a) that the worn surface micrograph of $\text{Co}=0$ HEA reveals scratches, microgrooves and material deformation along the sliding direction as confirmed by the 3D profile in Fig. 6.4 (c). Due to the lateral crack and delamination, thin, flat, irregular, and multilayer flake type debris are generated as shown in Fig. 6.5 (a). The average diameter of wear debris of $\text{Co}=0$ HEA as calculated from SEM micrograph is in the range of 23.9 μm to 28.042 μm . The difference in elemental compositions of the alloy surface before and after the wear test can also be observed in Table 5.6, and Table 6.1. The major changes occur in an atomic percentage of aluminium and nickel and a slight change in other elements gives an indication that material is transferred between the HEA pin sample and the rotating disc, due to frictional heat generated during the wear process [178, 179].

The worn surface is observed to contain a significant amount of oxygen i.e. 31.7 at.% (average value of Area-1, Area-2 and wear debris), which form oxide with the sample elements and decreases the material loss as seen in Fig. 6.2 (b) and the specific wear rate in case of $\text{Co}=0$ HEA is $4.983 \times 10^{-4} \text{ mm}^3/\text{Nm}$ under constant sliding condition of (2 m/s, 10N, 1000 m) and similar

observation was also made by Ji et al. [180]. The wear mechanism is the combined effect of adhesive wear along with delamination and oxidative wear. Wu et al. [39] conducted the wear study of $Al_xCoCrCuFeNi$ HEA and reported that the delamination is the main reason for sliding wear in the ductile, high entropy alloys.

Figure 6.4 (d) shows the SEM micrograph of the worn surface of Co=0.25 HEA under similar operating conditions as in the case of Co=0 HEA. The SEM micrograph shows deep grooves, flow of material along the sliding direction as confirmed by a 3D profile in Fig. 6.4 (f). The cracks on the surface generate the thin, flat and flake type wear debris with an average diameter in the range of 26.94 μm to 35.32 μm as shown in Fig. 6.5 (b). The elemental composition of worn surface and wear debris of Co=0.25 HEA indicate the presence of oxygen, i.e., 17.7 at.% (average value of Area-1, Area-2 and wear debris) which form oxide with the sample elements and help in reducing the wear [180]. Therefore the percentage increase in specific wear rate in case of Co=0.25 HEA is 22.65% is higher than Co=0 HEA at the similar sliding condition of (2 m/s, 10 N, 1000 m).

Figure 6.4 (g) shows the SEM micrograph of the worn surface of Co=0.5 HEA under the similar operating condition as in the case of Co=0 HEA. The SEM micrograph shows, scratches, micro-grooves and flow of material along the sliding direction as confirmed by 3D-profile in Fig. 6.4 (i). The wear debris produced under same operating condition was observed to be thin, flat, and flake type with plastic deformation as shown in Fig. 6.5 (c). The average diameter of wear debris is calculated from SEM micrograph and in the range of 35.22 μm to 40.68 μm . The elemental composition of worn surface and wear debris of Co=0.5 HEA indicate the presence of oxygen, i.e. 14.62 at.% (average value of Area-1, Area-2 and wear debris) which form oxide and help in reducing the wear [180]. Therefore, the percentage increase in specific wear rate in case of Co=0.5 HEA is 38.71% percentage is higher than in case of Co=0 HEA at the similar sliding condition of (2 m/s, 10 N, 1000 m).

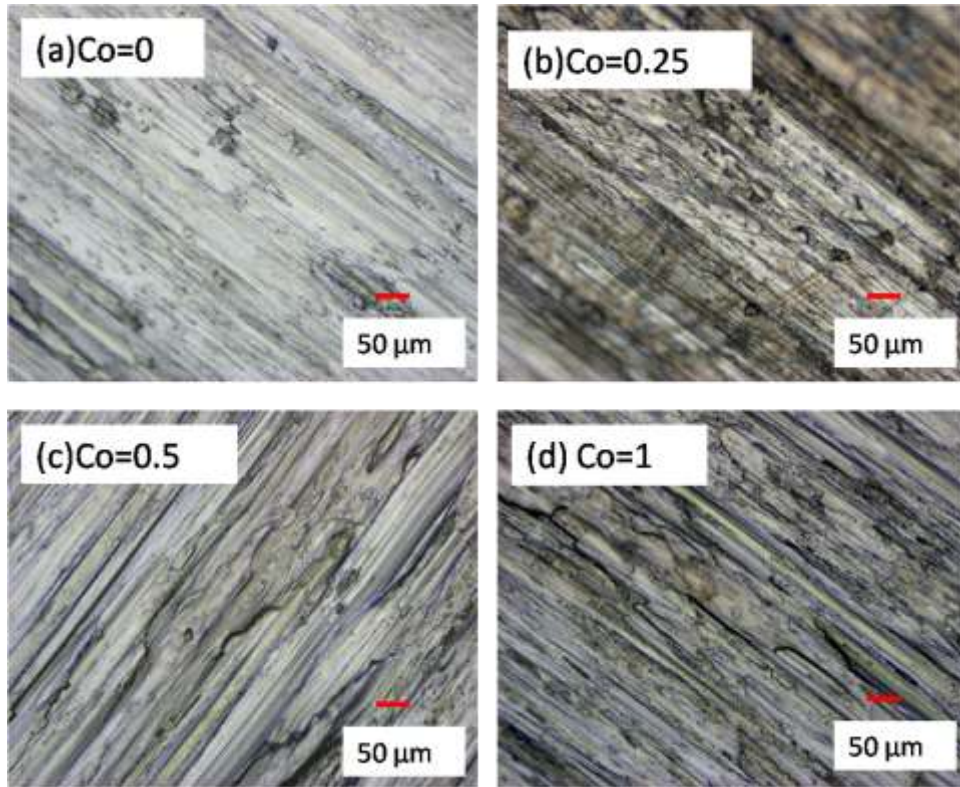


Fig. 6.3 (a-d) Optical micrographs of worn surfaces of $\text{Al}_{0.4}\text{FeCrNiCo}_x$ ($x=0, 0.25, 0.5$ and 1.0 mol) HEAs tested under the constant wear conditions of 2 m/s sliding speed, 1000 m sliding distance, and 10 N normal load.

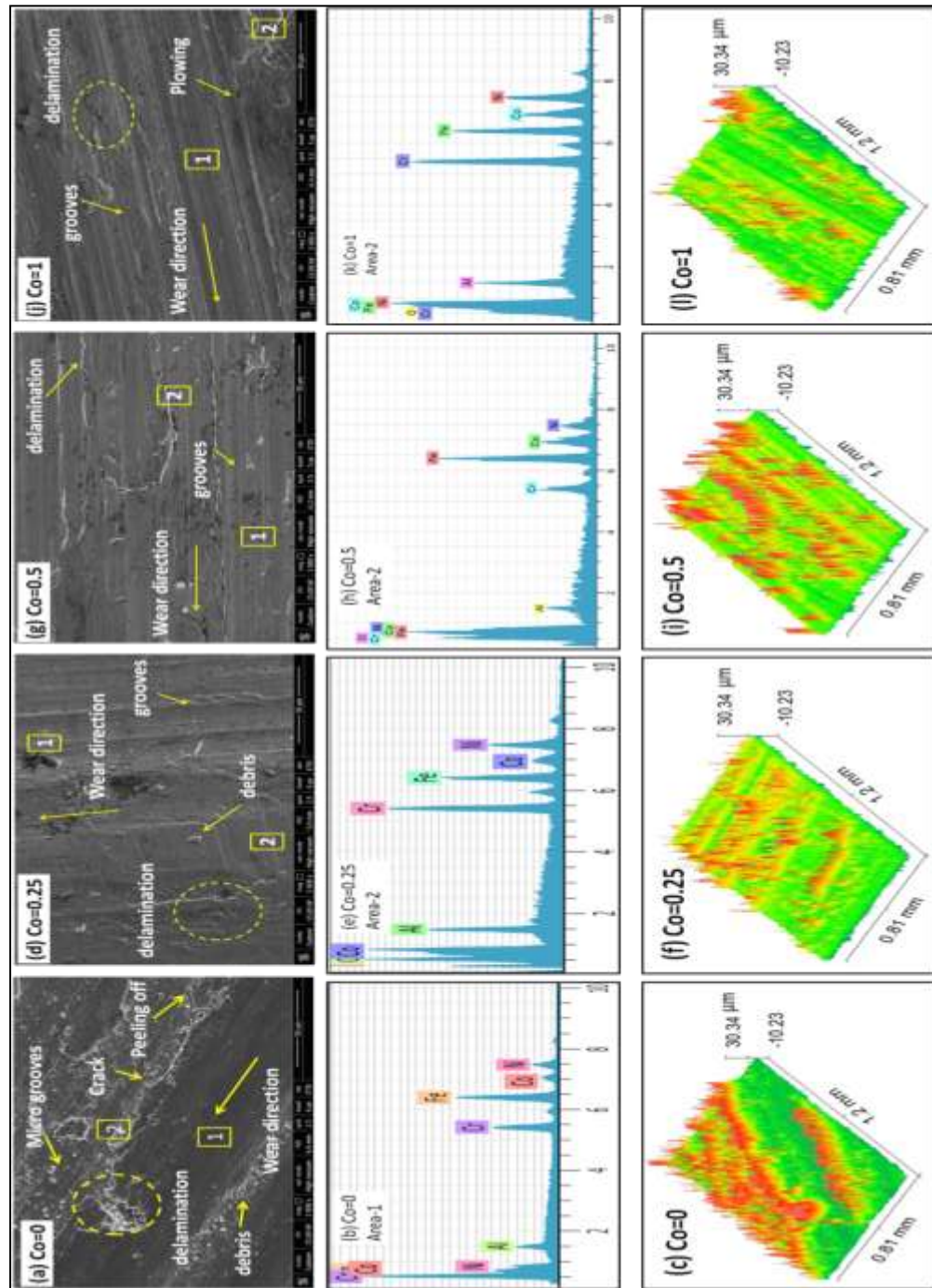


Fig. 6.4 (a, d, g and j) SEM micrographs of worn surfaces, (b, e, h and k) EDS result of worn surface and (c, f, i, and l) 3D profile of $\text{Al}_{0.4}\text{FeCrNiCo}_x$ ($x=0, 0.25, 0.5,$ and 1.0 mol) HEAs tested under the constant wear conditions of 2 m/s sliding speed, 1000 m sliding distance, and 10 N normal load.

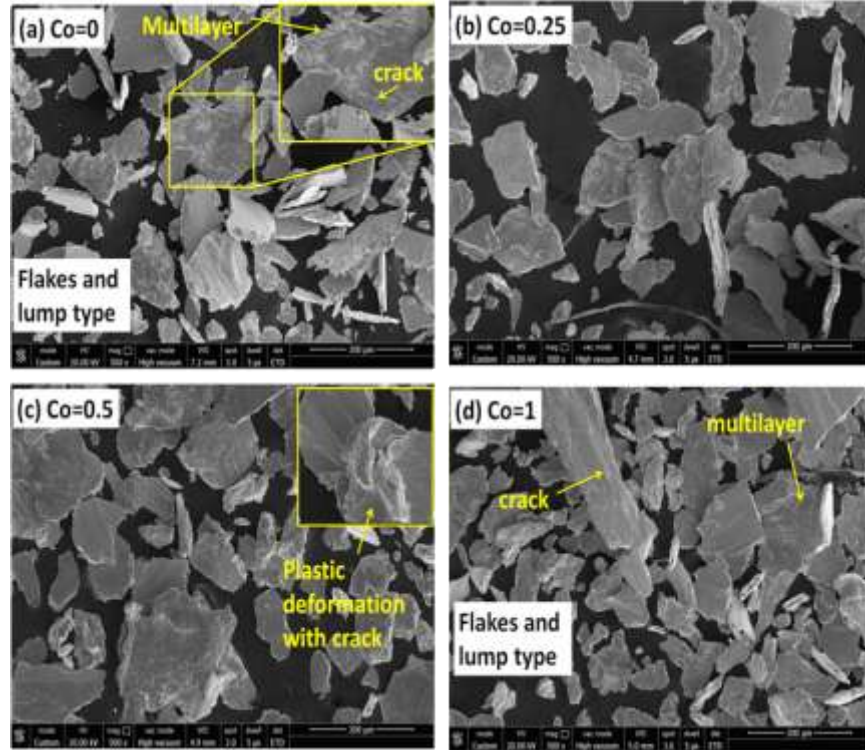


Fig. 6.5 (a-d) SEM micrographs of wear debris of $Al_{0.4}FeCrNiCo_x$ ($x=0, 0.25, 0.5$ and 1.0 mol) HEAs tested under the constant wear conditions of 2 m/s sliding speed, 1000 m sliding distance, and 10 N normal load.

Table 6.1 EDS results of worn surfaces and wear debris of $Al_{0.4}FeCrNiCo_x$ ($x=0, 0.25, 0.5$ and 1.0 mol) HEAs tested under the wear conditions of 2 m/s sliding speed, 1000 m sliding distance, and 10 N normal load

HEA	Area	Al	Fe	Cr	Ni	Co	O
Co=0	Area-1	3.62	25.14	10.28	8.52	-	52.44
	Area-2	6.0	27.11	18.94	18.06	-	29.89
	debris	5.77	24.53	25.13	31.54	-	13.03
Co=0.25	Area-1	10.16	25.21	28.14	24.26	6.61	5.62
	Area-2	8.71	18.44	18.14	17.30	4.24	33.17
	debris	7.24	21.60	24.58	26.08	5.90	14.60
Co=0.5	Area-1	7.27	22.31	20.75	22.93	22.28	4.46
	Area-2	3.38	38.65	7.87	11.39	13.43	25.28
	debris	7.97	15.18	19.20	26.97	14.56	14.12
Co=1	Area-1	6.64	16.32	16.20	17.09	13.53	30.22
	Area-2	8.92	25.47	22.99	25.68	13.92	3.02
	debris	9.87	24.43	25.63	26.76	13.32	0

Figure 6.4 (j) shows the SEM micrograph of the worn surface of Co=1 HEA under similar operating as in the case of Co=0 HEA. The worn surface indicates the sliding marks, grooves, ploughing and material flow along the sliding direction as confirmed by a 3D profile in Fig. 6.4 (l). The wear debris collected during the wear process resembles thin, flat and flake type debris with an average diameter in the range of 25.25 μ m to 30.46 μ m as shown in Fig. 6.5 (d).

The elemental composition as listed in Table 6.1, indicates the presence of oxygen, i.e., 11.08 at.% (average value of Area-1, Area-2 and wear debris) which forms an oxide with the sample elements and helps in reducing the wear [180]. It is observed that the percentage of oxygen decreases with increase in cobalt and in turns decreases the protective oxide layer thickness [181]. Therefore the specific wear rate in case of Co=1 HEA is 54.56% higher than Co=0 HEA at the same sliding condition of (2 m/s, 10 N, 1000 m).

6.3.2 Effect of normal loading on wear behavior of Al_{0.4}FeCrNiCo_x (x=0, 0.25, 0.5 and 1.0 mol) HEAs

Figure 6.6 (a) shows the effect of varying normal load on the coefficient of friction under the constant sliding conditions of 1 m/s sliding speed and 1000 m sliding distance. It is observed that the coefficient of friction (COF) value in case of 5 N load for Al_{0.4}FeCrNiCo_x (x=0, 0.25, 0.5 and 1.0 mol) HEAs are 0.271, 0.293, 0.296, and 0.301 respectively. The COF value in case of 20 N normal load for Al_{0.4}FeCrNiCo_x (x=0, 0.25, 0.5 and 1.0 mol) HEAs are 0.219, 0.226, 0.232, and 0.251 respectively. Therefore the percentage decrease in COF on increasing the normal loads from 5 N to 20 N is 19.18%, 22.86%, 21.62% and 16.61% respectively. Results indicated that on the increase the load, coefficient of friction decreases for all HEA samples. The COF decreases gradually in between 5 N to 15 N, and after 15 N it decreases rapidly.

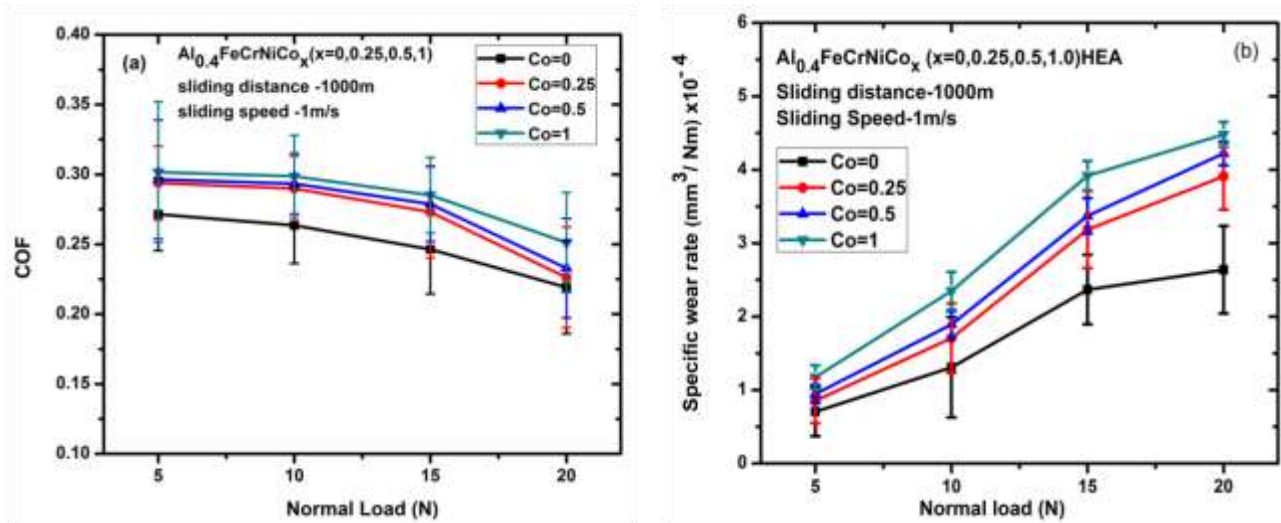


Fig. 6.6 Effect of variation in normal loading on (a) coefficient of friction (b) specific wear rate of Al_{0.4}FeCrNiCo_x (x=0, 0.25, 0.5 and 1.0 mol) HEAs.

It is because of two reasons, first reason as the load increases, the area of contact between the pin samples and the rotating disk increases, which increases the interface temperature and form oxide layer which give lubricating effect [182] and decreases the coefficient of friction. In the second reason, the presence of lose wear debris, came in contact between the two mating surface and decreases the real contact point and result in decreases of coefficient of friction.

Figure 6.6 (b) shows the variation of specific wear rate of Al_{0.4}FeCrNiCo (x= 0, 0.25, 0.5 and 1.0 mol) HEAs with increasing normal loads. It is observed that, the specific wear rate in case of 5 N normal load for Al_{0.4}FeCrNiCo_x (x= 0, 0.25, 0.5 and 1.0 mol) HEAs is $0.704 \times 10^{-4} \text{ mm}^3/\text{Nm}$, $0.853 \times 10^{-4} \text{ mm}^3/\text{Nm}$, $0.946 \times 10^{-4} \text{ mm}^3/\text{Nm}$, and $1.175 \times 10^{-4} \text{ mm}^3/\text{Nm}$ respectively. The specific wear rate in case of 20 N normal loads is $2.638 \times 10^{-4} \text{ mm}^3/\text{Nm}$, $3.912 \times 10^{-4} \text{ mm}^3/\text{Nm}$, $4.221 \times 10^{-4} \text{ mm}^3/\text{Nm}$, and $4.482 \times 10^{-4} \text{ mm}^3/\text{Nm}$ respectively. Therefore the percentage increase in specific wear rate on increasing the load from 5N to 20N is 274.33%, 358.46%, 346.03% and 281.19% respectively. The result indicates that on increasing the load, the specific wear rate increases, and similar trends were observed for all HEAs in different wear condition. The figure indicates that the specific wear rate varies in two different regimes. In First regime (normal load 5 N to 15 N) the specific wear rate increases rapidly. It is due to lose adherent of the oxide layer to the sample surface by frictional heating in between 5 N to 15 N. In the second regime (normal load 15 N to 20 N) the specific wear rate varies gradually. It is because at the higher loads more stable oxide layer form which avoids metal to metal contact and controls the wear rate.

6.3.2.1 Worn surface and wear debris analysis under normal loading condition

Figure 6.7 (a-d), Fig. 6.8 (a-l), and Fig. 6.9 (a-d) shows the optical micrograph of worn surface, SEM micrograph of worn surface, 3D profile, and wear debris of $\text{Al}_{0.4}\text{FeCrNiCo}_x$ ($x=0, 0.25, 0.5$ and 1.0 mol) HEAs after the wear test operating at the constant dry sliding condition (i.e., 20 N normal load, 1 m/s sliding speed, and 1000 m sliding distance). It is observed from the Fig. 6.8 (a) that the SEM micrograph of the worn surface of $\text{Co}=0$ HEA reveals scratch marks, microgrooves and material flow along the sliding direction as confirmed by 3D profile as seen in Fig. 6.8 (c).

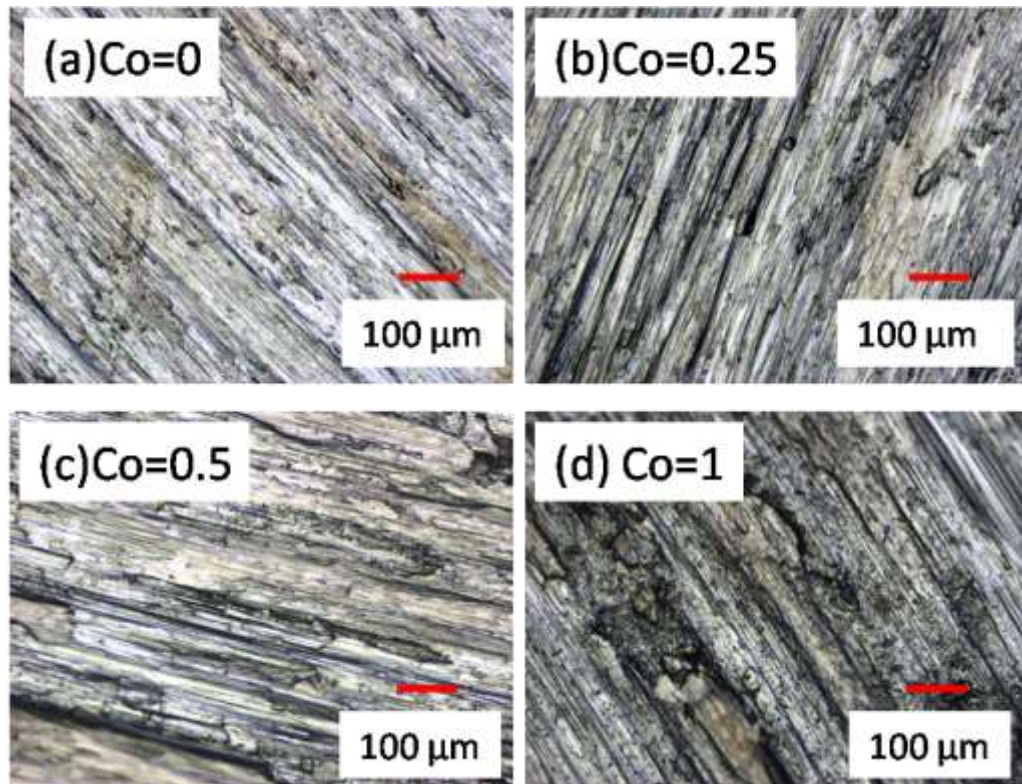


Fig. 6.7 Optical micrograph of worn surface of $\text{Al}_{0.4}\text{FeCrNiCo}_x$ ($x=0, 0.25, 0.5$ and 1.0 mol) HEAs tested under 20 N normal load, 1000 m sliding distance and 1 m/s speed.

The wear debris generated during the wear process is thin, flat, and flake type with a multilayered structure. The average diameter of wear debris varies from $33.83 \mu\text{m}$ to $45.35 \mu\text{m}$ which is calculated from the SEM micrograph as shown in Fig. 6.9 (a). The elemental

composition of the sample before and after the experiment is listed in Table 5.6 and Table 6.2. It indicates that the atomic percentage of chromium and nickel varies which indicate the material transfer occurs between the HEA sample and rotating disc. The presence of oxygen in case of Co=0 HEA is 13.10 at.% (average of area-1, area-2, and wear debris) percentage which form an oxide with the sample element and restricts the wear [180]. The specific wear rate in case of Co=0 HEA is $2.638 \times 10^{-4} \text{ mm}^3/\text{Nm}$ under the constant sliding condition of (20 N, 1 m/s, 1000m).

Figure 6.8 (d) shows the SEM micrograph of the worn surface of Co=0.25 HEA under similar wear condition as in the case of Co=0 HEA. It is observed that the scratch marks, microgrooves and material flow along the sliding direction as confirmed by a 3D profile in Fig. 6.8 (f). The wear debris generated during the wear process is thin, flat and flake type with a multilayered structure. The average diameter of wear debris varies from 23.76 μm to 31.33 μm as calculated from the SEM micrograph as shown in Fig. 6.9 (b). The oxygen content in the case of Co=0.25 HEA is 9.84 at.% which combine with the sample elements and form oxide, which restrict the wear [180]. The specific wear rate in case of Co=0.25 HEA is 48.29 % higher than in the case of Co=0 HEA.

Figure 6.8 (g) shows the SEM micrograph of the worn surface of Co=0.5 HEA under similar condition as in the case of Co=0 HEA. The worn surface indicates scratch marks and plastic deformation as confirmed by 3D-profile in Fig. 6.8 (i). Due to cracks and delamination, the wear debris produced during the wear process is thin, flat, and an irregular shape, as indicated in Fig. 6.9 (c). The average diameter of wear particle is in the range of 28.33 μm to 38.42 μm . The presence of oxygen in case of Co=0.5 HEA is 8.27 at.% which forms protective oxide layer and restricts the wear [39, 179-180]. The specific wear rate in case of Co=0.5 HEA is 60.0% higher than in the case of Co=0 HEA.

Figure 6.8 (j) shows the SEM micrograph of the worn surface of Co=1 HEA under the similar operating condition as in the case of Co=0 HEA. The worn surface after the wear test shows scratch marks, grooves, and plastic deformation along the sliding direction as confirmed by a 3D profile in Fig. 6.8 (l). Due to cracks and delamination, the wear debris produced during the wear process appears thin, flat, and irregular, as shown in Fig. 6.9 (d) the average diameter of wear particle is in the range of 31.63 μm to 38.44 μm .

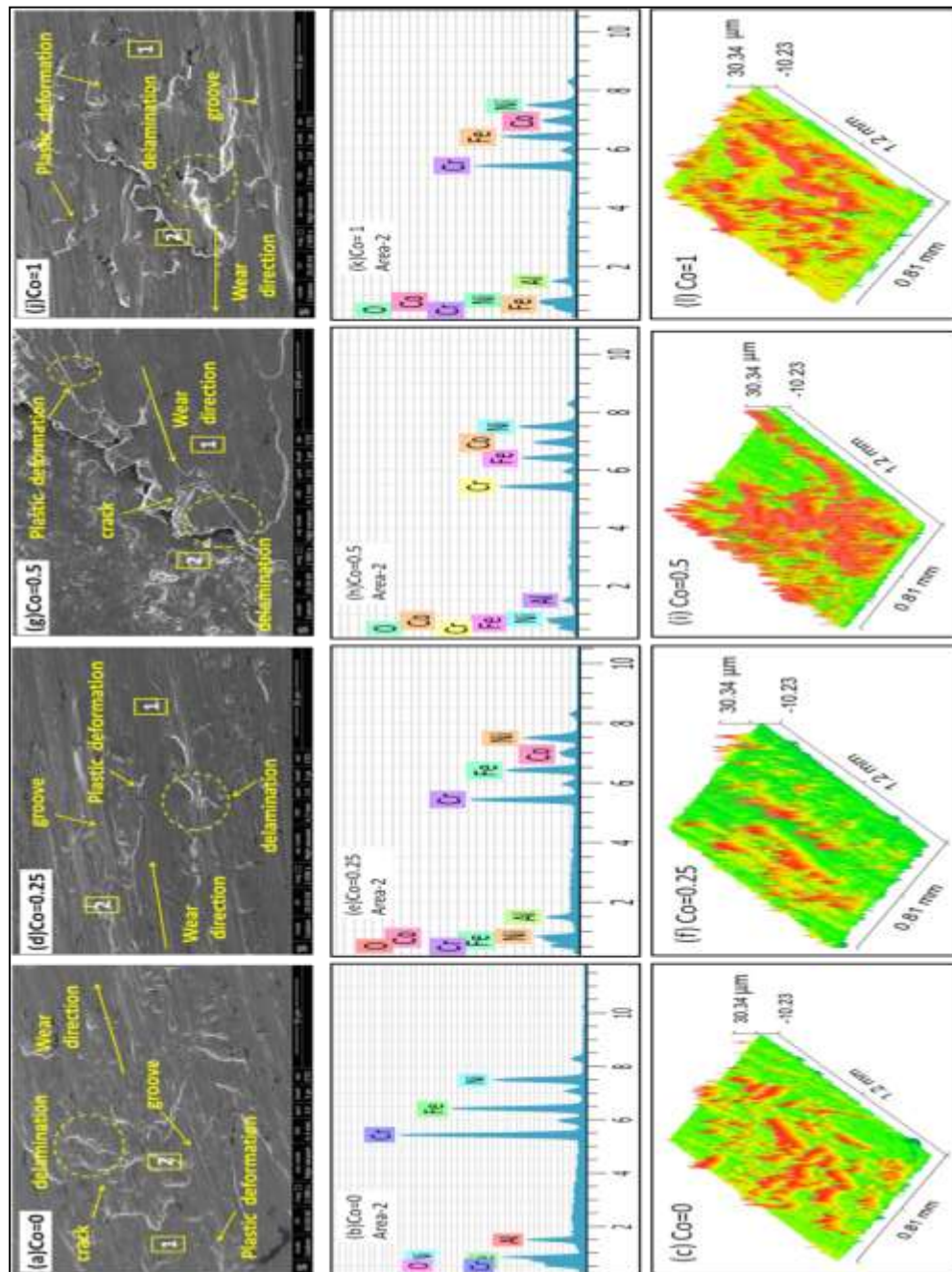


Fig. 6.8 (a, d, g and j) SEM micrographs of worn surfaces, (b, e, h and k) EDS result of worn surface and (c, f, i, and l) 3D profile of $\text{Al}_{0.4}\text{FeCrNiCo}_x$ ($x=0, 0.25, 0.5$ and 1.0 mol) HEAs tested under 20 N normal load, 1000 m sliding distance and 1 m/s speed.

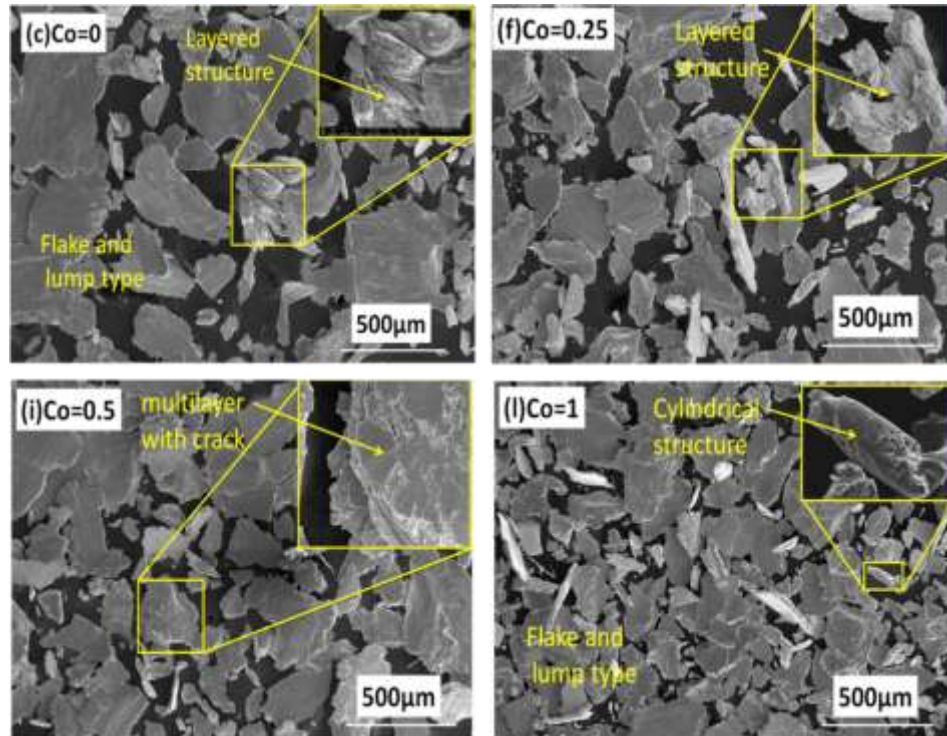


Fig. 6.9 (a-d) SEM micrograph of wear debris of $\text{Al}_{0.4}\text{FeCrNiCo}_x$ ($x=0, 0.25, 0.5$ and 1.0 mol) HEAs tested under 20 N normal load, 1000 m sliding distance and 1 m/s speed

At high magnification, the wear debris shows the cylindrical roller type structure, and it is generated due to the transformation of the thin, flat and irregular type of debris. It occurs when the flat type of debris detaches itself from the worn surface and continues to stay within the interface of the contacting surfaces.

Under these conditions, the debris gets plastically deformed and rolled into a cylindrical type [183] and help in decreasing the COF value [184]. The presence of oxygen in case of Co=1 HEA is 4.06 at.%. It is observed that as the cobalt content increases from $x=0$ to 1 mol, the oxygen content decreases from 13.10 at.% to 4.06 at.% and in turn decreases the protective oxide layer thickness [181]. The specific wear rate in case of Co=1 HEA is 69.90% higher than in the case of Co=0 HEA.

Table 6.2 EDS results of worn surface and debris of Al_{0.4}FeCrNiCo_x (x=0, 0.25, 0.5 and 1.0 mol) HEA tested under 20 N normal load, 1000 m sliding distance and 1 m/s speed.

HEA	Area	Al	Fe	Cr	Ni	Co	O
Co=0	Area-1	10.81	27.36	33.56	25.06	-	3.22
	Area-2	9.08	29.09	28.69	27.73	-	5.41
	debris	6.35	16.18	18.79	27.99	-	30.69
Co=0.25	Area-1	9.92	26.68	27.78	25.46	6.48	3.32
	Area-2	8.32	24.69	24.97	24.04	6.14	11.84
	debris	9.01	21.43	25.43	24.03	5.73	14.37
Co=0.5	Area-1	3.07	15.04	16.95	43.61	11.34	9.99
	Area-2	6.47	18.71	17.99	28.51	17.46	10.86
	debris	7.77	20.79	21.59	25.15	20.73	3.97
Co=1	Area-1	7.28	27.34	24.45	25.06	13.48	2.39
	Area-2	7.17	27.26	25.52	23.90	13.33	2.82
	debris	7.61	21.80	24.75	28.70	10.15	6.99

6.3.3 Effect of sliding distance on wear behavior of Al_{0.4}FeCrNiCo_x(x=0, 0.25, 0.5 and 1.0 mol) HEAs

Figure 6.10 (a) represents the average coefficient of friction of Al_{0.4}FeCrNiCo_x (x=0, 0.25, 0.5 and 1.0 mol) HEAs with varying sliding distance under constant wear condition of 10 N normal load, 1 m/s sliding speed. From the graph it is observed that the COF in case of Al_{0.4}FeCrNiCo_x (x=0, 0.25, 0.5 and 1.0 mol) HEAs at sliding condition of (1000 m, 1 m/s, 10 N) is 0.276, 0.282, 0.316, and 0.335 respectively. The COF under sliding condition of (4000 m, 1 m/s, 10 N) for Al_{0.4}FeCrNiCo_x (x=0, 0.25, 0.5, 1.0 mol) HEAs is 0.410, 0.421, 0.479, and 0.519 respectively. Therefore the percentage increase in COF value with increase in sliding distance from 1000 m to 4000 m for Al_{0.4}FeCrNiCo_x (x=0, 0.25, 0.5 and 1.0 mol) HEAs are 48.5%, 49.2%, 51.5%, and 54.9% respectively. The reason for the higher increase in the percentage of COF for x=1.0 mol HEA is due to the lowest value of hardness and strength which may cause more wear debris and as a result more rough surface. Therefore, higher value of COF.

Figure 6.10 (b) shows the variation of specific wear rate of Al_{0.4}FeCrNiCo_x (x=0, 0.25, 0.5 and 1.0 mol) HEAs with sliding distance. From the graph, it is observed that the specific wear rate occurs in two different regimes. In the first regime when sliding distance varies from 1000 m to

3000 m, the specific wear rate increases slowly. The specific wear rate of Co=0, Co=0.25, Co=0.5 and Co=1 HEAs under (1000 m, 1 m/s, 10 N) sliding condition is $2.289 \times 10^{-4} \text{ mm}^3/\text{Nm}$, $2.436 \times 10^{-4} \text{ mm}^3/\text{Nm}$, $3.003 \times 10^{-4} \text{ mm}^3/\text{Nm}$, and $3.817 \times 10^{-4} \text{ mm}^3/\text{Nm}$ respectively. The specific wear rate under (3000 m, 1 m/s, 10 N) sliding condition is $3.492 \times 10^{-4} \text{ mm}^3/\text{Nm}$, $3.697 \times 10^{-4} \text{ mm}^3/\text{Nm}$, $4.123 \times 10^{-4} \text{ mm}^3/\text{Nm}$, and $4.739 \times 10^{-4} \text{ mm}^3/\text{Nm}$ respectively. In the case of the second regime when sliding distance between 3000 m to 4000 m, the specific wear rate increases rapidly. The specific wear rate of Co=0, Co=0.25, Co=0.5 and Co=1 HEAs under (4000 m, 1 m/s, 10 N) sliding condition is $5.508 \times 10^{-4} \text{ mm}^3/\text{Nm}$, $6.501 \times 10^{-4} \text{ mm}^3/\text{Nm}$, $7.068 \times 10^{-4} \text{ mm}^3/\text{Nm}$, and $7.855 \times 10^{-4} \text{ mm}^3/\text{Nm}$ respectively.

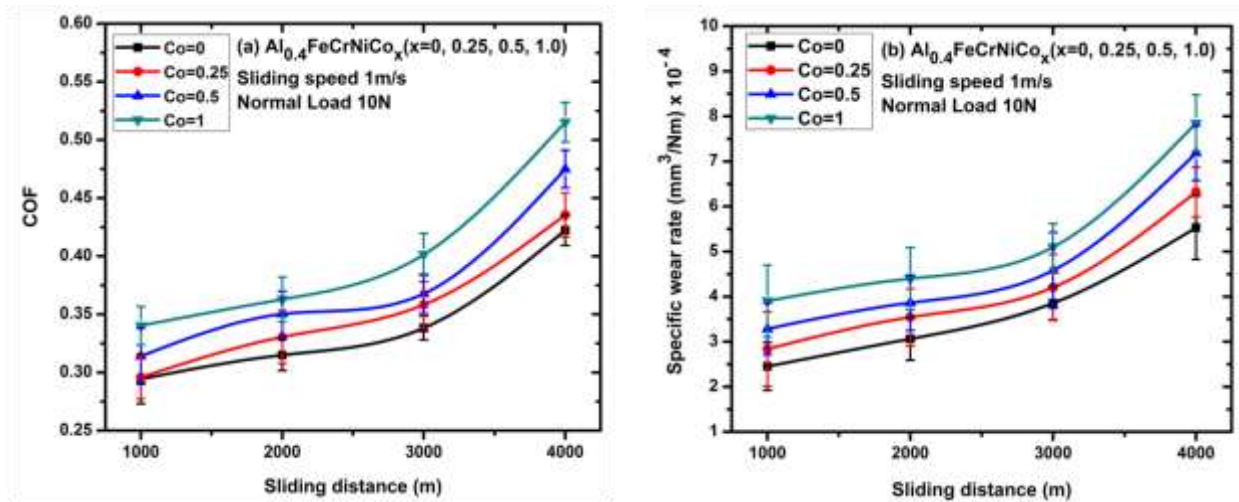


Fig. 6.10 Effect of variation in sliding distance on (a) coefficient of friction and, (b) specific wear rate of $\text{Al}_{0.4}\text{FeCrNiCo}_x$ ($x=0, 0.25, 0.5$ and 1.0 mol) HEAs

Therefore, the percentage change in specific wear rate of Co=0, Co=0.25, Co=0.5, and Co=1 HEA in first regime is 52.5%, 51.7%, 37.2%, and 24.1%. In second regime between, 3000 m to 4000 m. The percentage change in specific wear rate for Co=0, Co=0.25, Co=0.5, and Co=1 HEA is 57.7%, 75.8%, 71.4%, and 65.7% respectively.

6.3.3.1 Worn Surface and wear debris Analysis under sliding distance condition

Figure 6.11 shows the SEM micrograph of the worn surface, wear debris and distribution of wear debris diameter at the constant sliding condition of 4000 m sliding distance, 10 N normal load, and 1 m/s sliding speed for $\text{Al}_{0.4}\text{FeCrNiCo}_x$ ($x=0, 0.25, 0.5$ and 1.0 mol) HEAs. Figure 6.11 (a) shows the surface features after the wear test, that it reveals scratches, microgrooves, and material deformation along the sliding direction.

Due to delamination and cracks, thin flat, irregular, and multilayer flake type debris is generated as shown in Fig. 6.11 (b). The average diameter of wear debris of Co=0 HEA as calculated from SEM micrograph is $73.08\mu\text{m}$. Table 6.3 indicates the EDS results of worn surface and wear debris indicating the presence of oxygen on the worn surface which form oxide and may influence the loss of material. Therefore, the mode of wear is adhesion, plastic deformation, and delamination along with oxidative wear. Wu et al. [39] studied the wear behavior of $\text{Al}_x\text{CoCrCuFeNi}$ HEA and observed that delamination causes wear in ductile high entropy alloys.

Figure 6.11 (d, g and j) shows the SEM micrograph of the worn surface of Co=0.25, Co=0.5, and Co=1 HEAs. It reveals similar features as in the case of Co=0 HEA like scratches, microgrooves, cracks, and plastic deformation. The wear debris reveals thin, flat, irregular, and multilayer flake types which are generated due to crack and delamination as shown in Fig. 6.11 (e, h and k). The average debris diameter of Co=0.25, Co=0.5, and Co=1 HEAs are $93.58\mu\text{m}$, $68.67\mu\text{m}$, and $123.11\mu\text{m}$ respectively.

From Table 6.3, it is observed the changes in the atomic percentage of aluminium, iron, and nickel on the worn surface indicates that material is transferred between the high entropy pin sample and the counter-rotating disk, due to frictional heat generated during the sliding wear [178, 179]. It is noted that the presence of oxygen on the worn surface form oxide film which gives the lubricating effect and may decrease the material loss [182]. It is observed that the percentage of oxygen decreases with increase in cobalt content as listed in Table 6.3.

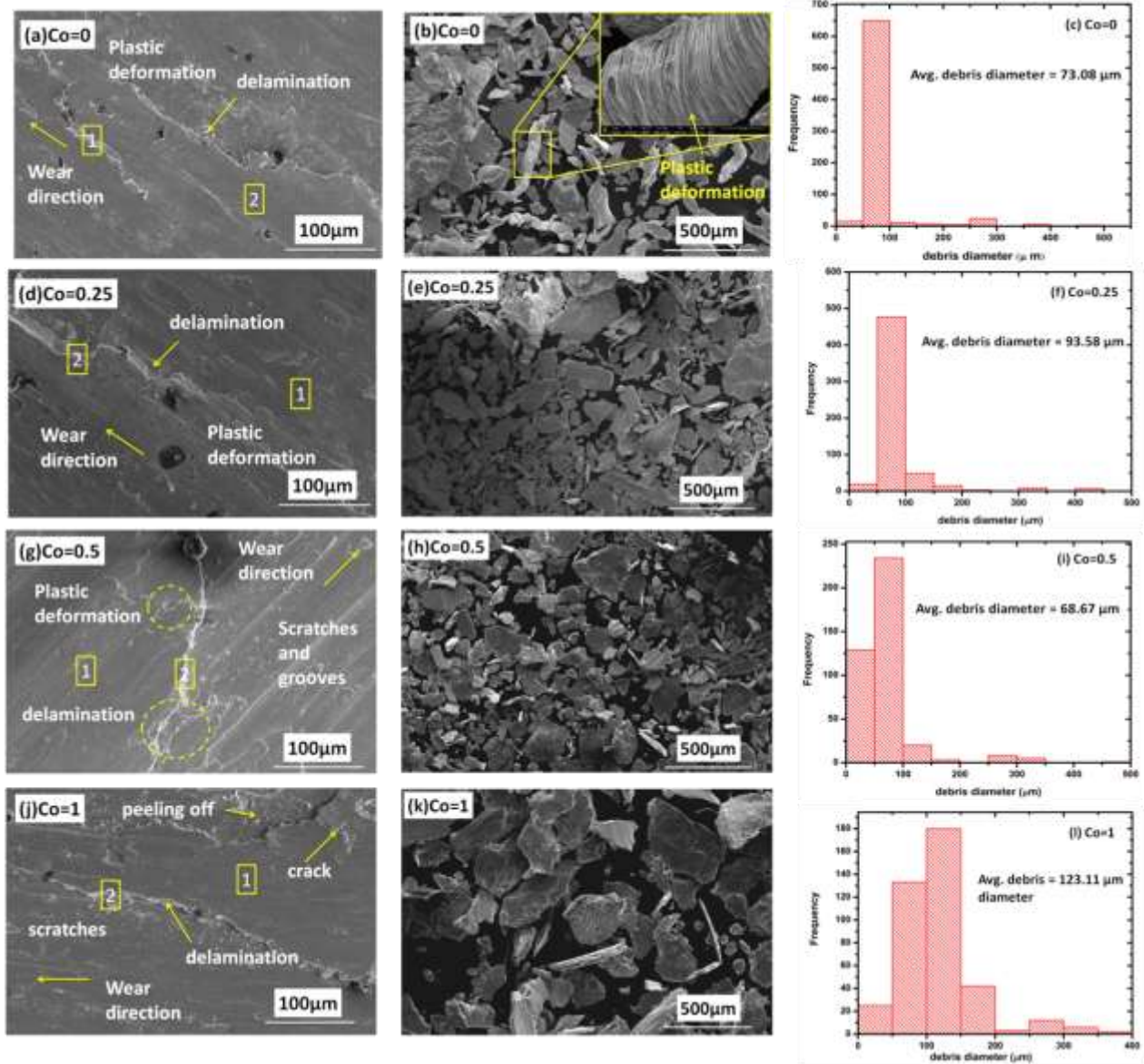


Fig. 6.11 SEM micrograph of worn surface, wear debris, and distribution of wear debris diameter of (a-c) Co=0 HEA, (d-f) Co=0.25 HEA, (g-i) Co=0.5 HEA and (j-l) Co=1 HEA.

Table 6.3 EDS results of worn surface and wear debris of $Al_{0.4}FeCrNiCo_x$ ($x=0, 0.25, 0.5$ and 1.0 mol) HEA produced under 4000 m sliding distance, 10 N normal load, and 1 m/s speed.

HEA	Region	Al%	Fe%	Cr%	Ni%	Co%	O%
Co=0	Area-1	1.18	12.21	16.32	65.47	-	3.36
	Area-2	1.55	9.67	28.67	33.18	-	26.93
	debris	4.70	12.83	16.40	33.18	-	32.88
Co=0.25	Area-1	7.45	28.36	28.36	25.95	6.90	2.98
	Area-2	10.10	18.02	21.01	31.51	4.51	14.85
	debris	4.60	14.40	20.21	44.10	3.46	13.23
Co=0.5	Area-1	8.26	22.28	20.81	26.48	9.42	12.75
	Area-2	7.92	19.28	19.81	31.48	8.42	13.9
	debris	6.74	19.34	21.83	38.66	8.52	4.92
Co=1	Area-1	7.67	23.65	22.29	21.38	22.13	2.88
	Area-2	5.69	20.45	19.66	22.58	19.68	11.94
	debris	4.90	14.64	15.99	30.96	12.41	21.10

Therefore, the specific wear rate of Co=0 HEA having higher oxygen content is lower than that of the Co=1 HEA which has lower oxygen content as shown in Fig. 6.10 (b). Another reason for the higher value of specific wear rate of Co=1 HEA is the lowest value of hardness among all HEAs.

6.3.4 X-ray photoelectron spectroscopy of $Al_{0.4}FeCrNiCo_{x=1}$ HEA under dry condition

Figure 6.12 (a-g) shows the x-ray photoelectron spectra (XPS) of the worn surface of $Al_{0.4}FeCrNiCo_{x=1}$ HEA obtained after the wear test under the dry sliding conditions of 1 m/s sliding speed, 1000 m sliding distance and 10 N normal load. All the XPS spectra were recorded after sputtering the few atomic layers of the worn surface by argon ion. The XPS spectra were analyzed by using the NIST open-access database and the literature.

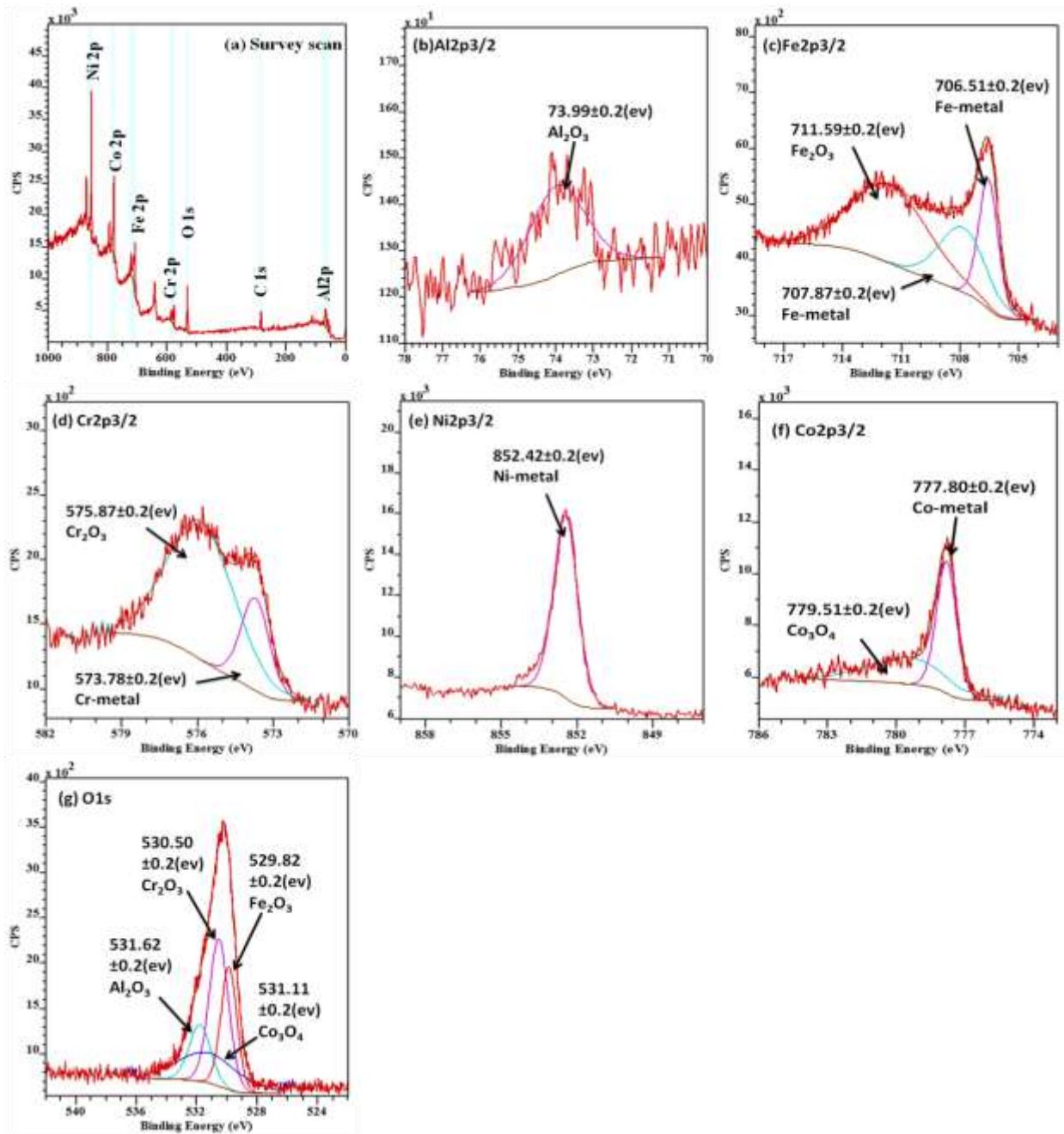


Fig. 6.12 XPS results of worn surface of Co=1 HEA tested at a constant wear condition of sliding speed of 1 m/s, sliding distance of 1000 m and normal load of 10N (a) survey spectra (b) Al₂p_{3/2} spectra (c) Fe₂p_{3/2} spectra (d) Cr₂p_{3/2} spectra (e) Ni₂p_{3/2} spectra (f) Co₂p_{3/2} spectra (g) O₁s spectra

Figure 6.12 (a) shows the survey spectra of worn surface indicating that the entire element presents in the binding energy range of (0 to 1000 eV). Figure 6.12 (b) shows the high-resolution XPS spectra of Al₂p_{3/2}, and the peak at a binding energy of 73.99±0.2 eV indicating the presence of Al₂O₃ oxide.

Figure 6.12 (c) shows the deconvoluted spectra of Fe₂p_{3/2} and the peak at a binding energy of 706.51±0.2 eV, 707.87±0.2 eV, and 711.59±0.2 eV associated with the pure metallic iron and Fe₂O₃ oxide. Figure 6.12 (d) shows the deconvoluted XPS spectra of Cr₂p_{3/3}, and the peaks at binding energy of 573.78±0.2 eV and 575.87±0.2 eV confirm the presence of pure metallic chromium and Cr₂O₃ oxide.

Figure 6.12 (e) shows the high-resolution XPS spectra of Ni₂p_{3/2} and the sharp peaks at a binding energy of 852.42±0.2 eV confirms the presence of pure metallic nickel without any oxide formation. Figure 6.12 (f) shows the deconvoluted XPS peaks of Co₂p_{3/3}, and the peaks at a binding energy of 777.80±0.2 eV, and 779.51±0.2 eV indicate the presence of pure metallic cobalt and Co₃O₄ oxide. Figure 6.12 (g) shows the deconvoluted XPS peaks of O_{1s}, and the binding energy associated with the peaks at 529.82±0.2 eV, 530.50±0.2 eV, 531.11±0.2 eV, and 531.62±0.2 eV, confirms the presence of Fe₂O₃, Cr₂O₃, Co₃O₄ and Al₂O₃ oxides on the worn surface of Co=1 HEA. Similar observations were also reported in the literature [77, 79].

Therefore the presence of Al₂O₃, Fe₂O₃, Cr₂O₃, and Co₃O₄ oxides on the worn surface of Co=1 HEA formed during the wear process act as the protective film or third body which may depend upon sliding velocity, normal load, and the environment [185]. It was reported that the oxide formed can protect or damage the sliding material depend upon thickness and composition of the oxide [181]. Generally, the metallic oxide causes high wear and intermediate friction, and the metallic iron causes severe adhesion [186].

6.4 Wear behavior of $\text{Al}_{0.4}\text{FeCrNiCo}_x$ ($x=0, 0.25, 0.5$ and 1.0 mol) HEAs under oil condition

6.4.1 Effect of Sliding Speed on wear behavior of $\text{Al}_{0.4}\text{FeCrNiCo}_x$ ($x=0, 0.25, 0.5$ and 1.0 mol) HEAs under lubricating oil condition

Figure 6.13 (a) and 6.13 (b) shows the variation of coefficient of friction (COF) and specific wear rate of $\text{Al}_{0.4}\text{FeCrNiCo}_x$ ($x=0, 0.25, 0.5$ and 1.0 mol) HEAs with varying sliding speed tested for a constant sliding distance of 1000 m under a normal load of 10 N and under oil lubrication condition. From Fig. 6.13 (a) it is observed that COF fluctuates in between 0.065 to 0.060 in case of $\text{Co}=0$ HEA. The initial decrease in COF in case of $\text{Co}=0$ HEA is due to the formation of the oil film in between the mating surfaces which keeps the two contacting surfaces separated against the normal load. In case of $\text{Co}=0.25$ HEA, the COF increases rapidly from 0.064 to 0.086 as sliding speed increase from 0.5 m/s to 1 m/s and afterward decreases gradually from 0.086 to 0.068 with an increase in sliding speed from 1 m/s to 2 m/s.

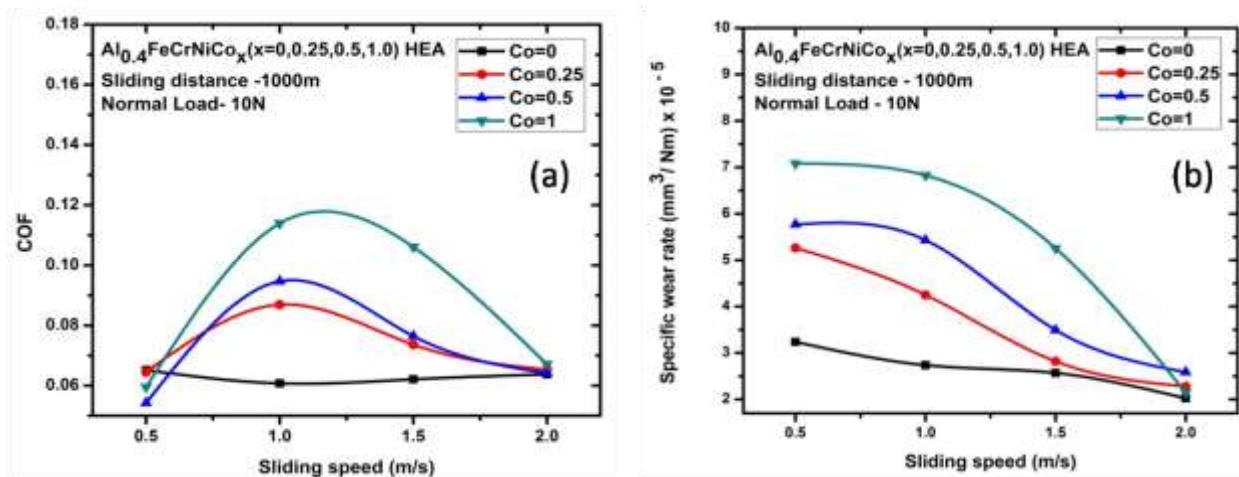


Fig. 6.13 Variation of (a) coefficient of friction and (b) specific wear rate of $\text{Al}_{0.4}\text{FeCrNiCo}_x$ ($x=0, 0.25, 0.5$ and 1.0 mol) HEAs under oil lubrication with varying sliding speed

The gradual decrease in COF values from 0.086 to 0.068 is due to formation of a continuous oil film at higher speed which reduces the chance of metal to metal contacts. In case of $\text{Co}=0.5$ and $\text{Co}=1$ HEA COF initially increases from 0.054 to 0.094 and from 0.059 to 0.113 as sliding speed increases from 0.5 m/s to 1 m/s, respectively. The reason behind the increase in COF is due to

breakage of the oil film at the interface which in turn due to the entrapment of wear debris. It is observed that on further increase in sliding speed, from 1 m/s to 2 m/s, the COF value decreases from 0.094 to 0.064 and from 0.113 to 0.067 in case of Co=0.5 and Co=1 HEAs, respectively. It is because, at higher sliding speed, under boundary lubrication condition, the tribo film is more effective than at lower speed.

Figure 6.13 (b) represents the variation of specific wear rate of $Al_{0.4}FeCrNiCo_x$ ($x=0, 0.25, 0.5$ and 1.0 mol) HEAs with varying sliding speed and at the constant wear condition of 1000 m sliding distance, and 10 N normal load. It is seen that as sliding speed increases from 0.5 m/s to 2 m/s, the specific wear rate of all HEA samples decreases. The higher specific wear rate at lower sliding speed is because of the fact that at lower sliding speed the lubricating oil film is not adequate and there is more metal to metal contact. The specific wear rate decreases from $3.240 \times 10^{-5} \text{ mm}^3/\text{Nm}$ to $2.023 \times 10^{-5} \text{ mm}^3/\text{Nm}$ in case of Co=0 HEA, i.e., a 37.56 % decrease in specific wear rate with an increase in sliding speed from 0.5 m/s to 2 m/s. In case of Co=0.25 HEA, the specific wear rate decreases from $4.833 \times 10^{-5} \text{ mm}^3/\text{Nm}$ to $2.279 \times 10^{-5} \text{ mm}^3/\text{Nm}$, i.e., a 52.84 % decrease in specific wear rate with an increase in sliding speed from 0.5 m/s to 2 m/s. In case of Co=0.5 HEA, the specific wear rate decreases from $5.770 \times 10^{-5} \text{ mm}^3/\text{Nm}$ to $2.588 \times 10^{-5} \text{ mm}^3/\text{Nm}$, i.e., a 55.14 % decrease in specific wear rate with an increase in sliding speed from 0.5 m/s to 2 m/s. In case of Co=1 HEA, the specific wear rate decreases from $7.080 \times 10^{-5} \text{ mm}^3/\text{Nm}$ to $2.149 \times 10^{-5} \text{ mm}^3/\text{Nm}$, i.e. 69.64 % decrease in specific wear rate with an increase in sliding speed from 0.5 m/s to 2 m/s.

6.4.2 Effect of sliding distance on wear behavior of $Al_{0.4}FeCrNiCo_x$ ($x=0, 0.25, 0.5$ and 1.0 mol) HEAs under lubricating oil condition.

Figure 6.14 (a) and 6.14 (b) shows the variation of coefficient of friction and specific wear rate of $Al_{0.4}FeCrNiCo_x$ ($x=0, 0.25, 0.5$ and 1.0 mol) HEAs with varying sliding distance tested under the constant sliding speed of 1 m/s and a normal load of 10 N and under oil lubrication condition. It is observed that as sliding distance varies from 1000 m to 4000 m, the COF varies in the range of 0.060 to 0.143 and follows similar trends for all HEAs. According to Fig. 6.14 (a), Co=1 HEA, has maximum COF value in every case, and this is due to a lower hardness value of Co=1

HEA, among all HEA samples. For Co=1 HEA, COF initially decreases from 0.10 to 0.096 as sliding distance increases from 1000 m to 2000 m. The decrease in COF value is due to the removal of frictional heat and debris by lubricating oil which smoothens the wear process. Afterward in between 2000 m and 4000 m, the COF start increasing from 0.096 to 0.143 in case of Co=1 HEA. The increase in COF after 2000 m is due to the presence of debris in oil between the disc and sample. It results in breakage of lubricating oil film and increases the metal to metal contacts between the surfaces and therefore, COF increases.

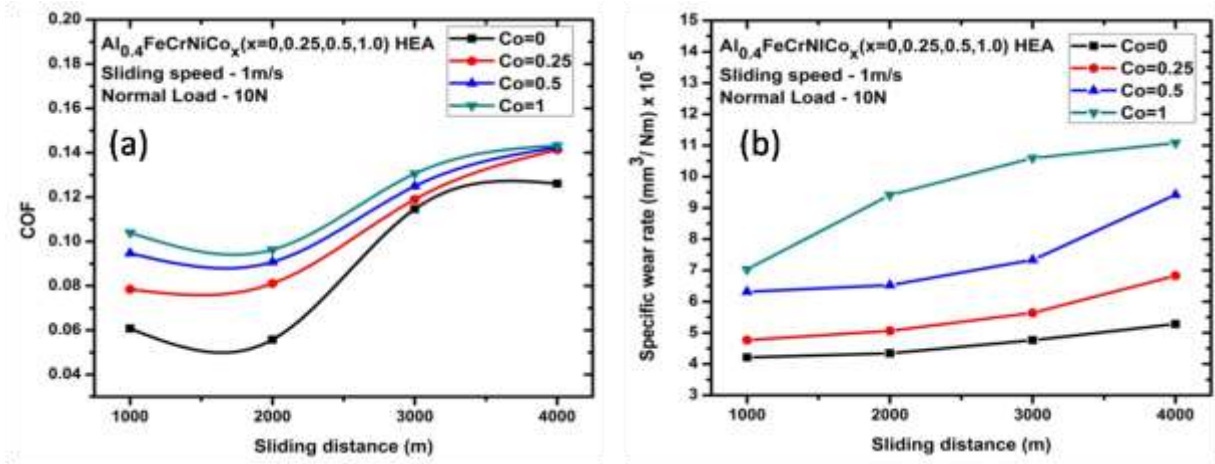


Fig. 6.14 Variation of (a) coefficient of friction and (b) specific wear rate of $\text{Al}_{0.4}\text{FeCrNiCo}_x$ ($x=0, 0.25, 0.5$ and 1.0 mol) HEAs under oil lubrication with varying sliding distance

Figure 6.14 (b) shows the variation of specific wear rate of $\text{Al}_{0.4}\text{FeCrNiCo}_x$ ($x=0, 0.25, 0.5$ and 1.0 mol) HEAs with varying sliding distance under oil lubrication. It is observed that as sliding distance increases from 1000 m to 4000 m, the specific wear rate increases. For Co=0 HEA, the specific wear rate increases from $4.215 \times 10^{-5} \text{ mm}^3/\text{Nm}$ to $5.280 \times 10^{-5} \text{ mm}^3/\text{Nm}$ i.e. a 25.2 % increase in value when the sliding distance increases from 1000 m to 4000 m. For Co=0.25 HEA, the specific wear rate increases from $4.766 \times 10^{-5} \text{ mm}^3/\text{Nm}$ to $6.830 \times 10^{-5} \text{ mm}^3/\text{Nm}$ i.e. a 30.2 % increase in value when the sliding distance increases from 1000 m to 4000 m. For Co=0.5 HEA, the specific wear rate increases from $6.315 \times 10^{-5} \text{ mm}^3/\text{Nm}$ to $9.423 \times 10^{-5} \text{ mm}^3/\text{Nm}$ i.e. a 32.9 % increase in value and in case of Co=1 HEA, the specific wear rate increases from $7.032 \times 10^{-5} \text{ mm}^3/\text{Nm}$ to $11.080 \times 10^{-5} \text{ mm}^3/\text{Nm}$ i.e. a 36.5 % increase in value when sliding distance

increases from 1000 m to 4000 m, respectively. The maximum value of the specific wear rate in case of Co=1 HEA among all sample is due to its lower value of hardness.

6.4.3 Effect of Normal Loads on wear behavior of $\text{Al}_{0.4}\text{FeCrNiCo}_x$ ($x=0, 0.25, 0.5$ and 1.0 mol) HEAs under lubricating oil condition

Figure 6.15 (a) and 6.15 (b) show the variation of coefficient of friction and specific wear rate of $\text{Al}_{0.4}\text{FeCrNiCo}_x$ ($x=0, 0.25, 0.5$ and 1.0 mol) HEAs with varying normal loads tested for a constant sliding distance of 1000 m and at a sliding speed of 1 m/s under oil lubrication respectively. It is observed from Fig. 6.15 (a) that as normal load increases from 5 N to 20 N, the coefficient of friction also increases in case of all $\text{Al}_{0.4}\text{FeCrNiCo}_x$ ($x=0, 0.25, 0.5$ and 1.0 mol) HEAs respectively.

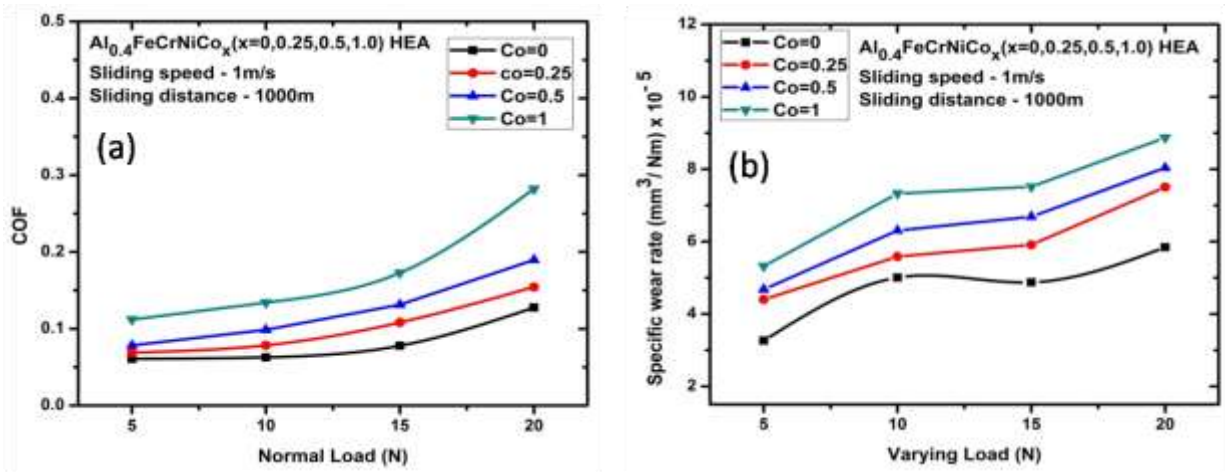


Fig. 6.15 Variation of (a) coefficient of friction and (b) specific wear rate of $\text{Al}_{0.4}\text{FeCrNiCo}_x$ ($x=0, 0.25, 0.5$ and 1.0 mol) HEAs under oil lubrication with varying normal load.

The increase in coefficient of friction with the increase in load is mainly due to an increase in contact area between the rotating disc and the HEA pin samples which requires more energy to break the contact and hence the COF value increases.

Figure 6.15 (b) shows the variation of specific wear rate with normal loads, and it is observed that as normal load increases, the specific wear rate also increases in three different regimes in

case of $Al_{0.4}FeCrNiCo_x$ ($x=0, 0.25, 0.5$ and 1.0 mol) HEAs. In the first regime as load increases from 5 N to 10 N, the specific wear rate increases rapidly in case of all HEAs and it is noted that the $Co=1$ HEA exhibits maximum specific wear rate among all HEAs. In the second regime, as the load increases from 10 N to 15 N, the specific wear rate varies gradually in case of all HEAs. In the third regime, as the load increases from 15 N to 20 N, the specific wear rate again increases in case of all HEAs. The reason behind these particular regimes with the increases in loads is mainly due to the variation in real contact area between the mating surfaces. As the load increases, more metal to metal contact occurs, and this leads to more material loss. As a result, the specific wear rate for $Co=0$ HEA increases from $3.262 \times 10^{-5} \text{ mm}^3/\text{Nm}$ to $5.843 \times 10^{-5} \text{ mm}^3/\text{Nm}$, i.e., 79.12 % increase in value when normal load increases from 5 N to 20 N. For $Co=0.25$ HEA the specific wear rate increases from $3.572 \times 10^{-5} \text{ mm}^3/\text{Nm}$ to $7.505 \times 10^{-5} \text{ mm}^3/\text{Nm}$, i.e., 110.10 % increase in value as the normal load increases from 5 N to 20 N. Similarly, in the case of $Co=0.5$ HEA, the specific wear rate increases from $3.768 \times 10^{-5} \text{ mm}^3/\text{Nm}$ to $8.040 \times 10^{-5} \text{ mm}^3/\text{Nm}$, i.e., 113.37 % increase in value and in case of $Co=1$ HEA, the specific wear rate increases from $4.124 \times 10^{-5} \text{ mm}^3/\text{Nm}$ to $8.871 \times 10^{-5} \text{ mm}^3/\text{Nm}$, i.e., 115.10 % increase in value when normal load increases from 5 N to 20 N. The reasons behind 115.10 % increase in the value of specific wear rate in case of $Co=1$ HEA. First, it is due to lower value of microhardness in case of $Co=1$. Second, due to lower value of oxygen content on the worn surface in case of $Co=1$ HEA as listed in Table 6.4 indicates lesser protective tribo film in comparison to other high entropy alloy specimen during wear process and hence lesser protectiveness in case of $Co=1$ HEA and more will be the material loss.

6.4.4 Worn surface and wear mechanism under lubricating oil condition

Figure 6.16 (a-d) shows the SEM micrographs of worn surfaces of $Al_{0.4}FeCrNiCo_x$ ($x=0, 0.25, 0.5$ and 1.0 mol) HEAs, after the wear test at the high magnification, with constant wear condition of (1000 m, 10 N, 1 m/s) under oil lubrication. The corresponding EDS results of a selected area of $Al_{0.4}FeCrNiCo_x$ ($x=0, 0.25, 0.5$ and 1.0 mol) HEAs are listed in Table 6.4. The micrograph was obtained after degreasing the oiled surface in the acetone bath. Figure 6.16 (a-d) illustrates the surface characteristic generated while sliding the HEA pin samples against the rotating disc under lubrication. The worn surface looks very smooth and indicating polishing of the worn surface. Figure 6.16 (a) indicate the SEM micrograph of $Co=0$ HEA and shows fine

scratches and grooves which are parallel to the sliding direction. It is also noted that the worn surface does not have any cracks, spalling, or damage surface. The specific wear rate of Co=0 HEA is minimum and that of Co=1 HEA is maximum among all HEAs as illustrated in Fig. 6.13 (b), Fig. 6.14 (b) and Fig. 6.15 (b) and this may be due to following reasons. First reason, the minimum specific wear rate of Co=0 HEA is due to the formation of a stable or unbroken oil film which minimizes the heating and washes away the debris generated during the wear process resulting in lower material loss. On the other hand, the maximum specific wear rate exhibited by Co=1 HEA, is due to the breakdown of the oil film. The unstable oil films or breakage of oil films is due to the presence of loose wear debris in between the mating surfaces, which leads to scratches, grooves and plastic deformation of the material as shown in Fig. 6.16 (d).

Table 6.4 EDS result of worn surface of $Al_{0.4}FeCrNiCo_x$ (x=0, 0.25, 0.5 and 1.0 mol) HEAs at (1000m, 10N, 1m/s) wear condition under oil lubrication.

HEA	Region	Al%	Fe%	Cr%	Ni%	Co%	O%
Co=0	Area-1	5.85	25.47	26.27	21.39	-	18.23
	Area-2	7.49	22.88	22.60	22.38	-	21.22
Co=0.25	Area-1	7.54	18.42	22.98	18.19	5.24	27.62
	Area-2	8.47	22.0	25.53	22.38	6.24	15.38
Co=0.5	Area-1	6.60	19.58	20.02	19.90	11.01	22.89
	Area-2	8.13	20.12	24.22	20.68	11.81	15.04
Co=1	Area-1	5.20	19.21	18.39	24.41	20.68	12.11
	Area-2	5.75	20.46	20.63	24.48	21.70	6.99

The generated grooves or unsmooth surface provide a side passage for the lubricant to flow out. The side leakage causes reduction or complete collapse of the oil film or breakdown of the oil film or the generation of an unstable oil film [187, 188]. So more metal to metal contacts occur and this increases the material loss. The second reason is due to the higher hardness of Co=0 HEA among all HEA samples. According to Archard wear equation, hardness is inversely proportional to material loss [174]. Therefore Co=0 HEA has the highest hardness among all HEA samples. This means that higher the hardness lower will be the material loss. The third

reason is might be due to the presence of oxygen on the worn surface of Co=0 HEA as listed in Table 6.4. It is observed that the oxygen content decreases from 19.72 at.% to 9.55 at.% (average value of area-1 and area-2) with the addition of cobalt from x=0 to 1.0 mol. It is known that the presence of oxygen on the worn surface forms a protective tribo layer and helps in reducing the material loss [181]. It is also noted that by the addition of cobalt, microstructural differences arise within the HEAs as shown in Fig. 5.11 (a-d). As the cobalt content increases, the amount of precipitate is observed to decrease in the microstructure (Fig. 5.11(a-d)). The EDS results as listed in Table 5.4 indicate that these precipitates are rich in aluminium and nickel. It is reported that these precipitate help in increasing the hardness of the alloy and hence decrease the material loss during wear. Therefore, with increasing cobalt content, the precipitate decreases and decreases the hardness as a result increases the wear [110, 111].

Figure 6.16 (b-d) shows the SEM micrographs of the worn surface of Co=0.25, Co=0.5, and Co=1 HEAs, respectively. The micrographs have illustrated the similar features as in the case of Co=0 HEA, but form deep scratches and grooves which are parallel to the sliding direction. The micrographs also reveal that there are some regions where peeling off, flow of material and formation of cracks occur in a direction perpendicular to sliding direction. Similar features are also observed in Fig. 6.16 (e-h) which shows the 3D profile of the worn surface of $Al_{0.4}FeCrNiCo_x$ (x=0, 0.25, 0.5 and 1.0 mol) HEAs after the wear.

The 3D profile also confirms that the scratches and grooves along with the material flow are parallel to the sliding direction during the wear process. The deep scratches and grooves in case of Co=1 HEA is because of two reasons. First, as cobalt content increases the hardness of HEA sample decreases and the second reason is due to the breakdown of the oil film. It occurs when the wear debris gets stuck in between the contacting surfaces and creates deep scratches as indicated in Fig. 6.16 (c, d) and Fig. 6.16 (g, h). It is observed from the Table 6.4 that as cobalt content increases from x=0 to 1 mol, the oxygen content decreases.

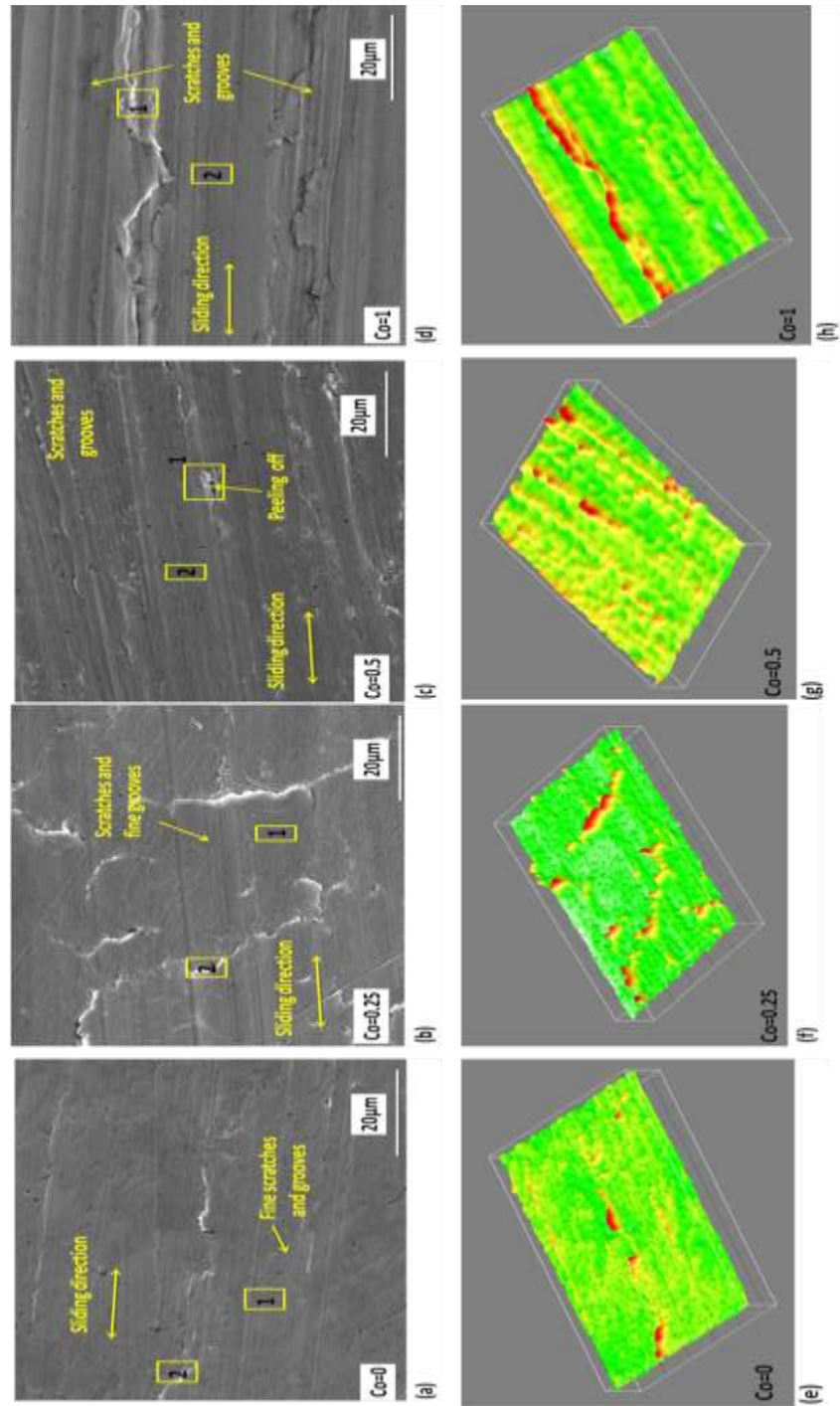


Fig. 6.16 (a-d) SEM micrographs, (e-h) 3D surface profile of worn surface of $\text{Al}_{0.4}\text{FeCrNiCo}_x$ ($x=0, 0.25, 0.5$ and 1.0 mol) HEAs at constant wear condition of (1000m, 10N, 1m/s) under oil lubrication.

Therefore, the protective nature of the tribofilm is lowered in the case of Co=1 HEA than in case of Co=0 HEA. The XPS spectra confirm that the oxide formed in Co=1 HEA is mainly consists of Al_2O_3 , Fe_2O_3 and Cr_2O_3 as seen in Fig. 6.16. Hence it may be concluded that the mode of wear is the combined effect of adhesive, and abrasive wear along with the third body and plastic flow of material.

6.4.5 X-ray Photoelectron Spectroscopy of $\text{Al}_{0.4}\text{FeCrNiCo}_{x=1}$ HEA under lubricating oil condition

Figure 6.17 (a-h) shows the XPS spectra of the worn surface of $\text{Al}_{0.4}\text{FeCrNiCo}_{x=1}$ HEA, after the wear test at the constant sliding condition of (1000 m, 10 N, 1 m/s) under oil lubrication. Before the examination, the sample was properly cleaned and degreased with acetone by ultrasonicing for 10 to 15 min and then dried. The XPS spectra were recorded after argon ion etching the surface with few atomic layers. Figure 6.17 (a) shows the XPS survey spectra in the binding energy range from 0 to 1000 eV, which includes the entire element present in the $\text{Al}_{0.4}\text{FeCrNiCo}_{x=1}$ HEA along with carbon and oxygen. Figure 6.17 (b-h) illustrate the deconvoluted XPS spectra of O1s, Al2p, Fe2p, Cr2p, Ni2p, Co2p, and C1s, respectively. The deconvoluted XPS spectra of O1s in Fig. 6.17 (b) indicate the presence Cr_2O_3 , Fe_2O_3 , and Al_2O_3 oxides at the binding energies of 529.90 ± 0.2 eV, 530.33 ± 0.2 eV, and 531.42 ± 0.2 eV. Figure 6.17 (c) shows the XPS spectra of Al2p_{3/2} and the deconvoluted peak at the binding energy of 72.10 ± 0.2 eV represent presence of pure Al metal, and the peaks at 73.85 ± 0.2 eV, and 74.90 ± 0.2 eV, represents Al_2O_3 . Figure 6.17(d) indicate the deconvoluted peak of Fe2p_{3/2} and the peaks at the binding energies of 706.40 ± 0.2 eV, 707.51 ± 0.2 eV, represent the presence of pure Fe metal and the peak at 711.21 ± 0.2 eV represents Fe_2O_3 .

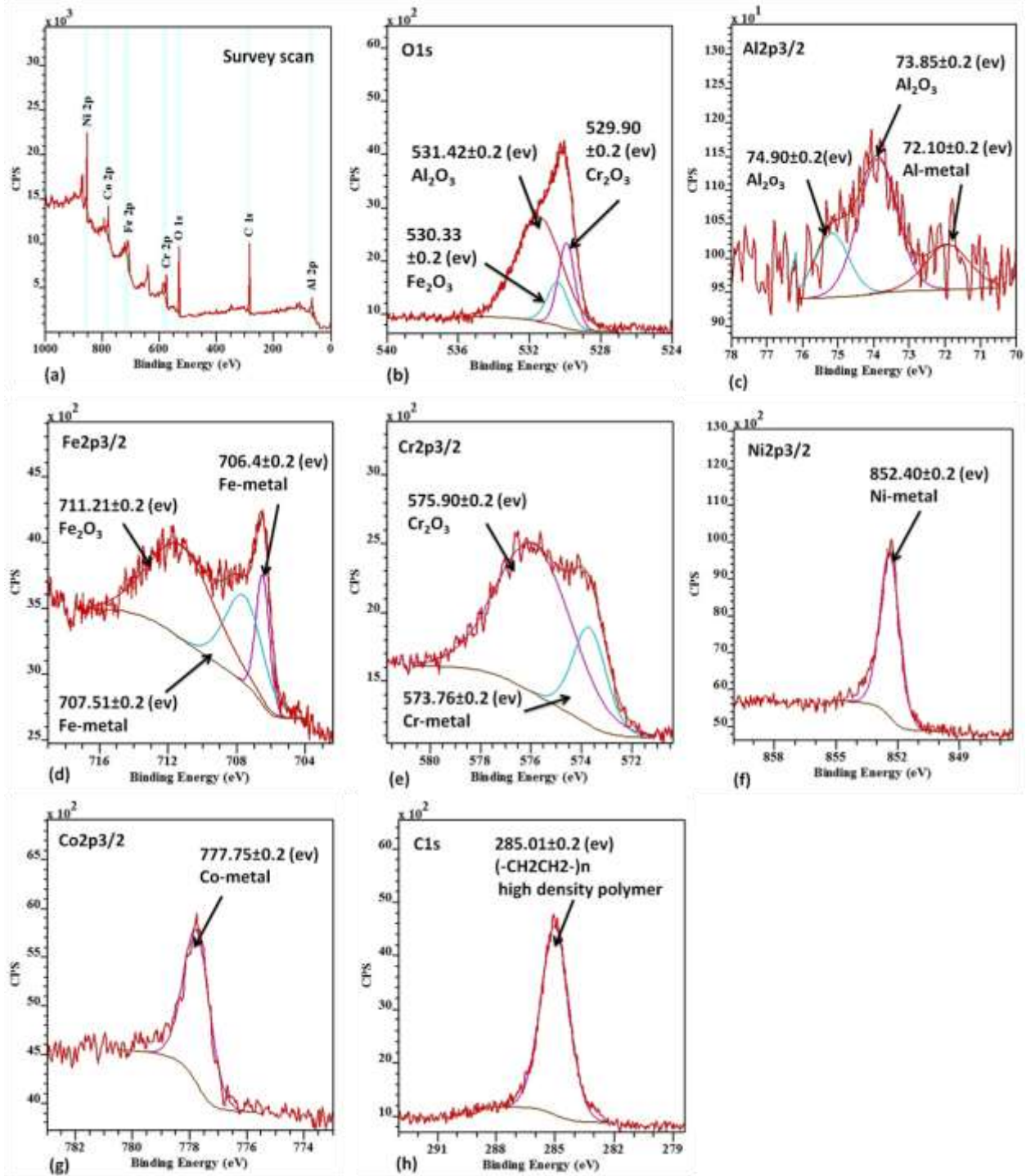
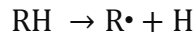


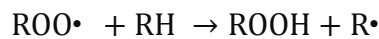
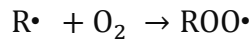
Fig. 6.17 X-ray photoelectron spectra of the worn surface of $\text{Al}_{0.4}\text{FeCrNiCo}_{x=1}$ HEA (a)survey scan, (b) O1s spectra, (c) Al2p spectra, (d) Fe2p spectra, (e) Cr2p spectra, (f) Ni2p spectra, (g) Co2p spectra, (h) C1s spectra

Figure 6.17(e) shows the XPS spectra of Cr2p3/2 and the deconvoluted peaks at the binding energies of 573.76±0.2 eV, and 575.90±0.2 eV indicate the presence of pure Cr metal and Cr₂O₃. Figure 6.17(f) and 6.17(g) represent the XPS spectra of Ni2p3/2 and Co2p3/2, respectively and the peaks at the binding energies of 852.40±0.2 eV, and 777.75±0.2 eV represent the presence of pure Ni and Co metal. Figure 6.17 (h) shows the XPS spectra of C1s at 285.01±0.2 eV representing the presence of high molecular weight polymer like (-CH₂CH₂-)_n. Its presence might be due to the contamination during ultrasonication of the HEA sample with acetone [189] or due to the formation of (alcoholic or ketone) group [190] by the thermal reaction of hydrocarbons present in the lubricating oil, which take place in four steps as follows. Similar findings have also been reported by Bhushan et al.[190, 191].

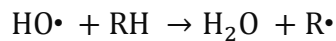
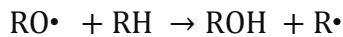
Step 1: Initiation



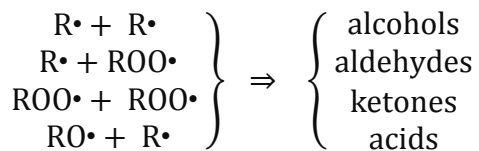
Step 2: Propagation



Step 3: Branching



Step 4: Termination



Therefore, during the wear process under oil lubricating condition, Al₂O₃, Fe₂O₃, and Cr₂O₃ oxide gets formed on the worn surface of Al_{0.4}FeCrNiCo_{x=1} HEA. This is because according to

the Ellingham diagram, the Gibbs free energy change for oxidation reaction show increasing trends $\text{Al}_2\text{O}_3 < \text{Cr}_2\text{O}_3 < \text{Fe}_2\text{O}_3 < \text{NiO} < \text{CoO}$. Therefore, Al_2O_3 , Cr_2O_3 , and Fe_2O_3 oxides have most negative values and have tendencies to form oxides even at room temperature. These oxides may decrease the material loss by providing a protective film or increase the material loss depending upon the sliding speed, normal load, environment, and film thickness [192]. Also, there is the presence of high molecular weight polymer or alcoholic group which may arise due to thermal reaction with hydrocarbon present in the lubricating oil or due to contamination during ultrasonication of high entropy samples in the acetone bath after the wear test.

6.5 Comparison with reported work

Tong et al. [34] have studied the wear behavior of $\text{Al}_x\text{CoCrCuFeNi}$ ($x = 0$ to 3.0) HEAs synthesized by arc melting in vacuum at 0.01 atm. The wear test is conducted on a pin-on-belt tribo-meter under different loads of 9.8N and 29.4N without any lubrication. A test pin of 8 mm diameter is used with a Al_2O_3 counter belt of 149 μm mesh, and a belt sliding speed of 0.5 m/s is maintained during the test. It has been observed that with increase in aluminium content the hardness and wear resistance increases due to transformation of FCC phase to BCC phase.

Du et al. [65] have studied the wear behavior of $\text{Al}_{0.25}\text{CoCrFeNi}$ HEA at various temperatures from room to 600°C. It is observed that on increasing the temperature, the wear rate increases due to high temperature softening of the samples. The dominant wear mechanism of the HEA changed from abrasive wear at room temperature to delamination wear at 200°C, delamination and oxidative wear at 300°C and became completely oxidative above 300°C. Moreover, the adhesive wear existed concomitantly below 300°C.

Chen et al. [66] have studied the wear behavior of $\text{Al}_{0.6}\text{CoCrFeNi}$ HEA in ambient air, deionized water, simulated acid rain, and simulated seawater conditions. They have observed that the wear rate of the as-cast HEA in the ambient air condition is significantly higher than that in any of the liquid environments. The wear resistance in seawater is superior to that in ambient air, deionized water, and acid rain. The dominant wear mechanism in the ambient air condition and deionized water is observed to be abrasive wear, delamination wear, and oxidative wear. By contrast, the wear mechanism in acid rain and seawater is mainly corrosion wear, adhesive wear, abrasive wear, and oxidative wear.

In the present study the wear behavior of $\text{Al}_{0.4}\text{FeCrNiCo}_x$ ($x = 0, 0.25, 0.5, \text{ and } 1.0$ mol) HEAs are studied under dry and engine oil conditions against a EN31 steel counter body. It is observed that the specific wear rate under dry condition, in all sliding conditions is higher than the wear under lubricating oil condition. The wear mechanism, in case of dry condition is observed to be the combined action of adhesive wear, plastic deformation, delamination and oxidation. The wear mechanism in case of lubricating oil condition is the combined action of adhesive and abrasive wear along with third body wear, and plastic flow of material.

Chapter summary

This chapter includes.

- Wear behavior of $\text{Al}_{0.4}\text{FeCrNiCo}_x$ ($x=0, 0.25, 0.5, 1.0$ mol) HEAs under dry sliding condition.
- Wear behavior of $\text{Al}_{0.4}\text{FeCrNiCo}_x$ ($x=0, 0.25, 0.5, 1.0$ mol) HEAs under oil lubricating condition.
- Worn surface and wear debris analysis of $\text{Al}_{0.4}\text{FeCrNiCo}_x$ ($x=0, 0.25, 0.5, 1.0$ mol) HEAs after dry and oil lubricating condition.

In the next chapter, experiment results were summerizes and putting suggestion for future work.

Conclusions and scope for future work

Based on the experimental work on Synthesis, and characterization of $Al_xFe_{1.5}CrMnNi_{0.5}$ ($x = 0.3$ and 0.5) high entropy alloys through mechanical milling and conventional sintering, and air jet erosion study of $Al_xFe_{1.5}CrMnNi_{0.5}$ ($x = 0.3$ and 0.5). Synthesis, and characterization of as-casted and homogenized $Al_{0.4}FeCrNiCo_x$ ($x = 0, 0.25, 0.5$ and 1.0 mol) HEAs through arc melting route. Wear behavior of $Al_{0.4}FeCrNiCo_x$ ($x = 0, 0.25, 0.5$ and 1.0 mol) HEAs under dry and oil lubricating condition. Following conclusion can be drawn.

7.1 Present research work can be summarized as follows

1. Thermodynamically $Al_xFe_{1.5}CrMnNi_{0.5}$ ($x = 0.3$ and 0.5 mol) HEAs satisfy the phase stability criterion.
2. After 20 hrs of milling the major phase is observed to be of BCC structure and the minor phase is observed to be of FCC structure.
3. DSC analysis has shown an exothermic peak at 537.0 °C in case of $Al_{0.5}Fe_{1.5}CrMnNi_{0.5}$ HEA, and an endothermic peak at 935.1 °C in case of the $Al_{0.3}Fe_{1.5}CrMnNi_{0.5}$ HEA.
4. After sintering $Al_xFe_{1.5}CrMnNi_{0.5}$ ($x = 0.3$ and 0.5 mol) HEAs in air and vacuum atmosphere BCC, B2, FCC and $Cr_5Fe_6Mn_8$ phases got formed.
5. Air sintered HEAs have been observed to exhibit better hardness and yield strength than vacuum sintered HEAs.
6. Erosion at 45° impingement angle is found to be higher than erosion at 90° angle.
7. Thermodynamically $Al_{0.4}FeCrNiCo_x$ ($x = 0, 0.25, 0.5$ and 1.0 mol) HEAs satisfies phase stability criterion.
8. In as cast HEA the transformation of FCC+BCC to FCC phase occurs and BCC phase decreases from 16.5% to 0%, with addition of cobalt from $x = 0$ to 1 mol.

9. Microhardness, compressive yield strength and thermal conductivities of as-cast HEAs decrease from 253.6 HV to 155.6 HV, 965.22 MPa to 233.37 Mpa, and 4.87 W/mK to 2.674 W/mK, respectively in case of $\text{Al}_{0.4}\text{FeCrNiCo}_x$ ($x=0, 0.25, 0.5$ and 1.0 mol) HEAs
10. Homogenized $\text{Al}_{0.4}\text{FeCrNiCo}_x$ ($x=0, 0.25, 0.5$ and 1.0 mol) HEAs show the formation of FCC+BCC, FCC, and B2 phases and BCC phase content decreases from 91.5% to 0% with the addition of cobalt from 0 to 1.0 mol.
11. The microhardness and room temperature compressive yield strength for homogenized $\text{Al}_{0.4}\text{FeCrNiCo}_x$ ($x=0, 0.25, 0.5$ and 1.0 mol) HEAs decreases from 377.7 HV to 199.5 HV and 1169.35 MPa to 57.63 Mpa, respectively.
12. The Co=1 HEA shows a maximum specific wear rate under all wear conditions tested under dry situation and the wear mechanism is observed to be of adhesive type along with oxidation, plastic deformation, and delamination.
13. XPS analysis confirms the formation of Al_2O_3 , Fe_2O_3 , Cr_2O_3 , and Co_3O_4 oxides on the worn surface in case of Co=1 HEA under dry condition.
14. The Co=1 HEA also shows maximum specific wear rate under all wear conditions tested under oil lubrication and the wear mechanism observed to be of adhesive, abrasive, three body type along with oxidation and plastic flow of material.
15. XPS analysis confirms the formation of Al_2O_3 , Fe_2O_3 , and Cr_2O_3 oxides along with high molecular weight polymers or alcoholic groups on the worn surface of Co=1 HEA for the wear test under oil lubrication condition.

7.2 Scope for future Work

Based on the present experimental work following research work can be performed in future.

1. The detailed study on electrical and magnetic property of proposed high entropy can be conducted.
2. The detailed study on machineability and weldability of proposed high entropy can be conducted.
3. Oxidation behavior of proposed high entropy alloys may be performed to suggest its application in high temperature.
4. Corrosion resistance of proposed high entropy alloys may be performed at different electrolytes and concentration
5. Rolling operation on the proposed high entropy alloys can be performed under different temperatures.

References

- [1] B. S. Murty, J. W. Yeh, S. Ranganathan, *High-Entropy Alloys*, Elsevier, London, 2014.
- [2] M. C. Gao, J. W. Yeh, P. K. Liaw, Y. Zhang, *High-entropy alloys Fundamentals and Applications*, Springer, Switzerland, 2016.
- [3] J.W. Yeh, *Physical Metallurgy of High-Entropy Alloys*, *Jom.*, 2015, 67, 2254–2261.
- [4] O. Maulik, D. Kumar, S. Kumar, S. K. Dewangan, V. Kumar, Structure and properties of lightweight high entropy alloys: a brief review, 2018, 5, 052001.
- [5] O. Maulik, N. Patra, D. Bhattacharyya, S. N. Jha, V. Kumar, Local atomic structure investigation of AlFeCuCrMg_x (0.5, 1, 1.7) high entropy alloys: X-ray absorption spectroscopy study, *Solid State Commun.*, 2017, 252, 73–77.
- [6] O.N. Senkov, G.B. Wilks, D. B. Miracle, C.P. Chuang, P. K. Liaw, *Refractory high-entropy alloys*, *Intermetallics*, 2010, 18, 1758–1765.
- [7] K.Y. Tsai, M. H. Tsai, J. W. Yeh, Sluggish diffusion in Co-Cr-Fe-Mn-Ni high-entropy alloys, *Acta Mater.*, 2013, 61, 4887–4897.
- [8] O.N. Senkov, G.B. Wilks, J.M. Scott, D.B. Miracle, Mechanical properties of Nb₂₅Mo₂₅Ta₂₅W₂₅ and V₂₀Nb₂₀Mo₂₀Ta₂₀W₂₀ refractory high entropy alloys, *Intermetallics*, 2011, 19, 698–706.
- [9] O.N. Senkov, S. V. Senkova, C. Woodward, Effect of aluminum on the microstructure and properties of two refractory high-entropy alloys, *Acta Mater.*, 2014, 68, 214–228.
- [10] O.N. Senkov, J. M. Scott, S. V. Senkova, D.B. Miracle, C.F. Woodward, Microstructure and room temperature properties of a high-entropy TaNbHfZrTi alloy, *J. Alloys Compd.*, 2011, 509, 6043–6048.
- [11] C.C. Juan, M. H. Tsai, C. W. Tsai, C. M. Lin, W. R. Wang, C.C. Yang, S.K. Chen, S.J. Lin, J. W. Yeh, Enhanced mechanical properties of HfMoTaTiZr and HfMoNbTaTiZr refractory high-entropy alloys, *Intermetallics*, 2015, 62, 76–83.
- [12] O. Maulik, D. Kumar, S. Kumar, D.M. Fabijanic, V. Kumar, Structural evolution of spark plasma sintered AlFeCuCrMg_x (x = 0, 0.5, 1, 1.7) high entropy alloys, *Intermetallics*, 2016, 77, 46–56.
- [13] R. Li, J. Gao, K. Fan, Study to Microstructure and Mechanical Properties of Mg containing high entropy alloys, *Mater. Sci. Forum.*, 2015, 650, 265–271.
- [14] K.M. Youssef, A.J. Zaddach, C. Niu, D. L. Irving, C.C. Koch, A novel low-density, high-hardness, high-entropy alloy with close-packed single-phase nanocrystalline structures, *Mater. Res. Lett.*, 2015, 3, 95–99.
- [15] L. Ma, L. Wang, T. Zhang, A. Inoue, Bulk Glass Formation of Ti-Zr-Hf-Cu-M (M=Fe, Co, Ni) Alloys, *Mater. Trans.*, 2002, 43, 277–280.
- [16] K. Zhao, X. X. Xia, H.Y. Bai, D. Q. Zhao, W. H. Wang, Room temperature homogeneous flow in a bulk metallic glass with low glass transition temperature, *Appl. Phys. Lett.*, 2011, 98, 141913.
- [17] A.C. Yeh, Y.J. Chang, C.W. Tsai, Y. C. Wang, J.W. Yeh, C. M. Kuo, On the Solidification and Phase Stability of a Co-Cr-Fe-Ni-Ti High-Entropy Alloy, *Metall. Mater. Trans. A.*, 2014, 45, 184–190.

- [18] C. J. Tong, Y. L. Chen, S. K. Chen, J.W. Yeh, T. T. Shun, C. H. Tsau, S. J. Lin, S.Y. Chang, Microstructure characterization of $Al_xCoCrCuFeNi$ high-entropy alloy system with multiprincipal elements, *Metall. Mater. Trans. A.*, 2005, 36, 881–893.
- [19] S. Guo, C.T. Liu, Phase stability in high entropy alloys: Formation of solid-solution phase or amorphous phase, *Prog. Nat. Sci. Mater. Int.*, 2011, 21, 433–446.
- [20] Y. Zhang, Y.J. Zhou, J.P. Lin, G.L. Chen, P.K. Liaw, Solid-solution phase formation rules for multi-component alloys, *Adv. Eng. Mater.*, 2008, 10, 534–538.
- [21] A. Takeuchi, A. Inoue, Calculation of Mixing Enthalpy and Mismatch entropy for ternary Amorphous Alloy, *Mater. Trans.*, 2000, 41, 1372–1378.
- [22] Pi Jinhong, P. Ye, Thermodynamic Analysis for Microstructure of High-Entropy Alloys, *Rare Met. Mater. Eng.*, 2013, 42, 232–237.
- [23] Y.Y. Chen, T. Duval, U. D. Hung, J. W. Yeh, H. C. Shih, Microstructure and electrochemical properties of high entropy alloys-a comparison with type-304 stainless steel, *Corros. Sci.*, 2005, 47, 2257–2279.
- [24] Y. J. Zhou, Y. Zhang, Y. L. Wang, G. L. Chen, Solid solution alloys of $AlCoCrFeNiTi_x$ with excellent room-temperature mechanical properties, *Appl. Phys. Lett.*, 2012, 90, 181904.
- [25] S. Varalakshmi, M. Kamaraj, B. S. Murty, Synthesis and characterization of nanocrystalline $AlFeTiCrZnCu$ high entropy solid solution by mechanical alloying, *J. Alloys Compd.*, 2008, 460, 253–257.
- [26] Y.P. Wang, D.Y. Li, L. Parent, H. Tian, Performances of hybrid high-entropy high-Cr cast irons during sliding wear and air-jet solid-particle erosion, *Wear*. 2013, 301, 390–397.
- [27] J.H. Zhao, X.L. Ji, Y.P. Shan, Y. Fu, Z. Yao, J.H. Zhao, X.L. Ji, Y.P. Shan, Y. Fu, Z. Yao, On the microstructure and erosion – corrosion resistance of $AlCrFeCoNiCu$ high-entropy alloy via annealing treatment, *Mater. Sci. Technol*. 2016, 32, 1271-1275.
- [28] R. B. Nair, K. Selvam, H. S. Arora, S. Mukherjee, H. Singh, H. S. Grewal, Slurry erosion behavior of high entropy alloys, *Wear*. 2017, 386–387, 230–238.
- [29] S. Kumar, D. Kumar, O. Maulik, A. K. Pradhan, V. Kumar, Synthesis and Air Jet Erosion Study of $Al_xFe_{1.5}CrMnNi_{0.5}$ ($x = 0.3, 0.5$) High-Entropy Alloys, *Metall. Mater. Trans. A.*, 2018, 49, 5607-5618.
- [30] R.B. Nair, H.S. Arora, A. Ayyagari, S. Mukherjee, H.S. Grewal, High Entropy Alloys: Prospective Materials for Tribo-Corrosion Applications, *Adv. Eng. Mater.*, 2018, 20, 1700946.
- [31] R.B. Nair, H.S. Arora, S. Mukherjee, S. Singh, H. Singh, H.S. Grewal, Exceptionally high cavitation erosion and corrosion resistance of a high entropy alloy, *Ultrason. Sonochem.*, 2018, 41, 252–260.
- [32] X. Ji, C. Ji, J. Cheng, Y. Shan, S. Tian, Erosive wear resistance evaluation with the hardness after strain-hardening and its application for a high-entropy alloy, *Wear*, 2018, 398–399, 178–182.
- [33] C. Y. Hsu, J. W. Yeh, S. K. Chen, T. T. Shun, Wear resistance and high-temperature compression strength of Fcc $CuCoNiCrAl_{0.5}Fe$ alloy with boron addition, *Metall. Mater. Trans. A.*, 2004, 35, 1465–1469.
- [34] C. J. Tong, M. R. Chen, S. K. Chen, J. W. Yeh, T. T. Shun, S. J. Lin, S. Y. Chang, Mechanical performance of the $Al_xCoCrCuFeNi$ high-entropy alloy system with multiprincipal elements, *Metall. Mater. Trans. A.*, 2005, 36, 1263–1271.

- [35] M. R. Chen, S. J. Lin, J. W. Yeh, S. K. Chen, Y. S. Huang, M. H. Chuang, Effect of vanadium addition on the microstructure, hardness, and wear resistance of $\text{Al}_{0.5}\text{CoCrCuFeNi}$ high-entropy alloy, *Metall. Mater. Trans. A*, 2006, 37, 1363–1369.
- [36] M. R. Chen, S. J. Lin, J. W. Yeh, S. K. Chen, Y. S. Huang, C. P. Tu, Microstructure and Properties of $\text{Al}_{0.5}\text{CoCrCuFeNiTi}_x$ ($x=0-2.0$) High-Entropy Alloys, *Mater. Trans.* 2006, 47, 1395–1401.
- [37] X. Liu, W. Lei, L. Ma, J. Liu, J. Liu, J. Cui, On the microstructures, phase assemblages and properties of $\text{Al}_{0.5}\text{CoCrCuFeNiSi}_x$ high-entropy alloys, *J. Alloys Compd.*, 2015, 630, 151–157.
- [38] S. Kumar, A. Patnaik, A.K. Pradhan, V. Kumar, Dry sliding wear behavior of $\text{Al}_{0.4}\text{FeCrNiCo}_x$ ($x=0, 0.25, 0.5, 1.0$ mol) High Entropy Alloys, *Metallogr. Microstruct. Anal.*, 2019.
- [39] J. M. Wu, S. J. Lin, J. W. Yeh, S. K. Chen, Y. S. Huang, H. C. Chen, Adhesive wear behavior of $\text{Al}_x\text{CoCrCuFeNi}$ high-entropy alloys as a function of aluminum content, *Wear*, 2006, 261, 513–519.
- [40] W. Y. Tang, M. H. Chuang, H. Y. Chen, J. W. Yeh, Microstructure and Mechanical Performance of Brand-New $\text{Al}_{0.3}\text{CrFe}_{1.5}\text{MnNi}_{0.5}$ High-Entropy Alloys, *Adv. Eng. Mater.*, 2009, 11, 788–794.
- [41] C.Y. Hsu, T. S. Sheu, J.W. Yeh, S.K. Chen, Effect of iron content on wear behavior of $\text{AlCoCrFe}_x\text{Mo}_{0.5}\text{Ni}$ high-entropy alloys, *Wear*, 2010, 268, 653–659.
- [42] S.T. Chen, W.Y. Tang, Y.F. Kuo, S.Y. Chen, C.H. Tsau, T.T. Shun, J.W. Yeh, Microstructure and properties of age-hardenable $\text{Al}_x\text{CrFe}_{1.5}\text{MnNi}_{0.5}$ alloys, *Mater. Sci. Eng. A.*, 2010, 527, 5818–5825.
- [43] S. Varalakshmi, G. A. Rao, M. Kamaraj, B.S. Murty, Hot consolidation and mechanical properties of nanocrystalline equiatomic AlFeTiCrZnCu high entropy alloy after mechanical alloying, *J. Mater. Sci.*, 2010, 45, 5158–5163.
- [44] W.Y. Tang, M.H. Chuang, H.Y. Chen, J.W. Yeh, Microstructure and mechanical performance of new $\text{Al}_{0.5}\text{CrFe}_{1.5}\text{MnNi}_{0.5}$ high-entropy alloys improved by plasma nitriding, *Surf. Coatings Technol.* 2010, 204, 3118–3124.
- [45] Y.P. Wang, D.Y. Li, L. Parent, H. Tian, Improving the wear resistance of white cast iron using a new concept - High-entropy microstructure, *Wear*, 2011, 271, 1623–1628.
- [46] M.H. Chuang, M.H. Tsai, W.R. Wang, S.J. Lin, J.W. Yeh, Microstructure and wear behavior of $\text{Al}_x\text{Co}_{1.5}\text{CrFeNi}_{1.5}\text{Ti}_y$ high-entropy alloys, *Acta Mater.*, 2011, 59, 6308–6317.
- [47] W.Y. Tang, M. H. Chuang, S. J. Lin, J. W. Yeh, Microstructures and mechanical performance of plasma-nitrided $\text{Al}_{0.3}\text{CrFe}_{1.5}\text{MnNi}_{0.5}$ high-entropy alloys, *Metall. Mater. Trans. A Phys. Metall. Mater. Sci.*, 2012, 43, 2390–2400.
- [48] M.H. Chuang, M. H. Tsai, C. W. Tsai, N. H. Yang, S.Y. Chang, J. W. Yeh, S. K. Chen, S. J. Lin, Intrinsic surface hardening and precipitation kinetics of $\text{Al}_{0.3}\text{CrFe}_{1.5}\text{MnNi}_{0.5}$ multi-component alloy, *J. Alloys Compd.*, 2013, 551, 12–18.
- [49] H. F. Sun, C. M. Wang, X. Zhang, R. Z. Li, L.Y. Ruan, Study of the microstructure and performance of high-entropy alloys $\text{Al}_x\text{FeCuCoNiCrTi}$, *Mater. Res. Innov.*, 2015, 19, S8-89-S8-93.
- [50] H. Ye, Y. Zhan, N. Nie, Development of novel $\text{CoCu}_{0.5}\text{FeNiVTi}_x$ ($x = 0, 0.5, 1, 1.5, 2$) high-entropy alloys, *Mater. Sci. Technol.*, 2018, 34, 952–960.

- [51] Q. Yang, Y. Tang, Y. Wen, Q. Zhang, D. Deng, X. Nai, Microstructures and properties of CoCrCuFeNiMo_x high-entropy alloys fabricated by mechanical alloying and spark plasma sintering, *Powder Metall.* 2018, 61, 115–122.
- [52] A. Zhang, J. Han, B. Su, J. Meng, A novel CoCrFeNi high entropy alloy matrix self-lubricating composite, *J. Alloys Compd.*, 2017, 725, 700–710.
- [53] B. Gwalani, A. V. Ayyagari, D. Choudhuri, T. Scharf, S. Mukherjee, M. Gibson, R. Banerjee, Microstructure and wear resistance of an intermetallic-based Al_{0.25}Ti_{0.75}CoCrFeNi high entropy alloy, *Mater. Chem. Phys.*, 2018, 210, 197–206.
- [54] S. A. Firstov, V. F. Gorban, N. A. Krapivka, M. V. Karpets, A. D. Kostenko, Wear Resistance of High-Entropy Alloys, *Powder Metall. Met. Ceram.*, 2017, 56, 158–164.
- [55] Y. Yu, J. Wang, J. S. Li, H. C. Kou, S. Z. Niu, S.Y. Zhu, J. Yang, W. M. Liu, Dry-sliding tribological properties of AlCoCrFeNiTi_{0.5} high-entropy alloy, *Rare Met.*, 2017, 1–7.
- [56] S. Yadav, A. Kumar, K. Biswas, Wear behavior of high entropy alloys containing soft dispersoids (Pb, Bi), *Mater. Chem. Phys.*, 2018, 210, 222–232.
- [57] M. Zhang, W. Zhang, Y. Liu, B. Liu, J. Wang, FeCoCrNiMo high-entropy alloys prepared by powder metallurgy processing for diamond tool applications, *Powder Metall.* 2018, 61, 123–130.
- [58] A. Kumar, A.K. Swarnakar, M. Chopkar, Phase Evolution and Mechanical Properties of AlCoCrFeNiSi_x High-Entropy Alloys Synthesized by Mechanical Alloying and Spark Plasma Sintering, *J. Mater. Eng. Perform.*, 2018, 27, 3304–3314.
- [59] K. Lentzaris, A. Poulia, E. Georgatis, A. G. Lekatou, A. E. Karantzalis, Analysis of Microstructure and Sliding Wear Behavior of Co_{1.5}CrFeNi_{1.5}Ti_{0.5} High-Entropy Alloy, *J. Mater. Eng. Perform.*, 2018, 27, 5177–5186.
- [60] A. Zhang, J. Han, B. Su, J. Meng, A promising new high temperature self-lubricating material : CoCrFeNiS 0.5 high entropy alloy, *Mater. Sci. Eng. A.*, 2018, 731, 36–43.
- [61] J. Miao, T. Guo, J. Ren, A. Zhang, B. Su, J. Meng, Optimization of mechanical and tribological properties of FCC CrCoNi multi-principal element alloy with Mo addition, *Vacuum*, 2018, 149, 324–330.
- [62] Y. Zhao, H. Cui, M. Wang, Y. Zhao, X. Zhang, C. Wang, The microstructures and properties changes induced by Al : Co ratios of the Al_xCrCo_{2-x}FeNi high entropy alloys, *Mater. Sci. Eng. A.*, 2018, 733, 153–163.
- [63] Z. S. Nong, Y. N. Lei, J. C. Zhu, Wear and oxidation resistances of AlCrFeNiTi-based high entropy alloys, *Intermetallics.* 2018, 101, 144–151.
- [64] A. Verma, P. Tarate, A. C. Abhyankar, M. R. Mohape, D. S. Gowtam, V. P. Deshmukh, T. Shanmugasundaram, High temperature wear in CoCrFeNiCu_x high entropy alloys : The role of Cu, *Scr. Mater.*, 2019, 161, 28–31.
- [65] L. M. Du, L.W. Lan, S. Zhu, H. J. Yang, X. H. Shi, P. K. Liaw, J.W. Qiao, Effects of temperature on the tribological behavior of Al_{0.25}CoCrFeNi high-entropy alloy, *J. Mater. Sci. Technol.*, 2019, 35, 917–925.
- [66] M. Chen, L. Lan, X. Shi, H. Yang, M. Zhang, J. Qiao, The tribological properties of Al_{0.6}CoCrFeNi high-entropy alloy with the σ phase precipitation at elevated temperature, *J. Alloys Compd.*, 2019, 777, 180–189.
- [67] S. Cao, J. Zhou, L. Wang, Y. Yu, B. Xin, Microstructure, mechanical and tribological property of multi-components synergistic self-lubricating NiCoCrAl matrix composite, *Tribol. Int.*, 2019, 131, 508–519.

- [68] Y.Y. Liu, Z. Chen, J. C. Shi, Z. Y. Wang, J. Y. Zhang, The effect of Al content on microstructures and comprehensive properties in $\text{Al}_x\text{CoCrCuFeNi}$ high entropy alloys, *Vacuum.*, 2019, 161, 143–149.
- [69] Y. Yu, F. He, Z. Qiao, Z. Wang, W. Liu, J. Yang, Effects of temperature and microstructure on the tribological properties of CoCrFeNiNb_x eutectic high entropy alloys, *J. Alloys Compd.*, 2019, 775, 1376–1385.
- [70] H. Duan, Y. Wu, M. Hua, C. Yuan, D. Wang, J. Tu, H. Kou, J. Li, Tribological properties of AlCoCrFeNiCu high-entropy alloy in hydrogen peroxide solution and in oil lubricant, *Wear*, 2013, 297, 1045–1051.
- [71] Y. Yu, W. M. Liu, T. B. Zhang, J. S. Li, J. Wang, H. C. Kou, J. Li, Microstructure and Tribological Properties of $\text{AlCoCrFeNiTi}_{0.5}$ High-Entropy Alloy in Hydrogen Peroxide Solution, *Metall. Mater. Trans. A.*, 2014, 45, 201–207.
- [72] V.F. Gorban, M. V. Karpets, Y.S. Makarenkoa, A.D. Kostenko, N.I. Danylenko, Friction of high-entropy $\text{Fe}_{25}\text{Cr}_{20}\text{Ni}_{20}\text{Mn}_{15}\text{Co}_{10}\text{Al}_{10}$ alloy for 65G steel, *J. Frict. Wear*. 2015, 36, 342–345.
- [73] Y. Liu, S. Ma, M. C. Gao, C. Zhang, T. Zhang, H. Yang, Z. Wang, J. Qiao, Tribological Properties of AlCrCuFeNi_2 High-Entropy Alloy in Different Conditions, *Metall. Mater. Trans. A*, 2016, 47, 3312–3321.
- [74] S. Kumar, A. Patnaik, A. K. Pradhan, V. Kumar, Room temperature wear study of $\text{Al}_{0.4}\text{FeCrNiCo}_x$ ($x=0,0.25,0.5,1.0$ mol) high-entropy alloys under oil lubricating condition, *J. Mater. Res.*, 2019, 34, 841-853.
- [75] Y. Yu, J. Wang, J. Li, H. Kou, H. Duan, J. Li, W. Liu, Tribological behavior of AlCoCrCuFeNi and $\text{AlCoCrFeNiTi}_{0.5}$ high entropy alloys under hydrogen peroxide solution against different counterparts, *Tribol. Int.*, 2015, 92, 203–210.
- [76] Y. Yu, J. Wang, J. Li, J. Yang, H. Kou, W. Liu, Tribological Behavior of AlCoCrFeNi ($\text{Ti}_{0.5}$) High Entropy Alloys under Oil and MACs Lubrication, *J. Mater. Sci. Technol.*, 2016, 32, 470–476.
- [77] Y. Wang, Y. Yang, H. Yang, M. Zhang, J. Qiao, Effect of nitriding on the tribological properties of $\text{Al}_{1.3}\text{CoCuFeNi}_2$ high-entropy alloy, *J. Alloys Compd.*, 2017, 725, 365-372.
- [78] A. Ayyagari, C. Barthelemy, B. Gwalani, R. Banerjee, T.W. Scharf, S. Mukherjee, Reciprocating sliding wear behavior of high entropy alloys in dry and marine environments, *Mater. Chem. Phys.*, 2018, 210, 162–169.
- [79] Y. Wang, Y. Yang, H. Yang, M. Zhang, S. Ma, Microstructure and wear properties of nitrided AlCoCrFeNi high-entropy alloy, *Mater. Chem. Phys.*, 2018, 210, 233-239.
- [80] M. Chen, X. H. Shi, H. Yang, P. K. Liaw, M. C. Gao, J. A. Hawk, J. Qiao, Wear behavior of $\text{Al}_{0.6}\text{CoCrFeNi}$ high-entropy alloys: Effect of environments, *J. Mater. Res.*, 2018, 33, 3310–3320.
- [81] Y. Yu, J. Wang, J. Yang, Z. Qiao, H. Duan, J. Li, J. Li, W. Liu, Corrosive and tribological behaviors of AlCoCrFeNi-M high entropy alloys under 90 wt. % H_2O_2 solution, *Tribol. Int.* 2018, 131, 24–32.
- [82] F. Meng, I. Baker, Nitriding of a high entropy FeNiMnAlCr alloy, *J. Alloys Compd.*, 2015, 645, 376–381.
- [83] Z. Wang, I. Baker, W. Guo, J.D. Poplawsky, The effect of carbon on the microstructures, mechanical properties, and deformation mechanisms of thermo-mechanically treated $\text{Fe}_{40.4}\text{Ni}_{11.3}\text{Mn}_{34.8}\text{Al}_{7.5}\text{Cr}_6$ high entropy alloys, *Acta Mater.*, 2017, 126, 346–360.

- [84] C. P. Lee, C. C. Chang, Y. Y. Chen, J. W. Yeh, H. C. Shih, Effect of the aluminium content of $\text{Al}_x\text{CrFe}_{1.5}\text{MnNi}_{0.5}$ high-entropy alloys on the corrosion behaviour in aqueous environments, *Corros. Sci.* 2008, 50, 2053–2060.
- [85] C.P. Lee, Y.Y. Chen, C.Y. Hsu, J.W. Yeh, H.C. Shih, Enhancing pitting corrosion resistance of $\text{Al}_x\text{CrFe}_{1.5}\text{MnNi}_{0.5}$ high-entropy alloys by anodic treatment in sulfuric acid, *Thin Solid Films.* 2008, 517, 1301–1305.
- [86] L. C. Tsao, C. S. Chen, C. P. Chu, Age hardening reaction of the $\text{Al}_{0.3}\text{CrFe}_{1.5}\text{MnNi}_{0.5}$ high entropy alloy, *Mater. Des.*, 2012, 36, 854–858.
- [87] N. A. P. K. Kumar, C. Li, K. J. Leonard, H. Bei, S. J. Zinkle, Microstructural stability and mechanical behavior of FeNiMnCr high entropy alloy under ion irradiation, *Acta Mater.* 2016, 113, 230–244.
- [88] Z. Wang, I. Baker, Interstitial strengthening of a f.c.c. FeNiMnAlCr high entropy alloy, *Mater. Lett.*, 2016, 180, 153–156.
- [89] D.G. Shaysultanov, G.A. Salishchev, Y. V. Ivanisenko, S. V. Zhrebtsov, M.A. Tikhonovsky, N.D. Stepanov, Novel $\text{Fe}_{36}\text{Mn}_{21}\text{Cr}_{18}\text{Ni}_{15}\text{Al}_{10}$ high entropy alloy with bcc/B2 dual-phase structure, *J. Alloys Compd.*, 2017, 705, 756–763.
- [90] N.D. Stepanov, D.G. Shaysultanov, R.S. Chernichenko, M.A. Tikhonovsky, S. V. Zhrebtsov, Effect of Al on structure and mechanical properties of Fe-Mn-Cr-Ni-Al non-equiatom high entropy alloys with high Fe content, *J. Alloys Compd.*, 2019, 770, 194–203.
- [91] S. Wu, Y. Pan, J. Lu, N. Wang, W. Dai, T. Lu, Effect of the addition of Mg, Ti, Ni on the decoloration performance of AlCrFeMn high entropy alloy, *J. Mater. Sci. Technol.*, 2019, 35, 1629-1635.
- [92] S.N. Karlsdottir, I. Csaki, I. V. Antoniac, C. A. Manea, R. Stefanoiu, F. Magnus, F. Miculescu, Corrosion behavior of AlCrFeNiMn high entropy alloy in a geothermal environment, *Geothermics.* 2019, 81, 32–38.
- [93] L. J. Zhang, K. Guo, H. Tang, M. D. Zhang, J. T. Fan, P. Cui, Y. M. Ma, P. F. Yu, G. Li, The microstructure and mechanical properties of novel A-Cr-Fe-Mn-Ni high-entropy alloys with trimodal distribution of coherent B2 precipitates, *Mater. Sci. Eng. A.*, 2019, 757, 160-171.
- [94] A. Munitz, S. Salhov, S. Hayun, N. Frage, Heat treatment impacts the micro-structure and mechanical properties of AlCoCrFeNi high entropy alloy, *J. Alloys Compd.*, 683, 2016, 221-230.
- [95] H. Shiratori, T. Fujieda, K. Yamanaka, Y. Koizumi, K. Kuwabara, T. Kato, A. Chiba, Relationship between the microstructure and mechanical properties of an equiatom AlCoCrFeNi high-entropy alloy fabricated by selective electron beam melting, *Mater. Sci. Eng. A.*, 2016, 656, 39–46.
- [96] Z. Tang, O. N. Senkov, C. M. Parish, C. Zhang, F. Zhang, L. J. Santodonato, G. Wang, G. Zhao, F. Yang, P.K. Liaw, Tensile ductility of an AlCoCrFeNi multi-phase high-entropy alloy through hot isostatic pressing (HIP) and homogenization, *Mater. Sci. Eng. A.* 2015, 647, 229–240.
- [97] A. Manzoni, H. Daoud, R. Völkl, U. Glatzel, N. Wanderka, Phase separation in equiatom AlCoCrFeNi high-entropy alloy, *Ultramicroscopy*, 2013, 132, 212–215.
- [98] I. Kuncce, M. Polanski, K. Karczewski, T. Plocinski, K.J. Kurzydowski, Microstructural characterisation of high-entropy alloy AlCoCrFeNi fabricated by laser engineered net shaping, *J. Alloys Compd.*, 2015, 648, 751–758.

- [99] T. Fujieda, H. Shiratori, K. Kuwabara, T. Kato, K. Yamanaka, Y. Koizumi, A. Chiba, First demonstration of promising selective electron beam melting method for utilizing high-entropy alloys as engineering materials, *Mater. Lett.*, 2015, 159, 12–15.
- [100] J. Chen, P. Niu, Y. Liu, Y. Lu, X. Wang, Y. Peng, J. Liu, Effect of Zr content on microstructure and mechanical properties of AlCoCrFeNi high entropy alloy, *Mater. Des.* 2016, 94, 39–44.
- [101] S. Mohanty, T.N. Maity, S. Mukhopadhyay, S. Sarkar, N.P. Gurao, S. Bhowmick, K. Biswas, Powder metallurgical processing of equiatomic AlCoCrFeNi high entropy alloy: Microstructure and mechanical properties, *Mater. Sci. Eng. A.* 2017, 679, 299–313.
- [102] Y. Liu, J. Chen, Z. Li, X. Wang, X. Fan, J. Liu, Formation of transition layer and its effect on mechanical properties of AlCoCrFeNi high-entropy alloy/Al composites, *J. Alloys Compd.*, 2019, 780, 558–564.
- [103] B. Cheng, F. Zhang, H. Lou, X. Chen, P. K. Liaw, J. Yan, Z. Zeng, Y. Ding, Q. Zeng, Pressure-induced phase transition in the AlCoCrFeNi high-entropy alloy, *Scr. Mater.* 2019, 161, 88–92.
- [104] D. Karlsson, G. Lindwall, A. Lundbäck, M. Amnebrink, M. Boström, L. Riekehr, M. Schuisky, M. Sahlberg, U. Jansson, Binder jetting of the AlCoCrFeNi alloy, *Addit. Manuf.*, 2019, 27, 72–79.
- [105] D. Karlsson, A. Marshal, F. Johansson, M. Schuisky, M. Sahlberg, J. M. Schneider, U. Jansson, Elemental segregation in an AlCoCrFeNi high-entropy alloy – A comparison between selective laser melting and induction melting, *J. Alloys Compd.*, 2019, 784, 195–203.
- [106] G. Qin, W. Xue, R. Chen, H. Zheng, L. Wang, Y. Su, H. Ding, J. Guo, H. Fu, Grain refinement and FCC phase formation in AlCoCrFeNi high entropy alloys by the addition of carbon, *Materialia.*, 2019, 6, 100259.
- [107] P. D. Niu, R. D. Li, T. C. Yuan, S.Y. Zhu, C. Chen, M. B. Wang, L. Huang, Microstructures and properties of an equimolar AlCoCrFeNi high entropy alloy printed by selective laser melting, *Intermetallics.* 2019, 104, 24–32.
- [108] Q. Tian, G. Zhang, K. Yin, W. Wang, W. Cheng, Y. Wang, The strengthening effects of relatively lightweight AlCoCrFeNi high entropy alloy, *Mater. Charact.* 2019, 151, 302–309.
- [109] V. Ferrari, W. Wolf, G. Zepon, F. G. Coury, M. J. Kaufman, C. Bolfarini, C. S. Kiminami, W. J. Botta, Effect of boron addition on the solidification sequence and microstructure of AlCoCrFeNi alloys, *J. Alloys Compd.* 2019, 775, 1235–1243.
- [110] T.T. Shun, Y.C. Du, Microstructure and tensile behaviors of FCC Al_{0.3}CoCrFeNi high entropy alloy, *J. Alloys Compd.*, 2009, 479, 157–160.
- [111] Y. F. Kao, T. J. Chen, S. K. Chen, J. W. Yeh, Microstructure and mechanical property of as-cast, -homogenized, and -deformed Al_xCoCrFeNi (0 ≤ x ≤ 2) high-entropy alloys, *J. Alloys Compd.*, 2009, 488, 57–64.
- [112] D. Li, C. Li, T. Feng, Y. Zhang, G. Sha, J. J. Lewandowski, P. K. Liaw, Y. Zhang, High-entropy Al_{0.3}CoCrFeNi alloy fibers with high tensile strength and ductility at ambient and cryogenic temperatures, *Acta Mater.*, 2017, 123, 285–294.
- [113] C. M. Lin, H. L. Tsai, Evolution of microstructure, hardness, and corrosion properties of high-entropy Al_{0.5}CoCrFeNi alloy, *Intermetallics.* 2011, 19, 288–294.

- [114] J. Joseph, T. Jarvis, X. Wu, N. Stanford, P. Hodgson, D. M. Fabijanic, Comparative study of the microstructures and mechanical properties of direct laser fabricated and arc-melted $\text{Al}_x\text{CoCrFeNi}$ high entropy alloys, *Mater. Sci. Eng. A.*, 2015, 633, 184–193.
- [115] P. F. Yu, H. Cheng, L. J. Zhang, H. Zhang, Q. Jing, M. Z. Ma, P. K. Liaw, G. Li, R. P. Liu, Effects of high pressure torsion on microstructures and properties of an $\text{Al}_{0.1}\text{CoCrFeNi}$ high-entropy alloy, *Mater. Sci. Eng. A.*, 2016, 655, 283–291.
- [116] T. Yang, Z. Tang, X. Xie, R. Carroll, G. Wang, Y. Wang, K. A. Dahmen, P. K. Liaw, Y. Zhang, Deformation mechanisms of $\text{Al}_{0.1}\text{CoCrFeNi}$ at elevated temperatures, *Mater. Sci. Eng. A.*, 2017, 684, 552–558.
- [117] L. Ma, L. Wang, Z. Nie, F. Wang, Y. Xue, J. Zhou, T. Cao, Y. Wang, Y. Ren, Reversible deformation-induced martensitic transformation in $\text{Al}_{0.6}\text{CoCrFeNi}$ high-entropy alloy investigated by in situ synchrotron-based high-energy X-ray diffraction, *Acta Mater.*, 2017, 128, 12–21.
- [118] M. Annasamy, N. Haghdadi, A. Taylor, P. Hodgson, D. Fabijanic, Dynamic recrystallization behaviour of $\text{Al}_x\text{CoCrFeNi}$ high entropy alloys during high-temperature plane strain compression, *Mater. Sci. Eng. A.*, 2019, 745, 90–106.
- [119] P. F. Zhou, D. H. Xiao, Z. Wu, X. Q. Ou, $\text{Al}_{0.5}\text{FeCoCrNi}$ high entropy alloy prepared by selective laser melting with gas-atomized pre-alloy powders, *Mater. Sci. Eng. A.* 2019, 739, 86–89.
- [120] S. Gangireddy, B. Gwalani, R. Banerjee, R. S. Mishra, Contrasting mechanical behavior in precipitation hardenable $\text{Al}_x\text{CoCrFeNi}$ high entropy alloy microstructure: single phase FCC vs. dual phase FCC-BCC, *Mater. Sci. Eng. A.*, 2019, 739, 158-166.
- [121] B. Gwalani, S. Gorsse, D. Choudhuri, Y. Zheng, R.S. Mishra, R. Banerjee, Tensile yield strength of a single bulk $\text{Al}_{0.3}\text{CoCrFeNi}$ high entropy alloy can be tuned from 160 MPa to 1800 MPa, *Scr. Mater.*, 2019, 162, 18–23.
- [122] M. Annasamy, N. Haghdadi, A. Taylor, P. Hodgson, D. Fabijanic, Static recrystallization and grain growth behaviour of $\text{Al}_{0.3}\text{CoCrFeNi}$ high entropy alloy, *Mater. Sci. Eng. A.*, 2019, 754, 282-294.
- [123] K. Liu, M. Komarasamy, B. Gwalani, S. Shukla, R. S. Mishra, Fatigue behavior of ultrafine grained triplex $\text{Al}_{0.3}\text{CoCrFeNi}$ high entropy alloy, *Scr. Mater.*, 2019, 158, 116–120.
- [124] J. Wang, Y. Zhang, H. Xiao, L. Li, H. Kou, J. Li, A novel strategy for enhancing mechanical performance of $\text{Al}_{0.5}\text{CoCrFeNi}$ high-entropy alloy via high magnetic field, *Mater. Lett.*, 2019, 240, 250-252.
- [125] J. Hou, M. Zhang, H. Yang, J. Qiao, Y. Wu, Surface strengthening in $\text{Al}_{0.25}\text{CoCrFeNi}$ high-entropy alloy by boronizing, *Mater. Lett.*, 2019, 238, 258–260.
- [126] Y. Lu, Y. Dong, S. Guo, L. Jiang, H. Kang, T. Wang, B. Wen, Z. Wang, J. Jie, Z. Cao, H. Ruan, T. Li, A promising new class of high-temperature alloys: Eutectic high-entropy alloys, *Nature.*, 2014, 4, 1–5.
- [127] Q. Chen, K. Zhou, L. Jiang, Y. Lu, T. Li, Effects of Fe Content on Microstructures and Properties of $\text{AlCoCrFe}_x\text{Ni}$ High-Entropy Alloys, *Arab. J. Sci. Eng.*, 2015, 40, 3657–3663.
- [128] C. Chen, S. Pang, Y. Cheng, T. Zhang, Microstructure and mechanical properties of $\text{Al}_{20-x}\text{Cr}_{20+0.5x}\text{Fe}_{20}\text{Co}_{20}\text{Ni}_{20+0.5x}$ high entropy alloys, *J. Alloys Compd.*, 2016, 659, 279–287.

- [129] Z. Wang, M. C. Gao, S. G. Ma, H. J. Yang, Z. H. Wang, M. Z. Moroz, J. W. Qiao, Effect of cold rolling on the microstructure and mechanical properties of $\text{Al}_{0.25}\text{CoCrFe}_{1.25}\text{Ni}_{1.25}$ High-entropy alloy, *Mater. Sci. Eng. A.*, 2015, 645, 163-169.
- [130] X. Gao, Y. Lu, B. Zhang, N. Liang, G. Wu, G. Sha, J. Liu, Y. Zhao, Microstructural origins of high strength and high ductility in an $\text{AlCoCrFeNi}_{2.1}$ eutectic high-entropy alloy, *Acta Mater.*, 2017, 141, 59-66.
- [131] I. S. Wani, T. Bhattacharjee, S. Sheikh, I. T. Clark, M. H. Park, T. Okawa, S. Guo, P. P. Bhattacharjee, N. Tsuji, Cold-rolling and recrystallization textures of a nano-lamellar $\text{AlCoCrFeNi}_{2.1}$ eutectic high entropy alloy, *Intermetallics*. 2017, 84, 42-51.
- [132] P. Ding, A. Mao, X. Zhang, X. Jin, B. Wang, M. Liu, X. Gu, Preparation, characterization and properties of multicomponent $\text{AlCoCrFeNi}_{2.1}$ powder by gas atomization method, *J. Alloys Compd.*, 2017, 721, 609-614.
- [133] J. Hao, Y. Ma, Q. Wang, C. Zhang, C. Li, C. Dong, Formation of cuboidal B2 nanoprecipitates and microstructural evolution in the body-centered-cubic $\text{Al}_{0.7}\text{NiCoFe}_{1.5}\text{Cr}_{1.5}$ high-entropy alloy, *J. Alloys Compd.*, 2019, 780, 408-421.
- [134] Y. Zhang, J. Li, X. Wang, Y. Lu, Y. Zhou, X. Sun, The interaction and migration of deformation twin in an eutectic high-entropy alloy $\text{AlCoCrFeNi}_{2.1}$, *J. Mater. Sci. Technol.*, 2019, 35, 902-906.
- [135] X. Jin, Y. Liang, L. Zhang, J. Bi, Y. Zhou, B. Li, Back stress strengthening dual-phase $\text{AlCoCr}_2\text{FeNi}_2$ high entropy alloy with outstanding tensile properties, *Mater. Sci. Eng. A.*, 2019, 745, 137-143.
- [136] G. Qin, W. Xue, C. Fan, R. Chen, L. Wang, Y. Su, H. Ding, J. Guo, Effect of Co content on phase formation and mechanical properties of $(\text{AlCoCrFeNi})_{100-x}\text{Co}_x$ high-entropy alloys, *Mater. Sci. Eng. A.*, 2018, 710, 200-205.
- [137] M. Kang, K. R. Lim, J. W. Won, Y. S. Na, Effect of Co content on the mechanical properties of A2 and B2 phases in $\text{AlCo}_x\text{CrFeNi}$ high-entropy alloys, *J. Alloys Compd.*, 2018, 769, 808-812.
- [138] Z. Chen, W. Chen, B. Wu, X. Cao, L. Liu, Z. Fu, Effects of Co and Ti on microstructure and mechanical behavior of $\text{Al}_{0.75}\text{FeNiCrCo}$ high entropy alloy prepared by mechanical alloying and spark plasma sintering, *Mater. Sci. Eng. A.*, 2015, 648, 217-224.
- [139] W. D. Callister, D. G. Rethwisch, *Material Science and Engineering An Introduction*, 8th ed., John Wiley and Sons Inc, USA, 2009.
- [140] M. Warlimont, *Handbook of condensed Matter and Materials Data*, Springer, Germany, 2005.
- [141] S. Praveen, B. S. Murty, R. S. Kottada, Alloying behavior in multi-component AlCoCrCuFe and NiCoCrCuFe high entropy alloys, *Mater. Sci. Eng. A.*, 2012, 534, 83-89.
- [142] O. Maulik, V. Kumar, Synthesis of AlFeCuCrMg_x ($x = 0, 0.5, 1, 1.7$) alloy powders by mechanical alloying, *Mater. Charact.*, 2015, 110, 116-125.
- [143] H. Khanchandani, P. Sharma, R. Kumar, O. Maulik, V. Kumar, Effect of sintering on phase evolution in $\text{AlMgFeCuCrNi}_{4.75}$ high entropy alloy, *Adv. Powder Technol.*, 2016, 27, 289-294.
- [144] C. Wang, W. Ji, Z. Fu, Mechanical alloying and spark plasma sintering of CoCrFeNiMnAl high-entropy alloy, *Adv. Powder Technol.*, 2014, 25, 1334-1338.

- [145] Y. L. Chen, Y. H. Hu, C. A. Hsieh, J. W. Yeh, S. K. Chen, Competition between elements during mechanical alloying in an octonary multi-principal-element alloy system, *J. Alloys Compd.*, 2009, 481, 768–775.
- [146] V. Soare, M. Burada, I. Constantin, D. Mitrica, V. Badilita, A. Caragea, M. Tarcolea, Electrochemical deposition and microstructural characterization of AlCrFeMnNi and AlCrCuFeMnNi high entropy alloy thin films, *Appl. Surf. Sci.* 2015, 358, 533–539.
- [147] D. Kumar, O. Maulik, S. Kumar, V. K. Sharma, Y. V. S. S. Prasad, V. Kumar, Impact of tungsten on phase evolution in nanocrystalline AlCuCrFeMnW_x (x = 0, 0.05, 0.1 and 0.5 mol) high entropy alloys, *Mater. Res. Express.*, 2017, 4, 114004.
- [148] H. A. Baghbaderani, S. Sharafi, M. D. Chermahini, Investigation of nanostructure formation mechanism and magnetic properties in Fe₄₅Co₄₅Ni₁₀ system synthesized by mechanical alloying, *Powder Technol.*, 2012, 230, 241–246.
- [149] X. Yang, Y. Zhang, Prediction of high-entropy stabilized solid-solution in multi-component alloys, *Mater. Chem. Phys.*, 2012, 132, 233–238.
- [150] A. Takeuchi, A. Inoue, Classification of Bulk Metallic Glasses by Atomic Size Difference, Heat of Mixing and Period of Constituent Elements and Its Application to Characterization of the Main Alloying Element, *Mater. Trans.*, 2005, 46, 2817–2829.
- [151] Z. Wang, S. Guo, C.T. Liu, Phase Selection in High-Entropy Alloys: From Nonequilibrium to Equilibrium, *Jom.*, 2014, 66, 1966–1972.
- [152] O.N. Senkov, C.F. Woodward, Microstructure and properties of a refractory NbCrMo_{0.5}Ta_{0.5}TiZr alloy, *Mater. Sci. Eng. A.*, 2011, 529, 311–320.
- [153] M. Divakar, V. K. Agarwal, S. N. Singh, Effect of the material surface hardness on the erosion of AISI316, *Wear.*, 2005, 259, 110–117.
- [154] J.R. L. Camacho, A. M. Chávez, J. V. M. Méndez, M. V. Torres, E. A. G. Hernández, Solid particle erosion of AISI 304, 316 and 420 stainless steels, *Wear.*, 2013, 301, 398–405.
- [155] Q.B. Nguyen, V. B. Nguyen, C.Y. H. Lim, Q.T. Trinh, S. Sankaranarayanan, Y.W. Zhang, M. Gupta, Effect of impact angle and testing time on erosion of stainless steel at higher velocities, *Wear*, 2014, 321, 87–93.
- [156] V. B. Nguyen, Q. B. Nguyen, Y.W. Zhang, C.Y. H. Lim, B. C. Khoo, Effect of particle size on erosion characteristics, *Wear*, 2016, 348–349, 126–137.
- [157] S. Niu, H. Kou, T. Guo, Y. Zhang, J. Wang, J. Li, Strengthening of nanoprecipitations in an annealed Al_{0.5}CoCrFeNi high entropy alloy, *Mater. Sci. Eng. A.*, 2016, 671, 82–86.
- [158] K. Jasiewicz, J. Cieslak, S. Kaprzyk, J. Tobola Relative crystal stability of Al_xFeNiCrCo high entropy alloys from XRD analysis and formation energy calculation, *J. Alloys Compd.*, 2015, 648, 307–312.
- [159] Y. Dong, X. Gao, Y. Lu, T. Wang, T. Li, A multi-component AlCrFe₂Ni₂ alloy with excellent mechanical properties, *Mater. Lett.*, 2016, 169, 62–64.
- [160] J. Wang, T. Guo, J. Li, W. Jia, H. Kou, Microstructure and mechanical properties of non-equilibrium solidified CoCrFeNi high entropy alloy, *Mater. Chem. Phys.*, 2018, 210, 192–196.
- [161] H. P. Chou, Y. S. Chang, S. K. Chen, J. W. Yeh, Microstructure, thermophysical and electrical properties in Al_xCoCrFeNi (0 ≤ x ≤ 2) high-entropy alloys, *Mater. Sci. Eng. B.*, 2009, 163, 184–189.

- [162] S. Uporov, V. Bykov, S. Pryanichnikov, A. Shubin, N. Uporova, Effect of synthesis route on structure and properties of AlCoCrFeNi high-entropy alloy, *Intermetallics.*, 2017, 83, 1–8.
- [163] B. Cantor, I.T. H. Chang, P. Knight, A. J. B. Vincent, Microstructural development in equiatomic multicomponent alloys, *Mater. Sci. Eng. A.*, 2004, 375–377, 213–218.
- [164] Y. Zhang, T. T. Zuo, Z. Tang, M. C. Gao, K. A. Dahmen, P. K. Liaw, Z. P. Lu, Microstructures and properties of high-entropy alloys, *Prog. Mater. Sci.*, 2014, 61, 1–93.
- [165] S. Guo, Phase selection rules for cast high entropy alloys: an overview, *Mater. Sci. Technol.*, 2015, 31, 1223–1230.
- [166] Y. Dong, Y. Lu, L. Jiang, T. Wang, T. Li, Effects of electro-negativity on the stability of topologically close-packed phase in high entropy alloys, *Intermetallics.*, 2014, 52, 105–109.
- [167] W. Chen, Z. Fu, S. Fang, H. Xiao, D. Zhu, Alloying behavior, microstructure and mechanical properties in a FeNiCrCo_{0.3}Al_{0.7} high entropy alloy, *Mater. Des.*, 2013, 51, 854–860.
- [168] C. M. Lin, H. L. Tsai, Evolution of microstructure , hardness , and corrosion properties of high-entropy Al_{0.5}CoCrFeNi Alloy, *Intermetallics.*, 2011, 19, 288–294.
- [169] ASM Volume 3: Alloy Phase Diagrams, 1992.
- [170] Y. Chen, Y. Li, S. Kurosu, K. Yamanaka, N. Tang, A. Chiba, Effects of microstructures on the sliding behavior of hot-pressed CoCrMo alloys, *Wear*, 2014, 319, 200–210.
- [171] V. Kukshal, A. Patnaik, I. K. Bhat, Effect of cobalt on microstructure and properties of AlCr_{1.5}CuFeNi₂Co_x high-entropy alloys, *Mater. Res. Express.*, 5, 2018, 046514.
- [172] C. Li, J. C. Li, M. Zhao, Q. Jiang, Effect of alloying elements on microstructure and properties of multiprincipal elements high-entropy alloys, *J. Alloys Compd.*, 2009, 475, 752–757.
- [173] M. M. Khrushov, Principles of abrasive wear, *Wear*, 1974, 28, 69–88.
- [174] I. Hutchings, P. Shipway, *Tribology Friction and Wear of Engineering Materials*, Elsevier, 2016.
- [175] G. Rasool, M.M. Stack, Mapping the role of Cr content in dry sliding of steels : Comparison between maps for material and counterface, *Tribology Int.*, 2014, 80, 49–57.
- [176] A. Gaard, N. Hallback, P. Krakhmalev, J. Bergstrom, Temperature effects on adhesive wear in dry sliding contacts, *Wear*, 2010, 268, 968–975.
- [177] P.C. Okonkwo, G. Kelly, B.F. Rolfe, M.P. Pereira, The effect of sliding speed on the wear of steel – tool steel pairs, *Tribology Int.*, 2016, 97, 218–227.
- [178] P. Heilmann, J. Don, T. C. Sun, D. A. Rigney, W. A. Glaeser, Sliding wear and transfer, *Wear*, 1983, 91, 171–190.
- [179] A. F. Smith, The influenc of surface oxidation and sliding speed on the unlubricated wear of 316 stainless steel at low load, *Wear*, 1985, 105, 91–107.
- [180] X. Ji, S.H. Alavi, S.P. Harimkar, Y. Zhang, Sliding Wear of Spark Plasma Sintered CrFeCoNiCu High-Entropy Alloy Coatings: Effect of Aluminum Addition, *J. Mater. Eng. Perform.*, 2018, 27, 5815–5822.
- [181] L. Conceicao, A. S. C. M. D’Oliveira, The effect of oxidation on the tribolayer and sliding wear of a Co-based coating, *Surf. Coatings Technol.*, 2016, 288, 69–78.
- [182] M. K. Mondal, K. Biswas, J. Maity, Dry sliding wear behaviour of a novel 6351 Al-Al4 SiC₄ composite at high loads, *Can. Metall. Q.*, 2016, 55, 75-93.

- [183] E.S. Zanoria, S. Danyluk, M.J. McNallan, Formation of cylindrical sliding-wear debris on silicon in humid conditions and elevated temperatures, *Tribol. Trans.*, 1995, 38, 721–727.
- [184] A. Zmitrowicz, Wear Debris: a Review of Properties and Constitutive Models, *J. Theor. Appl. Mech.*, 2005, 43, 3–35.
- [185] H. So, C.T. Chen, Y.A. Chen, Wear behaviours of laser-clad stellite alloy 6, *Wear*, 1996, 192, 78–84.
- [186] I. Velkavrh, F. Ausserer, S. Klien, J. Brenner, P. Foret, A. Diem, The effect of gaseous atmospheres on friction and wear of steel – steel contacts, *Tribology Int.*, 2014, 79, 99–110.
- [187] P. Sperka, I. Krupka, M. Hartl, The effect of surface grooves on film breakdowns in point contacts, *Tribology Int.*, 2016, 102, 249–256.
- [188] D. S. Wang, J. F. Lin, Effects of surface roughness on elastohydrodynamic lubrication of line contacts, *Tribol. Int.*, 1991, 24, 51–62.
- [189] T. Murakami, H. Mano, Y. Hibi, S. Sasaki, Friction and wear properties of Fe₇Mo₆-based alloy in ethyl alcohol, *Tribol. Int.*, 2010, 43, 2183–2189.
- [190] J. K. Mannekote, S. V. Kailas, The effect of oxidation on the tribological performance of few vegetable oils, *J. Mater. Res. Technol.*, 2012, 1, 91–95.
- [191] B. Hushan, *Modern Tribology handbook*, CRC Press, 2001.
- [192] E. M. D. Nascimento, L. M. D. Amaral, A.S.C.M. D.Oliveira, Characterization and wear of oxides formed on CoCrMoSi alloy coatings, *Surf. Coatings Technol.*, 2017, 332, 408–413.

LIST OF PUBLICATION FROM PHD WORK

1. **Saurav Kumar**, D. Kumar, O. Maulik, A.K. Pradhan, V. Kumar, A. Patnaik, Synthesis and Air Jet Erosion Study of $Al_xFe_{1.5}CrMnNi_{0.5}$ ($x = 0.3, 0.5$) High-Entropy Alloys, *Metallurgical and Materials Transaction A*, 49, 5607-5618, 2018.
2. **Saurav Kumar**, A. Patnaik, A. K. Pradhan, V. Kumar, Effect of cobalt content on thermal, mechanical, and microstructural property of $Al_{0.4}FeCrNiCo_x$ ($x=0, 0.25, 0.5$ and 1.0 mol) high entropy alloys, *Journal of Materials Engineering and Performance*, 28, 4111-4119, 2019.
3. **Saurav Kumar**, A. Patnaik, A. K. Pradhan, V. Kumar, Dry sliding wear behavior of $Al_{0.4}FeCrNiCo_x$ ($x=0, 0.25, 0.5, 1.0$ mol) High Entropy Alloys. *Metallography, Microstructure, and Analysis*, 8, 545-557, 2019.
4. **Saurav Kumar**, A. Patnaik, A. K. Pradhan, V. Kumar, Room temperature wear study of $Al_{0.4}FeCrNiCo_x$ ($x=0, 0.25, 0.5$ and 1.0 mol) high entropy alloys under oil lubricating condition, *Journal of Material Research*, 34, 841-853, 2019.
5. **Saurav Kumar**, P. Rani, A Patnaik, A K Pradhan, V Kumar, Effect of cobalt content on wear behavior of $Al_{0.4}FeCrNiCo_x$ ($x = 0, 0.25, 0.5, 1.0$ mol) high entropy alloys tested under demineralised water with and without 3.5 % NaCl solution, *Materials Research Express*, 6, 0865b3, 2019.
6. O. Maulik, D. Kumar, **Saurav Kumar**, S. Devagan, and V. Kumar, Light weight high entropy alloys: A brief review, *Materials research express*, 5, 052001, 2018.

LIST OF PUBLICATION OTHER THAN PHD WORK

7. D. Kumar, O. Maulik, **Saurav Kumar**, Y.V.S.S. Prasad, V. Kumar, Phase and thermal study of equiatomic AlCuCrFeMnW high entropy alloy processed via spark plasma sintering, *Material Chemistry and physics*, 210, 71-77, 2018.
8. D. Kumar, O. Maulik, **Saurav Kumar**, Y.V.S.S. Prasad, V.K.Sharma, V. Kumar, Impact of tungsten on phase evolution in nanocrystalline AlCuCrFeMnW $_x$ ($x=0, 0.05, 0.1$ and 0.5 mol) high entropy alloys, *Material research express*, 4, 2017.
9. O. Maulik, D. Kumar, **Saurav Kumar**, D. M. Fabijanic, and V. Kumar, Structural evolution of spark plasma sintered AlFeCuCrMg $_x$ ($x=0, 0.5, 1, 1.7$) high entropy alloys, *Intermetallics*, 77, 46-56, 2016.
10. S. P. Saini, **Saurav Kumar**, R. Barman, A. Dixit, V. Kumar, Oxidation Study of Mg-Li-Al based Alloy, *Materials Today Proceeding*, 3, 3035-3044, 2016.

BRIEF BIO-DATA OF THE AUTHOR

Mr. Saurav Kumar was born on 30th May 1988 in Allahabad, Uttar Pradesh, India. He completed his Bachelors' Degree in Mechanical Engineering in the year 2009, from Uttar Pradesh Technical University, Uttar Pradesh, India and Masters Degree in Metallurgical Engineering in the year 2013, from Indian Institute of Technology, (IIT BHU) Varanasi, Uttar Pradesh, India. He has one-year teaching experience in the academic year of 2014-15 from SLIET, Punjab (Deemed University under Government of India).

He has published ten research papers in various International journals and attended four international conferences, one national conference, three GIAN programs, and seventeen workshops at various Institutes, Research Centers and Universities within the country. Since Jan 2015, he is engaged in his Doctoral research in the area of synthesis and tribological study of high entropy alloy at Metallurgical and Materials Engineering Department, Malaviya National Institute of Technology Jaipur, Rajasthan, India under the Institute Research Fellowship scheme by Ministry of Human Resource Development, Government of India.
